CHEMICAL REVIEWS

Review

pubs.acs.org/CR

Surface Chemistry of Ruthenium Dioxide in Heterogeneous Catalysis and Electrocatalysis: From Fundamental to Applied Research

Herbert Over*

CONTENTS

Received: July 5, 2011
Published: March 16, 2012

dx.doi.org/10.1021/cr200247n | *Chem. Rev.* 2012, 112, 3356–3426

1. INTRODUCTION

Ruthenium is a chemical element that can easily adopt various formal oxidation states from −II to +VIII in chemical bonds,[1,2] thus giving rise to many compounds with interesting and often unique properties.[3,4] For instance, ruthenium is indispensable as a homogeneous catalyst in a variety of organic reactions.[5,6] Promoted metallic ruthenium is known to be the best hydrogenation catalyst for dinitrogen and therefore the most active catalyst in ammonia synthesis,[7,8] while RuO_2 turned out to be an excellent oxidation catalyst in heterogeneous catalysis[9] and electrocatalysis.[10]

Ruthenium is a relatively scarce metal, which may be hindering its wider commercialization. The annual production of ruthenium is estimated to be 25 t/year.[11] Because of the limited production, the market price per kg is high and has been quite volatile over the past 10 years (cf. Figure 1); still the price per kg of ruthenium is about 10 times lower than that of platinum.

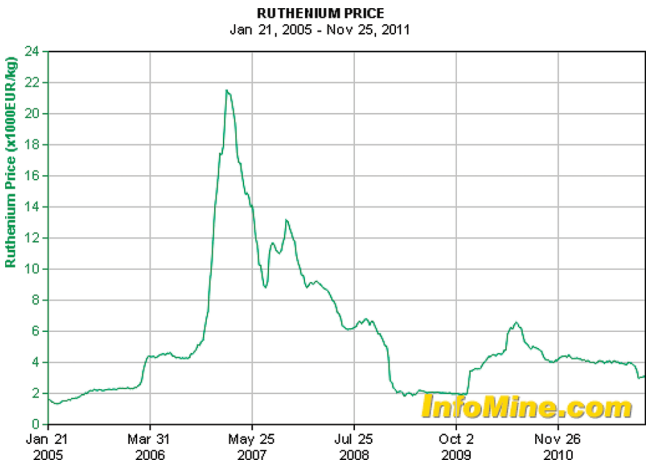

Figure 1. Evolution of the market price of ruthenium per kg in Euro over the past 10 years. Data retrieved from ref 12.

In 2010 about 3 t/year of ruthenium went into the fabrication of dimensionally stable anodes (DSAs) used in chlor-alkali electrolysis,[13] while most of the ruthenium is deployed as buffer layers and thin film resistors in the electronic industry (about 20 t in 2010).[13] To mitigate the problems caused by the limited availability of ruthenium, it is of utmost importance to understand the microscopic properties of RuO_2, especially those responsible for its chemical uniqueness. This molecular level understanding may also direct the search for alternative, more abundant materials.

However, molecular-level understanding calls for idealization of the experimental conditions including the use of model catalysts with low structural complexity such as single-crystalline surfaces and their investigation under well-controlled conditions such as ultrahigh vacuum (UHV). The trade-off for this so-called surface science approach[14] is the inevitable emergence of a pressure gap (10^{-13} bar versus 100 bar) and a materials gap (single crystal versus supported nanometer-sized particles) (cf. Figure 2), by which elementary

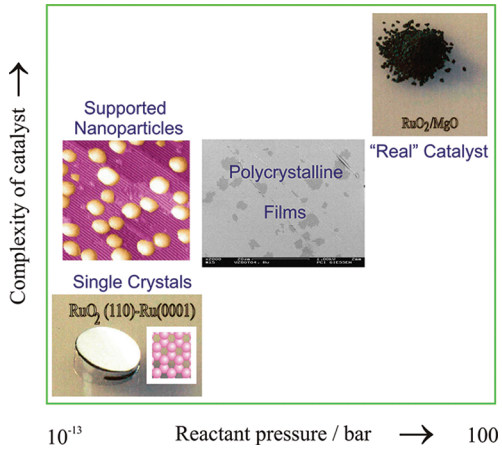

Figure 2. Model catalysis and practical catalysis are separated by two gaps: the pressure gap and the materials gap. The pressure gap is introduced by well-defined reaction and preparation conditions: In model catalysis UHV conditions are used, while typical pressures in practical catalysis may be as high as several 100 bar. The materials gap is introduced by the low structural complexity of the model catalyst. Typically, practical catalysts in heterogeneous catalysis are supported oxide or nanoparticles which are modified by electronic and structural promoters, while typical model catalysts consist of single crystals or single crystalline films or supported particles on flat oxide single crystalline supports.

reaction steps, reaction intermediates, the chemical state of the catalyst, etc. identified under well-defined conditions may not be transferable to realistic reaction conditions. In this review, I present a few examples such as the CO and the HCl oxidation over RuO_2 where both gaps have been successfully bridged.

A particularly interesting catalytic system is encountered with the CO oxidation over ruthenium. While under UHV conditions Ru(0001) is a poor catalyst for the CO oxidation,[15] at pressures in the mbar range and in particular under oxidizing reaction conditions Ru turns into an efficient catalyst.[16−18] CO oxidation over ruthenium is therefore considered as an intriguing example for a catalytic system with an apparent pressure gap. Under oxidizing reaction conditions and temperatures above 500 K, the surface phase has shown to turn into a catalytically active surface oxide.[9] Over the past decade, catalytically active surface oxides have also been identified for other platinum group metals.[19,20]

Ruthenium/ruthenium-dioxide reveals a complex and unique redox surface chemistry, which makes RuO_2 a versatile oxidation catalyst.[21] RuO_2 is successfully applied in various disciplines in chemistry such as in heterogeneous catalysis and in electrocatalysis without prompting a closer contact between these disciplines. Accordingly, progress has been made in many directions without recognizing the strength of similar developments in other fields. It was this unsatisfactory situation which motivated me to write a review article about RuO_2, a quite

dx.doi.org/10.1021/cr200247n | Chem. Rev. 2012, 112, 3356−3426

interesting but less explored material than other transition metal oxides such as TiO_2.[22−25]

In recent years, RuO_2-based catalysts have disclosed promising catalytic performance in a variety of important reactions.[26−28] RuO_2 is a promising catalyst material for the low-temperature dehydrogenation of small molecules in heterogeneous catalysis including NH_3,[29] HCl,[26] methanol,[28] and it has already been in industrial use as DSA in electrocatalysis for the chlorine-alkali electrolysis over the past 40 years.[10,30] Only recently Sumitomo Chemical[26,31] has developed and commercialized a stable and active Deacon catalyst on the basis of RuO_2 which catalyzes the gas phase oxidation of HCl with oxygen to recycle molecular chlorine. The Deacon process was discovered by Deacon some 140 years ago,[32] but due to massive problems with the stability and insufficient activity of the catalyst, the Deacon process had largely been displaced by electrolysis, a highly energy-consuming process. It is not only the activity but rather its stability which renders RuO_2 an excellent catalyst material under harsh reaction conditions such as chlorine evolution (electrochemistry) or the Deacon process (heterogeneous catalysis).

The Sumitomo process is considered as a true breakthrough in recent catalysis research since chlorine can now be recycled from HCl with low energy cost and conversion yields as high as 95%. In retrospect RuO_2-based catalysts seem to be the obvious choice for the Deacon process since such catalysts have already been in industrial use as DSA in the process of chlor-alkali electrolysis,[10] a reaction which is very much akin to the Deacon process. This example underscores the shortcoming of a highly specialized scientific community in which the expertise and knowledge of even closely related chemical disciplines such as electrocatalysis and heterogeneous catalysis are barely exchanged. Modern catalysis research needs to overcome this "community gap" to keep track with challenges ahead.[33,34]

Another intriguing property of RuO_2 is disclosed in electrocatalysis. The cyclic polarization of the ruthenium electrode between cathodic and anodic conditions results in the formation of hydrous ruthenium dioxide. Calcination of this material in air at 150 °C leads to a material containing about 10% water and revealing excellent performance as a super capacitor with a charge capacity of about 1000 F/g.[35] Accidentally or not, hydrous ruthenium dioxide with about 10% of water has also been found to be an excellent low temperature oxidation catalyst in the CO oxidation reaction[36] and in partial oxidation of alcohols.[37−39] This correlation between the performance as super caps and catalytic activity has been recognized by Rolison et al.[40] and by Yu et al.[39] Again, a close interplay of electrochemical and catalytic properties is obvious but far from being understood or being common knowledge in the catalysis community.

It is the primary scope of this review to comprehend on the fundamental physical and chemical properties of RuO_2 which are supported by experimental and theoretical data on the atomic level rather than presenting a compilation of mere empirical data. Dissimilation of this atomic scale knowledge of RuO_2 model systems across the virtual scientific borders is anticipated to be beneficial for a variety of chemical disciplines, most notably for the cross-fertilization of heterogeneous-, electro-, and photocatalysis. In the second part of this review the atomic-scale understanding of physicochemical properties of RuO_2 will guide us through the various applications of RuO_2. It is the hope that this review will promote additional RuO_2-related research in a variety of different chemical research fields.

In more detail, this review is organized as follows:

Section 2 summarizes the general physicochemical properties of RuO_2. Section 3 deals with various synthesis routes of RuO_2. This survey is not intended to be comprehensive but rather should bring the reader in contact with modern synthesis methods of RuO_2, ranging from single crystals to polycrystalline films and finally to nanostructured materials.

Section 4 is devoted to an atomic-level understanding of the complex ruthenium−oxygen surface redox chemistry. The unique redox chemistry makes RuO_2 a versatile material in various applied fields such as heterogeneous catalysis, electrocatalysis, and super capacitors. The gas phase oxidation and electro-oxidation as well as the chemical reduction of single crystalline RuO_2 surfaces are discussed at the atomic level. RuO_2 is a reducible oxide and therefore flexible against altering chemical environments. This atomic-scale information should lay the solid ground for an in-depth discussion of the chemical redox behavior of more complex RuO_2-based materials, such as powders, supported nanoparticles, and ultrathin films. Section 4.5 concludes with a comparison of the redox chemistry of RuO_2 with that of other late transition metal oxide surfaces. Platinum group metal catalysts (Ru, Rh, Pt, Ir, Pd) have shown to form also catalytically active surface oxides under oxidizing reaction conditions, thus having triggered a paradigm shift in model catalysis from a rigid catalyst toward a structural and chemically flexible catalyst which adapts itself to the reaction conditions.

Section 5 covers the atomic scale chemistry and surface properties of single crystalline $RuO_2(110)$ and $RuO_2(100)$ surfaces and briefly compares them with rutile $TiO_2(110)$.

Section 6 is devoted to the case study of CO oxidation over $RuO_2(110)$, demonstrating our current molecular understanding which is accomplished with this prototype reaction in surface chemistry. But this section shows also that even for this intensively studied system the high catalytic activity of metallic ruthenium in the CO oxidation reaction is still not fully settled.

Sections 7 and 8 cover current applications of RuO_2 in heterogeneous catalysis (7) and electrocatalysis (8). Whenever it is possible, I directly compare reactions at surfaces under gas phase conditions with those in an electrochemical environment. The simultaneous discussion of reactions at the gas/RuO_2 (Surface Science) and liquid/RuO_2 (Electrochemistry) interface represents a formidable task, since it presupposes an ability of the reader to understand the other disciplines' language.[41,42]

RuO_2 is used also in energy-related applications, such as fuel cells, batteries, and capacitors. This is the topic of section 9. Section 10 is devoted to applications of RuO_2 in the electronic industry, starting with extreme ultraviolet lithography (EUVL), the next generation of lithography and continuing with thin film technologies. Ruthenium dioxide has become an important material for improving the performance of critical components in computers and other electronic devices.

Finally I close this review in section 11 with some general conclusions about distinct properties of RuO_2 responsible for its extraordinary catalytic behavior and how surface chemistry is correlated to homogeneous coordination chemistry, electrochemistry, and heterogeneous catalysis.

2. PHYSICOCHEMICAL PROPERTIES OF RUTHENIUM OXIDES

The electronic configuration of elemental ruthenium (Ru) is $4d^7\ 5s^1$. Consequently ruthenium can form compounds with valences ranging from −II up to +VIII, making ruthenium a

dx.doi.org/10.1021/cr200247n | Chem. Rev. 2012, 112, 3356−3426

versatile metal center in complex chemistry.[1,43] Metallic Ru crystallizes in the hexagonal close packed (hcp) crystal structure. The electronic configuration of the Ru^{4+} cations is $4d^4$, if ruthenium dioxide (RuO_2) is considered to be fully ionic. In general, the electrons in d^n-oxides can quite easily be removed from the partially filled d orbitals so that d^n oxides are considered to be much more chemically active than d^0 oxides.

Ruthenium forms only one stable solid oxide phase, namely, RuO_2. Still there are persistent reports in the literature that there exists "at least two types of RuO_2",[44,45] namely, a high-temperature RuO_2 and a low temperature RuO_2.[46−48] These statements belong to the category of myths. Even a simple suboxide is thermodynamically unstable and spontaneously decomposes into RuO_2 and metallic Ru as will be shown in section 4.3. The RuO_2 bulk formation energy is −305 kJ/mol,[49] which is consistent with density functional theory (DFT) calculations of −316 kJ/mol[50] and −320 kJ/mol[51] with respect to bulk hexagonal Ru and molecular O_2. In a DFT study,[52] the corundum structure of Ru_2O_3 has shown to be thermodynamically less stable than rutile RuO_2, but it may exist as a metastable phase. There is experimental evidence from surface X-ray diffraction that this metastable phase indeed forms when Ru(0001) is exposed to high pressure of oxygen (1 mbar to 100 mbar) at temperatures below 500 K.[53]

Ruthenium dioxide crystallizes with rutile structure (cf. Figure 3), reflecting a strong tendency of Ru^{4+} to acquire octahedral coordination. The unit cell dimensions of bulk RuO_2 were determined by X-ray diffraction (XRD): a = 4.4911 Å ± 0.0008 Å, c = 3.1065 A ± 0.0003 Å at room temperature.[54] Thermal expansion coefficient can be found in ref 55. At high pressures (typical values of 100 GPa), the rutile structure of RuO_2 transforms into the cubic fluorite structure,[56] with an increase in the metal coordination number from 6 to 8. Interestingly, the bulk modulus of cubic-RuO_2 is close to that of diamond.[57,58]

Ruthenium dioxide belongs to the class of metallic conducting transition metal oxides whose electrical resistivity is 35.2 ± 0.5 μΩ·cm at room temperature,[59] that is, only a factor of 2 higher than that of metallic ruthenium (about 16 μΩ·cm). The high electronic conductivity of RuO_2 is one of the prerequisites for its intensive use as electrocatalyst and electric contacts in microelectronic devices. The electrical resistance of RuO_2 is virtually isotropic and increases with increasing temperature (characteristic for metallic conductivity). The temperature effect is readily explained by electron−phonon and electron−electron interband scattering.[59]

Ruthenium, like most other platinum group metals (PGM), is fairly resistant to chemical attack. O_2 oxidizes Ru above 700 K in an ambient environment. When bulk Ru or sintered Ru powder is exposed to air for several days at room temperature or temperatures up to 473 K, a thin film (4−8 Å thick) of native oxide forms which prevents further oxidation.[60]

The distorted RuO_6 octahedron of RuO_2 (cf. Figure 3) consists of two nonequivalent groups of O atoms: four equatorial O atoms forming Ru−O bonds of 1.984 Å and two apical O atoms having a Ru−O bond length of 1.942 Å.[61] Within the molecular orbital (MO) theory two of the five d-orbitals of Ru in RuO_2 are combined with s and three p functions of Ru to form the six hydrid orbitals $e_g^2sp^3$. These hydrid orbitals of Ru point toward the six O-ligands forming strong σ-bonding with the sp^2 hydrids of O. The rutile structure is governed by these strong σ Ru−O bonds. The other three d-orbital left (t_{2g}) form two metal−metal bonds, one σ- and one

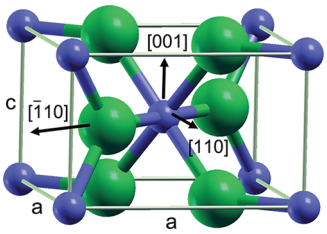

Figure 3. The three-dimensional unit cell of the rutile structure (Ru_2O_4 unit) as encountered with RuO_2 and TiO_2. Blue balls are the ruthenium atoms, and green balls are the oxygen atoms. The RuO_6 octahedron can be seen in the center of the unit cell attached to four equatorial O and the two axial O. The lattice vectors and particular directions are indicated.

π-bond along the shared edges of the octahedron, and a week π-bond with the apical O atom. Metal−metal bonds are weak and therefore structurally not significant, forming a narrow band conducting oxide (see Figure 4). The Fermi energy lies in the t_{2g} range of the density of states (DOS).[62,63] The Fermi energy falls in the relative minimum of the DOS between peaks originating from ruthenium−oxygen π and π^* states (cf. Figure 4b). Therefore, the π^* states are empty, explaining the stability of RuO_2.

The electric conductivity of RuO_2 is determined by the delocalized metal−metal states along the Ru rows in the a-direction and by electron hopping along the c-direction, leading still to an isotropic conductivity.[59]

The electronic structure of RuO_2 has been investigated both by experiments and (ab initio) electronic structure modeling. Magnetothermal oscillations in RuO_2 at a temperature of 1.3 K and magnetic fields of 10.5 T allowed a detailed mapping of the Fermi surface[64] whose topography is quite simple and consistent with electronic structure calculations.[65,66] Further Fermi surface measurements of RuO_2 include the De Haas−van Alphen effect,[67] magnetoresistance,[68] and cyclotron resonance.[69]

Valence-band photoemission measurements[71−74] can be interpreted using simple one-electron MO (molecular orbital) arguments (no intervention of various types of electron−electron and electron−lattice interactions are encountered) and are found to agree remarkable well with band structure calculations.[62,65,75−79] Quite in contrast, the electronic structure of TiO_2 is strongly affected by exchange and correlation effects so that reliable ab initio calculations have only recently appeared in the literature.[80,81]

The experimental valence band spectrum of a single crystal RuO_2 oriented in the (110) direction is shown in Figure 4a. In a simple one-electron interpretation, the angular-integrated UP spectrum reflects the DOS, weighted by the ionization cross-section.[63] The sharp Fermi-level cutoff is characteristic of a metal. The emission close to the Fermi energy is attributed to the narrow Ru-4d band with t_{2g} symmetry (indicative of a weak metal−metal bonding). To lower binding energies the O2p-derived states appear (2−10 eV below E_F) and between 20 and 25 eV below E_F O2s-derived states are located. The separation of O2p and O2s of about 15 eV compares well with the orbital energies of O2s and O2p (ε_{2s} = −32.4 eV, ε_{2p} = −15.9 eV).[82] The interpretation of the experimental valence band photoemission spectrum of RuO_2 is well reconciled with projected DOS (cf. Figure 4b) as provided for example by DFT calculations.[70]

Optical reflectivity measurements were performed with single-crystal rutile RuO_2 in the energy range 0.5−9.5 eV.[83]

dx.doi.org/10.1021/cr200247n | Chem. Rev. 2012, 112, 3356−3426

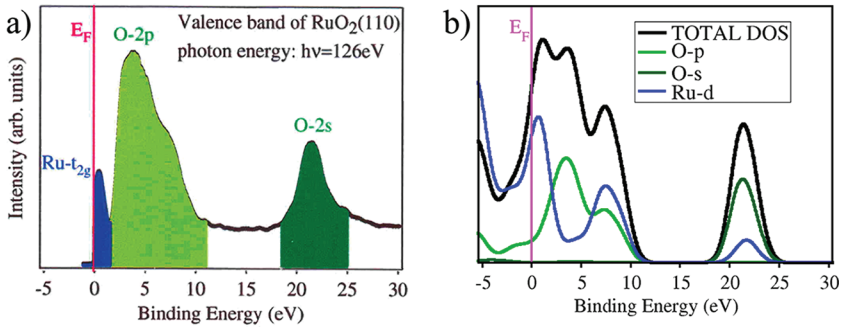

Figure 4. (a) PES data shown are taken at MAX II in Lund. The photon energy was chosen so that the cross sections for ionization of d and p electron are similar. (b) DFT calculated density of states (DOS): total DOS and projected-DOS.[70]

With the help of a Kramers−Kronig analysis of the reflectivity data the spectral dependencies of the real and imaginary parts of the complex dielectric constant were determined. The observed spectral transitions could be uniquely assigned to electronic transitions between occupied and unoccupied states.[65,79] The plasma frequiencies of RuO_2 are found in experiments between 3.0 and 3.4 eV,[83,84] while first principles theory calculated values between 3.4 and 3.7 eV.[79,85]

RuO_2 can clearly be discriminated against metallic Ru in high resolution core level shift (HRCLS) spectroscopy. Ru in rutile-RuO_2 exhibits a Ru3d doublet at 280.7 and 285.0 eV due to spin orbit splitting with a characteristic satellite feature at 282.7 eV.[86−88] The O1s related feature of RuO_2 has a binding energy of 529.5 eV.[89,88] The metallic conducting behavior of RuO_2 leads to a plasmon excitation in core level shifts of Ru3d[74,86,90] and an asymmetric shape of O1s core level spectrum,[89] which is indicative of electron−hole excitations close to the Fermi level.

The vibrational properties of single-crystalline RuO_2 have been studied by Raman spectroscopy.[91,92] The Raman active phonon modes are B_{1g} (165 cm^{-1} = 20.5 meV), E_g (528 cm^{-1} = 6.5.2 meV), A_{1g} (646 cm^{-1} = 80.0 meV), B_{2g} (716 cm^{-1} = 88.7 meV)[91] consistent with recent DFT-LDA calculations.[93] The strongest Raman active mode is the E_g mode at 528 cm^{-1} in agreement with experimental Raman studies.[44,92] To further elucidate the phonon dispersion of RuO_2, inelastic neutron scattering was applied.[93]

There are two other Ru-oxide phases discussed in the literature, namely, RuO_3 and RuO_4. RuO_4 is volatile at temperatures above 313 K and toxic. At temperatures above 373 K RuO_4 decomposes virulently into RuO_2 and O_2. Vibrational fingerprints of RuO_4 consist of stretching modes at 880 cm^{-1} (Raman) and 920 cm^{-1}/330 cm^{-1} (IR bands).[94−97] RuO_4 is important for the growth of RuO_2 single crystals by chemical vapor transport in a flowing gas reaction system.[54] From a technological standpoint, the formation of RuO_4 is of major concern as it is considered to be the main source of catalyst loss in oxidative reaction systems.[98] RuO_4 has clearly been identified as a discrete stoichiometric oxide. Quite contrary, the existence of RuO_3, which cannot be synthesized as a unique compound, has been the subject of ongoing controversy.[2]

Occasionally, RuO_3 and RuO_4 have apparently been identified with X-ray photoelectron spectroscopy (XPS) and Raman spectroscopy on RuO_2 surfaces,[99−101] but the assignments of $Ru3d_{5/2}$ features to RuO_3 and RuO_4 are debatable (or simply wrong) as discussed in more detail in ref 86. Raman and XPS experiments were performed during the high-pressure oxidation of ruthenium.[101] The assignment to RuO_3 and RuO_4 was mainly based on Raman features at 800 cm^{-1} and 875 cm^{-1}, respectively. Raman spectroscopy is, however, not sensitive to the chemical nature of the species so that this assignment is far from being conclusive. The interpretation of Ru3d and O1s core level shifts (O1s: 531.5 eV) in terms of RuO_2 is even wrong[101] with negative implications for instance for the interpretation of oxidation data of Ru-capped mirrors for EUVL applications.[102] The Ru3d features ascribed to RuO_4 and RuO_3[101] can equally be explained by contamination with water and CO. Unfortunately, the apparent observation of RuO_3 and RuO_4 on RuO_2 surfaces persists in the literature of heterogeneous catalysis and that of electrochemistry, although the experimental evidence is elusive.

3. SYNTHESIS OF RUO_2

In this section, I review various synthesis routes to produce RuO_2 in a variety of different shapes and structured on different length scales. This section is not intended to be comprehensive, but rather it should provide the reader with a quick access to modern synthesis methods of RuO_2-based materials, ranging from single crystals to nanostructured materials.

3.1. RuO_2 Single Crystals

For model investigations, a well-defined atomic structure of RuO_2 with a high degree of crystallinity is desirable such as RuO_2 single crystals which can be grown by deposition from the vapor phase. The reactive agents Cl_2, $TeCl_4$, or O_2 are known to carry the components Ru and O in the gas phase, forming $RuCl_3$, $RuCl_4$, RuO_3/RuO_4, RuO_nCl_m, etc. with sufficient partial pressures (50 mbar and higher). In general, O_2 is used as transporting agent.[54] This bears the advantage that only the constituents of Ru-oxides are in the reactor, minimizing the impurity level in the grown RuO_2 single crystals. Oxygen flow (1 bar) is passed over polycrystalline RuO_2 at 1600 K which results in a (equilibrium) mixture of RuO_3/RuO_4 in the gas phase according to RuO_2(solid) + $n/2O_2$ (gas) ⇌ $RuO_{(2+n)}$ (gas).

The outlet zone of the reactor is kept at a lower temperature, say 1450 K, where the RuO_3/RuO_4 gas mixture decomposes and RuO_2 crystallizes in the form of 1−3 mm thick blue-black plates (up to 6 × 10 mm^2) (cf. Figure 5). The (101) facet is present on most of the growth habits and appears to be the predominant orientation, followed by the (100) and (110) faces.[54,103] In order to use these crystals in surface science, the sample has to be heated in a vacuum above the decomposition temperature (about 1000 K) resulting in an ultrathin metallic layer capping the RuO_2 crystal. Subsequently, the sample is reoxidized with molecular oxygen or NO_2 at 700 K. This treatment results in a RuO_2 surface with bright and sharp

dx.doi.org/10.1021/cr200247n | Chem. Rev. 2012, 112, 3356−3426

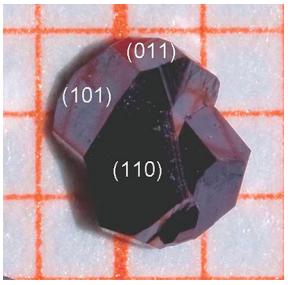

Figure 5. A small RuO_2 single crystal, exposing different facets. The size can be estimated from the underlying mm-grid. Some of the orientations of the facets are indicated.[105]

low-energy electron diffraction (LEED) patterns for the various orientations (110), (100), (101).[103,104]

3.2. Polycrystalline RuO_2

For polycrystalline RuO_2, one can simply use RuO_2 powder from commercial suppliers. Most of the exposed facets are oriented along the [110] direction (cf. Figure 6). In the past,

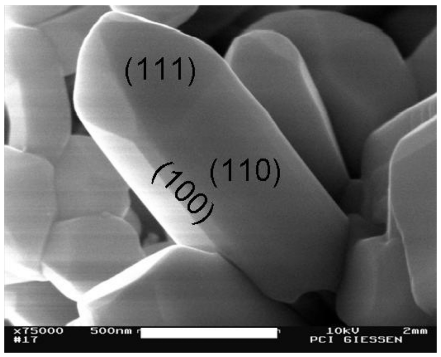

Figure 6. Scanning electron microscopy (SEM) image of polycrystalline RuO_2. The typical size of RuO_2 column is 500 nm × 500 nm (cross section) and several micrometers tall. The white bar corresponds to 500 nm. The orientations of the facets were determined by using electron back scattering diffraction.[108]

one could purchase a micrometer-scaled RuO_2 powder, but nowadays only RuO_2 nanopowder is available. The drawback of nanopowder is facile sintering and therefore missing structural stability. In order to produce microgranulated powder, one has to reduce the RuO_2 nanopowder at 770 K by hydrogen. This reduction process is sufficient to form microscale Ru metal powder as indicated by XRD. Subsequently, the microscale Ru powder is reoxidized at 1000 K in an O_2 atmosphere for several hours.[106,107] The resulting RuO_2 powder is microscaled and structurally stable.

3.3. RuO_2 Thin Film Preparation

In order to produce single crystalline RuO_2 films with specific surface orientations, one can start from metallic Ru single crystals which are cut along particular directions. A well-ordered crystalline RuO_2 film is grown by exposing the single crystalline Ru surfaces to large amounts of molecular oxygen (say 10^6 L, at 10^{-5} mbar) at temperatures in the range from 600 to 750 K. This procedure leads to the growth of a 1−2 nm thick RuO_2 film. On the Ru(0001) surface, a single crystalline RuO_2 film in (110) orientation is preferentially formed,[9,109] while on the Ru(10$\bar{1}$0) a high-quality RuO_2 film in (100) orientation can be grown.[110,111] Occasionally other orientations are observed on the Ru(0001) and Ru(10$\bar{1}$0) single crystal surfaces, such as (101).[111,112] Unfortunately RuO_2 films thicker than 3−5 nm can only be formed at higher surface temperatures, where a pronounced roughening of the oxide surface takes place.

Thicker but still flat single crystalline RuO_2(110) films with variable thickness of several 10 nm can be grown on TiO_2(110) single crystals.[90,113,114] As a Ru precursor Ru-carbonyls are frequently used and the actual oxidation process is assisted by an oxygen plasma. The adsorption and decomposition of $(Ru)_3(CO)_{12}$ over TiO_2(110) has been studied in great detail by XPS and reflection−absorption infrared spectroscopy (RAIRS).[115,116] At growth temperatures above 700 K Ti and Ru interdiffuse to form mixed $Ru_xTi_{2-x}O_2$ epitaxial films. This mixed oxide film can be utilized to minimize the lattice mismatch between RuO_2(110) and TiO_2(110), thereby producing single crystalline unstrained RuO_2(110) films of more than 20 nm thickness.[90]

Thin films of RuO_2 can also be produced either by deposition and subsequent oxidation of Ru films, or directly by deposition of RuO_2. For instance, ultrathin Ru(0001) films can be deposited on Si(001) by magnetron sputtering[117] and subsequently be oxidized at various temperatures,[118] exposing molecular oxygen, ozone, NO_2 or plasma-activated O_2.

To deposit RuO_2 thin films on dissimilar substrates, sputtering[119,120] is the most commonly used technique. O_2-containing plasmas are frequently utilized for Ru etching.[121] The Ru etching rate can be increased by Cl_2 addition to an O_2 plasma.[122] Magnetron plasma sputtering[123−125] or even better reactive sputtering in O_2 atmosphere produces RuO_2 films with a Ru/O film stoichiometry of 1:2.[44,126] These oxide films are in general polycrystalline, although it is also possible to produce X-ray amorphous RuO_2 films, depending on the substrate temperature.

Metal organic chemical vapor deposition (MOCVD) provides another method to form thin RuO_2 films.[127−130] However, these films suffer sometimes from carbon contamination. With this method, conductive RuO_2 films could be prepared either with (110)- or with (101)-textured orientations on SiO_2/Si(001).[131] The structural texture of the RuO_2 films can be controlled by both temperature and growth rate. The roughness of MOCVD-grown RuO_2 films can be reduced by codeposition of iodine containing molecules.[132] Very clean thermally stable Ru films can be produced by chemical vapor deposition (CVD) using RuO_4[133−136] or hydrous-RuO_2[137] as the metallic precursor. The Ru-films produced by hydrous-RuO_2 were characterized by XPS and micro-Raman analysis.[138]

Ruthenium oxide films can be prepared by a sol−gel spin coating technique[139] onto a Si(001) wafer. The precursor solution consists of an aqueous solution of ruthenium(III)-nitrosylnitrate $Ru(NO)(NO_3)_3$ in 2-methoxyethanol. Typical film thicknesses achieved are several 100 nm after calcinations at 1000 K for 2 h. Both thin and thick RuO_2−TiO_2 coatings on Ti substrate can be produced by the sol−gel process.[140] RuO_2 nanocrystalline films were produced by dip-coating from alcoholic solutions of $Ru(OEt)_3$ and subsequent thermal treatment in air or N_2 between 370 and 770 K.[141]

Pulsed laser deposition (PLD) is another powerful method to deposit RuO_2 films on dissimilar substrates such as $LaAlO_3$,[142] which form an epitaxial RuO_2 film with the (100) orientation normal to the surface. RuO_2 films were also grown on a MgO(100) substrate using PLD.[143] High quality films could be produced for sample temperatures above 870 K resulting in RuO_2 films that are expitaxial and (110) oriented.[144] Under oxygen deficient conditions, the RuO_2 film grows in

dx.doi.org/10.1021/cr200247n | Chem. Rev. 2012, 112, 3356−3426

(101) orientation on Si.[145] Epitaxial single crystalline films of Ru(0001) and other platinum group metals can be produced on YSZ-buffered Si(111) wafers by pulse laser deposition (PLD).[146] Subsequent oxidation leads to the growth of ultrathin RuO_2(110) films.

Thin RuO_2 films can also be prepared by electrodeposition from aqueous solution[147] or cyclo voltammetry.[148]

Thin films of metallic Ru have been grown on thin Al_2O_3 and TiO_2 films by atomic layer deposition (ALD), employing bis(cyclopentadienyl)ruthenium ($RuCp_2$) and oxygen as precursors.[149] ALD film growth is self-limited and based on surface reactions, which offers the possibility to control the deposition process on the atomic scale. For instance two- and three-dimensional (2D and 3D) objects can be coated layer-by-layer with atomic precision.[150] By keeping the precursors separate throughout the coating process, atomic layer control of the grown film can be obtained as precise as ~0.1 Å per monolayer. Oxygen has been used in Ru ALD as a reactant gas for several Ru precursors. The supplied Ru precursor is adsorbed on the surface in a first pulse and reacts with the oxygen in the second pulse. The ligands of the Ru precursor are completely or partly oxidized to volatile byproduct, mainly H_2O and CO_2. In the next pulse the Ru precursor is adsorbed onto the surface and again oxidized. The cyclization of this two-step process leads to a layer-by-layer growth of the Ru or RuO_2.[151,152] RuO_2 films were grown by ALD using O_2 and bis-(ethylcyclopentadienyl) ruthenium ($Ru(ThCp_2)_2$) as the Ru containing precursor at a deposition temperature of 540 K. Alternatively, the RuO_2 films can be deposited by liquid injection ALD.[153]

3.4. Supported RuO_2 Nanoparticles

Supported Ru catalysts Ru/MgO and Ru/SiO_2 can be prepared by the metal organic chemical vapor deposition (MOCVD) method[154] or by impregnation techniques.[16,17,155,156] Conventional ruthenium compounds which are used as precursors include K_2RuO_4, $RuCl_3{\cdot}3H_2O$, $Ru_3(CO)_{12}$, $Ru(NO)(NO_3)_3$, and $Ru(NH_3)_5Cl_3$.[157−160] For MOCVD, $Ru_3(CO)_{12}$ is typically used as the Ru containing precursor and deposited on commercially available supports such as MgO and SiO_2. The choice of the support material depends on whether basic or acidic properties of the support are needed. Afterward the precursor is thermally decomposed by a stepwise heating up to 723 K in high vacuum, thereby forming Ru nanoparticles.[154] Prior to the oxidation of the Ru particles a reductive pretreatment by H_2 up to 773 K is carried out.[161] In this way, supported Ru nanoparticles (on MgO or SiO_2) with dimensions of 1−2 nm are formed, which can be fully oxidize only above 470 K. At 400 K oxidation leads to a shell core particle with an ultrathin RuO_2 film coating the Ru core.[162]

Crystalline RuO_2 nanoparticles with a narrow size distribution within 2−3 nm are synthesized by the reaction of $NaBH_4$ with $RuCl_3$ in an ionic liquid (1-*n*-butyl-3-methylimidazolium hexafluorophosphate ($BMI{\cdot}PF_6$).[163]

In general, the Ru loading and the calcinations temperature determine the size of the supported Ru particles. However, conventional preparation of catalysts, consisting of the impregnation of a support with an aqueous solution of a soluble Ru precursor, makes it difficult to control the final size and shape of the supported metal particle. In order to obtain supported catalysts with well-defined metal particles and a narrow size distribution, catalyst preparation from metal colloids is advantageous. Recently, Vidoni et al.[164] succeeded first in obtaining a stable ruthenium colloid.

An improved synthesis route for supported Ru catalyst was proposed by Miyazaki et al.[165] A stable Ru colloid with a sharp size distribution was synthesized by using the polyol method.[166] $RuCl_3.nH_2O$ was dissolved in ethylene glycol, reduced at 453K and deposited on the support γ-alumina.[165]

Zeolite-confined nanometer-sized RuO_2 clusters were synthesized by a one-step hydrothermal method.[167,168] The RuO_2 nanoclusters contain on the average 5 Ru atoms and resemble structurally hydrous RuO_2. RuO_2 clusters are anchored in the super cages of faujasite zeolite and cannot diffuse out through the relatively narrow channels. This kind of catalyst turned out to be a selective and efficient catalyst for aerobic alcohol oxidation. A similar synthesis route leads to RuO_2 clusters within MFI zeolite (ZSM-5) channels.[169] Recently hydrothermal synthesis was applied for the encapsulation of RuO_2 clusters within sodium-LTA zeolite cages, thereby producing a caged RuO_2-based catalyst.[170]

Uniform ruthenium nanoparticles with a controlled size of 2−6 nm and a narrow size distribution were synthesized via a colloidal route[171] by a polyol reduction method using $Ru(acac)_3$ as the precursor and poly(vinylpyrrolidone) (PVP) as the surface-capping stabilizer. The Ru nanoparticles were produced by evacuation at 400 K and final drying at 480 K. The produced nanoparticles were deposited on a silicon wafer via a Langmuir Blodget approach, resulting in a two-dimensional array of Ru nanoparticles.

3.5. Nanoscale RuO_2 in Diverse Forms

As with other oxide materials, such as TiO_2[172] and ZnO,[173] RuO_2 is able to grow in a variety of nanoscaled moieties either directly or template directed.

Highly crystalline RuO_2 nanowires were grown on silica covered Si(001) wafers, by vapor transport at 930 K and atmospheric pressure.[174] These nanowires are 80−100 nm wide and several 10 μm long. The nanowires grow along the (001) direction as determined by TEM and Raman spectroscopy.[150]

RuO_2 nanometer-sized rods with pyramidal tips have been synthesized on Cu-coated Si(100) substrates using MOCVD.[175] The Ru precursor was bis(2,2,6,6,-tetramethyl-3,5-heptanedionato) (1,5-cyclooctadien)ruthenium ($(C_{11}H_{19}O_2)_2(C_8H_{12})Ru$ with ultra pure oxygen as carrier gas and a growth temperature of 710 K. First, a 4 nm thick copper layer were sputtered on Si(100). The sputtered Cu nuclei provide nucleation sites to promote the 1D growth of RuO_2 nanorods. Self-assembled and well aligned RuO_2 nanorods have been grown at 720 K via MOCVD on sapphire substrates[176] or on $LiNbO_3$(100),[177] using bis(ethylcyclopentadienyl)ruthenium as the precursor. The synthesis of RuO_2 nanorods can also be carried out by a template-based method.[178,179]

RuO_2 nanorods can be grown using reactive sputtering to generate RuO_3 as a precursor for the RuO_2 nanorod synthesis.[180,181] The growth mode changes with substrate temperature from a smooth flat film (470 K), to short rods (570 K), and finally to perfectly faceted nanorods at 720 K (cf. Figure 7). The same group[182] reported the heteroepitaxial growth of rutile TiO_2 on these RuO_2 nanorods, forming TiO_2/RuO_2 shell−core structures with promising physical properties.[181] Ruthenium-coated RuO_2 nanorods were produced in solution from $RuCl_3$ and H_2PtCl_4 in deionized water using Zn powder as the reducing agent.[183] RuO_2 nanorods are epitaxially grown on top of the tips of rutile TiO_2 nanorods. This template-directed growth led to twinned V shaped RuO_2 nanorods.[184]

dx.doi.org/10.1021/cr200247n | *Chem. Rev.* 2012, 112, 3356−3426

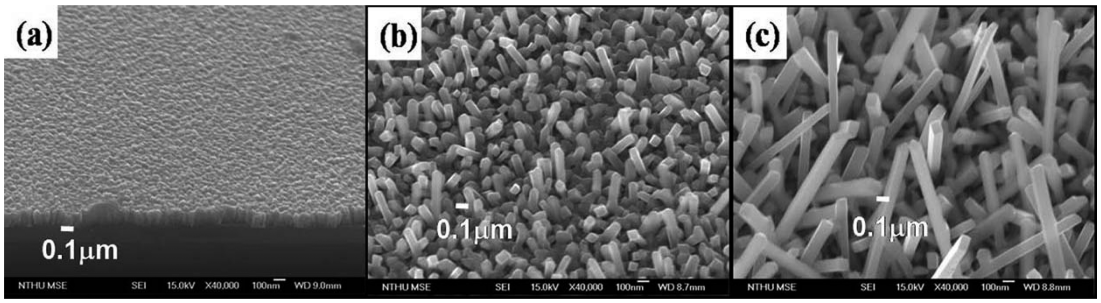

Figure 7. Morphology of RuO_2 which were prepared by deposition of RuO_3 (produced by reactive sputtering). The sample temperature was varied from 470 K (a), to 570 K (b), and 670 K (c).[180] Copyright 2006 American Institute of Physics.

Single crystalline RuO_2 nanowires were produced by using a thermal evaporation technique. The size (width from 40 to 200 nm and lengths from 1 to 8 μm) and the length to width ratio of the nanowires were controlled by tuning the growth time.[185] These well-aligned RuO_2 nanocrystals grown on sapphire substrates were characterized using Raman scattering.[186] The formation of supercooled liquid nanodroplets has been argued to be responsible for the growth of these nanowires.[174]

Monodispersed and stable Ru/RuO_2 core−shell nanoparticles of an average size of 2 nm have been synthesized using an electrochemical approach in water at room temperature without adding stabilizing agents[187] (cf. Figure 8). The

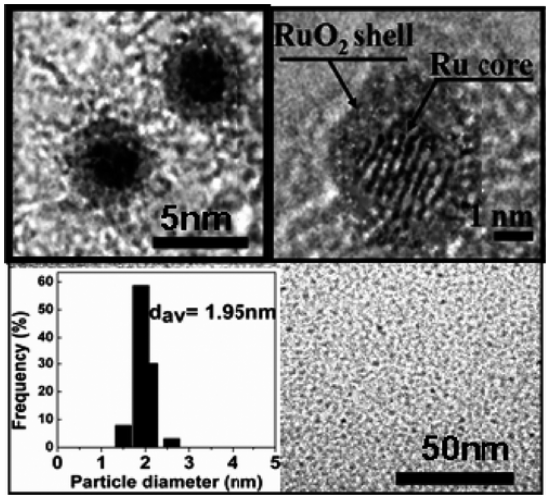

Figure 8. TEM images of the RuO_2/Ru nanoparticles, indicating a core−shell structure and a narrow size distribution of about 2 nm. Reprinted with permission from ref 187. Copyright 2010 American Chemical Society.

molecular precursor was $RuCl_3$. The core−shell structure consists of a single crystalline Ru core coated with an amorphous RuO_2 shell.

Nanoporous RuO_2 was synthesized by electrochemical lithiation.[188] This synthesis strategy is based on the observation that transition metal oxide electrodes such as RuO_2 can be reversibly discharged down to the metal level at room temperature:[189]

$$RuO_2 + 4Li \rightarrow Ru + 2Li_2O$$

In general, the electrochemical reaction leads to a formation of metal/LiO_2 nanocomposite accompanied by a large volume expansion of the order of 100%. Electrochemical delithiation leads then to nanoporous RuO_2 with a high internal surface area of 240 m^2/g via $Ru/Li_2O \rightarrow RuO_2$ (nanoporous) + 4Li. Mesoporous RuO_2[29,190] can also be prepared by a one-step nanocasting method using mesoporous silica (KIT-6) as a hard template. $RuCl_3$ is impregnated and calcined at 770 K for 3 h. Finally, the silica template is removed by NaOH.

Nanowires of crystalline RuO_2 were used to electronically connect to the interior of a mesoporous silica gel.[191] The RuO_2 nanocrystals were prepared by cryogenic decomposition of RuO_4. The RuO_2/SiO_2 composite consists of a 3D web of interconnected RuO_2 crystallites (4 nm in diameter). The resulting monolithic RuO_2/SiO_2 composite retains the free volume of the aerogel and exhibits pure electronic conductivity.

Electrospinning is a powerful method to produce both nanofibers of RuO_2 (cf. Figure 9) and mixed RuO_2/TiO_2 wires with rutile structure.[192,193] $RuCl_3 \cdot H_2O$ in DMF and $Ti(OiPr)_4$ were used as precursors for Ru and Ti, respectively. The fibers were electrospun at 0.8 kV/cm in 25% humidity and collected on a Si wafer. The fibers were calcined at 750 K for 30 min. Depending on the applied polymer both polycrystalline nanorods and tubes can be produced (cf. Figure 9).

3.6. Hydrous $RuO_2 \cdot xH_2O$

Hydrous $RuO_2 \cdot xH_2O$ can be purchased directly from commercial suppliers, or it can be synthesized by oxidation of $RuCl_3 \cdot xH_2O$ with H_2O_2,[194] or via a sol−gel process starting from $RuCl_3 \cdot xH_2O$ and NaOH.[195] The water content in hydrous RuO_2 can be adjusted by annealing to predefined temperatures.

Hydrous ruthenium oxide films are formed at Ru metal electrodes by potential cycling many times from 0 V to about 1.4 V above the hydrogen reversible potential.[196] Initially monolayer oxide formation and reduction take place. Upon continuous cycling, the oxide film progressively grows since it is not fully reduced to Ru metal at the least positive potential of the sweeps. The key point with RuO_2 is that once a thick (and rough) hydrous RuO_2 layer is formed by potential cycling, it is never reduced back to the metal in a cathodic half-cycle, so that a lower oxidation state oxide film remains on the metal surface down to the H^+/H_2 reversible potential.[196]

Nanotubular array architectures of hydrous RuO_2 nanotubes have been prepared by means of a membrane-templated synthesis route such as the anodic deposition of $RuO_2 \cdot xH_2O$.[197] The anodic deposition was achieved from its chloride precursor using a conductive binder in the form of $RuO_2 \cdot xH_2O$ nanocrystallites prepared by a hydrothermal synthesis method.[198] The nanotubular structure is clearly seen in SEM images (cf. Figure 10) when the $RuO_2 \cdot xH_2O$ nanotubes are annealed at 470 K for 2 h.

Nanocrystalline RuO_2 can be prepared by a sol−gel approach, using ruthenium(II) nitrosylnitrate and annealing the amorphous precursor in air to predefined temperatures of

dx.doi.org/10.1021/cr200247n | Chem. Rev. 2012, 112, 3356−3426

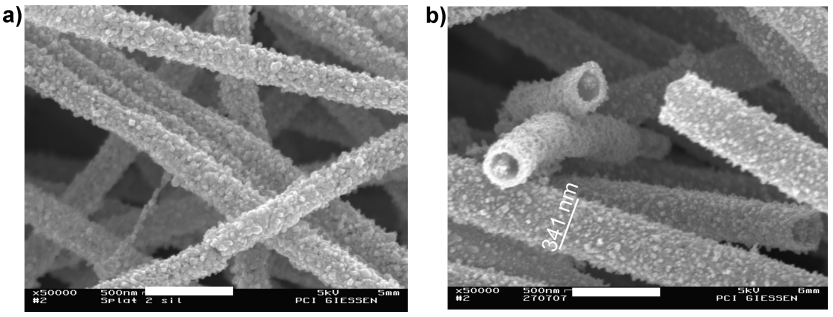

Figure 9. (a) RuO_2 nanorods and (b) RuO_2 nanotubes. Both are prepared by electrospinning.[193] The white bars correspond to 500 nm.

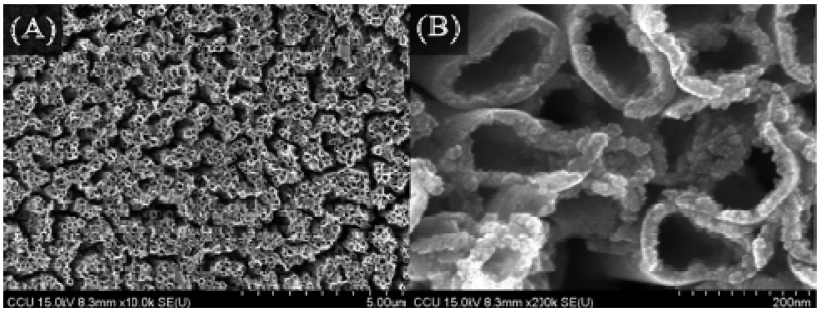

Figure 10. (A, B) SEM images of the top of an electrode of arrayed $RuO_2 \cdot xH_2O$ nanotubes. Reprinted with permission from ref 197. Copyright 2006 American Chemical Society.

670 and 1170 K.[199] The resulting unsupported RuO_2 nanoparticles have a characteristic size of 10−50 nm. In Figure 11 HRTEM images of the 670 K annealed sample are compared to the 1170 K annealed sample, showing particles of reconstructed shape. Obviously, the nanocrystals annealed at 670 K expose preferentially (110), (100), and (101) faces, as expected from the calculated surface energies (Wulff construction) by Lopez et al.[200] Nanocrystals prepared at 1170 K show in addition to these faces also (410) facets at the expense of (110) facets.

3.7. RuO_2-Based Electrode Coatings

RuO_2-based electrode coatings are called dimensional stable anodes (DSA) and these electrodes are employed in the electrochemical evolution of chlorine (CER: chlorine evolution reaction) and oxygen (OER: oxygen evolution reaction). DSA are commonly prepared by painting $RuCl_3$ or a mixture of $RuCl_3$ with titanium isopropoxide onto a Ti plate and firing the deposit in air or oxygen at 670−770 K. The painting and firing procedure is usually repeated some 10−12 times to produce a relatively thick conducting film.[201] It has been suggested that electrocatalytic properties and stability of DSA can be significantly improved if the active coating is prepared by a sol−gel procedure,[202,203] as an alternative to the commonly used preparation procedure that involves thermal decomposition of metal chlorides.[201] The electrochemical behavior for the CER depends sensitively on the aging time of RuO_2 and TiO_2 sols.[204]

A typical cracked-mud morphology of a RuO_2-based DSA is depicted in Figure 12. SnO_2 is frequently used as an additive in industrial RuO_2-based electrodes to enhance their selectivity for chlorine evolution with respect to OER.[45]

Alternative preparation methods have been developed to reduce the number of required calcination steps in the painting and firing procedure. With electrodeposition, metal ions can be precipitated in the form of amorphous oxide and hydroxides which are transformed into the crystalline oxides by subsequent thermal treatment. Zhitomirsky succeeded first in the simultaneous electro-deposition of TiO_2 and RuO_2 onto a Ti plate in the form of a mixed oxide layer.[206,207] Since the electrodeposited films are thicker than those produced by painting, fewer calcinations steps are required to produce a similarly thick DSA coating.

Improved DSA materials are in the focus of current chlor-alkali research. Recently, Chen et al.[208] synthesized a novel structure of coating which consists of active nanocrystals of rutile RuO_2/TiO_2 supported on anatase TiO_2. Anatase TiO_2 stabilizes the high dispersion and inhibits the growth and agglomeration of active rutile particles.

4. COMPLEX SURFACE-REDOX-CHEMISTRY OF RUTHENIUM

In this section the complex surface redox chemistry of ruthenium will be reviewed, focusing on well-defined model systems in order to provide atomic level understanding of the underlying processes. I shall be starting with the gas phase oxidation in comparison with electro-oxidation of well-defined Ru surfaces such as Ru(0001) and Ru(10$\bar{1}$0). Subsequently the reduction behavior of these well-defined RuO_2 surfaces is discussed and compared to the redox behavior of more complex Ru-based materials. In the last section, the redox properties of other platinum group metals are discussed for low index single crystal surfaces.

4.1. Gas Phase Oxidation of Single Crystalline Ruthenium Surfaces

4.1.1. Ru(0001). When exposing the close-packed Ru(0001) surface to molecular oxygen under UHV condition, oxygen molecules dissociate without activation forming strong O−Ru bonds. These chemisorbed oxygen atoms interact with each other and form ordered (2×2)-O[209−211] or (2×1)-O[212−214] overlayers with coverages of 0.25 and 0.5 ML,

dx.doi.org/10.1021/cr200247n | Chem. Rev. 2012, 112, 3356−3426

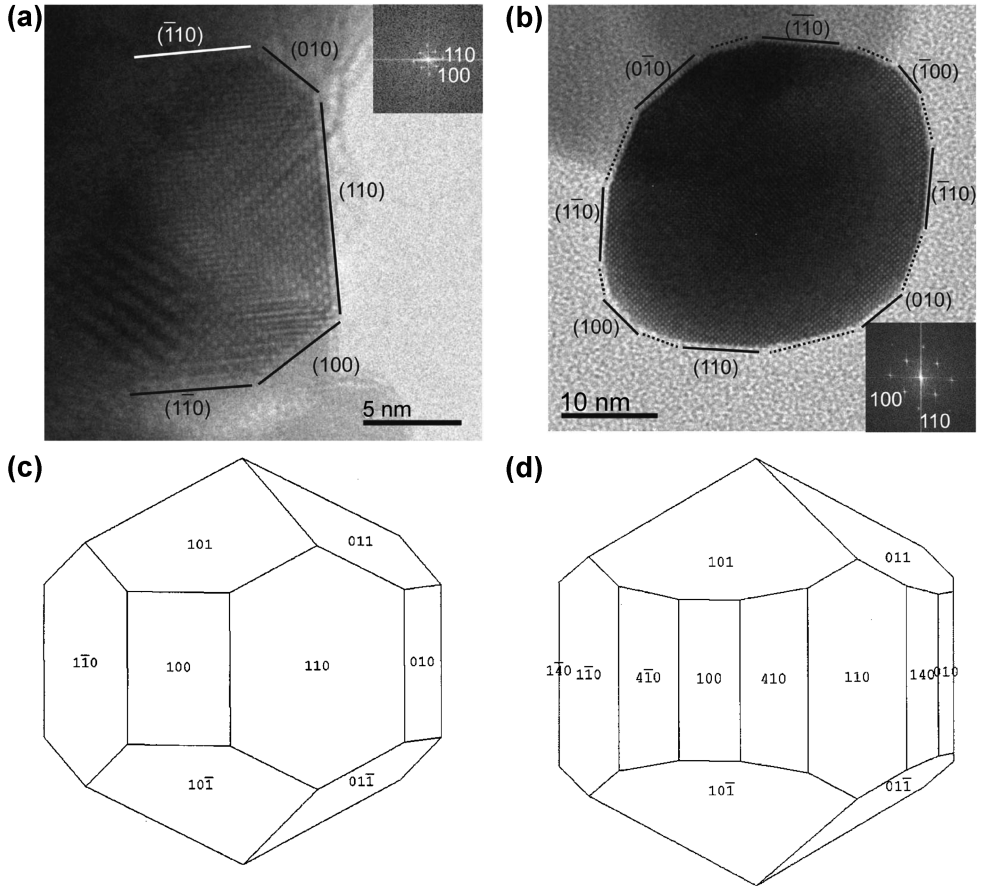

Figure 11. HRTEM image of a typical nanocrystal prepared at 670 K (a) and 1170 K (b) in the projection along the direction [001]. The inset shows the diffraction pattern obtained by fast Fourier transform of the HRTEM. The straight lines were added to guide the eye and mark the corresponding crystal faces. Reconstructed shapes are shown of a typical nanocrystal prepared at 670 K (c) and 1170 K (d). Reprinted with permission from ref 199. Copyright 2006 The Electrochemical Society.

respectively;[215] one monolayer (1 ML) corresponds to a coverage of as many adsorbates on the surface as metal atoms in the topmost layer. The (2×1) and the (2×2) overlayer have surface unit cells which are two times longer along one high symmetry direction and one respectively two times longer along the other high symmetry direction of the Ru(0001) substrate (cf. Figure 13). The dissociative sticking coefficient drops from almost one at low coverages to less than 10^{-3} at 0.5 ML, that is, one out of 1000 impinging O_2 molecules dissociates. Therefore, under typical UHV conditions the (2×1)-O phase had been considered as the saturation surface O phase.[209] Since the symmetry of the (2×1) O-phase is lower than that of the substrate, three rotational domains are formed on the surface (cf. Figure 13, STM image).

A molecular chemisorption state of O_2 has not been identified for Ru(0001).[217] Dosing much more of molecular oxygen, say more than 1000 L (one Langmuir: 1 L corresponds to a dose of 1.3×10^{-6} mbar·s) or high exposures of NO_2 (100 L) at surface temperatures of about 500 K the Ru(0001) surface is able to stabilize two additional ordered surface phases of chemisorbed O, namely, the (2×2)-3O[218−220] and the (1×1)-O[221] with coverages of 0.75 and 1.0 ML, respectively. Oxygen adsorption on the Ru(0001) surface takes place exclusively in the 3-fold hollow (hcp) site, independent of the O coverage[222] (cf. Figure 13).

Vibrational losses (O-metal stretch vibration) of the chemisorbed O on Ru(0001) are found to be at 520, 581,

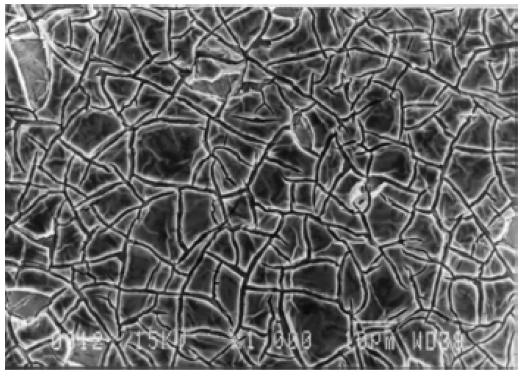

Figure 12. Typical surface morphology of a DSA with 30 mol % RuO_2 and 70 mol % TiO_2. Reprinted with permission from ref 205. Copyright 2006 Elsevier.

640, 646 cm^{-1} for the (2×2)O, (2×1)O, (2×2)3O, (1×1)O, respectively.[217,218,223−225] The O−Ru binding energies are 5.55 eV (2×2)O, 5.10 eV (2×2)3O, 5.28 eV (2×1)O, 4.84 eV (1×1)O with respect to free O atoms.[226,227] Chemisorbed O on Ru(0001) is stronger bound than O in RuO_2; that is, the decomposition temperature of RuO_2 is lower than the desorption temperature of chemisorbed O under UHV conditions.[228] The dissociative sticking coefficient of oxygen over the Ru(0001)-(1×1)O surface is estimated to be less than 10^{-6}.[229] Excessive exposures of oxygen or NO_2 at elevated

dx.doi.org/10.1021/cr200247n | Chem. Rev. 2012, 112, 3356−3426

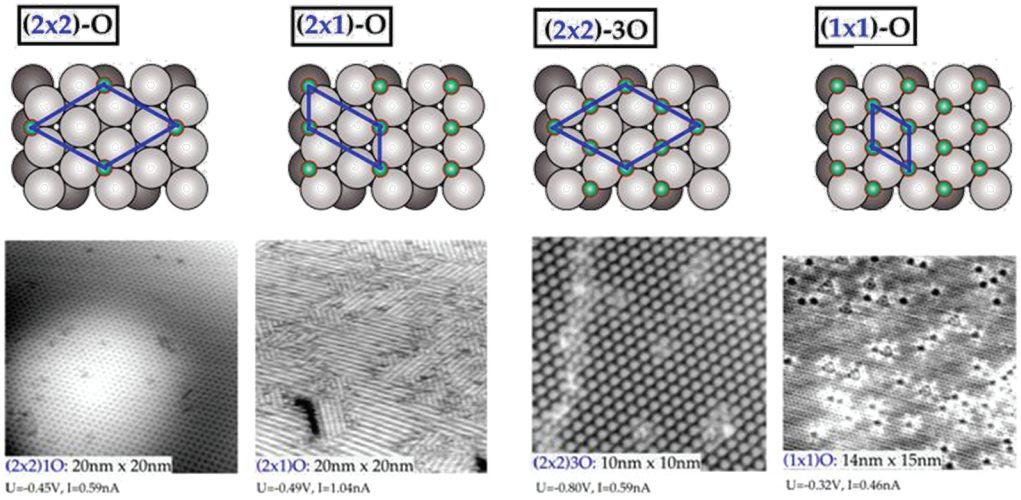

Figure 13. Chemisorbed oxygen (green balls) surface structures on Ru(0001) including the surface unit cell in blue and corresponding STM images.[216]

temperatures (>500 K) are required to accommodate more than 1 ML of oxygen in the Ru(0001) system.[87,103,109,230−232] With thermal desorption spectroscopy (TDS), up to 100 times more O_2 was observed (50 ML) than with a well-defined (2×1)O phase (1/2 ML).[231] Gas phase oxidation of Ru(0001) was first reported for high NO_2 exposure at 800 K on the basis of Ru3d core level shift spectra.[231] Consequently, oxygen uptake beyond a coverage of 1 ML is considered to be rate controlling for the initial oxidation of Ru(0001).

The RuO_2(110) film grows via a "nucleation and growth mechanism" on Ru(0001) above temperatures of 550 K, as directly observed in STM.[233] In-situ surface X-ray diffraction (SXRD) measurements,[109] where the X-ray intensity of a typical RuO_2 related reflection is monitored as a function of the oxygen exposure time, are consistent with the proposed nucleation and growth mode which can also be considered as an autocatalytic oxidation process of ruthenium.[234] The long induction period observed in these data together with a threshold O_2 pressure of 10^{-5} mbar (at T = 650 K) required to oxidize the Ru(0001) sample suggests that the formation of critical RuO_2 nuclei initiates the oxide growth. The formation of a RuO_2 nucleus is a dynamical process of growth and decomposition. Only beyond a critical size is the RuO_2 nucleus stable (critical nucleus) which affords a minimum oxygen pressure depending on the sample temperature. This explains also why oxidation of the Ru(0001) does not take place under typical UHV conditions when only 10^{-7} mbar of oxygen is introduced.

The grown RuO_2(110) film on Ru(0001) is 1.6 nm thick over a wide temperature range from 550 to 650 K and a pressure range of 10^{-4} mbar to 10 mbar,[109] manifesting a self-limited growth of RuO_2(110) on Ru(0001). A similar thickness of the oxide was derived from a XPS study.[235] From the l-scans in SXRD, which probes the structure normal to the surface, the RuO_2(110) film surface is found to be very flat; that is, both the surface and the interface Ru/RuO_2 are very smooth. The atomic structure of the Ru/RuO_2 interface is unknown. The oxide film grows epitaxially and incommensurately to the underlying Ru(0001) substrate,[236] while the size of the RuO_2(110) domains is several 10 nm across, when the oxide film is grown below 650 K.[109] With SXRD the in-plane lattice parameters of the RuO_2(110) film were found to be 3.10 Å × 6.39 Å.[109] These values correspond to values of the bulk-truncated unit cell, namely, 3.11 Å × 6.38 Å. Together with the incommensurate growth, the found lattice parameters support the model of an unstrained RuO_2(110) film grown on the Ru(0001) surface. Since the RuO_2(110) oxide film with its rectangular unit cell exhibits no 3-fold symmetry as the Ru(0001) substrate, three domains rotated by 120° coexist on the Ru(10001) surface (cf. Figure 14). If oxygen exposure is not too high, the (1×1)O phase coexists with the RuO_2(110) oxide phase as observed in STM (Figure 14)[237] and also in LEED.[236]

With quantitative LEED and DFT, the atomic structure of the RuO_2(110) surface has been determined with its surface structure being close to bulk-truncated RuO_2(110) structure.[236] The orientation of the RuO_2 film formed by gas phase oxidation depends on the orientation of the supporting Ru substrate and the preparation procedure. For instance, on the Ru(0001) surface RuO_2 grows preferentially in the (110) orientation,[236] while on the Ru(10$\bar{1}$0) surface RuO_2 grows mainly in the (100) orientation.[110] However, the electrochemical oxidation of Ru(0001) results in the growth of a rough RuO_2(100) oriented film.[238] The bulk-truncated RuO_2(100) surface has a rectangular unit cell of 4.49 Å and 3.11 Å. The long side matches well the periodicity of the Ru(0001) in the [10$\bar{1}$0] direction (4.69 Å) within 4.5%; the RuO_2(100) would be expanded along the [010] direction (cf. Figure 15) in order to match the Ru(0001) lattice. The unit cell of the RuO_2(100) film grown on Ru(0001) is close to a (2×2) surface structure.

Below a threshold temperature of about 500 K, Ru(0001) cannot be oxidized by O_2 exposure.[109,239] Instead in the temperature range 400−500 K a so-called transient surface oxide (amorphous oxygen rich phase with subsurface oxygen) has been proposed to evolve.[240,241] If not molecular oxygen but NO_2 is used for the oxidation of Ru(0001) at 800 K, then many monolayers of oxygen can be accommodated on the Ru(0001) surface forming an oxide on the surface.[231] However, NO_2 exposure of 500 L at lower temperatures, say 600 K, can incorporate about 4−5 ML of oxygen in the near surface region without forming an oxide;[103] these high coverage O phases reveal a (1×1)O surface structure in LEED which cannot be transformed to an oxide simply by postannealing the sample to higher temperatures.

dx.doi.org/10.1021/cr200247n | Chem. Rev. 2012, 112, 3356−3426

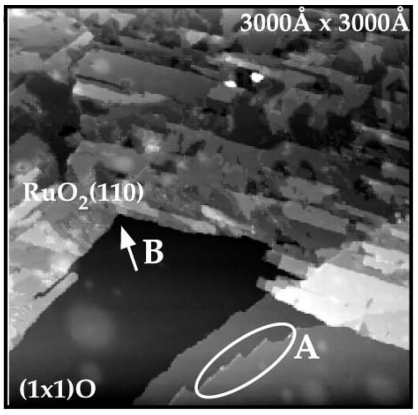

Figure 14. Large-scale experimental STM images 3000 Å × 3000 Å of the oxidized Ru(0001) surface, showing both large $RuO_2(110)$ and (1×1)O patches coexisting on the surface. STM parameters: U = −0.95 V, I = 0.09 nA. The initial oxide at the step edges of the (1×1)O areas are indicated by A. The intersection of two rotational domains of $RuO_2(110)$ are marked by B. Reprinted with permission from ref 237. Copyright 2002 Elsevier.

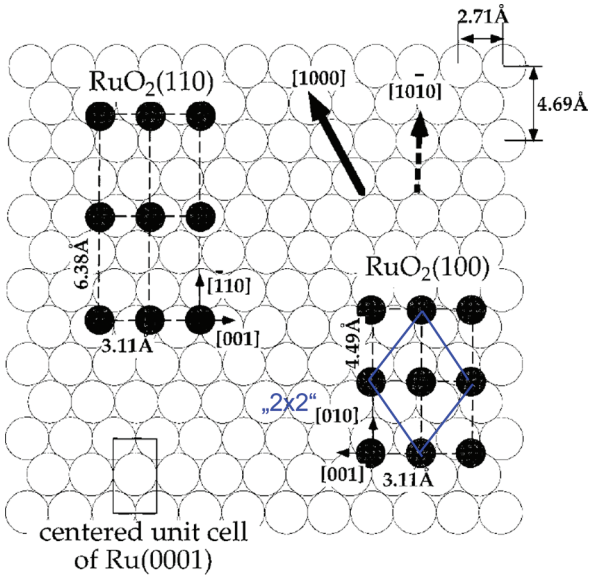

Figure 15. Schematic (top view) of the domains of $RuO_2(110)$ and $RuO_2(100)$ on Ru(0001) which are aligned along the [1000] and [10$\bar{1}$0] directions of the Ru(0001) substrate. The $RuO_2(100)$ film on Ru(0001) forms a quasi (2×2) structure. Reprinted with permission from ref 110. Copyright 2001 American Chemical Society.

In order to determine which surface structures are stable when the Ru(0001) is in contact with an O_2 phase, ab initio thermodynamic calculations[242,243] were carried out by Stampfl et al. (cf. Figure 16).[244] The surface structure with the lowest free energy for a given chemical potential of oxygen is the thermodynamically stable phase; the free energy depends linearly on the chemical potential of oxygen $\Delta\mu_O$. The clean Ru(0001) is stable for $\Delta\mu_O < -2.7$ eV. For -2.7 eV $< \Delta\mu_O <$ -1.4 eV various chemisorbed O-phases (2×2)O, (2×1)O, (2×2)3O, (1×1)O are stable besides a $(\sqrt{3}\times\sqrt{3})R30°$ −2O structure, which has not been observed experimentally.[244] Above a chemical potential increment of −1.4 eV bulk RuO_2 represents the most stable phase. For fixed temperature the chemical potential can be translated into O_2 pressures as indicated in Figure 16.

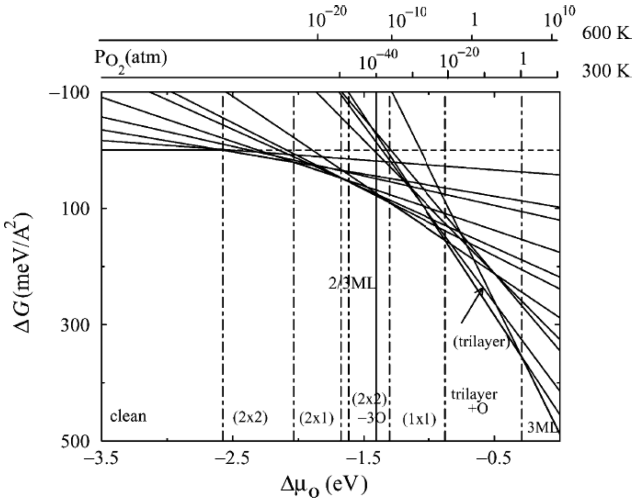

Figure 16. Calculated free energy for selected low energy O−Ru(0001) structures. The chemical potential is given with respect to half of the energy of molecular O_2 in the gas phase. The vertical continuous line indicates the theoretical formation of RuO_2 per O atom. Reprinted with permission from ref 244. Copyright 2005 Elsevier.

On most metal surfaces, high oxygen exposure and relatively high temperatures drive the transition from chemisorbed O to the formation of an ultrathin oxide film (1−2 nm thick). Stuckless et al.[245] proposed for the case of nickel that a critical coverage of chemisorbed O is required to induce surface oxidation and that this transition is thermodynamically and not kinetically determined.

The transition from oxygen adsorption to oxide formation on Ru(0001) is structurally quite complex due to the coexistence of various oxygen phases on the surface and roughening of the oxide surface[112] that results in a complex pattern formation on the micrometer scale as studied with PEEM,[246] SPEM,[87] and LEEM.[247,248] For instance, for the "star-like" pattern observed in PEEM[246] a detailed STM investigation has shown that this morphology is caused by faceting of the RuO_2 film with predominating (100) oriented facets.[249] Above 750 K the RuO_2 film is able to grow thicker but at the expense of a substantially surface roughened of $RuO_2(110)$.[109,249]

The oxidation mechanism has not been settled on the atomic scale. Frequently, the involvement of subsurface oxygen has been invoked to precede the actual oxidation step.[229,232,240,250] Subsurface oxygen in Ru(0001) has structurally been observed with medium energy ion scattering.[251] However, the experimental evidence whether subsurface O is required for the actual oxidation process is only of indirect nature and not conclusive. There is also no experiment available in the literature that demonstrates oxide formation induced by simple annealing of a subsurface oxygen phase. On the basis of DFT calculations a O−Ru−O trilayer has been proposed as the precursor for the oxidation of Ru(0001),[252] but experimentally this trilayer has not unambiguously been identified.

In a recent in situ LEEM study the oxidation process of Ru(0001) using NO_2 was shown to be governed by an intricate interplay of energetics and growth kinetics.[248] The observed quasi (2×2) micro-LEED pattern was assigned to the formation of a O−Ru−O trilayer.[247] However, recent SXRD experiments indicate that the quasi (2×2) phase is traced to the growth of $RuO_2(100)$ on Ru(0001)[53] (cf. Figure 15). Blume et al. suggested without providing further evidence that

dx.doi.org/10.1021/cr200247n | Chem. Rev. 2012, 112, 3356−3426

the TSO (transient surface oxide) is related to the O−Ru−O trilayer.[240,241]

The oxidation of Ru(0001) at 600K-800K in a mixture of 115 ppm of O_2 in Ar produced a monolayer of ordered $RuO_2(110)$ in the form of rectangular stripes.[253] The growth of these $RuO_2(110)$ stripes is unidirectional, starting from step edges. These ultra thin stripes may be associated with O−Ru−O trilayers. Thermodynamically, ultrathin surface oxides are stabilized by the adhesion energy at the interface to the metal substrate. This contribution to the free energy lowers the O_2 pressure for the growth of a thin oxide film below that required for bulk-oxide stability.[254] Combined STM and SPEM experiments on Rh(111) and Ru(0001) have demonstrated that oxide films grow more promptly in step bunching regions than on flat terraces.[255] This observation has been confirmed on Ru(0001) by in situ LEEM experiments.[248]

Although there is no conclusive evidence for the precursor behavior of the O−Ru−O trilayers in the oxidation of Ru(0001), this trilayer motif has been identified unambiguously with STM, SXRD, and XPS in the surface oxidation of other platinum group metal (PGM) surfaces, such as Rh(111),[256] Rh(110),[257] Rh(100),[258] and Ir(111).[259]

4.1.2. Ru(10$\bar{1}$0). Exposing a single crystalline Ru(10$\bar{1}$0) surface to molecular oxygen leads to the formation of a c(2×4)-2O and a (2×1)p2 mg-2O overlayers[260,261] with coverages of chemisorbed O of 0.5 and 1 ML, respectively. The atomic structures of both O-overlayers were determined by LEED and DFT,[262] indicating that in both phases the oxygen atoms adsorb in 3-fold hollow sites along the flanks of the Ru trenches, forming zigzag chains. These zigzag chains have been visualized with STM.[263] O−Ru stretch vibrations of the chemisorbed O on Ru(10$\bar{1}$0) are found to be at 536 and 512 cm^{-1} for the c(2×4)2O and (2×1)2O, respectively,[262] while the O−Ru metal binding energy is 2.81 and 2.59 eV with reference to free $^1/_2$ O_2, respectively. Higher O coverages on Ru(10$\bar{1}$0) are realized under UHV conditions by exposing NO_2, an efficient oxidant. At 2 ML of surface oxygen a "streaky" (1×2) structure is observed in LEED, which is discussed in terms of a precursor state for the oxidation of Ru(10$\bar{1}$0).[110] Higher oxygen exposures of 1000 L are equally able to form the (1×2) precursor phase on Ru(10$\bar{1}$0).[110,241,264] Chemisorbed O on Ru(10$\bar{1}$0) is stronger bound than O in RuO_2: the decomposition temperature of RuO_2 is lower than the desorption temperature of chemisorbed O under UHV conditions.[110]

Even higher exposures of NO_2 or O_2 to Ru(10$\bar{1}$0) at elevated temperatures (600−660 K) lead to the growth of a crystalline expitaxial RuO_2 film which is oriented in the (100) direction along the surface normal of the substrate.[110,111,264,265] The $RuO_2(100)$ film grows lattice-matched with its [010] direction along the [0001] direction of Ru(10$\bar{1}$0) (4.5% compressively strained), while the [001] direction of $RuO_2(100)$ on Ru(10$\bar{1}$0) grows incommensurately along the [$\bar{1}$2$\bar{1}$0] direction of Ru(10$\bar{1}$0) (cf. Figure 17). The minimum temperature required for the oxidation of Ru(10$\bar{1}$0) is about 500 K.[264] The dimensions of the surface (1×1) unit cell of $RuO_2(100)$ on Ru(10$\bar{1}$0) film has been determined by SXRD to be 4.28 Å × 3.12 Å,[266] and the atomic structure of the $RuO_2(100)$ surface has been solved by quantitative LEED and DFT. Besides small relaxations of the atomic positions at the surface, the structure is closely related to the bulk-truncated structure of RuO_2 along the (100)

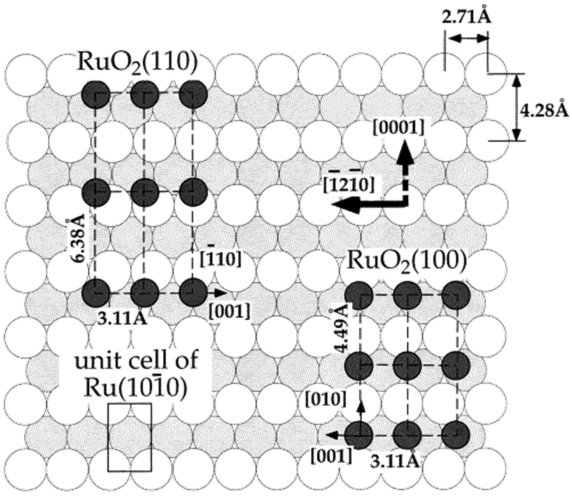

Figure 17. Schematic (top view) of the domains of native bulk-truncated $RuO_2(110)$ and $RuO_2(100)$ on Ru(10$\bar{1}$0) which are aligned along the [0001] and the [$\bar{1}$2$\bar{1}$0] directions of the Ru(10$\bar{1}$0) substrate. Actually, the $RuO_2(100)$ film is compressed in the [0001] direction from 4.49 Å to 4.28 Å. Reprinted with permission from ref 110. Copyright 2001 American Chemical Society.

direction.[110] The surface energy of $RuO_2(100)$ is 87 meV/Å^2, slightly higher than for $RuO_2(110)$ with 71 meV/Å^2.[267]

Exposing the Ru(10$\bar{1}$0) surface to high doses of oxygen at sample temperatures in the range of 700−800 K results in a LEED pattern with c(2×2) symmetry. CO adsorption experiments demonstrate that the c(2×2) LEED pattern is actually a superposition of (1×1) domains and c(2×2) domains.[110] The atomic structure of the c(2×2) has not been resolved so far. STM studies have confirmed the coexistence of (1×1) and c(2×2) patches on the $RuO_2(100)$ surface (cf. Figure 18).[111,112] While CO adsorbs readily on the (1×1)

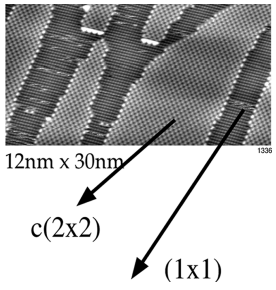

Figure 18. Experimental STM image (constant current mode, taken at room temperature) of the $RuO_2(100)$ surface: 12 nm × 30 nm, U = −0.80 V, I = 0.59 nA. The checkerboard structure is a c(2×2) phase, while the striped structure comprises a (1×1) of $RuO_2(100)$. Reprinted with permission from ref 112. Copyright 2004 John Wiley and Sons.

patches, no CO adsorption takes place on the c(2×2) domains. At least for the CO oxidation reaction the c(2×2) domains are catalytically inactive.

Since the decomposition temperature of $RuO_2(110)$-c(2×2) is slightly higher than that of the $RuO_2(100)$-(1×1), the c(2×2) has been suggested to be a reconstructed $RuO_2(100)$-c(2×2) surface phase with a lower surface energy than bulk-truncated $RuO_2(100)$. Under similar preparation conditions, STM studies provide evidence that besides the (100) orientation also RuO_2

dx.doi.org/10.1021/cr200247n | Chem. Rev. 2012, 112, 3356−3426

domains with (111) orientation[111] and (101) orientation[112] grow on Ru(10$\bar{1}$0).

4.2. Electro-oxidation of Ru(0001)

For acidic solutions the electrochemical processes during electro-oxidation can be summarized as[97]

$$Ru + 2H_2O \rightarrow RuO_2 + 4H^+ + 4e^-$$

However this simple reaction equation does not offer any atomic level insight into the process of electro-oxidation of Ru. The electrochemical uptake of oxygen on a Ru(0001) model electrode and its electro-oxidation was studied by a combined EC-UHV experiment with a closed sample-transfer system.[238] Ordered (2×2), (3×1), and (1×1) oxygen-related adlayers were identified by ex-situ LEED and AES on the Ru(0001) electrode emersed from 0.1 M $HClO_4$ solution at potentials of 0.22, +0.34, and 1.34 V versus RHE, respectively. A similar voltammetric curve was measured for Ru(0001) in a deoxygenated 0.05 M H_2SO_4 solution[253] (cf. Figure 16, left). Taking the LEED IV curves as finger prints,[268] the electrochemically prepared (1×1) oxygen related phase is shown to be identical to that obtained by gas-phase preparation of the (1×1) O under UHV conditions.[221] In particular, the first Ru layer distance was determined to be 2.22 Å in the EC-prepared (1×1) O phase. Exactly the same Ru interlayer distance was derived from in situ X-ray reflectivity experiments when the Ru(0001) surface was emersed from a 1 M H_2SO_4 solution at a potential of +1.0 V versus the reversible hydrogen electrode (RHE).[269]

When the potential of the Ru(0001) electrode is kept at 1.34 V (vs RHE) for 2 min, RuO_2 grows epitaxially with its (100) plane parallel to the surface of Ru(0001) as deduced from ex-situ RHEED.[238] The RuO_2(100) film is very rough, growing as 3D domains with an average size of 2 nm, whereas the nonoxidized Ru(0001) surface is still flat. Polarizing the Ru(0001) electrode at 2.20 V (vs RHE) for 2 min results in a surface which is fully covered by a rough oxide film. The observed oxidation of Ru in the form of RuO_2 at such high positive potentials is consistent with the corresponding Pourbaix diagrams.[270]

The electro-oxidation of Ru(0001) in 0.05 M H_2SO_4 was also studied by in situ STM[253] (cf. Figure 19, right). Clearly, the oxidation starts at the step edges in the form of small clusters (size about 2−3 nm) at a potential of 1.17 V versus RHE. Bulk oxidation of Ru(0001) starts at potentials above 1.27 V vs RHE. STM images indicate smooth regions (chemisorbed O on Ru(0001)), oxide islands along the step edge (size about 2−3 nm), and larger oxide island on the terraces (5 nm). The authors concluded that the Ru atoms necessary for oxide growth stem from the dissolution of step edges.[253]

Altogether these experiments show that the initial state of Ru(0001) electro-oxidation involves oxygen adsorption of up to one full monolayer at potentials below the onset of Ru bulk oxidation in acidic solutions. The electro-oxidation of Ru(0001) proceeds starting from a (1×1)O overlayer via a "nucleation and growth" type of mechanism.[238]

This behavior resembles closely that of the gas phase oxidation of Ru(0001).[234] Using atomic oxygen, the gas phase oxidation of Ru(0001) above 650 K was studied by STM.[233] The oxidation of Ru(0001) starts with the corrosion of the steps and the formation of small RuO_2 cluster leading to STM images which are strikingly similar to those shown in Figure 19, right. This finding may offer the prospect to gain atomic insights into electrochemical oxidation processes by using atomic O instead of molecular oxygen in gas phase experiments.

During the oxidation of polycrystalline Ru electrodes at high potentials and for long time periods the oxygen evolution is accompanied by corrosion of the electrode in acid media.[95] Kötz et al. found with in situ differential reflectance spectroscopy that corrosion of a Ru electrode in deoxygenated 0.5 M H_2SO_4 solution at 1.17 V (versus SCE: saturated calomel electrode) produces RuO_4 in the solution. A similar conclusion was drawn by Wohlfahrt-Mehrens and Heitbaum applying online mass spectrometry[271] and by Walker et al. on the basis of in situ potential-modulated reflectance spectroscopy.[272] In-situ IR spectroscopy studies[97] of ruthenium electrodes in acid and alkaline solutions indicate that RuO_4 is observed at 1.4 V (versus RHE) during corrosion in acid solution, while perruthenate anions (RuO_4^-) are identified in alkaline solution. Corresponding systematic experiments on single crystal Ru electrodes are missing.

4.3. Reduction of RuO_2(110)

RuO_2 is an oxide which can be readily reduced but less easily be reoxidized. There are several ways to reduce RuO_2(110) back to the Ru metal, either chemically by exposing reducing agents including CO, H_2, or methanol at temperatures above 420 K, or

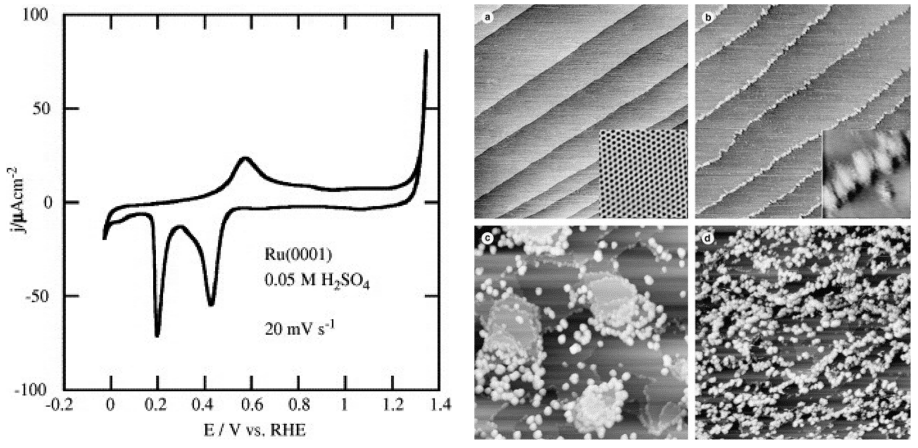

Figure 19. (Left) Voltammetric curve of a Ru(0 0 0 1) surface in deoxygenated 0.05 M H_2SO_4. (Right) EC-STM images of the oxidation of Ru(0 0 0 1) in 0.05 M H_2SO_4 at (a) 1.0 V, (b) 1.17 V, (c) 1.27 V, and (d) 1.35 V. Image (a) 500 × 500 nm, *Z* range 2 nm, inset 4 × 4 nm; (b) 230 × 230 nm, *Z* range 2 nm, inset 20 × 20 nm, *Z* range 2 nm; (c) 165 × 165 nm, *Z* range 10 nm; and (d) 250 × 250 nm, *Z* range 10 nm. Reprinted with permission from ref 253. Copyright 2004 Elsevier.

dx.doi.org/10.1021/cr200247n | *Chem. Rev.* 2012, 112, 3356−3426

simply by heating the sample in a vacuum to 850−1000 K. The thermal decomposition reaction of RuO_2 in vacuum is described by the reaction equation $RuO_2 \rightarrow Ru + O_2$; that is, RuO_2 decomposes by releasing O_2 at 950 K,[232,273] forming either a metallic Ru layer on top of RuO_2[104,237] or ultimately a pure Ru metal surface. It should be emphasized that no intermediate bulk Ru-suboxide RuO_x ($x < 2$) has ever been identified. Rather the RuO_2 surface reduces in a way that metallic Ru islands are formed on intact RuO_2 patches.[274] The thermal decomposition of $RuO_2(110)$ single crystal at elevated temperatures was investigated by using SEM, XRD, XPS, and Raman spectroscopy.[275] The anisotropic decomposition of $RuO_2(110)$ by vacuum annealing causes longitudinal surface fissures and stripes of Ru nuclei.

4.3.1. Reduction by Hydrogen. The reduction of a $RuO_2(110)$ surface by molecular hydrogen exposure at 413 K was monitored with in situ SXRD.[109] In Figure 20 the X-ray intensity of a typical $RuO_2(110)$ related diffraction spot as a function of the hydrogen exposure at various temperatures up to 413 K is shown. The temperature of 413 K coincides with the maximum H_2O desorption.[276,277] Below 373 K, RuO_2 cannot be bulk-reduced, but at a sample temperature of 413 K the surface oxide disappears after a total H_2 dose of 3×10^4 L. From the SXRD data (l- and h-scans), it was observed that neither the thickness nor the mean size of the oxide domains changes during the reduction process; only the number of domains diminishes. In fact, this kind of reduction process was verified with STM[278] for the thermal decomposition of $RuO_2(110)$ under UHV, visualizing that a partially reduced surface consists of holes in RuO_2 down to the underlying Ru(0001) substrate in an otherwise intact $RuO_2(110)$ film. Obviously, the oxide does not decompose in a layer-by-layer fashion.

At temperatures lower than 393 K the $RuO_2(110)$ surface is also partially reduced by hydrogen exposure but much less efficiently[280] (cf. Figure 20). Chemical reduction of $RuO_2(110)$ by hydrogen exposure can even be performed at room temperature, at least partly, since at this temperature already water is formed on the $RuO_2(110)$ surface.[274] An in-depth reduction of $RuO_2(110)$ is not observed at room temperature even if pressures of 100 mbar are applied[281] presumably because the formed water cannot leave the surface via desorption thus inhibiting the further reduction process.

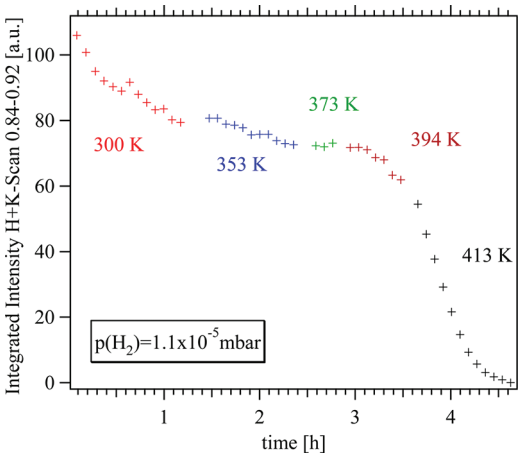

Figure 20. Surface X-ray diffraction data that demonstrate the reduction of $RuO_2(110)$ on Ru(0001) by hydrogen exposure at various sample temperatures. Even at room temperature the $RuO_2(110)$ starts to be reduced. However, after 1 h the reduction process at room temperatures slowed down substantially. Above 390 K the reduction process is very efficient, reducing the $RuO_2(110)$ layer completely within one hour.[279]

4.3.2. Reduction by CO. At temperatures around 420 K exposure of the $RuO_2(110)$ surface to 10^{-5} mbar of CO for 1 h fully reduces the oxide film to metallic Ru.[109] Blume et al.[239] used high-pressure XPS (HP-XPS) to study the CO oxidation in excess CO. They found that above 400 K RuO_2 was chemically reduced. Below 400 K a full reduction of $RuO_2(110)$ has not been observed. Similar to the reduction by hydrogen neither the thickness nor the sizes of the RuO_2 oxide domains was observed in SXRD to change during the reduction process; only the number of oxide domains is reduced during the reduction process.[109]

STM in combination with high resolution core level spectroscopy demonstrates that a chemical reduction of $RuO_2(110)$ by CO exposure results in an ultrathin metallic Ru film that caps the RuO_2 surface.[112] Similar results were reported for the reduction of RuO_2 single crystals.[104] These findings suggest the development of a buried RuO_2.

4.3.3. Reduction by Methanol. With in situ HP-XPS,[241,282] it has been shown that methanol is an extraordinarily efficient agent in the chemical reduction of $RuO_2(110)$ at temperatures above 420 K (the desorption temperature of water) and with methanol pressures as low as 10^{-6} mbar.

4.4. Reduction and Oxidation Behavior of Structurally More Complex Ru-Based Materials

4.4.1. Polycrystalline Powder and Supported Nanoparticles of Ru and RuO_2. Temperature programmed reduction (TPR) experiments reveal that the RuO_2 powder catalyst can be fully reduced at 560 K when using CO and H_2 as reducing agents.[106,107,283] The TPR experiments applying H_2 as the reducing agent indicate that RuO_2 powder catalysts can already be reduced at 440 K in a few minutes,[106] fully consistent with the reduction of $RuO_2(110)$ nanofilms.[118] Facile reduction of RuO_2 powder samples by hydrogen has been reported to take place at even 370 K on the basis of thermogravimetric analysis (TGA) measurements.[284] The same study indicates that a full reoxidation of the once reduced RuO_2 powder needs high temperatures (about 1000 K) and oxygen exposure time longer than 90 min. For the bulk oxidation of microscale RuO_2/Ru shell core particles in flowing oxygen, temperatures above 573 K were found to be sufficient.[106] A full oxidation of supported Ru nanoparticles on MgO or SiO_2 in flowing oxygen takes place already at 470 K,[162] while reduction in H_2 takes place below 430 K.[285] With in situ X-ray diffraction, it has been shown that Ru nanoparticles can reversibly be reduced at about 400 K and oxidized at about 500 K.[286,287]

4.4.2. Polycrystalline Ru Films. Recent XPS studies of 6 nm thick Ru films supported on Si(001)[118] showed that the oxidation by molecular oxygen exposure takes place only beyond a threshold temperature of 473 K. The nanometer size character of the Ru film does not facilitate the initial oxidation process. At room temperature only chemisorbed O and oxygen located in the grain boundaries are identified with photoemission spectroscopy. The chemical reduction of such oxidized Ru nanofilms by molecular hydrogen is highly effective and proceeds already at 370 K. Similar experiments were carried out by applying an oxygen plasma keeping the sample at room temperature.[288] For 3 nm thick Ru films both subsurface

dx.doi.org/10.1021/cr200247n | Chem. Rev. 2012, 112, 3356−3426

O and oxidation has been reported as well as etching of the Ru film via RuO_4 formation.[120]

Kötz and co-workers[289] studied the electro-oxidation of a thick polycrystalline Ru film in 1 M H_2SO_4 by ex-situ XPS. At a potential of 0.75 V against SCE chemisorbed O on Ru was identified, while at a potential of 1.2 V characteristic shifts in the O1s and Ru3d core levels occurred which were interpreted as a transition toward the hydrated oxide phase. Upon anodic oxidation, the $Ru3d_{5/2}$ peak shifted to 281 eV and O1s emission to 529.8 eV (cf. Figure 21). From a comparison with HRCLS

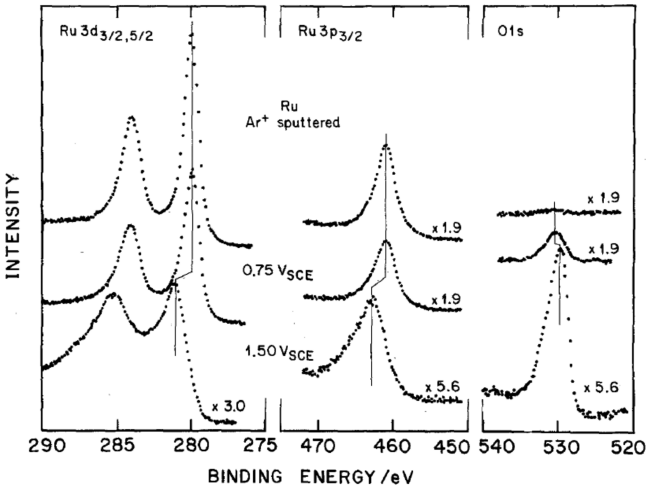

Figure 21. XPS spectra of Ru3d, Ru3p, and O1s core levels of a polycrystalline bulk Ru film electrode exposed to Ar^+ sputtering (4 keV, 2.5 mA, 30 min), 1 M H_2SO_4 (15 min) at potentials of 0.75 and 1.5 V against SCE. Reprinted with permission from ref 289. Copyright 1983 The Electrochemical Society.

experiments of oxidized Ru(0001) under UHV conditions, the observed shifts by Kötz et al. point rather to the formation of anhydrous instead of hydrous RuO_2 (cf. Table 1).

Nishiyama et al. reported that exposure of atomic hydrogen, produced by a cyclotron resonance plasma source, can efficiently reduce ultrathin RuO_2 films on a crystalline Ru film even at room temperature.[100,102,290] This observation is consistent with previous experiments by Weinberg and co-workers who found that chemisorbed oxygen on Ru(0001) (chemisorbed O is stronger bound to the surface than O in RuO_2) can readily be removed by titrating atomic hydrogen above 200 K under UHV conditions.[291,292]

4.5. Redox Surface Chemistry of other Platinum Group Metal Single Crystals

In this section the oxidation behavior of platinum group metals other than ruthenium will be reviewed. With ex-situ XPS the oxidation of Pd and Pt was already intensively studied in 80s of the last century.[293,294] Recently, for rhodium, palladium, platinum, and iridium an ultrathin surface oxide has shown to form under conditions at which the catalyst is most active in the CO oxidation.[19,20,259,295] Over the past 10 years, a tremendous increase in the atomic-scale understanding has been seen for the oxidation of catalytically relevant transition metals.[259,296−300] The dominating structural motif in these ultrathin oxide films turns out to be the O-Me-O trilayer. Actually the first report of an O-Me-O trilayer (without naming it) goes back to Mitchell and co-workers who studied the surface structure during initial oxidation of Zr(0001) with LEED.[301,302] The O-Me-O trilayer was later revisited by theoreticians for the O/Ru(0001) system.[252]

4.5.1. Rhodium. Rhodium surfaces are able to stabilize a variety of overlayer structures with chemisorbed O without forming a surface or bulk oxide.[303] However, beyond a critical oxygen exposure and temperature surface oxidation sets in. On the low index surfaces with (111), (110), and (100) orientation, these surface oxides consist of the same structural motif, namely, the O−Rh−O trilayer (cf. Figure 22).[297] In the following we will briefly review the oxygen-Rh surface chemistry.

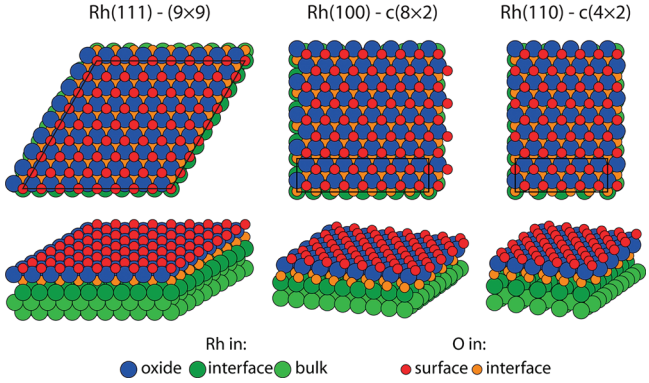

Figure 22. Models of the surface oxide structure as found on Rh(1 1 1), Rh(1 0 0), and Rh(1 1 0) consisting of a O−Rh−O trilayer motif. The surface unit cells are indicated. Reprinted with permission from ref 20. Copyright 2009 Elsevier.

4.5.1.1. Rh(111). Under typical UHV conditions, a (2×2)O and a (2×1)O overlayer is formed on the Rh(111) surface,[304,305] where chemisorbed oxygen atoms reside in fcc-hollow sites. Exposing 10^{-3} mbar of oxygen to Rh(111) at 400 to 500 K is able to stabilize two further chemisorption phases, namely, a $(2\sqrt{3}\times2\sqrt{3})R30° - 8O$ and a (2×2)3O phase with O coverages of 2/3 ML and 3/4 ML, respectively.[306] Using atomic O a metastable (1×1)O phase can be prepared.[307] Small amounts of subsurface oxygen has been identified in Rh(111) with photoelectron diffraction.[308]

The surface oxide grows on Rh(111) at a temperature of 750 K when applying oxygen partial pressure of 5×10^{-4} mbar for 30 min.[256] The LEED pattern exhibits a moiré surface structure with (9×9) symmetry. Detailed investigations, applying the methods of LEED, STM, HRCLS, SXRD, and DFT, disclose a self-limiting growth of a O−Rh−O trilayer constituting the surface oxide structure. Bulk oxidation proceeds by stacking such O−Rh−O trilayers interlinked with single Rh planes to form the (0001) surface of corundum Rh_2O_3. In the internal interface between the surface oxide and the Rh(111) substrate the oxygen is most strongly bound in on-top positions of the substrate lattice. This is quite in contrast to chemisorbed O which prefers to occupy fcc-hollow sites on the Rh(111) surface.

The oxidation of a vicinal Rh(553) surface at 10^{-6} mbar and a temperature of 650 K leads to the evolution of (331) facets at which a one-dimensional (1D) oxide is formed along the steps.[309] Further increase of pressure and temperature results in the formation of (111) facets, which are covered by an O−Rh−O trilayer surface oxide.

CO reduction studies of the (9×9) phase show that CO molecules do not adsorb directly on the (9×9) although the surface oxide can be chemically reduced.[310] According to DFT

dx.doi.org/10.1021/cr200247n | Chem. Rev. 2012, 112, 3356−3426

calculations CO adsorbs first on the nonoxide part of the Rh(111) surface. Subsequently the (9×9) decomposes by expelling O from the oxide to the metal surface where CO is oxidized. The (9×9) serves therefore as a sacrificial source of surface oxygen in the CO oxidation. Equally well can the (9×9) be reduced by hydrogen exposure although the oxide is inert with respect to hydrogen adsorption. Again nonoxidic areas on the Rh(111) surface are seen to be responsible for the uptake of hydrogen which initiates the chemical reduction of the (9×9) surface oxide.[311]

4.5.1.2. Rh(100). Under typical UHV conditions, p(2×2)-O, c(2×2)-O, and (2×2)-pg-2O overlayers are formed on the Rh(100) surface with O coverages of 1/4 ML, 1/4 ML-1/2 ML, and exactly 1/2 ML, respectively.[312−316]

A c(2×8) surface oxide is formed when the Rh(100) surface is exposed to 5×10^{-5} mbar of O_2 for 600s at 700 K. The experimental data as obtained from LEED, STM, and HRCLS prove a similar O−Rh−O trilayer surface oxide as observed on Rh(111). The atomic structure of this surface oxide was determined by quantitative LEED and SXRD analysis[258] as well as by photoelectron diffraction.[317]

4.5.1.3. Rh(110). Oxygen adsorption on the Rh(110) surface leads to a number of ordered surface structures,[222,303,318] namely, (2×2)p2mg-2O, c(2×6)-8O, c(2×8)-12O, and (2×1)p2mg-2O with O coverages increasing from 1/2 ML up to 1 ML (cf. Figure 23).

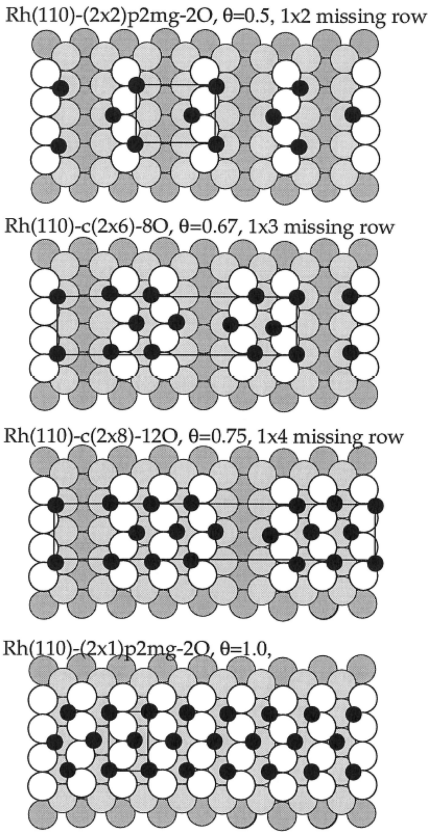

Figure 23. The stable O-phases on Rh(110) are shown as these develop with increasing O coverage; note the number of missing rows depends on the actual O uptake.[222] The surface unit cells are indicated. "c" means centered unit cell. "g" stands for glide plane symmetry, while "m" indicates a mirror plane. Reprinted with permission from ref 222. Copyright 1998 Elsevier.

Common to all O-chemisorption phases is that oxygen induces a (1xn) missing row type reconstruction on the Rh(110) surface (n = 5, 4, 3, 2) and that the oxygen atoms form zigzag chains with oxygen located in the 3-fold coordinated sites along alternating flanks of the troughs with a Rh−O bond distance of 2.0 Å[319] (cf. Figure 23). Starting from the (2×2)p2mg-2O phase a metastable (2×10) structure can be prepared by exposing the surface to 30 L of O_2 at 200 K and annealing to 500 K.[320] STM together with HRCLS and DFT identified this (2×10) phase with a 1D oxide,[321,322] consisting of Rh row segments which are decorated with O atoms on both sides. This kind of oxide was also found along the steps of a vicinal Rh surface.[309,323] Exposing the Rh(110) surface to oxygen pressures of 10^{-4} mbar at 750 K, a well-ordered oxide film is formed with c(2×4) symmetry.[324] The atomic structure of this surface oxide consists of a O−Rh−O trilayer[257] as also observed on Rh(111) and Rh(100).

4.5.2. Palladium. *4.5.2.1. Pd(111).* Besides the (2×2)-1O overlayer a surface oxide with $\sqrt{6}$ times the nearest-neighbor distance of Pd was observed at high oxygen exposure and temperatures of 600 K (referred to as $\sqrt{6}$ structure).[325] The oxidation of Pd(111) was previously studied by high temperature STM.[326] High pressure XPS[327] during the oxidation of Pd(111) in the 3×10^{-3} mbar O_2 range revealed a number of oxygen species, including a 2D surface oxide,[328] supersaturated adsorbate O layers, dissolved oxygen and a $(\sqrt{67}\times\sqrt{67})R12.2°$ structure. A detailed analysis applying STM, DFT, LEED, HRCLS, and SXRD[328,329] has resolved the atomic structure of the surface oxide to be a Pd_5O_4 overlayer. The surface oxide is related neither to any known bulk oxide of Pd nor to a simple continuation of the bulk Pd(111) surface. The surface oxide layer binds to the substrate via on-top O or bridging O on Pd(111).

The oxidation of vicinal Pd(553) surface has been studied from UHV to atmospheric pressures with STM, LEED, SXRD, HRCLS, and DFT.[330] In the pressure range from 10^{-6} mbar to 1 mbar and a sample temperature of 570−670 K, a surface oxide forms and rearranges the (553) surface facets into (332) facets. The surface oxide can be described as a O−Pd−O trilayer (strained PdO(101)). Above 1 mbar, the surface oxide is replaced by PdO bulk oxide.

4.5.2.2. Pd(100). Oxygen exposure under UHV conditions leads to the observation of several ordered surface structures, (2×2)-1O, c(2×2)O, $(\sqrt{5}\times\sqrt{5})R27°$. The oxidation of Pd(100) was examined by high temperature STM.[331] While the (2×2) and c(2×2) are clear O-overlayer structures, the $(\sqrt{5}\times\sqrt{5})R27°$ structure turned out to be a surface oxide whose atomic structure has been solved by applying STM, LEED, DFT, and HRCLS.[332,333] This surface oxide can be considered as a well-ordered but strained PdO(101) layer on Pd(100), or as a O−Pd−O trilayer structure as identified with the surface oxidation of rhodium. The oxidation process of Pd(100) was followed by in situ SXRD from 10^{-6} mbar to ambient pressures of oxygen. Depending on the environmental conditions, either the formation of the $(\sqrt{5}\times\sqrt{5})R27°$ surface oxide, or the growth of a 4 nm thick poorly ordered and rough PdO bulk oxide was observed, predominantly with PdO(001) orientation.[334] The role of steps and the oscillatory occurrence of the Pd surface oxide have been shown to govern the activity in the CO oxidation over Pd(100).[335]

4.5.2.3. Pd(110). The interaction of the Pd(110) surface with oxygen was first described by Ertl and Raul,[336] who reported a number of surface structures such as p(1×3), p(1×2), c(2×4),

dx.doi.org/10.1021/cr200247n | Chem. Rev. 2012, 112, 3356−3426

c(2×6), and a "complex" structure. Since then, the O/Pd(110) system has been intensely investigated.[129,337−349] The strong oxygen−oxygen interaction leads to the formation of a "zig-zag" type missing row structure with c(4×2) symmetry. If more oxygen is incorporated into the surface, antiphase domain boundaries are formed consisting of filled missing rows whose density increases with oxygen coverage, producing a continuous displacement of the diffraction spots.[350] The complex structures, also denoted the $(7\times\sqrt{3})$ and $(9\times\sqrt{3})$[349] with a coverage of 6/7 and 8/9 ML respectively, are a consequence of the relaxation of the stress induced by the close proximity of the oxygen atoms in a fictitious (2×1)-2O structure. The structure cannot be called a surface oxide, since none of the bond lengths are similar to those in bulk PdO. Although DFT predicts a structure similar to the surface oxides found on Pd(111) and Pd(100), such structures are inhibited experimentally by the extra energy gained from the formation of domain walls in the $(7x\sqrt{3})$ and $(9x\sqrt{3})$ structures.[349]

4.5.3. Platinum. *4.5.3.1. Pt(111).* Under UHV conditions, oxygen forms a simple (2×2)O overlayer structure on Pt(111).[351,352] On-surface structures up to 0.75 ML were prepared by exposing NO_2.[353] Using atomic O as the oxidizing agent, several high-coverage O phases up to surface oxidation could be prepared and characterized.[354,355] At higher O_2 exposures and sample temperatures around 700 K a surface oxide is formed with a (8×8) superlattice which consists of bulk-like, strongly distorted α-PtO_2 trilayers with a thickness of 4−5 Å.[356] The α-PtO_2 trilayer is stable on Pt(111)[357,358] for two reasons: α-PtO_2 is the stable bulk oxide in oxygen at room temperature and atmospheric pressure, and it consists of a layered structure with isolated O−Pt−O trilayers.

The initial growth of PtO_2 on Pt(111) was induced by an atomic oxygen beam and monitored with STM.[359] It turned out that oxygen atoms arrange into p(2×1) structures above a O coverage of 0.25 ML. These features were attributed to Pt-oxide chains. As the coverage increases to 0.75 ML, the chains interconnect to form a Y-shaped network. The stability of the 1D (2×1) Pt-oxide was studied by DFT calculations.[360] It was shown that the Pt-oxide chains involve oxygen atoms near hcp sites and form close packed Pt rows that run parallel to the (2×1)O rows of chemisorbed oxygen. More recently, the high temperature oxidation (1250−1350 K in 5×10^{-5} mbar of oxygen) of Pt(111) with molecular oxygen was studied with STM, indicating a self-limiting growth of well-ordered PtO_2 nanoclusters which reveal a O−Pt−O trilayer structure.[361]

Concerning the activity of the oxidized Pt(111) surface toward CO oxidation, there are conflicting results. Some experiments show that oxidized Pt(111) is less active than the metallic surface,[362,363] while others indicate that Pt-oxide is extraordinarily active in the CO oxidation.[364] DFT calculations predict that the oxidized Pt(111) is active in the CO oxidation.[358]

4.5.3.2. Pt(110) and Pt(100). A surface oxide on Pt(110) was found and characterized by combining STM, TPD, and DFT.[365] As in the case of Rh(553), a 1D PtO_2 oxide grows on Pt(110) surface and along the steps of a vicinal Pt(332) surface. The 1D oxide on Pt(332) is highly reactive in the CO oxidation[366] similar to that on Pt(110).[367] The 1D oxide is stable in an oxygen pressure range where bulk oxides of Pt are metastable. Therefore the 1D PtO_2 was considered to be a precursor for the Pt bulk oxidation.

Besides the 1D surface oxide a 2D surface oxide on Pt(110) with (12×2) periodicity was identified with STM.[365] This surface oxide is reminiscent of a buckled version of the PdO(101) surface observed on Pd(100), a similarity which may be associated with the same bulk oxide structure of PtO and PdO. Oxidation of Pt(110) was shown to enhance the catalytic activity toward CO oxidation substantially.[19]

So far no experimental data are available for the oxidation of Pt(100). However, recent DFT calculations predict the stability of a PtO_2 trilayer on Pt(100).[357] An epitaxial registered (2×1) oxide bilayer was experimentally observed on narrow Pt(100) nanofacets.[368]

4.5.4. Iridium. Chemisorbed oxygen forms a (2×2)O overlayer on Ir(111)[325,369] and a $(\sqrt{3}\times\sqrt{3})R30°$ phase at higher NO_2 exposures and sample temperatures of 590 K;[370] in both phases O atoms adsorb in fcc sites. The oxidation of the Ir(111) surface by O_2 exposure was studied by in situ SXRD and DFT calculations.[259] At 575 K and an O_2 partial pressure of 10^{-3} to 1 mbar, a hexagonal O−Ir−O trilayer forms on Ir(111), resembling the initial oxidation of Rh(111).[256] Increasing the O_2-pressure to 100 mbar leads to the formation of the O−Ir−O trilayer, onto which a hexagonal multilayer oxide with a corundum structure grows. The hexagonal multilayer oxide is a metastable precursor toward the bulk oxide formation. According to DFT calculations, both the trilayer and multilayer surface oxides are thermodynamically not stable with respect to the bulk rutile IrO_2, and are thus considered to be transient, kinetically stabilized structures. At higher temperatures (775 K or above), the O−Ir−O trilayer surface oxide forms at intermediate pressures (around 1 mbar) and transforms at higher pressures (around 100 mbar) into bulk like rutile IrO_2, exhibiting predominantly (110)- and (100)-oriented domains. The oxidation of the Ir(111) follows the general trend for oxidation of the late transition metals in that the formation of a few-atomic-layer-thin, so-called surface oxide, precedes the bulk oxidation. The oxidation of Ir(111) and properties of IrO_2(110) were studied independently by Zhang et al. applying DFT calculations.[371]

The temperature-induced deoxygenation of single crystal IrO_2(110) in the temperature range 403−493 K was explored by HRCLS experiments in combination with DFT calculations.[372] The reduction process starts by removing the bridging O atoms and forming quite strong cus Ir/on-top O bonds. DFT calculations indicate that the rate determining step for the decomposition of IrO_2 is the recombination of two on-top O adatoms. The thermally induced decomposition of IrO_2(110) sets in already at 433−443 K.[275]

On Ir(210) nanoscale faceting was observed upon oxidation.[373]

5. ATOMIC SCALE CHEMISTRY AND PROPERTIES OF SINGLE-CRYSTALLINE RUO_2 SURFACES

In this section, I shall discuss the atomic scale characterization of single-crystalline RuO_2 with various surface orientations and how these surfaces interact with molecules from the gas phase. Most of the data are available for the RuO_2(110) surface, little is known for the RuO_2 (100) surface, and practically nothing is known for the other surface orientations of RuO_2. Not all the adsorption systems on RuO_2 surfaces are discussed in depth, but rather I shall be concentrating here on those adsorbates which are required for the discussion in later sections. These systems include the adsorption of hydrogen, water, oxygen, and CO. Water and H_2 adsorption are particularly important

dx.doi.org/10.1021/cr200247n | Chem. Rev. 2012, 112, 3356−3426

for the discussion of electrochemical processes at RuO_2-based electrodes.

5.1. RuO_2(110) Surface

The RuO_2(110) is a convenient model system for an oxidized metal surface in surface chemistry because it is structurally well-characterized, it is a metallic conducting oxide which is amenable to high quality quantum chemical calculations and typical surface science characterization techniques, and it is active in the CO oxidation.[21] The low energy crystal planes of RuO_2 are (110), (100), and (101). From DFT calculations Seitsonen determined the surface energies of bulk-truncated RuO_2(110), RuO_2(100), and RuO_2(101) to be 71 meV/Å^2, 87 meV/Å^2, and 76 meV/Å^2, respectively.[103] Therefore the (110) orientation is expected to be the most abundant orientation of polycrystalline RuO_2. However, the (100) and the (101) surfaces undergo severe surface reconstruction[103] (whose atomic structures are still unknown) so that the surface energies of these reconstructed surfaces may be even lower than that of the (110) orientation.

5.1.1. General (Atomic Scale) Properties of the Stoichiometric RuO_2(110) Surfaces. RuO_2 crystallizes in the rutile structure where the O atoms adopt the sp^2 hybridization, whereas the Ru atoms are coordinated to six O atoms forming a slightly distorted octahedron (slightly compressed along the apical Ru−O direction by 2%). The surface structure of stoichiometric RuO_2(110) has been determined by LEED in combination with DFT calculations.[236] The pristine RuO_2(110) surface exposes two kinds of under-coordinated surface atoms (cf. Figure 24A): These are the bridging oxygen atoms (O_{br}), which are coordinated to two (instead to three) Ru atoms underneath (Ru−O bond length: 1.94 Å), and the 1f-cus Ru atoms, that is, one-fold under-coordinated Ru atoms (1f-cus Ru), which are coordinated to five (instead to six) O atoms; cus stands for coordinatively unsaturated sites. The DFT calculated surface energies of the stoichiometric RuO_2(110) surface is 71−90 meV/Å^2.[51,103,200,374] The other Ru−O bond lengths are between 1.90 Å and 2.03 Å. The structural parameters obtained by LEED and DFT agree quantitatively[236] and the atomic geometry has been corroborated by several recent ab initio studies.[51,375,376] When removing the bridging O atoms, 2-fold under-coordinated Ru atoms (2f-cus Ru) are exposed (cf. Figure 24B). The surface energy of this mildly reduced RuO_2(110) surface is as high as 145 meV/Å^2,[103] so that this surface is prone to decompose into metallic Ru and a stoichiometric RuO_2.

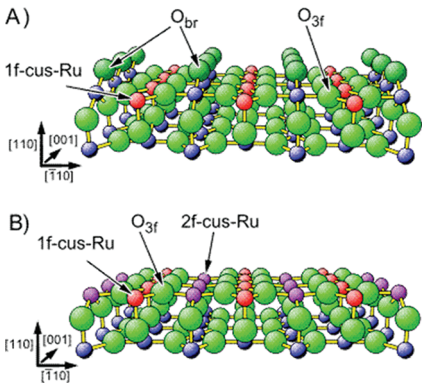

Figure 24. Ball and stick model of the (A) stoichiometric RuO_2(110) surface and (B) mildly reduced RuO_2 (110) surface, where all bridging O atoms are removed. The green balls are the oxygen atoms, and the small blue, red, and purple balls are the Ru atoms. At the surface there are two types of under-coordinated atoms, the bridging O atoms (O_{br}) and the 1f-cus Ru site (red); 1f-cus stands for one-fold coordinatively unsaturated site. Removing the O_{br} atoms leave the 2f-cus sites (purple) exposed (B).

Counting the formal charges of the Ru and O with +4 and −2, respectively, the bulk-truncated RuO_2(110) surface is auto compensated in that the of number electrons missing at the surface O_{br} atoms are compensated by the surplus electrons at the 1f-cus Ru sites (electron counting rule). While charge auto compensation plays a vital role in the stability of semiconducting and isolating oxide surface,[377] this effect is irrelevant for oxide surfaces exhibiting metallic conductivity because the dipole contributions from deeper layers are efficiently screened. The actual charge on the Ru and O atoms in RuO_2 is however much smaller than +4 and −2 as estimated by a detailed Bader analysis based on DFT calculations:[51] +1.73 for bulk-Ru and −0.87 for bulk-O, whereas 1f-cus Ru carries a charge of +1.60 and O_{br} −0.80. For comparison: Assuming that each Ru−O bond polarizes 2/3 of a unit charge the formal charge of O_{br} is −4/3 and that of the 1f-cus Ru is +3 1/3.

The electronic structure of RuO_2(110) was examined by superposition density maps (cf. Figure 25) which are defined as the difference between the total valence electron density (as derived from DFT calculations) and a linear superposition of radially symmetric atomic valence electron densities.[9,228] These plots reflect the polarization of Ru and O upon bond formation in the solid phase.[62,77] From Figure 25 one can clearly recognize the sp^2 hybridization of O (red contours: three lobes in plane forming an angle of 120°) and the d^2sp^3 ($e_g^2sp^3$) hybridization (blue contours point to the 6 O atoms forming a octrahedron) of Ru for the bulk coordinated sites. These hybrids form strong Ru−O σ bonds. Along the Ru−O bonds a substantial charge transfer from Ru (blue contours) to O (red contours) occurs, which is in line with the expected ionic Ru−O bonding.

The three d-Ru orbitals not involved in the $e_g^2sp^3$ hybridization are used to form σ and π Ru−Ru bondings and a weak Ru−O π-bonding. The observed charge accumulation along the Ru−Ru bonds (red contours) reveals metallic bonding, both σ (superposition density of Figure 25a middle panel) and π bonds (superposition density of Figure 25a right panel). The $2p_z$ orbital of O, which is defined to be perpendicular to the sp^2 hybrid orbitals of O, can also be reconciled from the density plots in Figure 25a as the electron densities are higher in the vicinity of O than expected from the three lobes of a pure sp^2 hybrid.

The shape of superposition charge density maps of O and Ru is virtually identical in the bulk and at the surface of RuO_2. This observation implies that the bulk hybridizations of Ru and O atoms persist at the surface, corroborating the concept of dangling bonds at the surface. The superposition electron density plots at the 1f-cus Ru sites indicate a slightly larger charge depletion of the outward directed lobe with σ symmetry than in bulk environment, making the 1f-cus Ru site in chemical terms a Lewis acid, that is, an electron accepting site. This interpretation explains the high propensity of 1f-cus Ru toward chemisorption of electronegative molecules from the gas phase. The 1f-cus Ru sites at the surface reveal also electron accumulation with π symmetry in the superposition electron density. Both orbitals together are able to form strong donor−acceptor bonds for instance with adsorbed CO.[378,379]

The dangling bond of O_{br} reveals a large and more contracted charge accumulation than bulk O which is characteristic of a Brønsted base, that is, a hydrogen accepting site. Both under-coordinated sites of RuO_2(110) (1f-cus Ru and O_{br})

dx.doi.org/10.1021/cr200247n | Chem. Rev. 2012, 112, 3356−3426

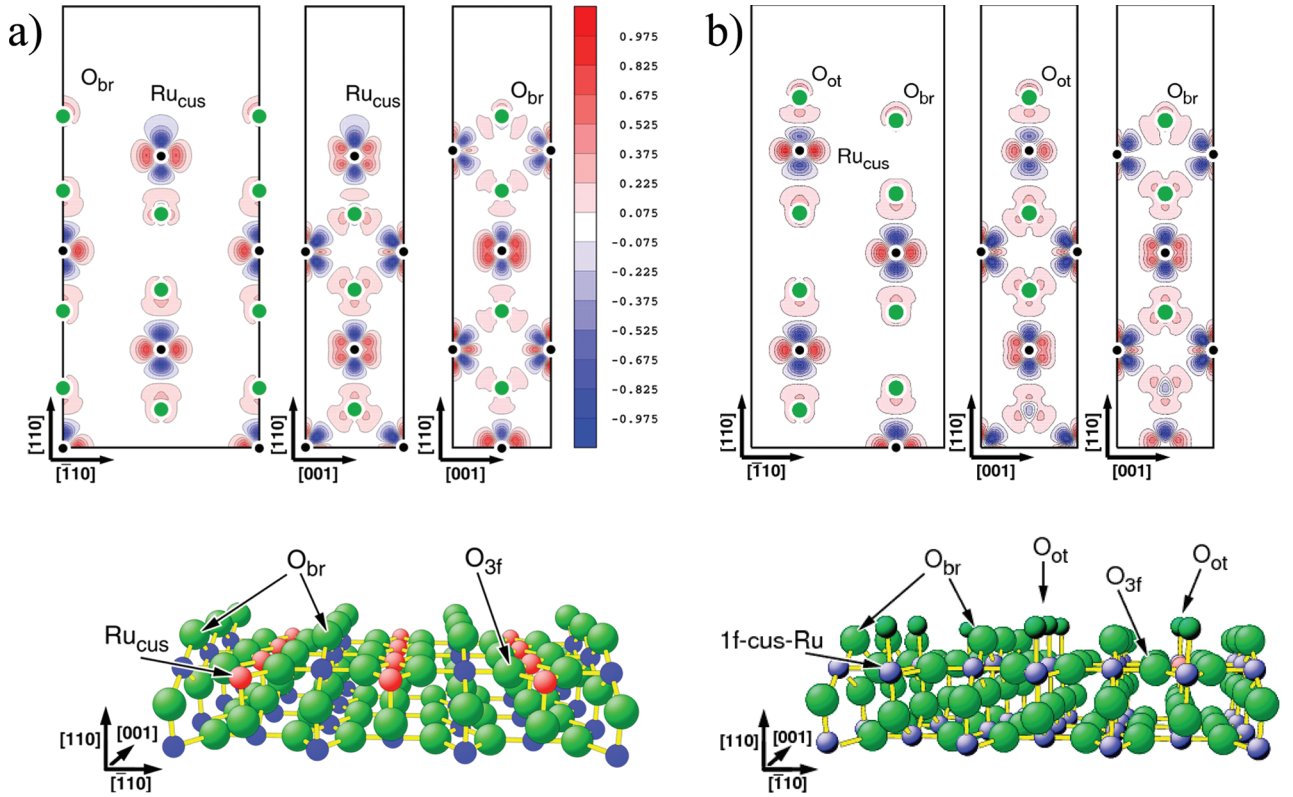

Figure 25. (a) Pseudovalence electron density contour plots (superposition density maps) of the stoichiometric $RuO_2(110)$ surface cut through the cus-Ru atom along the [$\bar{1}$10] and the [001] directions (left and middle). On the right side, the surface is cut through the bridging O atom along the [001] direction. These plots are defined as the difference between the total valence electron density, as determined by DFT calculations, and a linear superposition of radially symmetric atomic charge densities. Contours of constant charge density are separated by 0.15 $e^-/Å^3$. Areas of electron depletion and accumulation are marked by blue and red fillings. (b) Pseudovalence charge density contour plots of on-top O on $RuO_2(110)$ cut through the 1f-cus-Ru atom along the [$\bar{1}$10] and the [001] directions (left and middle) and on the right side, the surface is cut through the bridging O site along the [001] direction.[9,228] Reprinted with permission from ref 267. Copyright 2009 Elsevier.

are considered to be the catalytically active surface sites of $RuO_2(110)$.[89,380] The O_{3f} sites on the surface show some charge accumulation along the surface normal which stems from the $2p_z$ orbital. This electron density serves as acceptor in hydrogen bonds with hydrogen containing molecules such as molecular hydrogen, water, ammonia, or hydrocarbons. Hydrogen adsorption[274,381,382] and dehydrogenation experiments[241,383−385] have shown that bridging O sites act indeed as efficient Brønsted bases, that is, accepting H atoms and forming bridging O−H groups. Recent DFT calculations have also shown that the O_{3f} sites can bind hydrogen, although much weaker than on O_{br}.[386]

Since the surface atoms are only one-fold under-coordinated, O_{br} and 1f-cus Ru atoms retain their original (bulk) hybridization at the surface. However, if the surface oxygen atoms are 2-fold under-coordinated, as in the case of the O_{ot} species adsorbing in terminal position above the 1f-cus Ru atoms, then the bulk sp^2 hybridization is replaced by a simple sp-type hybridization as illustrated in Figure 25b. The O_{ot} species is formed by dissociative oxygen adsorption from the gas phase.[228] From the contour plots in Figure 25b, O_{br} forms two σ-bonds with Ru, while O_{ot} only one σ-bond; no O_{ot}-Ru π bond can be discerned. This difference in bond order is also reflected in total energy calculations: The O_{br} species is by 150 kJ/mol stronger bound than O_{ot}.[50,51,228]

The under-coordinated surface atoms of $RuO_2(110)$ possess unique spectroscopic fingerprints. The high resolution electron energy loss (HREEL) spectrum (cf. Figure 26a) of the stoichiometric $RuO_2(110)$ surface is dominated by a vibrational loss at 69 meV, which is attributed to the stretching mode of the (under-coordinated) bridging O atom O_{br} against the Ru atoms underneath. This assignment was based on DFT calculations, which determined the O_{br}−Ru stretching mode on the clean $RuO_2(110)$ surface to be 63 meV.[228] The O_{ot} covered $RuO_2(110)$ surface leads to an additional loss at 103 meV in the HREEL spectrum. DFT calculations determined the O_{ot}-against-1f-cus-Ru stretching mode to be 99 meV,[228,387] which compares well with the experimental value of 103 meV.

The under-coordinated 1f-cus Ru atoms have a distinct spectroscopic fingerprint in high-resolution core level shift (HRCLS) spectroscopy (cf. Figure 26b) of $Ru3d_{5/2}$.[89] The $Ru3d_{5/2}$ spectrum of $RuO_2(110)$ reveals two core level components. The emission at 280.76 eV is related to bulk-coordinated Ru atoms in $RuO_2(110)$, and the second component at 280.47 eV is ascribed to 1f-cus Ru atoms on the $RuO_2(110)$ surface based on DFT calculations. The various O species on the $RuO_2(110)$ surface can be seen with core level shift spectroscopy of O1s. In the O1s core level region (cf. Figure 26b), two RuO_2 related components are identified at 529.5 and 528.8 eV. On the basis of DFT calculations, these features

dx.doi.org/10.1021/cr200247n | Chem. Rev. 2012, 112, 3356−3426

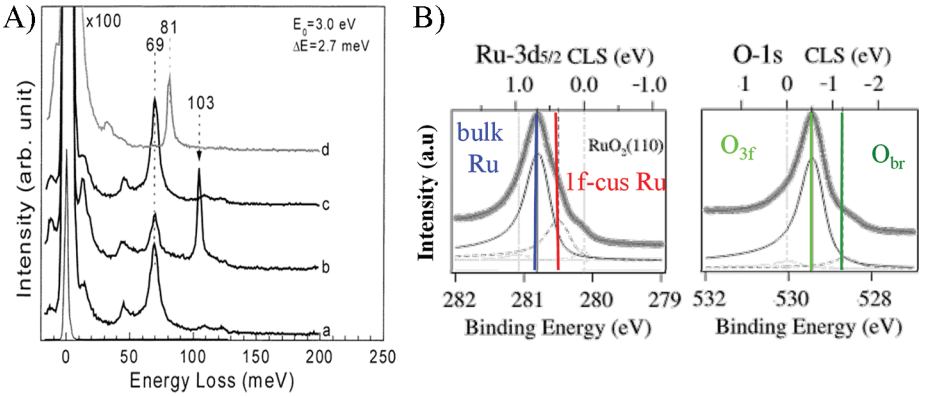

Figure 26. (A) High-resolution electron energy loss (HREEL) spectra[228] for the clean $RuO_2(110)$ surface (a) and O_{ot}–$RuO_2(110)$ (b). The clean spectrum is dominated by a vibrational loss (69 meV) due to O_{br} against Ru. The additional loss at 103 meV in the O_{ot}–$RuO_2(110)$ is assigned to atomic oxygen in the terminal position above 1f-cus Ru. Both assignments are based on DFT calculations. (c) O–$RuO_2(110)$ after heating to 550 K in order to remove O_{ot}. (B) High resolution core level shift spectrum of $Ru3d_{5/2}$ and O1s of an ultrathin $RuO_2(110)$ film on Ru(0001) which coexists with small areas of (1×1)O.[89] Reprinted with permission from ref 228. Copyright 2001 American Chemical Society. Reprinted with permission from ref 89. Copyright 2001 Elsevier.

are assigned to bulk O in $RuO_2(110)$ (529.5 eV) and bridging O (528.8 eV).[89]

While a few studies of Ru3d and O1s core levels have appeared already in the literature,[87,88,90,99,104,289,388] clearly identifying the bulk Ru and bulk O species of RuO_2, high resolution core level shift spectroscopy is needed to identify also the under-coordinated surface sites of $RuO_2(110)$. Further Ru3d and O1s core level binding energies for various adsorbate species on Ru(0001), Ru(10$\bar{1}$0), and $RuO_2(110)$ are compiled in Table 1.

With scanning tunneling microscopy (STM) the bridging O atoms of $RuO_2(110)$ can be directly imaged.[112,237,396] Recall that STM topographies are always the result of both electronic and geometric effects. Therefore, the unique assignment of the observed features in the STM images to particular surface species calls for DFT-simulations. The 1f-cus Ru atoms of $RuO_2(110)$ are imaged as depressions, while the bridging O atoms are imaged as protrusions with an apparent corrugation of 0.3 Å across the bridging O rows (cf. Figure 27). This STM contrast of $RuO_2(110)$ is different from the case of $TiO_2(110)$,[397] where electronic effects are prevailing so that the 1f-cus Ti atoms are imaged as protrusions.

5.1.2. Chemical Properties of the $RuO_2(110)$ Surface: General Adsorption and Reaction Behavior. An important concept in the reactivity of oxide surfaces is that of coordinative unsaturation of metal and oxygen on the surface.[380] The under-coordinated bridging O and the 1f-cus Ru sites on $RuO_2(110)$ govern the interaction of the oxide surface with the environment.[21] Indeed most of the molecules studied so far on the $RuO_2(110)$ surface, CO,[378] H_2O,[276,277,382] O_2,[228,387] N_2,[378] methanol,[241,383,398] CO_2,[399] NO,[400,401] ethylene,[398,402,403] NH_3,[384] ethane, methane,[404] HCl,[200,405] adsorb first from the gas phase directly above the 1f-cus Ru atoms. Only the adsorption of atomic hydrogen on 1f-cus Ru[274,382] has been shown to be endothermic with respect to $^1/_2$ H_2 in the gas phase. The under-coordinated bridging oxygen atom O_{br} is not an active adsorption site for most of these molecules. However, the bridging O sites are important in the adsorption of H_2 forming $O_{br}H$ groups,[274,382] and these sites are indispensable in the dissociative adsorption of HCl forming $O_{br}H$ and Cl_{ot}.[200,385,395,405] The O_{br} species are also important for strengthening the adsorption of NH_3 and H_2O by forming additional H-bonds. The adsorption energies of the studied molecules on $RuO_2(110)$ are compiled in Table 2.

The 1f-cus Ru sites form 1D chains on $RuO_2(110)$ which are separated by rows of bridging O rows. As soon as the activity is dictated solely by the 1f-cus Ru sites without communication between adjacent 1f-cus Ru rows, the $RuO_2(110)$ represents a 1D model catalyst system. This one-dimensionality of $RuO_2(110)$ has been discussed to explain the O_2 dependence of the activity in the HCl oxidation reaction (Deacon process)[385] and the observed selectivity in the ammonia oxidation.[414]

Coordinatively unsaturated oxygen sites act as basic adsorption sites, but also these are bonded to the lattice less strongly than coordinatively saturated ones so that they may be more easily removed. The CO molecule, for instance, adsorbs first on the 1f-cus-Ru site and then can easily recombine with the neighboring bridging O atom to form CO_2 above room temperature.[9,396,415−417] In the CO induced reduction process of $RuO_2(110)$, the bridging O atoms are consumed rather than serving as a true reactive center. Quite in contrast, hydrogen molecules have been shown to interact with the bridging O atoms above 150 K, forming bridging hydroxyl groups.[274,277,381] Dissociative HCl adsorption on $RuO_2(110)$ needs both types of under-coordinated sites (1f-cus Ru and O_{br}).[200,385]

Another intriguing feature of the $RuO_2(110)$ surface is the high diffusion barriers for the lateral migration of adsorbed species. With DFT calculations, the diffusion barrier for on-top CO along the 1f-cus rows is determined to be 90 kJ/mol[374] and 160 kJ/mol.[50] A similar high diffusion barrier (120 kJ/mol) is found with the on-top O species;[374] for on-top oxygen diffusion even higher activation energies were calculated by DFT 160 kJ/mol[407] and 200 kJ/mol.[412] For comparison, the diffusion barriers of atoms and small molecules on metal surfaces are typically only 20–50 kJ/mol.[419] The high diffusion barrier on $RuO_2(110)$ has a significant impact on the CO oxidation reaction mechanism on $RuO_2(110)$ (cf. section 6.2/6.3). In Table 3 diffusion barriers of some simple molecules/atoms on $RuO_2(110)$ are compiled.

In Figure 28 two STM images[112] are shown for the illustration of the high diffusion barrier of the on-top O species. Room-temperature exposure of molecular oxygen leads exclusively to pairs or multiple of pairs of protrusions between

dx.doi.org/10.1021/cr200247n | Chem. Rev. 2012, 112, 3356–3426

Table 1. Compilation of O1s and Ru3d Core Level Binding Energies for Metallic Ru and RuO_2 under UHV Conditions and in Contact with Oxygen, Hydrogen, Water, and CO

system	core level binding energies in eV	assignment	reference
Ru(0001)	$Ru3d_{5/2}$: 280.1	bulk-Ru	389
	$Ru3d_{5/2}$: 279.75	surface Ru	389
Ru(0001)-O	$Ru3d_{5/2}$: 280.1	bulk-Ru	389
	$Ru3d_{5/2}$: 280.1	Ru-1Oad	389
	$Ru3d_{5/2}$: 280.5	Ru-2Oad	389
	$Ru3d_{5/2}$: 281.0	Ru-3Oad	389, 89
	O1s: 530.07	O-chem	89
Ru(0001)-CO	O1s: 532	on-top CO	390, 391
	C1s: 285.7	on-top CO	392
Ru(0001)−OH	O1s: 531−531.7	OH	393
	O1s: 533.2	OH_2	393
$Ru(10\bar{1}0)$	$Ru3d_{5/2}$: 280.1	bulk-Ru	394
	$Ru3d_{5/2}$: 279.6, 279.9	surface-Ru	394
$Ru(10\bar{1}0)$-O	$Ru3d_{5/2}$: 280.34, 280.54	Ru-2O	394, 264
$RuO_2(100)$	$Ru3d_{5/2}$: 280.9	bulk-Ru	104, 264
	O1s: 529.1	bulk-O	104, 264
$Ru(10\bar{1}0)$-1×2 surface oxide	$Ru3d_{5/2}$: 280.6	transient surface oxide (TSO): 2 ML of O, subsurface O	241
	O1s: 529.75		241
$RuO_2(110)$	$Ru3d_{5/2}$: 280.8	bulk-Ru	89
	$Ru3d_{5/2}$: 280.5	cus-Ru	89
	$Ru3d_{5/2}$: 281.8	cusRu + O_{ot}	86
	O1s: 529.5	bulk O	89
	O1s: 528.8	bridging O	89
TSO-RuO_x	$Ru3d_{5/2}$: 280.5−280.6	transient surface oxide (TSO)	240
$RuO_2(110)$-H	O1s: 530.3 (530.8)	O_{br}-H	274
	O1s: 529.8	O_{br}-H H-bonded to Oot	274
	O1s: 531.9 (532.4)	O_{ot}-H_2 (water)	274
$RuO_2(110)$-CO	O1s: 532.4	on-top CO	395
	O1s: 531.4	bridge CO	395
RuO_2 (110)-methanol	O1s: 531.2	CH_3O	279
	O1s: 532.2	CH_2O	279
hydrous RuO_2	$Ru3d_{5/2}$: 281.1	bulk-Ru	88
	$Ru3d_{3/2}$: 285.4	bulk-Ru	88
	O1s: 529.4	O-bulk	88
	O1s: 530.8	OH	88
	O1s: 532.4	OH_2	88
		remark: rigid shift of 0.5 eV if compared to RuO_2 (110)	
poly-RuO_2	$Ru3d_{5/2}$: 280.7 $Ru3d_{5/2}$: 280.7, 281.2	bulk-Ru	88
	$Ru3d_{5/2}$: 280.0	bulk-Ru	383
	$Ru3d_{3/2}$: 285.0	bulk-Ru	388
	O1s:529.7, 529.4	bulk-Ru	88, 383
		O-bulk	

the rows of bridging O atoms (cf. Figure 28a). The separation between neighboring protrusions is identical to the distance between neighboring 1f-cus Ru sites (i.e., 3.11 Å). From the registry of these additional features with regard to the bridging

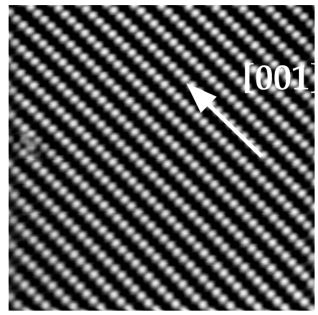

Figure 27. Experimental high resolution STM image (constant current mode, taken at RT) of a stoichiometric $RuO_2(110)$ surface: 11 nm × 11 nm, U = 0.95 V, I = 0.46 nA.[112] The rows bridging O atoms along the [001] direction are clearly visible. On the right side a single adsorbed pair of neighboring on-top O atoms is visible. Reprinted with permission from ref 112. Copyright 2004 John Wiley and Sons.

Table 2. Adsorption Energies (with Respect to Molecules in the Gas Phase) and Desorption Temperatures of Small Molecules on Stoichiometric $RuO_2(110)$ (s-$RuO_2(110)$) and Reduced $RuO_2(110)$ (r-RuO_2 (110)) Where All the Bridging O Atoms Are Replaced by CO[a]

adsorption system	adsorption energies/ kJ/mol	desorption temperature in K	references
CO on s-$RuO_2(110)$	120−140	300−400	378, 406−408
CO on r-$RuO_2(110)$	160−180	400−500	379, 407−409
N_2 on s-$RuO_2(110)$	58	120−180	378
H_2O on s-$RuO_2(110)$	80−90	350−425	200, 276, 277, 382
NO on s-$RuO_2(110)$	120−190	500	375, 400, 410−412
HCl on s-$RuO_2(110)$	30−50		200, 395
NH_3 on s-$RuO_2(110)$	113−150	420	384, 410
CO_2 on s-$RuO_2(110)$	35	190	399, 413
O_2 on s-$RuO_2(110)$	80	120	51, 228
H_2 on s-$RuO_2(110)$	35	100	274, 381, 382
Cl on s-$RuO_2(110)$	120 −180 (depending on Cl coverage)	550−600	200, 405
O on s-$RuO_2(110)$	85−120	400	50, 51, 228, 408
O_2 on O-$RuO_2(110)$	40	140	228, 387
O_2 on s-$RuO_2(110)$	125		387
C_2H_4/ s-$RuO_2(110)$	25	100	398, 402
C_2H_4/ O-$RuO_2(110)$		500; reaction: CO_2	403
methanol on c-$RuO_2(110)$	78	300−400	241, 383, 398

O atoms along the [001] rows, this oxygen species is inferred to adsorb on-top of the 1f-cus Ru atoms. Consecutive STM images of the same region disclose that the mobility of the on-top O is negligibly small at room temperature. In contrast, oxygen exposure at 400 K leads mostly to isolated on-top O species on the $RuO_2(110)$ surface, as illustrated in Figure 28b; note that still some of the oxygen atoms are paired.

dx.doi.org/10.1021/cr200247n | Chem. Rev. 2012, 112, 3356−3426

Table 3. Activation Barriers for Diffusion of Small Molecules on the $RuO_2(110)$ Surface As Determined by ab Initio DFT Calculations

system	diffusion process	activation energies/ kJ/mol	references
CO on s-$RuO_2(110)$	$CO_{ot} \rightarrow CO_{ot}$	100 (170)	378 (407)
	$CO_{ot} \rightarrow CO_{br}$	60 (130)	378 (407)
	$CO_{br} \rightarrow CO_{br}$	60	407
O on s-$RuO_2(110)$	$O_{ot} \rightarrow O_{ot}$	120 (160)	228, 414 (407)
	$O_{ot} \rightarrow O_{br}$	70 (100)	418 (407)
Cl on s-$RuO_2(110)$	$Cl_{ot} \rightarrow Cl_{ot}$	80	200, 385
N on s-$RuO_2(110)$	$N_{ot} \rightarrow N_{ot}$	90 (200)	414 (412)
OH on s-$RuO_2(110)$	$O_{ot}H \rightarrow O_{ot}H$	50 (110)	274 (414)
H-$RuO_2(110)$	H diff along O_{br} rows	240	410
H–O_{ot}-$RuO_2(110)$	H diff along O_{ot} rows	21	274
H–O_{ot}-$RuO_2(110)$	H diff from O_{br} to O_{ot}	28 (53)	274 (200)

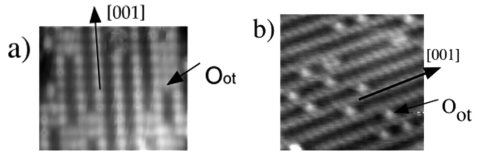

Figure 28. STM images of O_{ot} on stoichiometric $RuO_2(110)$: (a) 50 Å × 40 Å STM image (constant current mode, RT) of a $RuO_2(110)$ surface which was exposed to 0.1 L oxygen at room temperature. U = 0.01 V, I = 0.46 nA. (b) 60 Å × 60 Å STM image (constant current mode, RT) of a $RuO_2(110)$ surface which was exposed to 0.01 L oxygen at 400 K. U = −0.25 V, I = 1.83 nA. Reprinted with permission from ref 112. Copyright 2004 John Wiley and Sons.

This STM experiment indicates that at 400 K the on-top O species is mobile enough to diffuse on the $RuO_2(110)$ surface which is consistent with a diffusion barrier of 120 kJ/mol,[112,396] but hardly be reconciled with a DFT-calculated diffusion barrier of 160 kJ/mol[407] and 200 kJ/mol.[412]

A few of the adsorbate systems on $RuO_2(110)$ in Table 2 are important for the wider scope of the present review article since these systems have either direct counterparts in electrochemistry or are of particular interest in the study of surface reaction in heterogeneous catalysis. These systems include O_2, CO, H_2, and H_2O adsorption. In particular the interaction of H_2 and H_2O with $RuO_2(110)$ is the starting point to compare with electrochemical model experiments in aqueous electrolytes.

5.1.3. Interaction of Oxygen with the $RuO_2(110)$ Surface. Oxygen exposure at low temperatures (100 K and below) leads to the population of molecular oxygen on the $RuO_2(110)$ surface which desorbs at 140 K.[228] This adsorbed molecular oxygen species has initially been considered as a peroxide species bridging to neighboring 1f-cus Ru sites. However, using plane wave DFT calculations Wang et al.[387] argued that all molecular O_2 species are prone to dissociate on the $RuO_2(110)$ as soon as there are two neighboring vacant 1f-cus Ru sites available. Only when isolated 1f-cus Ru sites are generated by dissociative oxygen adsorption, molecular O_2 can be stabilized in this vacancy by 40 kJ/mol.

Oxygen exposure to the stoichiometric $RuO_2(110)$ surface at room temperature leads to the population of the atomic oxygen adsorbed on-top of the 1f-cus Ru atoms (cf. O_{ot} in Figure 25). Exposure of 5 L of O_2 at room temperature saturates 86% of the 1f-cus Ru atoms by on-top O atoms (O_{ot}) if diffusion is ignored.[51,228] Exposing the $RuO_2(110)$ surface to molecular oxygen at 500 K and cooling the sample to room temperature in an oxygen atmosphere of 10^{-7}mbar leads however to a surface where practically all 1f-cus Ru sites are occupied by on-top O.[420] In DFT calculations the adsorption energy on on-top O is only 100−120 kJ/mol against $^1/_2$ O_2 in the gas phase,[50,51,267] whereas from TDS 80 kJ/mol is derived.[228,229] Although the Ru−O_{ot} bond distance is as short as 1.85 Å (experiment)[228] and 1.72 Å (DFT),[50,51,228] contrasted with 2.00 Å in bulk $RuO_2(110)$, the low adsorption energy of O_{ot} and the superposition density in Figure 22 indicates clearly that the Ru−O_{ot} bond consists of a single σ bond with practically no contribution of π bonding. We should mention that Horokawa et al.[421] considered the Ru-on-top O bonding as a double bond without giving further evidence. A Ru−O_{ot} bond strength of about 100 kJ/mol on $RuO_2(110)$ is much smaller than that of terminal O on other transition metal oxide surfaces including MoO_3[422] and V_2O_5.[423] For instance, the vanadyl oxygen in V_2O_5 and V_2O_3 is considered to bind with a double bond to vanadium;[423,424] that is, π-bonding is observed with vanadyl oxygen.

The initial dissociative sticking coefficient of O_2 on the stroichiometric $RuO_2(110)$ is 0.7; that is, 70% of the impinging O_2 molecules adsorb dissociatively on the surface.[229] Experimentally, the work function of the $RuO_2(110)$ oxide film is 5.8 eV, which increases to 6.6 eV when the oxide surface is saturated by additional on top O.[229] The DFT calculated work function of the stoichiometric $RuO_2(110)$ surface is 5.9 eV, which rises to 7.40 eV when the surface is saturated by on-top O.[50] On-top adsorbed oxygen on $RuO_2(110)$ can readily fill in bridging O vacancies, therefore being important for replenishing the partly reduced oxide surface. But on-top oxygen is also important to remove hydrogen from the bridging O row via hydrogen-transfer.[274,277]

5.1.4. Interaction of CO with the $RuO_2(110)$ Surface. The $RuO_2(110)$ surface is able to adsorb CO molecules quite strongly. This adsorption behavior of RuO_2 is quite different from other (more ionic) metal oxides such as MgO, TiO_2, and Al_2O_3.[380] DFT calculations show that the adsorption energies vary from 120 to 180 kJ/mol, depending on the coverage and the adsorption site of CO on $RuO_2(110)$.[378,379,425]

The adsorption mechanism of CO on $RuO_2(110)$ is explained by the so-called Blyholder model,[426] which originally was introduced to rationalize the strong adsorption energy of CO on transitions metal surfaces. The adsorption of CO on $RuO_2(110)$ proceeds via donation of electronic charge from the 5σ MO of CO to $RuO_2(110)$ that is counterbalanced by a back-donation of electronic charge from the $RuO_2(110)$ surface into the 2π* MO of CO.

CO exposure at low temperature (200 K) leads to the population of an on-top CO species on the stoichiometric $RuO_2(110)$ surface with a bond strength of 120 kJ/mol.[378] Above room temperature CO exposure is able to reduce (at least partly) the $RuO_2(110)$ surface:[379] Bridging O atoms from the stoichiometric $RuO_2(110)$ surface are removed by CO oxidation and subsequently are replaced by bridging CO molecules (either symmetric or asymmetric bridge CO).[379,409]

dx.doi.org/10.1021/cr200247n | Chem. Rev. 2012, 112, 3356–3426

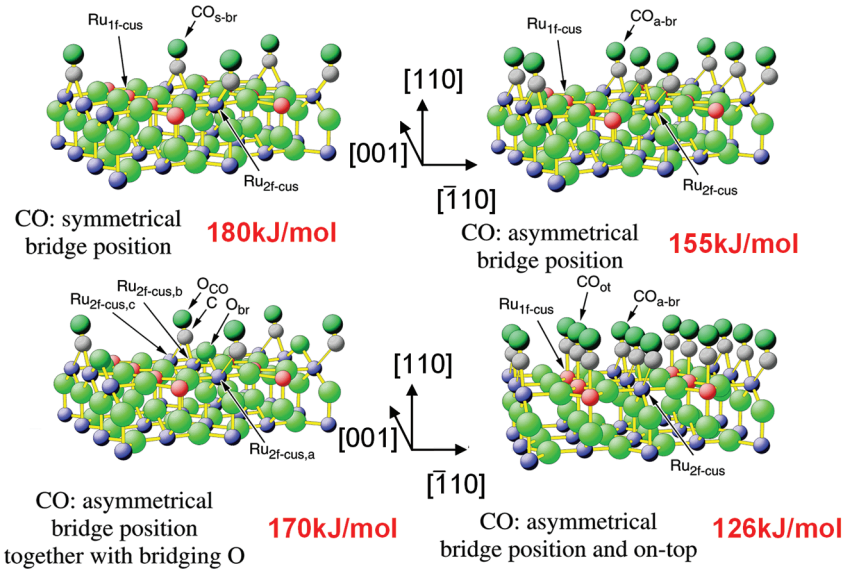

Figure 29. Various CO adsorption sites are possible on the mildly reduced $RuO_2(110)$ surface. The energetically most favored CO adsorption site is the symmetric bridging site (180 kJ/mol), followed by the asymmetric bridging position (155 kJ/mol). For this adsorption case all bridging O atoms are replaced by CO, while for the symmetric bridging CO only every second pair of 2f-cus Ru atoms is bridged over. Below 320 K also the 1f-cus Ru atoms are occupied by CO. The averaged adsorption energy decreases to 126 kJ/mol.[379]

The adsorption energies of bridging CO species range from 155 to 180 kJ/mol depending on the coverage (cf. Figure 29).

5.1.5. Interaction of H_2 with the $RuO_2(110)$ Surface. At low temperatures, say below 100 K, molecular hydrogen can be stabilized on $RuO_2(110)$ in that H_2 adsorbs on the 1f-cus Ru sites or forms a bridging dihydride species O_{br}-H_2.[381] Recently this bridging water species O_{br}-H_2 was shown to be substantially stabilized by terminal chlorine on-top of 1f-cus Ru up to room temperature.[395] The adsorption energy of H_2 on 1f-cus-Ru is 30 kJ/mol, thus thermally stabilizing this species up to about 100 K.[274,382] Atomic H adsorption on 1f-cus Ru is slightly endothermic with respect to $^1/_2$ H_2 in the gas phase.

At room temperature H_2 exposure to $RuO_2(110)$ leads first to the formation of bridging hydroxyl groups $O_{br}H$.[274,381,427] These hydroxyl groups can recombine at temperatures above 600 K to form water and bridging vacancies.[274,427] However, water can even be formed at room temperature by hydrogen exposure.[428] Extensive hydrogen exposure at 420 K leads to a complete reduction of the $RuO_2(110)$ surface.[109]

If a hydroxylated $RuO_2(110)$ surface, where the bridging O atoms are capped by hydrogen, is exposed to oxygen at room temperature, then the resulting on-top O species has been shown to pick up the hydrogen from O_{br}-H forming O_{ot}-H via a first hydrogen transfer and via a second H-transfer on-top water O_{ot}-H_2.[277] If the bridging O atoms are replaced by CO (5 L of CO exposure at 350 K) and subsequently the surface is exposed to oxygen at 200 K, then hydrogen is not able to be accommodated at the surface, although 1f-cus Ru sites are available.[274] From these data, the on-top O atoms are considered to be not able to directly coordinate hydrogen. Rather bridging O atoms are considered to be the entrance channel for hydrogen adsorption, and via a hydrogen transfer on-top O picks up the hydrogen atoms.[274,420]

Even more surprising is the fact that free 1f-cus Ru sites are not required for the adsorption of hydrogen on the $RuO_2(110)$. The 1f-cus Ru sites can be capped by on-top O; this can be accomplished by nearly 100% as verified with RAIRS[274] and STM.[420] If such a surface is exposed to molecular hydrogen, even more water is produced than with a 50% on-top O covered $RuO_2(110)$ surface. Temperature-dependent measurements indicate that the adsorption process of H_2 over on-top O covers $RuO_2(110)$ is slightly activated by 6 kJ/mol.[274] It should be noted that these conclusions were disputed in the literature.[420,427,429]

The surface chemistry of O_{br}-H-terminated $RuO_2(110)$ surface is distinctly different from that of the stoichiometric $RuO_2(110)$ surface. For instance, the hydroxylated $RuO_2(110)$ surface cannot be reduced by CO exposure at 400 K[265] (while the stoichiometric $RuO_2(110)$ is readily reduced). The chlorination in bridge positions by HCl exposure is much more efficient on the hydroxylated $RuO_2(110)$ surface than on the stoichiometric surface.[395]

5.1.6. Interaction of Water with $RuO_2(110)$ Surface. Water adsorption on surfaces has received a great deal of attention over the past decades. The reader interested in this topic is referred to the following review articles.[430−432]

Water adsorption on $RuO_2(110)$ proceeds in the following way: part of the water splits into OH and H, forming two different hydroxyl groups on the surface,[276,433] the O_{ot}−H and the O_{br}−H species. Both water and OH groups have been identified with HREELS[276] and HRCLS.[433] When annealing the surface to 400 K most of the hydrogen from HO_{br} recombines with HO_{ot} to form surface water H_2O_{ot} which desorbs immediately. Below this temperature two hydroxyl groups passivate both active sites on the $RuO_2(110)$ surface, making the RuO_2 surface at water saturation practically inactive for the interaction with other molecules impinging from the gas phase. This finding may explain the water-induced poisoning of the CO oxidation on $RuO_2(110)$.[106,402]

The structure of the water−$RuO_2(110)$ interface in 0.1 M NaOH solution was studied by in situ SXRD.[434] At a potential of 330 mV against Ag/AgCl, the surface is covered by bridging and on-top hydroxyl groups. Increasing the anodic potentials to 500 mV (close to oxygen evolution), the extraneous water layer and the surface hydroxide layer form a bilayer similar to ice. At a cathodic potential of −200 mV, bridging OH and on-top water are formed in a low-density water layer (cf. Figure 30).

dx.doi.org/10.1021/cr200247n | Chem. Rev. 2012, 112, 3356−3426

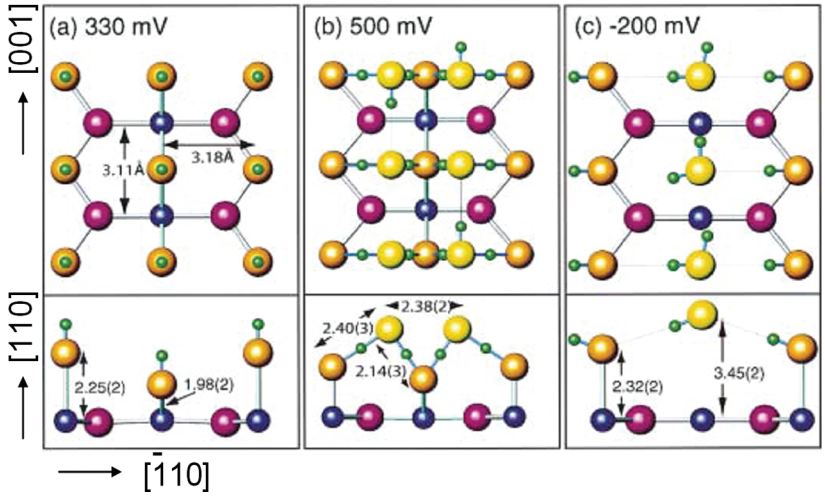

Figure 30. Structure of the water−RuO_2(110) interface in 0.1 M NaOH for various polarization potentials against the Ag/AgCl electrode. Ball-and-stick models for (a) 330 mV, (b) 500 mV, and (c) −220 mV structures: Upper panels are top views and the lower panels are side views. The blue balls represent the Ru atoms. The red, orange, and yellow balls represent oxygen atoms in the bulk, on the surface bonded to Ru, and in the water molecules, respectively. The small green balls represent the hydrogen atoms, conjectured to form hydrogen bonds. Reprinted with permission from ref 434. Copyright 2001 by the American Physical Society.

5.1.7. Chemical Reduction of the RuO_2(110) Surface. The first step in the reduction of RuO_2(110) is the removal of bridging O atoms at the surface by easy leaving groups such as CO_2 and water. Exposing the RuO_2(110) surface to CO at room temperature results in a surface, where all bridging O are replaced by strongly bonding bridging CO. Below 400 K a full reduction of RuO_2(110) has not been observed, since the bridging CO molecules stabilize the mildly reduced RuO_2(110) against further reduction. Annealing such a mildly reduced RuO_2(110) surface to 600 K in vacuum results in the desorption of bridging CO molecules and the appearance of pits in the STM image which are decorated by one monolayer thick small Ru islands.[237] These holes are viewed to be produced by the migration of 3-fold coordinated lattice O atoms to the bridge position, thereby repopulating the surface with bridging oxygen atoms. As a consequence, the coordination of the Ru surface atoms attached to the released O_{3f} atoms becomes too low so that these highly under-coordinated Ru atoms become unstable and agglomerate into small metal clusters at the rims of the holes (cf. Figure 31c). The Ru agglomeration in turn liberates further oxygen atoms which are used to cap 2f-cus-Ru atoms by bridging O atoms. Consequently, the mildly reduced RuO_2(110) surface separates after annealing to 600 K into a restored stoichiometric RuO_2(110) with holes and small Ru clusters. This process has been studied in situ with infrared spectroscopy.[435]

The bridging O at the RuO_2(110) surface can be removed equally efficiently by hydrogen and methanol exposure. The bridging O leaves then the RuO_2(110) surface in the form of water.[274] The reduction process was also studied by STM (cf. Figure 31).[436] Exposure of 0.1 L of methanol at room temperatures, followed by heating the RuO_2(110) surface to 520 K lead to the formation of isolated vacant bridging O vacancies. Upon annealing to 590 K, these vacancies arrange into stripes, and finally at 660 K these stripes agglomerate into rectangular holes in the oxides (1 RuO_2 layer deep) which are decorated by small monatomic high metallic Ru islands at the rims. Similar STM images have been reported for the reduction of RuO_2(110) by H_2[274] and by CO.[237] These experiments demonstrate that the initial reduction process at higher temperatures leads to a separation in an intact RuO_2(110) region and small metallic Ru islands rather than to the formation of an RuO_x suboxide.

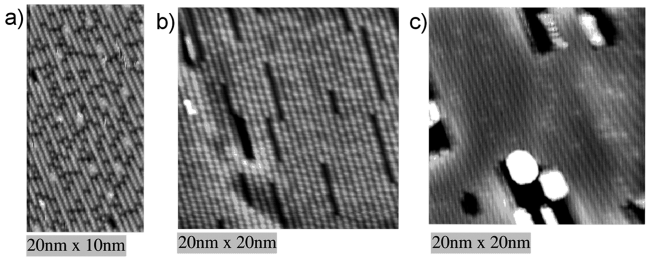

Figure 31. STM images illustrating the reduction of RuO_2(110) upon methanol exposure and subsequent annealing to 520, 590 and 660 K. (a) 0.1 L of methanol is exposed to RuO_2(110) at room temperature and then the surface is annealed to 520 K. Single well-resolved vacancies (dark features) are formed along the bridging O rows. (b) Annealing this surface to 590 K results in the agglomeration of the isolated vacancies into dark stripes of vacancies. (c) Annealing this surface to 660 K results in the agglomeration of the stripes in dark holes in the topmost RuO_2 layer which are decorated by single layer metallic Ru islands (white features).[436]

5.2. RuO_2(100) Surface

5.2.1. General Properties of RuO_2(100). Single crystalline RuO_2 film in (100) orientation can be grown by excessive exposure of a well-prepared Ru(10$\bar{1}$0) surface to molecular oxygen (ca. 3×10^5 L O_2), keeping the sample temperature at 600−700 K. Excessive O_2 exposure of Ru(10$\bar{1}$0) surface at 800 K leads to a surface oxide that exhibits a c(2×2) LEED pattern.[110,265] The c(2×2) unit cell is centered and the unit cell vectors are twice as long in both principal surface directions as the bulk-truncated RuO_2 (100) surface.

The RuO_2(100)-(1×1) surface exposes bridging O atoms and 1f-cus Ru atoms (cf. Figure 32) so that the surface is autocompensated in that the densities of under-coordinated O and Ru atoms are identical. The main difference between RuO_2(110) and RuO_2(100) is that on RuO_2(100) the bridging O atoms and the 1f-cus Ru atoms are attached to each other, while on RuO_2(110) both kinds of under-coordinated surface atoms are well separated. The atomic structure of the RuO_2(100)-(1×1) surface has been determined to be close to

dx.doi.org/10.1021/cr200247n | Chem. Rev. 2012, 112, 3356−3426

that of a bulk-truncated $RuO_2(100)$ surface with a 1f-cus Ru−O_{br} bond length being 2.01 Å (LEED) and 1.95 Å (DFT), while the other Ru−O bonds are in the range of 1.90−2.05 Å.[110] The calculated surface energy of stoichiometric surface is 87 meV/Å^2.[374] Quite in contrast, the surface structure of $RuO_2(100)$-c(2×2) is largely unknown. The existing data from the $RuO_2(100)$-c(2×2) structure point to a far reaching reconstruction of the $RuO_2(100)$ surface. There is some theoretical evidence that sp^3-hybridized surface Ru atoms are formed.[437] While the (1×1) phase of $RuO_2(100)$ is catalytically active in the oxidation of CO, the c(2×2) is not active at all.[265] The emergence of the c(2×2) phase of $RuO_2(100)$ leads to a passivation of the oxide surface.

The electronic structure of $RuO_2(100)$ was examined by superposition density maps (cf. Figure 32),[228,386] reflecting the

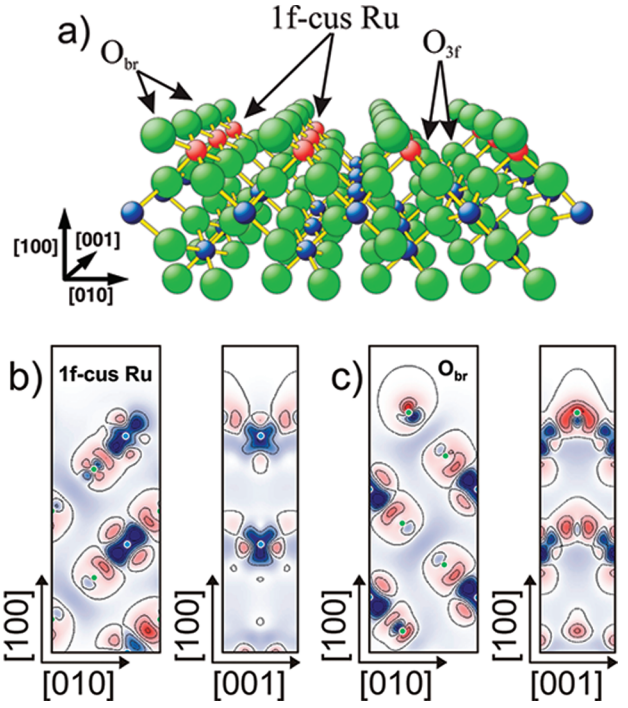

Figure 32. (a) Ball-and-stick model of the bridging terminated $RuO_2(100)$ surface. Large balls represent oxygen and small balls represent ruthenium atoms. The one-fold coordinatively unsaturated Ru atoms (1f-cus Ru: red balls) as well as the bridge bonded and 3-fold coordinated lattice O atoms are indicated. The bridge bonded O atoms are directly coordinated to the 1f-cus Ru atoms on $RuO_2(100)$. (b) Pseudo valence density contour plots of $RuO_2(100)$ cut through the 1f-cus-Ru atoms. These plots are defined as the difference between the total electron density and a linear superposition of radially symmetric atomic charge densities. Electron depletion and accumulation are marked by blue and red regions, respectively. (c) Pseudo valence density contour plots of $RuO_2(100)$ cut through the bridging O (O_{br}) atoms.[110,386]

polarization of Ru and O upon bond formation in the solid phase. From Figure 32 one can recognize that the shape of superposition charge density maps of bulk O and Ru reflect sp^2 and $e_g^2sp^3$ hybridization. Quite in contrast to $RuO_2(110)$, the hybridization of the under-coordinated 1f-cus Ru at the surface changes in that the lobes of 1f-cus Ru with electron accumulation are rotated by about 40° toward the surface normal. For the O_{br} atoms, the electron accumulation in the two remaining bonds is more contracted than for bulk O. Nevertheless, the dangling bonds at 1f-cus Ru are clearly visible in these plots (electron depletion: blue), pointing toward the direction where the next oxygen atom should adsorb.

5.2.2. Adsorption Properties of $RuO_2(100)$. The binding energy of CO on the 1f-cus Ru sites of $RuO_2(110)$ is 90 kJ/mol, which is consistent with a desorption temperature of 250 K and therefore substantially lower than on $RuO_2(110)$ (120 kJ/mol).[265] Consistently, the CO TPD maxima of $RuO_2(100)$ in the temperature range between 200 and 400 K are shifted by 40 K to lower temperatures in comparison with the CO-$RuO_2(110)$ system. Annealing a CO covered $RuO_2(100)$ surface to high temperatures leads to the evolution of CO_2. The CO_2 yields of $RuO_2(110)$ and $RuO_2(100)$ are comparable.[103,265]

Actually, the $RuO_2(100)$ surface is able to stabilize two surface phases, a (1×1) and a c(2×2). While CO can readily adsorb on the (1×1) regions, CO adsorption is suppressed on the c(2×2) domains above 100 K.[265] Quite in contrast, N_2 does adsorb on the c(2×2) at 160 K so that the c(2×2) surface is presumed to expose also under-coordinated Ru atoms. This difference in CO and N_2 adsorption on c(2×2) is puzzling since the bond formation of CO and N_2 with transition metal atoms is expected to be quite similar. With STM (cf. Figure 33a), this adsorption behavior of CO can be visualized: CO adsorbs only

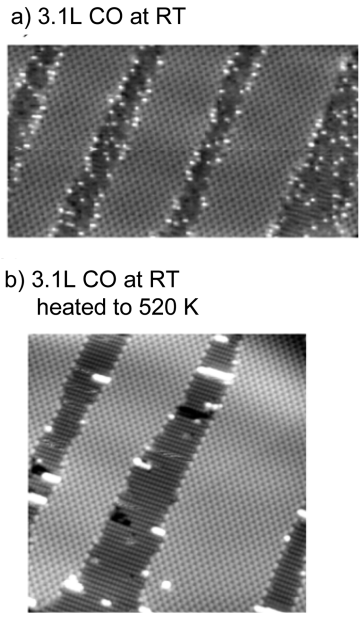

Figure 33. (a) STM image (14 nm × 30 nm, U = −0.14 V, I = 0.46 nA) of the $RuO_2(100)$ surface after exposure of 3.1 L CO at room temperature. Under these conditions the $RuO_2(100)$-(1×1) surface is mildly reduced in that all bridging O atoms are partly replaced by CO molecules. The bright protrusions with an apparent height of 0.6 Å are CO molecules. The $RuO_2(100)$-c(2×2) phase is not affected by the CO exposure. (b) STM image (20 nm × 20 nm, U = 0.20 V, I = 0.40 nA) of the $RuO_2(100)$ surface after exposure of 3.1 L CO at room temperature and annealing at 520 K. Only the $RuO_2(100)$-(1×1) surface is affected by this treatment in that small pits are formed which are decorated by small protrusions interpreted as islands of single layer metallic Ru. Reprinted with permission from ref 112. Copyright 2004 John Wiley and Sons.

on the (1×1) patches but not on the c(2×2) regions. Subsequent annealing of the surface to 520 K results in a loss of the CO molecules and the appearance of small holes in the (1×1) areas together with the observation of small Ru clusters (cf. Figure 33b). This behavior is akin to that observed during

dx.doi.org/10.1021/cr200247n | Chem. Rev. 2012, 112, 3356−3426

the CO induced reduction of $RuO_2(110)$. The c(2×2) patches are not affected by this CO adsorption/annealing treatment.

If the $RuO_2(100)$ surface is exposed to molecular oxygen at 200 K, two desorption features are observed in TDS, one peak at 450 K and a broad shoulder at 700 K. In comparison with the $RuO_2(110)$ surface the desorption peak at 450 K is attributed to the recombination of on-top O atoms on neighboring 1f-cus Ru sites. DFT calculations indicate that the binding energy of this species is about 90 kJ/mol with respect to $^1/_2$ O_2 with an 1f cus-Ru-O_{ot} bond length of 1.77 Å, that is, similar as on $RuO_2(110)$. The shoulder in the O_2-TDS centered at 700 K is tentatively assigned to the recombination of on-top O with bridging O.[265]

DFT calculations of water on $RuO_2(100)$ show that water adsorbs on the 1f cus-Ru sites, forming a strong hydrogen bond to the O_{3f} site.[386]

5.3. Comparison with Rutile TiO_2 Single Crystals

Several excellent review articles are available in the literature, covering the surface chemistry of rutile TiO_2.[22−25] Therefore, the present section can be kept concise. TiO_2 is probably the most studied oxide in surface science. This scientific interest has been spurred by the promise of TiO_2 to be an efficient photocatalyst for water splitting,[438,439] opening a wide field of possible and already realized applications.[440]

TiO_2 behaves in many respects complementary to RuO_2. The semiconducting behavior of TiO_2 is based on the electronic configuration of Ti (d^0), while RuO_2 is a metallic conducting oxide based on the electronic configuration of Ru (d^4). The theoretical description of TiO_2 is much more involved than that of RuO_2, since electron correlation plays an important role in TiO_2,[441] thus requiring sophisticated and computer-time demanding theoretical approaches (such as hybride methods[80]) for a proper description of the electronic properties of TiO_2. Quite in contrast, electronic properties of RuO_2 can be described within simple one-electron MO-arguments.[62,65,77,267]

Electron correlation becomes essential when studying the electronic and catalytic properties of bridging O vacancies at the $TiO_2(110)$ surface. Simple DFT calculations lead to an artificially metallic surface due to delocalization of the electron in the bridging O vacancy.[442] This problem has thoroughly been discussed by Kowalski et al.[443] The atomic geometry of $TiO_2(110)$ has only recently been settled by a quantitative LEED analysis after a long-standing controversial discussion in the literature.[444] $TiO_2(100)$ reconstructs into (110)-like facets.[445] This kind of reconstruction has not been observed on $RuO_2(100)$.

Stoichiometric TiO_2 is catalytically inactive,[23] while the ordinary unsaturated surface sites are the catalytically active sites on stoichiometric $RuO_2(110)$.[21] Surface defects such as bridging oxygen vacancies do not play a decisive role in the catalytic activity of $RuO_2(110)$. Quite in contrast, the catalytic activity of $TiO_2(110)$ is governed by surface defects[22,23,439] and bulk defects.[446,447] For instance, dissociative oxygen adsorption is endothermic on the stoichiometric $TiO_2(110)$ by more than 200 kJ/mol[448,449] but exothermic on the defected surface.[442] There is a delicate interplay between bulk defects and surface defects in TiO_2 (110),[450,451] which makes the surface chemistry of defects even more complicated. This kind of interplay between surface and bulk defects has not been observed with RuO_2.

When TiO_2 is bulk-reduced, a series of so-called Magneli phases (Ti_nO_{2n-1}; n = 2, 3, ..., 8) are formed.[452,453] These phases exist in the composition range between TiO_2 and Ti_2O_3, and they consist of slabs of the rutile structure separated by a regular array of shear planes on which the Ti density is higher than in TiO_2. Under oxidizing reaction conditions the excess Ti cations of the shear planes in the Magneli phases are driven toward the surface where these Ti atoms form TiO_2 islands with the incoming oxygen molecules.[23,447] Magneli phases are not known for RuO_2.

Besides photocatalysis, TiO_2 is used as carrier for supported catalysts. Rutile-TiO_2 can be coated for instance by the active component RuO_2, thus providing an extraordinarily active and stable catalyst for the HCl oxidation reaction.[26] Gold nanoparticles supported on $TiO_2(110)$ have been shown to be an excellent oxidation catalyst.[454]

6. CASE STUDY: CO OXIDATION OVER RUO_2

6.1. Scientific Background

In surface chemistry, the simple CO oxidation reaction catalyzed over metal surfaces serves as a prototypical reaction with a broad experimental and theoretical documentation, thereby allowing for a deep understanding down to the microscopic level. The complexity of the catalyzed CO oxidation reaction is quite low as only catalytic activity matters. However, not only does the catalyzed reaction count but also the interaction of the catalyst's surface with the reaction mixture and how this may modify the chemical nature of the catalyst. A particularly interesting catalytic system is encountered with the CO oxidation over ruthenium. While under UHV conditions Ru(0001) is a poor catalyst in the CO oxidation,[15,455,456] at pressures in the mbar range (which are high with respect to standard-UHV: 10^{-8} to 10^{-10} mbar) and in particular under oxidizing reaction conditions ruthenium turns into an efficient catalyst.[16−18] CO oxidation over ruthenium is therefore an intriguing example for a catalytic system where the catalytically active surface phase adjust itself to the actual reaction conditions such as sample temperature and the composition of the reactant gas mixture.[107,457,458]

Currently two catalytically active phases of ruthenium have been identified for the CO oxidation: a nonoxidic phase and the RuO_2 phase.[459] While the surface structure and composition of the RuO_2 phase is well characterized,[9,21] the chemical nature of the active nonoxidic phase is still elusive and a matter of ongoing discussion.[239,247,460−462] The nonoxidic phase may be identified with the "transient surface oxide (TSO)" as mentioned in the literature,[239,463] or with subsurface O as discussed in refs 87 and 464, or with the Ru−O trilayer structure[247] (or all three proposed phases are indistinguishable). The transient surface oxide is a kind of disordered suboxide which is not visible in SXRD but can be spectroscopically seen with HP-XPS. The catalytic activities of the nonoxidic phase and the RuO_2 phase are practically identical up to 520 K,[239,457] although the dependencies on the CO and O_2 partial pressures are distinctly different:[457,460] The reaction order in CO is one for the nonoxidic phase consistent with Peden and Goodman's work,[18] while it is zeroth order in CO for $RuO_2(110)$.[459]

Over the past few years several other platinum group metals (PGM) such as Rh, Pt, and Pd have been shown to form surface oxides under CO oxidation reaction conditions concomitant with an enhanced reactivity.[256,295,324,328,465] Whether these surface oxide phases are particularly active in the CO oxidation is currently debated.[295,363,466,467] These new findings has challenged the generally accepted chemical view whereupon oxide formation is considered to deteriorate rather than to improve the activity of transition metals in the oxidation of CO.[468,469] A systematic DFT study[470] of the CO oxidation indicates that the activation barriers for the recombination of CO and O on the rutile metal oxide surfaces are in general lower than that on the corresponding metal surfaces. The

dx.doi.org/10.1021/cr200247n | Chem. Rev. 2012, 112, 3356−3426

higher activity of surface metal oxides is mainly attributed to the favorable surface geometry of the transition state.

For the catalytic system "CO oxidation over ruthenium dioxide", ample experimental data are available ranging from single crystalline surface, over powder samples to supported Ru catalysts under UHV and high pressure conditions together with extensive DFT calculations on RuO_2 single crystal surfaces.[107,267,407,416,425,471] This unique situation allowed for a successful bridging of both the materials and the pressure gaps for the CO oxidation.[107] Besides catalytic activity, the reaction mechanism and deactivation processes have been thoroughly investigated on the atomic scale. First experiments on the electrochemical oxidation of CO at single crystalline Ru(0001) electrode are available,[472] so that this reaction system allows for a discussion across the discipline borders of electrocatalysis and heterogeneous catalysis.

6.2. CO Oxidation over RuO_2(110): Reaction Mechanism

6.2.1. Experimental Evidence. The high catalytic activity of stoichiometric RuO_2(110) toward CO oxidation was demonstrated to be controlled on the atomic scale by the presence of 1f-cus Ru atoms.[21] This point should be stressed since defects (such as oxygen vacancies, steps, and kinks) do not govern the catalytic activity as for most other oxide catalysts,[380] but rather the regular, under-coordinated surface atoms are responsible for the observed reactivity of RuO_2. On the stoichiometric RuO_2(110) surface, CO molecules adsorb strongly (adsorption energy exceeds 120 kJ/mol[378]) on-top of the 1f cus-Ru atoms from where the actual CO oxidation reaction takes place via recombination with under-coordinated surface oxygen atoms (either bridging O or on-top O atoms).[473] The strong adsorption of CO results in a high CO coverage under reaction conditions. Under typical reaction conditions, oxygen molecules from the gas phase adsorb dissociatively.[228,387] Molecular O_2 is quite strongly bound to the RuO_2(110) surface (up to 125 kJ/mol) with only a small energy barrier (20 kJ/mol) for dissociation.[387] Therefore, the molecular oxygen precursor state leads to a temperature-dependent sticking coefficient with a negative apparent activation energy. CO and O_2 are competing for the same active sites (1f-cus Ru) on RuO_2(110). High resolution energy electron loss spectroscopy (HREELS) measurements[415,474] and STM experiments[9,396,417] have essentially confirmed this reaction mechanism, and DFT calculations have elucidated the kinetics of these and other elementary reaction steps.[267,374,408,416,425,473,475]

The efficiency for CO oxidation has been shown to be almost independent of the orientation of RuO_2 (at least for the (110), (100), and (101) orientations) and is determined by the actual concentration of 1f-cus Ru sites.[103] Since the (110), (100), and the (101) surfaces are also the low energy surfaces of RuO_2, these orientations prevail on polycrystalline RuO_2.[103,200] Hence, the activity of polycrystalline RuO_2 is expected to be equally determined by the presence of 1f-cus Ru sites.[21]

Under typical reaction conditions, the RuO_2(110) surface offers the adsorbed CO molecule two potentially catalytically active oxygen species to form CO_2. In addition to the bridging O atoms, the RuO_2(110) surface stabilizes an on-top oxygen species which is by 150 kJ/mol more weakly bound to RuO_2 than the bridging O atoms.[51,228,425] Chemical intuition would therefore anticipate that the on-top O species dominates the activity of RuO_2(110), a conclusion that was supported by HREELS experiments[427] but challenged by isotope labeling experiments with ^{18}O, revealing that the bridging O species is practically as active in oxidizing CO as the on-top O species.[476]

Under strongly oxidizing reaction conditions (excess oxygen in the ($CO + O_2$) gas feed) the removed bridging O atoms are replenished by on-top O atoms so that on average the bridging O rows are intact and CO sits preferentially on top of 1f cus-Ru sites. As a net reaction adsorbed CO consumes exclusively on-top O to form CO_2.

In-situ SXRD experiments in combination with online mass spectrometry[457] indicate that under oxidizing reaction conditions in the mbar range and sample temperatures up to 700 K the oxide phase is structurally stable while maintaining high catalytic activity; above 700 K the oxide phase is slowly growing in thickness under reaction conditions.[457] Below 500 K the reaction order is zero in O_2 and CO and above 540 K first and half order kinetics in CO and O_2, respectively. The apparent activation energy for the CO oxidation reaction over RuO_2(110) turned out to be 75−80 kJ/mol.[457,459]

Under reducing reaction conditions, that is, with excess CO in the gas feed, both reactants adsorb initially over the 1f-cus Ru atoms and the adsorbed CO molecules easily recombine with on-top O (O_{ot}) and bridging O atoms (O_{br}) to form CO_2. In principle, the removed bridging O atoms can by replenished by on-top O originating from the dissociative adsorption of molecular oxygen from the gas phase. However, since CO is in excess on the surface most of the reacted-off bridging O atoms will be replaced by strongly adsorbed bridging CO molecules (1.85 eV[379]), thereby stabilizing the oxide catalyst against further chemical reduction up to reaction temperatures of 400 K. Therefore, after an induction period most of the bridging O atoms are replaced by bridging CO molecules as evidenced by in situ RAIRS measurements.[435] The actual reaction takes place mainly between adsorbed CO (bridge and on-top) and on-top O on the working RuO_2 catalyst. Complete reduction of the RuO_2 catalyst sets in for a reaction temperature above 400 K and strongly reducing $CO + O_2$ reaction mixtures.[109,239]

The activity in the CO oxidation on RuO_2(110) is maximized for a stoichiometric reaction mixture; that is, the ratio of CO and O_2 in the gas feed is close to 2:1, both under UHV conditions[474] and pressures in the mbar range.[459] At the beginning CO molecules react with both oxygen species, the on-top O and the remaining bridging O species.[415] However, under steady state reaction conditions and sample temperatures below 400 K, the bridging O is (mostly) replaced by bridging CO as shown by in situ RAIRS,[435] by ex-situ HREELS experiments,[474] and by STM.[396] In-situ SXRD experiments of pressures up to 100 mbar range and temperatures up to 700 K indicate that the RuO_2 surface is structurally stable under stoichiometric reaction conditions.[457,459]

With in situ RAIRS,[435] the pressure gap could be successfully bridged for the model catalyst RuO_2(110) as the vibrational spectra under reaction conditions were shown to be stable in the pressure ranging from UHV to 10^{-3} mbar.

With HP-XPS in combination with online mass spectrometry, the CO oxidation at $P(CO) = 4 \times 10^{-4}$ mbar and $P(O_2) = 1.6 \times 10^{-4}$ mbar was followed as a function of temperature.[282] It turned out that the RuO_2(110) surface is stable under these reaction conditions and catalytically active with a maximum activity at 450 K (cf. Figure 34). The decline in activity is due to thermodynamics as the reactants on the surface start to equilibrate with the gas phase.

6.2.2. Theoretical Modeling. The key parameter that controls the rate of chemical reactions is the activation energy of the rate determining step (rds).[477] For the CO oxidation reaction on RuO_2(110), the rate determining step in the CO oxidation has been identified with the recombination of adsorbed CO with under-coordinated surface O atoms.[267,374,416,425,473,475]

dx.doi.org/10.1021/cr200247n | Chem. Rev. 2012, 112, 3356−3426

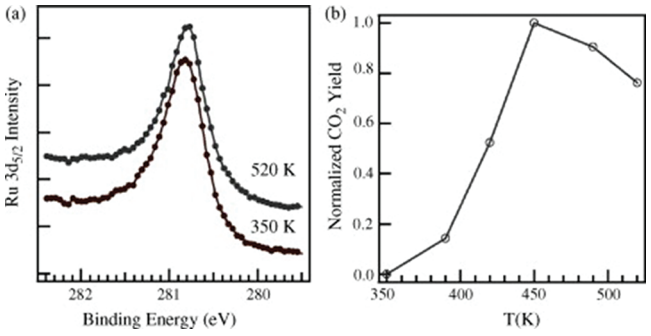

Figure 34. Oxidation of CO over RuO_2 (110) at T = 350−500 K for a reaction mixture of $P(O_2) = 1.6 \times 10^{-4}$ and $P(CO) = 4.0 \times 10^{-4}$ mbar. (a) Ru $3d_{5/2}$ spectra taken during the CO + O_2 reaction illustrating the preserved RuO_2 state for reaction temperatures 350−520 K. (b) Normalized CO_2 mass spectra intensity as a function of temperature. Reprinted with permission from ref 282. Copyright 2007 Elsevier.

There are two potentially active oxygen species on RuO_2(110), namely, the bridging and on-top O atoms whose adsorption energy differs by more than 150 kJ/mol.[228] Assuming that the activation of adsorbed O governs the activation energy of the CO+O recombination step as encountered with transition metal surfaces,[478] then the Brønsted−Evans−Polanyi (BEP) relation[479−481] suggests that the O_{ot} species on RuO_2(110) is much more active in the oxidation of CO than the O_{br} atoms.[482] The on-top species of oxygen is in the optimum binding energy window for the CO oxidation as implied on the basis of the BEP relation.[481,482]

Besides two active O-species on the RuO_2(110) surface there are two distinct CO adsorption sites on RuO_2(110), namely, the bridging CO (CO_{br}) and the on-top CO (CO_{ot}) species. This makes four elementary reaction steps for the recombination of CO and O at the RuO_2(110) surface: $CO_{ot} + O_{ot}$, $CO_{br} + O_{ot}$, $CO_{br} + O_{br}$, and $CO_{ot} + O_{br}$ (cf. Figure 35).

In Table 4 calculated values for the corresponding activation barriers of these four elementary reaction pathways are compared among various first principles calculations found in the literature. Clearly, the activation barriers scatter markedly among these studies. Quite in contrast to DFT calculations by Seitsonen et al.,[267] the activation barriers of the association of on-top CO with on-top O and bridging O in refs 416 and 425 differ by about 40 kJ/mol. More recently Kiejna et al.[408] performed a comparative study between full potential calculations (as used in ref 425) and pseudopotential calculation based on DFT (as used in refs 416 and 475). This comparison revealed that the former difference in activation energies of 40 kJ/mol reduces to 20 kJ/mol. Still, a difference in activation energies of 20 kJ/mol would imply that both reaction pathways should be readily resolved in temperature programmed reaction experiments, incompatible with experimental findings.[473,476]

From STM data, an activation energy of 90 kJ/mol was deduced for the recombination of on-top CO with on-top O, when all bridging O are replaced by CO.[396] HREELS data[415] for RuO_2(110) saturated with oxygen in on-top position and subsequently exposed to various CO doses at 300 K show that about 50% of on-top O are first consumed by CO oxidation and then both O_{ot} and O_{br} are reduced by CO. From this experiment one can deduce that the activation barriers for on-top CO recombination with O_{ot} and O_{br} do not differ by more than 6 kJ/mol.

Other elementary reaction steps between CO and O on the RuO_2(110) have previously been discussed.[374,425,473] The bridging CO can react either with bridging O or with on-top O. The corresponding activation barriers are determined to be 130 and 60 kJ/mol, respectively,[473] consistent with other studies.[408,425] Quite in contrast, the activation barrier between bridging CO and on-top O is the lowest among the possible elementary reaction pathways and therefore intrinsically important for the reaction kinetics. The diffusion barriers for on-top O and on-top CO along the 1f-cus Ru rows are quite high with about 100 kJ/mol, while diffusion perpendicular to the 1f-cus Ru rows into O-bridge vacancies is activated by only 70 kJ/mol.[374] Therefore, both CO molecules and on-top O atoms can readily hop from the 1f-cus Ru atoms into the O_{br} vacancies, thereby increasing their binding energies to the surface by 50 and 150 kJ/mol, respectively.[473] Even higher diffusion barriers were reported by Reuter and Scheffler.[425]

A recent DFT study,[267] using the improved pseudo potentials of Kiejna et al.,[408] tackled the question of whether the promotion of the active O species constitutes the critical step in the elementary reaction. In doing so, the total activation barrier E_a was decomposed into contributions describing the changes in the binding energy of the reactants when moving from the initial state (IS) to the transition state (TS) of the reacting system. This approach has been successfully applied for determining general trends in the energy barriers of catalytic reactions among various transitions metal surfaces.[478,486] For the case of RuO_2(110), it turned out that the activation of adsorbed CO dominates the barrier for the recombination of on-top CO with both bridging O and on-top O atoms. Since the activation energies of CO are similar for both elementary reactions steps, the quasi degeneracy of the activation barriers of the recombination of CO with on-top O and bridging O[267] is naturally explained despite the marked difference of the binding energies of on-top O and bridging O on RuO_2(110).

The activation barriers of the elementary recombination steps of CO and O on RuO_2(110) can also be derived from temperature programmed reaction experiments of well-designed CO + O coadsorbate layers.[473,476] These values are compiled in last column of Table 4. Microkinetic modeling of the steady-state CO oxidation reaction over RuO_2(110) has been performed by using kinetic Monte Carlo (KMC) simulations.[471] The input parameters to these KMC simulations are the rate constants of 18 elementary surface processes, including adsorption, desorption, diffusion, and chemical surface reactions with activation energies provided by experiment (see Table 4 right column) and accounting for micro reversibility.[471] Adsorption processes are modeled within the kinetic gas theory. With KMC simulations the turnover frequency (TOF: number of produced CO_2 molecules per surface area and second) was determined as a function of the reactant feed ratio $p(CO)/p(O_2)$, while keeping the partial pressure of oxygen constant at 10^{-7} mbar and the sample temperature at 350 K (cf. Figure 36). These KMC-based TOF values are compared to experimental values[474] obtained for the same reaction conditions.

The KMC simulated TOF values, based on the semiempirical parameter set of Table 4, are systematically greater by a factor of 2.5 than the experimentally determined ones. On the other vhand, the dependence of the TOF as a function of the reactant feed ratio is well reproduced. Under optimum reaction conditions the most important elementary reaction step governing the overall kinetics of the CO oxidation is identified with the recombination between on-top CO and bridging O

dx.doi.org/10.1021/cr200247n | Chem. Rev. 2012, 112, 3356−3426

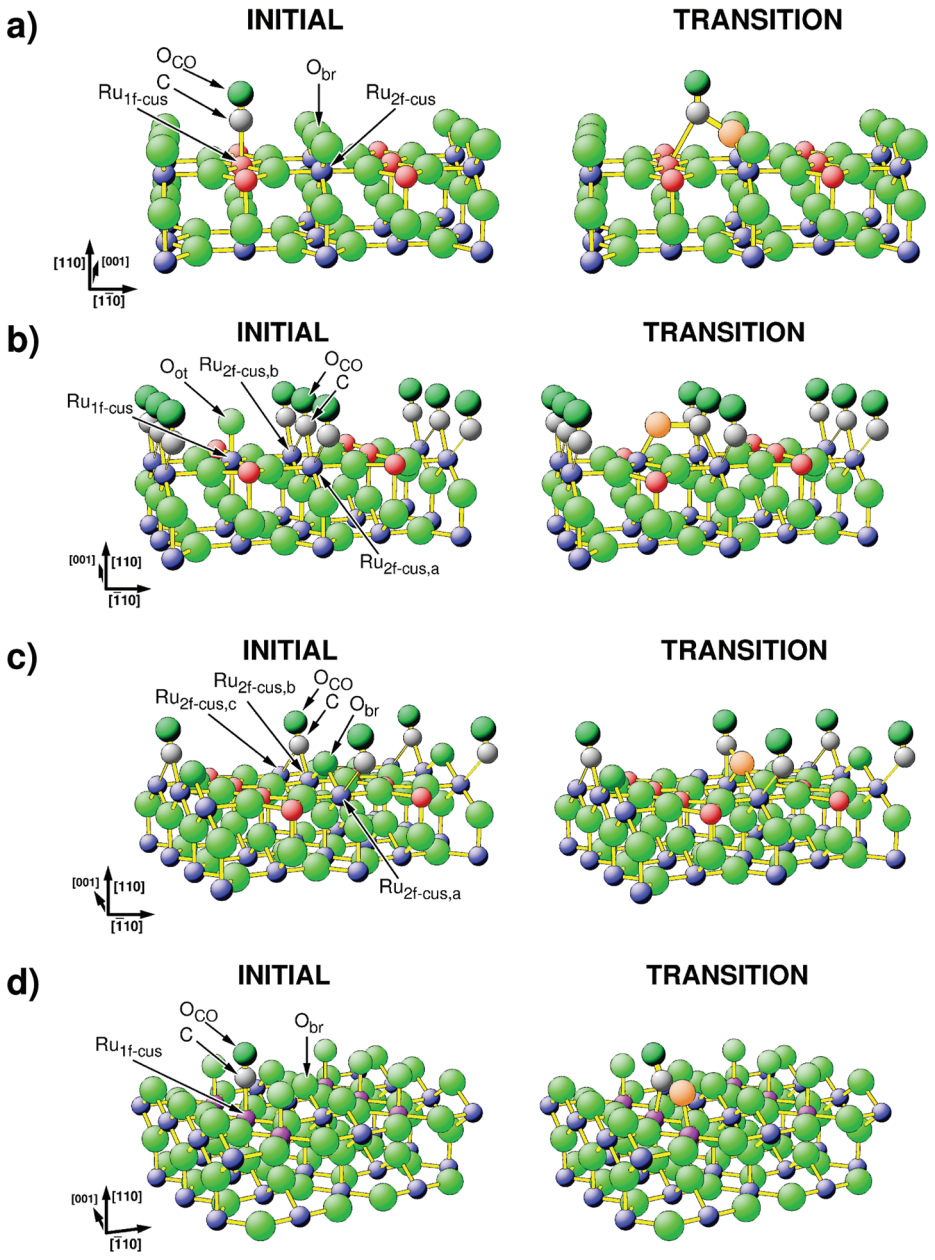

Figure 35. Ball-and-stick model of the initial and transition state of the four elementary CO + O recombination reactions on $RuO_2(110)$ surface. (a) On-top CO recombines with bridging O atoms: $CO_{ot} + O_{br}$. (b) Bridging CO recombines with on-top O atoms: $CO_{br} + O_{ot}$. (c) Bridging CO recombines with bridging O atoms: $CO_{br} + O_{br}$. (d) On-top CO recombines with on-top O atoms: $CO_{ot} + O_{ot}$. Reprinted with permission from ref 475. Copyright 2003 Elsevier.

Table 4. Activation Energy (kJ/mol) for the Recombination of the on-top CO and Bridging CO with Bridging O and with on-top O over $RuO_2(110)$ as Determined by Various Ab-Initio Calculations[a]

reaction barriers in kJ/mol	pseudo-DFT[475,374]	pseudo-DFT[267]	pseudo-DFT[416]	FP-LAPW[425]	FP-LAPW[408]	experiment[471]
$CO_{ot} + O_{ot}$	68	71	86	89	78	86
$CO_{br} + O_{ot}$	60	60		76	61	83
$CO_{br} + O_{br}$	130	140		154	148	124
$CO_{ot} + O_{br}$	71	74	121	125	99	83

[a]FP-LAPW: Full potential DFT code,[483] pseudo-DFT: pseudopotential DFT code.[416,484] Theoretical studies[267,408,425] used the same type of generalized gradient approximation for the exchange-correlation functional PBE.[485]

due to the relatively low energy barrier and the large abundance of both surface species. The next frequent elementary recombination step is $CO_{br} + O_{ot}$, which is by a factor of 4 smaller than $CO_{ot} + O_{br}$. The recombination of on-top CO with on-top O is by more than 1 order of magnitude less frequent than $CO_{ot} + O_{br}$ under optimum reaction conditions.

For three typical reaction conditions $p(CO)/p(O_2) = 1/2, 2, 10$ the surface configurations are shown as snapshots of the

dx.doi.org/10.1021/cr200247n | Chem. Rev. 2012, 112, 3356–3426

KMC simulations after steady-state conditions have been reached (cf. Figure 36 insets). At optimum reaction conditions

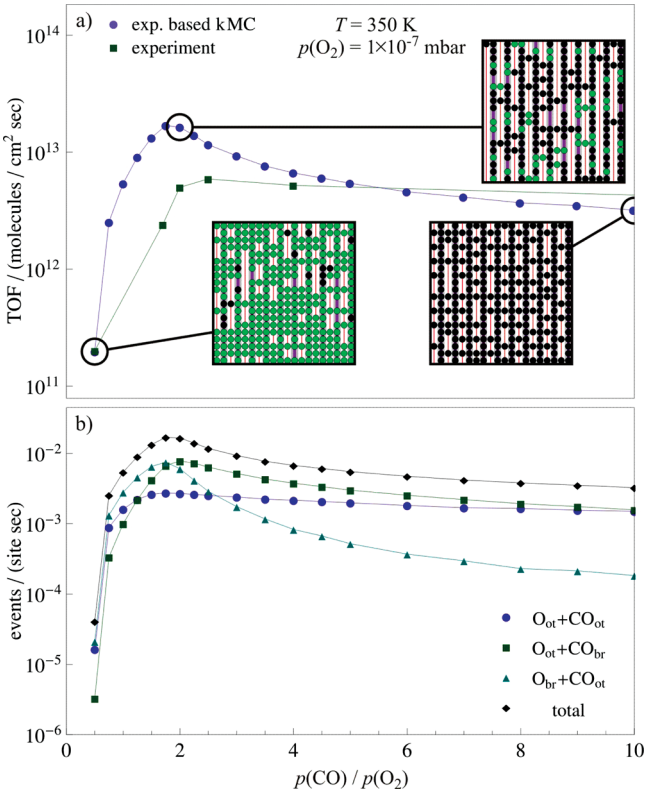

Figure 36. Oxidation of CO over $RuO_2(110)$ at 350 K with constant $p(O_2) = 10^{-7}$ mbar. (a) TOF as a function of the reactant feed ratio $p(CO)/p(O_2)$: KMC simulation (circles) and experimental values[474] (squares). Insets show the KMC simulated spatial distributions of reactants at the surface for three different feed ratios $p(CO)/p(O_2)$ = 0.5, 2, 10. Color code: O (green), CO (black), vacant 1f-cus Ru sites (red stripes), vacant 2f-cus Ru sites (purple stripes). (b) Contributions of the elementary O + CO recombination steps (O_{ot} + CO_{ot}, O_{ot} + CO_{br}, and O_{br} + CO_{ot}) to the total TOF. Because of the high activation barrier for O_{br} + CO_{br}, this elementary step does not contribute significantly to the overall rate at 350 K and is therefore not shown here.[471]

with highest TOF ($p(CO)/p(O_2) \sim 2$), most of the bridging O atoms are replaced by CO and the rest of the 2f-cus Ru sites are vacant or occupied by bridging O. The 1f-cus Ru sites are mostly vacant and only a few on-top CO are visible, indicating that most of the on-top CO molecules react easily with oxygen to form CO_2. This distribution of CO and O on the $RuO_2(110)$ surface is fully reconciled with the RAIR spectrum, where mostly bridging CO is seen as a vibrational CO stretch band at 1866 cm^{-1}.[435]

For oxidizing reaction conditions (Figure 36, $p(CO)/p(O_2)$ = 1/2), the surface is mainly covered by bridging O and on-top O. The few CO molecules found on the surface reside mostly in a bridge position. CO molecules which adsorb in the vacant on-top positions readily recombine with neighboring O, thus explaining the residual activity of this surface and the absence of on-top CO in the KMC snapshot.

Under strongly reducing reaction conditions ($p(CO)/p(O_2)$ = 10), the 2f-cus Ru sites are almost exclusively occupied by bridging CO. About half of the 1f-cus-Ru sites are populated by CO while the other half remains vacant. The incomplete coverage of on-top CO, despite the strongly reducing gas mixture, is due to the maximum in CO_{ot} desorption at 320 K and the small CO partial pressure of 10^{-7} mbar. This surface is not poisoned by CO but rather should be quite active, as also experimentally observed. Besides partly ordered (2x1) CO domains there are regions where between neighboring on-top CO there are several vacant 1f-cus sites on which molecular oxygen adsorbs dissociatively. Subsequently, on-top O and on-top CO recombine rapidly to form CO_2, so that in the KMC snapshot no on-top O is visible.

The great advantage of KMC simulations is that the overall TOF can be decomposed into the contributions of the relevant elementary recombination steps. This information is not readily available by experiments. In Figure 36b, the contributions of the three leading elementary recombination steps (O_{ot} + CO_{ot}, O_{ot} + CO_{br}, and O_{br} + CO_{ot}) are detailed. Under oxidizing reaction conditions the main contributions come from the recombination of on-top CO with both bridging O and on-top O, while under strongly reducing conditions the recombination of on-top O with both bridging CO and on-top CO determines the TOF. For the optimal reaction mixture $p(CO)/p(O_2) \approx 2$ all three recombination steps are equally important for the CO oxidation reaction.

The energy barriers in the kinetic modeling can also be taken from first principles calculations. With these "first principles" kinetic MC simulations,[407,487] the experimental kinetic data at T = 350 K and various partial pressure of CO and O_2 in the pressure range of 10^{-7} mbar[474] could be reproduced, although these simulations indicate deactivation under oxidizing reaction conditions which is experimentally not observed. The most important elementary reaction step determining the overall kinetics of the CO oxidation was argued to be the recombination between on-top CO and on-top O due to the relatively low energy barrier and the large abundance of both species on the surface. The authors concluded that despite having the lowest activation energy the reaction step between bridging CO and on-top O does not occur since the population of bridging CO under typical gas feed stoichiometries is negligibly small.[407]

However, these conclusions from "first-principles" KMC simulations[407,487] contradicts recent in situ RAIRS experiments[435] (RAIRS: reflection absorption infra red spectroscopy) for the same reaction conditions. The RAIRS study has shown that bridging CO molecules are abundantly formed during the CO oxidation reaction over a wide pressure (10^{-7} mbar to 10^{-3} mbar) keeping the sample temperature at 350 K. The presence of bridging CO molecules is consistent with degenerate energy barriers for the recombination of on top CO with on-top O and bridging O.[267] The presence of bridging CO is, however, also reconciled with previous ex-situ HREELS experiments for a stoichiometric CO/O_2 reaction mixture in the 10^{-7} mbar range and a sample temperature of 350 K[474] in which substantial amounts of bridging CO and the removal of most of the bridging O atoms have been found after the reaction. For a critical assessment of "first-principles" based KMC simulations the reader is referred to a recent comparative study.[488]

6.3. CO Oxidation over RuO_2 Powder and Supported RuO_2 Catalysts: Bridging the Materials Gap

It has been demonstrated that a crucial step in the preparation of active RuO_2 powder and supported RuO_2 catalysts constitutes the chemical prereduction of the oxide catalysts at 773 K using hydrogen followed by a mild reoxidation of the

dx.doi.org/10.1021/cr200247n | Chem. Rev. 2012, 112, 3356–3426

particles either under oxidizing reaction conditions (supported catalyst) or by oxygen pretreatment (450 K in air; powder catalyst).[161] This pretreatment results in a shell−core structure of the catalyst particle in which the metallic Ru core is coated by an ultrathin RuO_2 film of 1−2 nm, as concluded from XRD and diffuse reflection infrared Fourier transform spectroscopy (DRIFTS).[107] The activation energy for the CO oxidation reaction over this type of core−shell particle is about 80 kJ/mol. Fully oxidized particles are less active in the CO oxidation,[106] and their apparent activation energy is about 100 kJ/mol compatible with previous studies on the same system.[16,17] As shown by in situ SXRD experiments the model catalyst $RuO_2(110)$ consists also of an shell−core structure, namely, the self-limiting growth of a 1.6 nm thick oxide film covering the Ru(0001) "core".[109]

In Figure 37 the turnover frequencies (TOF: number of produced CO_2 molecules per second and active site) of the

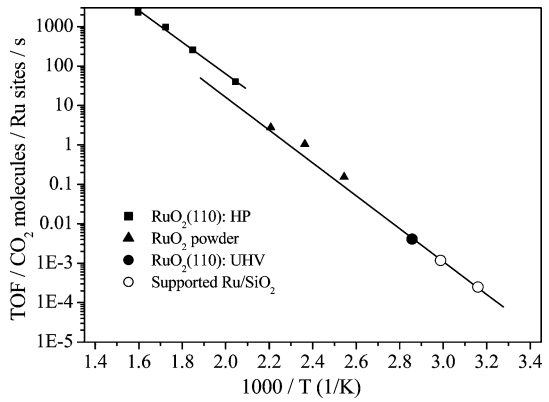

Figure 37. Arrhenius plot of turnover frequencies TOF (CO_2 molecules formed per Ru site and second) measured for the oxidation of CO over RuO_2 powder[107] (filled triangle), supported RuO_2 on SiO_2[161] (open circles), UHV experiment on $RuO_2(110)/Ru(0001)$[474] (filled circle). For these systems, the determined activation energy was 82 kJ/mol.[107] These TOF data from the literature are compared to those for $RuO_2(110)$ in the 10 mbar pressure range (HP = high pressure: filled squares) which yield an activation energy of 78 ± 10 kJ/mol. Reprinted with permission from ref 457. Copyright 2009 Elsevier.

hydrogen pretreated (powder and supported) RuO_2 catalysts are compared to single crystalline $RuO_2(110)$ model catalyst under UHV and high pressure conditions.[457] From the excellent agreement of the activation energies (slope of the curves) of about 80 kJ/mol, the materials gap is concluded to be bridged from a kinetic point of view. Maximum activity is achieved for a stoichiometric reaction mixture of CO and O_2 for all three types of catalysts.

6.4. Deactivation and Poisoning of RuO_2-Based Catalysts

6.4.1. Structural Deactivation. For Ru-based catalysts, a strong activity loss was reported for the CO oxidation reaction. In particular under oxidizing reaction conditions the activity of supported Ru catalysts declined substantially.[16,489] Cant et al.[16] concluded that portions of the metallic ruthenium surface are converted into an inactive oxide layer, whereas Kiss and Gonzalez[17] suggested that the partial deactivation of Ru/SiO_2 is the result of the formation of lattice oxygen.

Deactivation in the CO oxidation has been reported for the single crystalline RuO_2 surfaces as well. First of all, on $RuO_2(100)$ a unique c(2×2) phase was identified which is inactive in CO oxidation.[265,378] But also a $RuO_2(110)$ film can deactivate when the oxidation temperature is beyond 700 K. Under these conditions the $RuO_2(110)$ roughens considerably, exposing preferentially facets with inactive c(2×2) areas.[249] Thermal desorption experiments indicate that such rough $RuO_2(110)$ surfaces inhibit CO and O_2 adsorption and therefore the CO oxidation.

With this knowledge in mind and the awareness that the pressure and materials gap have been successfully been bridged,[107] the deactivation of supported and powder RuO_2 catalyst can be traced to the evolution of c(2×2) domains on the particles under oxidizing reaction conditions. More specifically, the RuO_2 particles expose preferentially (110) and (100) facets. Upon CO oxidation under net oxidizing conditions, the active $RuO_2(100)$ facets of the RuO_2 particle transform into the inactive $RuO_2(100)$-c(2×2) phase. But also the $RuO_2(110)$ facets will deactivate partly under oxidizing conditions: The $RuO_2(110)$ facets roughen considerably, thereby forming additional $RuO_2(100)$ facets which reconstruct into the inactive c(2×2) phase. These processes are the more efficient the higher the temperature is. Finally, the RuO_2 particle exposes predominantly catalytically inactive $RuO_2(100)$-c(2×2) facets and only small areas of active $RuO_2(110)$ facets. This deactivation scheme is applicable for supported RuO_2 catalysts[107] and also for RuO_2 powder catalysts.[249,489]

Rosenthal et al.[458,489] studied recently the CO oxidation over powder RuO_2 at atmospheric pressures. When RuO_2 was precalcined in pure oxygen at 1073 K, the powder catalyst was shown to be completely inactive. However, after a long induction period (>3 h) in a net-oxidizing feed stream at 503 K, the precalcined RuO_2 powder was reactivated with 100% conversion, revealing by in situ XRD no structural changes in the bulk structure.

In order to prepare active and stable RuO_2-based catalysts, the once reduced Ru particles should be only mildly oxidized (oxide film of 1−2 nm thickness) in order to avoid the growth of a rough oxide layer. This simple recipe implies however a substantial activity dependence on the particle size, since very small particles are expected to fully oxidize. Indeed, a recent study on uniform nanoparticles of Ru with a tunable particle size from 2 to 6 nm gives evidence that the activity in CO oxidation increases with the particle size: the 6 nm Ru particle catalyst exhibits an order of magnitude higher activity than catalysts with 2 nm particles.[171]

6.4.2. Poisoning of the Catalyst. On single crystalline $RuO_2(110)$ water coadsorption has been shown to impede the CO oxidation since water adsorbs strongly on the 1f-cus Ru site, thereby blocking those sites for oxygen and CO adsorption.[402] This water-induced poisoning process is expected to be less severe above a sample temperature of 350 K, where water starts to desorb.[276] However, on polycrystalline RuO_2 powder catalysts already 2.4% of water in the gas feed suppresses completely the CO oxidation of a stoichiometric mixture in the temperature range up to 453 K.[106] Obviously, water adsorbs and desorbs continuously along the catalyst bed so that water poisoning is even observed at 453 K. Co-fed water under reaction conditions blocks active 1f cus-Ru site either directly by adsorbed water or by dissociation, thereby transferring the H to another on-top O and blocking two 1f-cus Ru sites per adsorbed water molecule.[274] In this context it is quite remarkable that hydrous RuO_2 oxidizes CO even at room temperature and under humid conditions.[36]

dx.doi.org/10.1021/cr200247n | Chem. Rev. 2012, 112, 3356−3426

An irreversible and strong poisoning of the RuO_2 powder catalyst was observed when the oxide was pretreated with HCl at 500 K. The subsequent CO oxidation was completely suppressed and could not be restored by high temperature treatment and hydrogen treatment.[490] HCl exposure at 500 K leads to the chlorination of the RuO_2 surface in that the bridging O atoms are selectively replaced by chlorine.[405] The poisoning of chlorine proceeds then in two different ways.[491] One is of electronic nature: The bridging Cl atoms, which are produced by HCl exposure, increase the activation energy for CO + O recombination step on the surface by about 6 kJ/mol. A second effect is that the bridging chlorine can dynamically shift from bridge to on-top sites, thereby blocking the active sites along the 1f-cus Ru rows. Site blocking is of particular importance when 1D confinement of the reactants along the 1f-cus Ru rows is considered. On-top Cl not only blocks a single catalytically active 1f-cus Ru site but Cl_{ot} also inhibits the approach of O_{ot} and CO_{ot} along the 1D 1f-cus Ru rows.

Another type of poisoning of the CO oxidation over $RuO_2(110)$ was proposed from high pressure STM experiments. After exposing the $RuO_2(110)$ surface to 1 bar of O_2, a carbon containing species was observed in STM.[492] On the basis of thermal desorption spectroscopy and XPS, this species was assigned to a strongly adsorbed carbonate species leaving the surface only above 540 K. A direct identification of such a carbonate species under CO oxidation reaction conditions is still missing. However, recent high pressure reaction experiments of the CO oxidation on $RuO_2(110)$ in a batch reactor have indicated that product poisoning by CO_2 occurs under oxidizing reaction conditions and temperatures up to 600 K. CO_2 is considered to form a carbonate species on the surface but after evacuation of the batch reactor the catalyst activity was restored.[457] DFT calculations have been devoted to the surface poisoning process during CO oxidation over $RuO_2(110)$. Wang et al.[413,493] suggested that the surface bicarbonate (HCO_3^-) rather than a carbonate species (CO_3^{2-}) deactivates $RuO_2(110)$ over a wide range of CO and O_2 pressures in the presence of trace amounts of water.

6.5. Comparison with the Electrochemical Oxidation of CO at $RuO_2(100)$ Model Electrodes

The electrocatalytic oxidation of CO is different from the gas phase oxidation as not molecular oxygen but rather water serves as the oxidant. On pure Ru and Pt surfaces, it is "generally accepted" (meaning plausible but not conclusively demonstrated) that the electro-oxidation of adsorbed CO follows a Langmuir–Hinshelwood mechanism in which adsorbed CO reacts with an oxygen-containing species present on the surface:[494,495]

$$H_2O + * \rightarrow OH_{ad} + H^+ + e^- \quad (1)$$

$$OH_{ad} + CO_{ad} \rightarrow CO_2 + H^+ + e^- + 2* \quad (2)$$

(* denotes the empty active sites on the surface).

To account for the frequently reported Tafel slope of about 60 mV/decade for Pt the reaction, step (2) is split into two separate steps:

$$OH_{ad} + CO_{ad} \rightarrow COOH_{ad} + * \quad (2a)$$

$$COOH_{ad} \rightarrow CO_2 + H^+ + e^- + * \quad (2b)$$

with step 2b being rate determining.[496,497]

Quite in contrast on single crystalline Pt(111), step 1 is considered to be rate-determining so that CO_2 evolution set in as soon as OH is present on the surface.[498] Frelink et al.[499,500] proposed that a surface O species rather than OH should be the reactant with which adsorbed CO on Pt recombines to form CO_2. Already this brief survey may document that the reaction mechanism of electrochemical CO oxidation on platinum is still not fully clarified.

Because of the stronger O–Ru bond, adsorption of OH or O appears in a potential region far below the CO_2 evolution. Therefore, on metallic ruthenium step 2 is considered to be rate determining, occurring at an overpotential that is 300 mV lower than on Pt.[495]

For the case of $RuO_2(100)$ the oxygen-surface bonds are weaker than on Ru(0001) and dissociation of H_2O is facile. Therefore, RuO_2 is expected to be more active in the electrocatalytic oxidation of CO than Ru(0001). The activities of Ru(0001) and $RuO_2(100)$ in the electro-oxidation of CO were compared by cyclic voltammetry (CV),[501] and indeed $RuO_2(100)$ was shown to be more active than Ru(0001). This conclusion was supported by in situ FTIR experiments.[472]

6.6. CO Oxidation over RuO_2: Concluding Remarks and Open Questions

The most active RuO_2-based catalyst consists of a shell–core particle where the Ru core is covered by 1–2 nm thick RuO_2 film, while thicker RuO_2 films tend to deactivate the catalyst. This type of active core–shell catalysts is realized by hydrogen pretreatment at 700–800 K of both supported and powder RuO_2 catalysts followed by mild reoxidation.[107] The self-limiting growth of $RuO_2(110)$ film on Ru(0001) model catalyst[109] in a wide temperature range represents a "flat" shell–core motif.

The CO oxidation over such RuO_2-based catalysts is well-understood on the atomic scale, proceeding via a Langmuir–Hinshelwood mechanism where adsorbed CO recombines with under-coordinated O atoms on the surface to form CO_2. Maximum reactivity is established with a stoichiometric CO + O_2 gas feed. Under such conditions, the oxygen bridge positions of the working model catalyst $RuO_2(110)$ are mostly replaced by CO, at least at reaction temperature below 400 K.[435]

Although RuO_2 is indeed a remarkable active oxidation catalyst for the CO oxidation reaction, the high catalytic activity studied in the seminal work of Goodman and Peden[18] is still not (well) understood.[461] Even under the most strongly oxidizing reaction condition where pure oxygen is supplied in the reactant feed, the oxidation of Ru to RuO_2 metal takes place only for temperatures higher than about 500 K. This threshold temperature was found for single crystalline Ru(0001)[109,239] and for 7 nm thick nanocrystalline Ru films on Si.[118] Since most of the experiments in ref 18 were conducted at temperatures well below this threshold temperature, RuO_2 cannot be the catalytically active phase in ref 18. However, under typical CO oxidation reaction conditions in the 100 mbar range supported Ru catalysts even oxidize at room temperature, since the reaction heat drives locally the catalyst beyond the threshold temperature.[106] Therefore, the RuO_2 phase is decisive but not unique to explain the high activity of supported Ru catalysts under realistic CO oxidation reaction conditions and excess oxygen in the reactant feed.

The chemical nature of the active phase in ref 18 is still not settled. Goodman et al.[460] have favored a (1×1)O surface as the active phase in their experiments. Recent high pressure core level shift experiments indicate that a kind of nonstoichiometric

dx.doi.org/10.1021/cr200247n | Chem. Rev. 2012, 112, 3356–3426

transient surface oxide (TSO) is stabilized at reaction temperatures below 500 K[239] and TSO is active in the CO oxidation. Yates and co-workers[502a] demonstrated that a stepped Ru(0001) surface is actually active in the CO oxidation even under UHV conditions, while the CO oxidation is suppressed in the absence of steps. However, one has to recall that CO molecules efficiently dissociate at the step edges thereby blocking the active steps sites.[502b] The active role of steps on Ru(0001) in the CO oxidation has been corroborated by recent DFT calculations.[503]

Recent LEEM experiments[247,248] have shown that the active surface consists of three phases coexisting on the Ru(0001) surface. Besides RuO_2(110) a second catalytically active phase with a quasi (2×2)-LEED pattern is observed which was ascribed to the O−Ru−O-trilayer phase[247] or RuO_2(100) grown on Ru(0001).[53] The third phase was assigned to the (1×1)O and is shown to be catalytically inactive.

It is quite puzzling that the activation barrier in the CO oxidation on nonoxidized ruthenium found by Peden and Goodman (82 kJ/mol)[18] is practically identical to that found on RuO_2(110).[459] However, the partial reaction orders of the oxidation of CO on both surfaces are different and therefore indicative of two distinct active phases.[459] Further work is required to settle the chemical nature and structure of the catalytically active nonoxidic Ru(0001) phase.

7. APPLICATION OF RUO_2 IN HETEROGENEOUS CATALYSIS

The catalytic properties of Ru and RuO_2 are complementary. Both Ru and RuO_2 are good dehydrogenation catalysts, that is, facilitate hydrogen abstraction from organic molecules, although the underlying microscopic processes in the dehydrogenation of hydrocarbons are different. On RuO_2 the under-coordinated metal atoms accommodate the hydrocarbon (fragment), while the under-coordinated O atom accepts the abstracted hydrogen atom. This simple view has been corroborated by DFT calculations.[398] On metallic ruthenium the metal atoms can accept both the hydrocarbon fragment and the hydrogen atoms. If oxygen atoms are present on the metal surface, an OH species is formed on ruthenium. However, there are distinct differences in the activity as well. Metallic Ru is considered to be a poor oxidation catalyst, while RuO_2 is an efficient catalyst for the oxidation of CO and other molecules.[9] On the contrary, Ru is an excellent hydrogenation catalyst, such as for the ammonia synthesis[155] or the hydrogenation of olefins, while RuO_2 is a very poor hydrogenation catalyst as hydrogen exposure leads rather to the reduction of RuO_2 by forming water and thereby consuming lattice O of RuO_2.[109,274]

Over the past decade, RuO_2-based catalysts have evolved from a pure target of fundamental research into a promising practical catalyst with a wide range of potential applications. The simple CO oxidation reaction, for instance, can be catalyzed even at room temperature and in a humid environment. This holds the promise for zero-energy air purification.[36] Methane is oxidized totally over RuO_2, while metallic Ru is able to partially oxidize methane to CO and water.[283]

Further applications of RuO_2 are found in the field of "green chemistry". Matsumoto and Ito[504] first demonstrated that RuO_2 transforms allylic alcohols to unsaturated carbonyl compounds under mild reaction conditions. The oxidative dehydrogenation of simple alcohols proceeds already at low temperatures.[28] Ru-oxide nanoclusters immobilized in faujasite zeolite have been shown to be a highly selective and efficient catalyst for the aerobic oxidation of alcohols[167] and cyclohexane.[168] RuO_2 domains catalyze the oxidation of various alcohols to aldehydes and ketones at 373 K.[505−508] A broader introduction into the catalytic oxidation of alcohols with molecular oxygen on solid catalysts can be found in a recent review article.[5] The aerobic oxidation of benzyl alcohol catalyzed by hydrous Ru-oxide[509] supported on carbon nanotubes was shown to be closely related to its performance as a super capacitor. The catalytic activity can be predicted from the specific capacitance of RuO_2, suggesting that highly active RuO_2 nanocatalysts are also good super capacitors.[39] RuO_2 supported on TiO_2 allows for the wet-air oxidation of aqueous solutions of formic acid, acetic acid, and phenol.[510]

The atomic structure of nanocrystalline RuO_2 has shown modifications of the rutile structure in that the oxygen octahedrons are anisotropic, while in micro-RuO_2 powder these octahedrons are quasi-isotropic. For the total methane oxidation on RuO_2 powder a distinct structure−activity relation has been observed.[511]

RuO_2 supported on alumina efficiently catalyzes the oxidation of primary and secondary amines to form nitriles and imines.[27,512] Efficient oxidation of primary amines to amides over supported ruthenium hydroxide catalysts was reported by Kim et al.[513] But also the direct combustion of carbon can be performed with RuO_2 at substantially lower temperatures than with alternative catalysts.[514,515] This process may find application for the automotive exhaust purification of diesel engines. Composite $RuO_2/BaTi_4O_9$ represents an environmentally benign solid catalyst for the oxidative cleavage of olefins.[516] Catalytic conversion of elemental mercury to its oxidized form is considered as an effective way to enhance mercury removal from coal-fired power plants. RuO_2-modified SCR catalysts have shown to be efficient in Hg removal at lower levels of HCl in the flue gas, without deteriorating the selective catalytic reduction (SCR) of NO_x.[517]

The first large-scale chemical plant for the low-temperature oxidation of HCl, which is based on RuO_2 (coated on rutile-TiO_2) as the catalytically active component, was erected by the Sumitomo Chemicals Cooperation in 2004.[518] While metallic Ru is an excellent catalyst for ammonia synthesis, RuO_2 turned out to be a promising catalyst for the oxidation of ammonia to NO at relatively low temperatures of 550 K and UHV conditions[384] compared to 1000 K-1200 K for standard Rh-stabilized Pt gauzes.[519] Recent kinetic experiments with RuO_2 powder and pressures in the mbar range indicate clearly that NH_3 oxidation is not selective toward NO, suggesting a pressure gap for this reaction.[412]

All these practical and potential applications of RuO_2 have in common that unhydrous and hydrous RuO_2 is active for the total and partial oxidation reactions at low temperatures.

In the following I summarize the atomic scale knowledge gained for some of these reactions. Although all of these reaction systems are gas phase reactions catalyzed by RuO_2, some of them have direct electrochemical counterparts. For instance, the HCl oxidation is similar to the chlor-alkali electrolysis and water formation is akin to the oxygen reduction reaction (ORR).

7.1. Low Temperature CO Oxidation

CO oxidation is an important reaction in controlling the vehicle exhaust emission.[520] However, the catalytic CO oxidation at low temperatures and in humid air is also a key process in respiratory protection and industrial air purification.

dx.doi.org/10.1021/cr200247n | Chem. Rev. 2012, 112, 3356−3426

Zang and Kisch reported on a stable and efficient low temperature catalyst for the CO oxidation by humid air.[36] Untreated $RuO_2 \cdot xH_2O$ with 82 wt % of water and annealed samples (730−870 K) with 0.6 wt % of water were catalytically inactive, while hydrous ruthenium dioxide with 9−10 wt % water (annealed at 330−430 K) is very active in the CO oxidation even at room temperature. The activation barrier was determined to be as low as 36 kJ/mol. Hydrous-RuO_2 can also be used as sensitive CO sensor, as its conductivity has shown to decrease upon CO exposure; the original conductivity recovers after passing air over the sample.[521]

If hydrous RuO_2 is supported on an oxidic semiconducting/isolating carrier, deactivation due to strong adsorption of the product CO_2 in the form of carbonates is observed. Upon visible light irradiation the $RuO_2 \cdot xH_2O/TiO_2$ catalysts turned out to be as efficient as the unsupported $RuO_2 \cdot xH_2O$ catalyst.[522] We should note that supported ruthenium hydroxides exhibit also high catalytic activity in the aerobic oxidation of alcohols[38] and for the N-alkylation of ammonia and amines with alcohols as alkylating reagents.[523] The reaction mechanism for the aerobic alcohol oxidation over supported Ru hydroxide was modeled by ab initio quantum calculations by using an octahedral complex $Ru(OH)_3(H_2O)_3$ as the active catalyst.[524] This kind of complex may equally explain the high activity in CO oxidation observed by Zang and Kisch.[36]

Another RuO_2-based catalyst with excellent catalytic activity for the CO oxidation at room temperature together with long-term stability is mesoporous RuO_2 which has been pretreated with oxygen at 200 °C.[525]

7.2. Water Production

The hydrogen oxidation by O_2 has been studied under UHV conditions with temperature programmed reaction, and activation energies were determined by calculations.[274,277] For the reaction mechanism, a cooperative interplay of the two types of under-coordinated sites on $RuO_2(110)$ has been proposed[277] in that hydrogen adsorption takes place either directly over the under-coordinated bridging O sites or via 1f-cus-Ru sites forming hydroxyl groups $O_{br}H$, while dissociative O_2 adsorption is accomplished solely by the 1f-cus-Ru sites forming on-top O species (cf. Figure 38). In a second step on-top O accepts the hydrogen from $O_{br}H$ via a hydrogen transfer reaction without any noticeable energy barrier.[277] The second hydrogen transfer to $O_{br}H$ either from O_{br}-H or from another neighboring O_{ot}-H results in $O_{ot}H_2$, on-top water, which is by 100 kJ/mol bound to 1f-cus Ru.[200,274,276,381] According to DFT studied, this second hydrogen transfer is activated by 20 kJ/mol.[200,274] The most energy demanding step in the catalytic cycle of the gas phase water reaction is identified with the desorption of water.

7.3. Methanol Oxidation

Selective partial oxidation of methanol to formaldehyde pose a challenge in terms of selectivity, since total oxidation to CO_2 is the thermodynamically favored pathway.[526,527] The first paper devoted to the partial oxidation of methanol over RuO_2 to form formaldehyde was published by Madhavaram et al.[383] The main focus of that paper was to show that the activities of single crystalline RuO_2 under UHV conditions and powder RuO_2 at atmospheric pressure behave similarly with respect to the oxidation of CO and methanol. The activity was studied by temperature programmed reaction (TPR) experiments when the surfaces were exposed to methanol and/or oxygen prior to the TPR experiment.

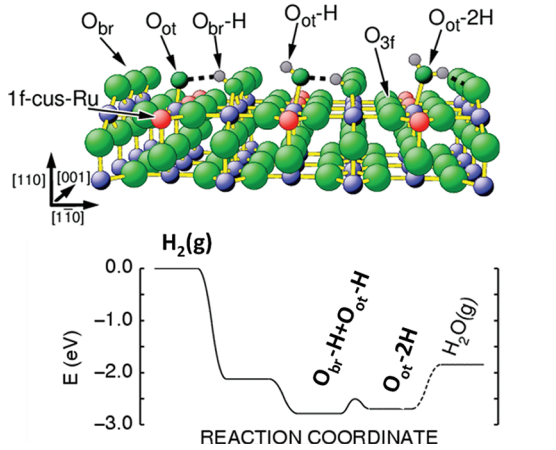

Figure 38. (Top) Ball-and-stick model of the $RuO_2(110)$ surface, summarizing the microscopic steps in the hydrogen transfer reaction.[277] On-top O sits above 1f-cus Ru forming a hydrogen bond (broken line) with an adjacent hydroxyl group O_{br}-H (left). Via hydrogen transfer the H atom of O_{br}-H moves to the on-top O atom forming a hydroxyl group O_{ot}-H without a noticeable activation barrier. The O_{ot}-H can establish a hydrogen bond with a further O_{br}-H species (middle). By a further hydrogen transfer this O_{ot}-H transforms into O_{ot}-2H (activated by 28 kJ/mol), a water molecule adsorbed on top of the 1f-cus Ru site (right) which is stabilized by a hydrogen bond to O_{br}. (Bottom) Energy diagram of the water formation along the reaction path calculated from DFT. Hydrogen bonds are indicated by dashed lines. Reprinted with permission from ref 277. Copyright 2005 American Chemical Society.

The principal mechanism for the partial oxidation of methanol is illustrated in Figure 39. The first step in the

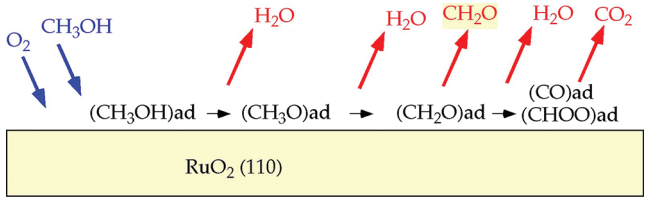

Figure 39. General mechanism for the partial and total oxidation of methanol on $RuO_2(110)$. On RuO_2 dehydrogenation forms water. If no oxygen is present, the RuO_2 will be partly reduced during the partial oxidation reaction of methanol.

methanol oxidation over RuO_2 is H elimination by under-coordinated O atoms forming a methoxy species on the surface. Once the methoxy species is formed, elimination of the less acidic methyl hydrogen is more difficult. The activation energy of this rate determining step is 70 kJ/mol.[398] According to DFT modeling,[398] further oxidation of formaldehyde is unlikely. Rather, CH_2O is to be desorbed into the gas phase.

The hydrogen abstraction by under-coordinated O atoms leads to water formation which subsequently desorbs above 400 K. Under oxygen-deficient conditions the RuO_2 surface will (partly) be reduced. Typical reaction temperatures for the oxidation of methanol over RuO_2 powder are between 360 and 450 K. Formaldehyde is produced around 360 K where also methanol desorbs from the surface. For a single crystalline $RuO_2(110)$ film, the lowest reaction temperature for CO_2 production is found to be 500 K, while for powder RuO_2 the temperature for total oxidation is between 360 and 450 K.[383]

dx.doi.org/10.1021/cr200247n | Chem. Rev. 2012, 112, 3356−3426

Experimentally, most of the methanol is total-oxidized to CO_2 over stoichiometric RuO_2 catalysts.[383] For powder RuO_2 which was previously reduced by H_2, the product distribution changed considerably. About 20% of the methanol is transformed to formaldehyde and 11% methyl formate at 360 K, while still almost 50% are transformed into CO_2.[383]

A more detailed investigation of the methanol oxidation over $RuO_2(110)$ films was reported by Blume et al. applying the technique of HP-XPS[528] under reaction conditions.[241,282] It was shown that methanol easily reduced $RuO_2(110)$ either to metallic Ru or to the transient surface oxide (TSO),[241] depending on the methanol to oxygen feed ratio. The most active phase in the partial oxidation of methanol to form formaldehyde was identified with the TSO.[241] However, substantial formaldehyde formation sets in only when the pressure of the reaction mixture exceeds 0.1 mbar.[282] Far below this pressure, most of the methanol is predominantly converted to CO_2. Under reaction conditions where $RuO_2(110)$ is stable, methanol is predominantly transformed to CO_2. These experiments conflict with a recent ab initio study.[398]

The selective oxidation was shown to proceed on supported ruthenium-oxide clusters at quite low temperatures of 370 K.[28] The supported RuO_2 domains gave an unprecedented methanol conversion rate and allowed the MeOH oxidation reaction to proceed at significant rates at 370 K with >99% combined selectivities to useful products such as formaldehyde, methylformate, and dimethoxymethane products. Liu and Iglesia[28] traced this unique reactivity to the ability of small RuO_2 domains to undergo fast redox cycles without formation of unselective Ru metal clusters. The secondary reaction pathways between formaldehyde and methanol to produce methylformate and dimethoxymethane are considered to be acid-catalyzed by the support (see reactions scheme Figure 40).

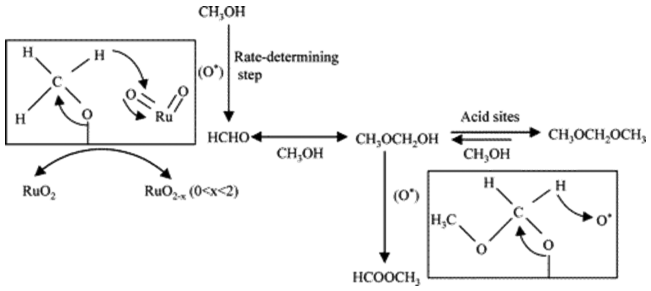

Figure 40. Proposed primary and secondary CH_3OH reaction pathways over supported RuO_2 clusters. Reprinted with permission from ref 28. Copyright 2005 American Chemical Society.

The catalytically active phase for the selective oxidation of methanol has not been clarified. Although indicated in Figure 40, Ru-O double bonds are not known in the literature.

The selective oxidation of MeOH to methyl formate at low temperatures was studied on ZrO_2-supported RuO_x catalysts as a function of Ru loading.[529] The high catalytic activity for low Ru loadings was ascribed to the presence of RuO_4^{2-}, while RuO_2, which was formed at higher Ru densities, is less active. Contrary, the aerobic oxidation of 2-butanol to the corresponding alcoholate is discussed in terms of a ruthenium hydroxide catalyst.[524] The outstanding catalytic performance of $Ru(OH)_x$/support is likely attributed to the presence of coordinatively unsaturated Ru centers and basic hydroxide groups. Ab-initio quantum chemical calculations have supported this view by modeling the supported Ru hydroxide by $Ru(OH)_3(H_2O)_3$.[524]

7.4. Ammonia Oxidation and Related Reactions

The oxidation of ammonia is an important technical process to produce nitric acid which in turn is the starting point to produce N-containing fertilizers. Since ammonia oxidation leads to various products, such as NO, N_2O, N_2, and NO_2, selectivity becomes a critical issue for the choice of a proper catalyst system.[530]

In general, the oxidation reaction of ammonia (1) is catalyzed over Rh stabilized Pt gauzes at temperatures as high as 1000−1200 K with great efficiency and high selectivity toward NO.[530,412] This reaction is known as the Ostwald process and its microscopic reaction steps have been examined quite intensively.[519,531−533]

$$2NH_3 + \frac{5}{2}O_2 \xrightleftharpoons[1000K-1200K]{Pt} 2NO + 3H_2O \quad (1)$$

There is one major shortcoming of the Ostwald process in that the Pt gauzes must be replaced routinely every 6−10 months since Pt is corroded by the formation of volatile PtO_2 under these harsh reaction conditions.[534,535]

Alternative NH_3 oxidation catalysts consist of transition metal oxides,[536,537] which allow operation at lower temperatures and which produce less N_2O than commercial Pt gauzes. The main disadvantages of oxide catalysts are the requirement of using leaner NH_3/air mixtures of less than 10% of NH_3 and the higher flow resistance.

A surface science study has indicated that $RuO_2(110)$ is an efficient and selective catalyst for the oxidation of ammonia under UHV conditions to form NO, running at a temperature as low as 550 K and for O_2/NH_3 = 20.[384] The proposed reaction mechanism is based on HREELS and TPD experiments. It consists of sequential dehydrogenation steps of adsorbed NH_3 by coadsorbed oxygen and the final recombination of adsorbed N and O to form adsorbed NO which at higher temperatures is released into the gas phase. The rate determining step (rds) was identified with the desorption of NO.[384] In essence, this reaction mechanism of Wang et al.[384] was confirmed and refined on the basis of DFT calculations and experimental N1s photoemission data.[410]

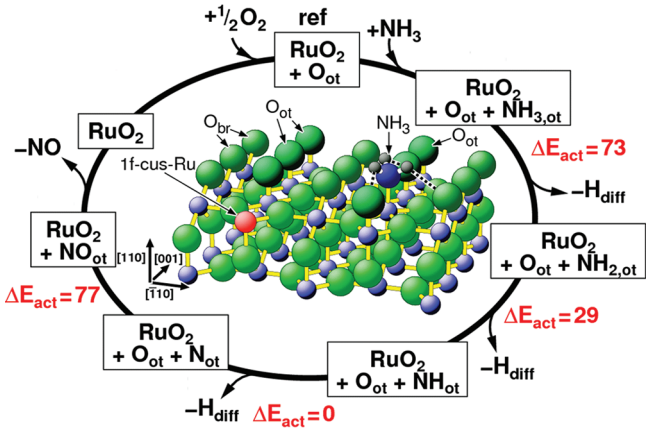

Figure 41. Illustration of the microscopic reaction steps in the oxidation of NH_3 over $RuO_2(110)$. All energies are given in kJ/mol. $-H_{diff}$ means that the abstracted H from NH_x is removed from its direct neighborhood by diffusion along the various O species on the surface. Reprinted with permission from ref 410. Copyright 2009 Elsevier.

dx.doi.org/10.1021/cr200247n | Chem. Rev. 2012, 112, 3356−3426

In Figure 41 the various microscopic reaction steps are compiled including the respective energy barriers ΔE_{act} (in red color). The adsorption energy of NH_3 on O precovered $RuO_2(110)$ is 165 kJ/mol, in good agreement with another DFT study.[538] The hydrogen abstraction of NH_3 by O_{br} is activated by 65 kJ/mol, while that to the on-top O is activated by 73 kJ/mol. The second H-elimination is activated by 29 kJ/mol and the last H transfer step from NH to N proceeds even without any noticeable activation. Altogether these calculated activation barriers suggest that further H elimination proceeds spontaneously as soon as the first hydrogen is transferred from an ammonia molecule to the on-top oxygen. The most active O species in the recombination of N and O to form NO is the on-top O species with an activation energy of 77 kJ/mol. This activation barrier is slightly too low to be compatible with a required reaction temperature of about 350−400 K.[384,410] However, 400 K is just the temperature where water desorbs from the $RuO_2(110)$ surface.[274,276] Therefore, the NO production was suggested to be hindered by O_{ot}-H groups in the direct vicinity of N.[410] Only when the O_{ot}-H groups recombine to form water and desorbs at 400K, nitrogen can react with the remaining O_{ot} on the surface to form NO. Fully consistent with this proposed reaction scheme, a recent HREELS study indicated that the majority of NO is produced only when the H_2O species desorbs at 400 K.[384] The resulting NO molecule is quite strongly adsorbed on the surface by 191 kJ/mol so that desorption of NO molecules takes place only above 500 K as recently observed in a temperature programmed reaction.[384] Slightly lower values for the NO adsorption energies were reported in recent DFT studies.[375,412,539]

The reaction mechanism for ammonia oxidation over $RuO_2(110)$ has been confirmed by an independent DFT study.[539] A more recent DFT study by Lopez et al.[412] arrived essentially at the same conclusions about the reaction mechanism.

For the microkinetic modeling of the experimental data,[384] Hong et al. performed KMC simulation based on DFT calculated energy barriers.[414] This ab initio based KMC study can well reproduce the kinetic data of Wang et al.[384] concerning both the experimentally observed reactivity as well as selectivity. The high selectivity is traced to the one-dimensionality of the active 1f-cus Ru sites on $RuO_2(110)$, as already discussed for the HCl oxidation.[385] More specifically, the limited N diffusion along the 1f-cus Ru rows due to hindering of various reaction intermediates present on $RuO_2(110)$ severely inhibits the recombination for $N + N \rightarrow N_2$ but interferes far less with that for the $N + O \rightarrow NO$ owing to the nearby availability of O from dissociation of O_2. An alternative explanation was put forward by Lopez and co-workers[412] in that the selectivity of the NH_3 oxidation under UHV conditions is traced to high diffusion barriers of adsorbed N and O calculated to be 2 eV. Considering that such high diffusion barriers are inconsistent with other DFT studies[410,414] and experiments,[265] this explanation is less convincing than that of dimensional confinement of Hong et al.[414]

These surface science studies might now give the impression that a new catalyst for the ammonia oxidation has been discovered. However, previous atmospheric pressure experiments indicate that NH_3 oxidation over supported RuO_2 for temperatures 520−620 K and O_2/NH_3 ratios of 5 to 18 produce only N_2 and N_2O.[540] Recently, Cui et al.[29] reported that mesoporous RuO_2 oxidized 80% of the NH_3 to N_2 in a wide temperature range 370−620 K and $O_2/NH_3 = 20$. Various other Ru-based supported catalysts display N_2 selectivities of >90% in wet oxidation of ammonia.[541−543]

In order to resolve this discrepancy between single crystalline $RuO_2(110)$ under UHV conditions and supported RuO_2 catalyst under ambient pressures, Perez-Ramirez and co-workers[412] conducted NH_3 oxidation experiments over poly crystalline RuO_2 powder samples at ambient pressure. Polycrystalline RuO_2 with its prevailing surface orientation of (110) and (101)[200,383] may be considered as a natural link to bridge the materials gap from single crystals to supported catalysts. These experiments[412] show clearly that for ammonia oxidation over RuO_2 powder N_2 is the predominant product. In the UHV experiments of Wang et al.,[384] NO selectivity approached 100% at 530 K, when the O_2/NH_3 exceeded 20, while on polycrystalline RuO_2 at atmospheric pressure the maximum achieved NO selectivity was 65%. A comparison with DFT calculations of the NH_3 oxidation over $RuO_2(110)$ and $RuO_2(101)$[412] suggested that the discrepancy to UHV experiments is not related to the materials gap but rather to the pressure gap (8 orders of magnitude higher pressures). At high pressures the formation of N_2O as reaction intermediate and its decomposition to form N_2 was argued to be the glue to understand this pressure gap.[412] To prove this idea, high pressure experiments on $RuO_2(110)$ single crystalline films are called for.

Although RuO_2 seems to be not a good catalyst for the ammonia oxidation to form NO, mesoporous CuO_2/RuO_2 has been demonstrated to be an excellent catalyst for the oxidation of ammonia to N_2 with >95% selectivity at 450 K.[29] This type of catalyzed reaction is required for the abatement of ammonia in oxygen-containing waste streams containing <1000 ppm NH_3.[544,545]

7.5. HCl Oxidation: Deacon Process

Industrial chemistry intensively employs chlorine as an oxidizing agent in a variety of organic processes, rendering chlorine the "energy carrier" the industrial chemistry. In the course of these processes, hydrogen chloride is formed as an inevitable byproduct either directly by the substitution reaction or by the subsequent production steps to attain chlorine-free final products. In this way, about 40% of the Cl_2 produced worldwide (50 Mt per year) is reduced to HCl.[546] Industrial uses exist for HCl for instance in the polyvinylchloride (PVC) production, but chlorine processes produce much more of the byproduct HCl than the market can absorb, resulting in a severe toxic-waste disposal problem. The primary method of HCl disposal is by neutralization, which is costly and far from being sustainable since "energetic" HCl is transformed into less-useful chloride salts.

Consequently, there has been growing interest in finding cost-effective methods for recycling chlorine from hydrogen chloride in order to design closed process cycles in industrial (chlorine-related) chemistry.[26,547] The heterogeneously catalyzed HCl oxidation (so-called Deacon process), that is,

$$2HCl\,(g) + \frac{1}{2}O_2\,(g) \rightleftharpoons Cl_2\,(g) + H_2O\,(g);$$
$$\Delta_r H = -59\ kJ/mol(300K)$$

is one such process in which chlorine is recycled almost energy-neutral from the byproduct hydrogen chloride (green chemistry route).

Although the Deacon process has been known for some 140 years,[548] this process has not found its way into industrial applications. The reasons are manifold but the original Deacon

dx.doi.org/10.1021/cr200247n | Chem. Rev. 2012, 112, 3356−3426

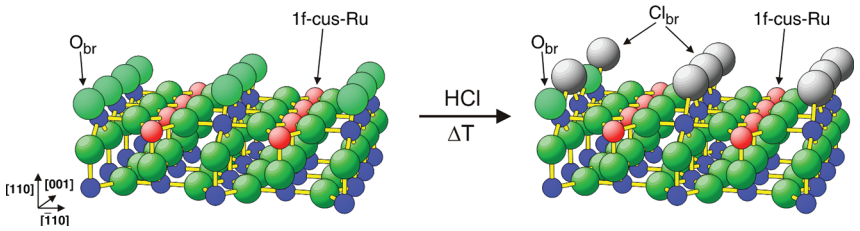

Figure 42. Schematic representation of the chlorination of $RuO_2(110)$. Ball-and-stick model of bulk truncated $RuO_2(110)$ (left) revealing under-coordinated surface atoms: bridging O atoms (O_{br}) and one fold coordinatively unsaturated Ru-sites (Ru 1f-cus). Upon HCl exposure at higher temperatures the stoichiometric surface transforms into a chlorinated surface (right) where part of the bridging O_{br} atoms are replaced by bridging chlorine (Cl_{br}) atoms (shown in gray color).[395,405] Reprinted with permission from ref 395. Copyright 2010 American Chemical Society.

process catalyzed with $CuO/CuCl_2$ has suffered most notably from the missing stability of the deployed catalyst and from too high reaction temperatures above 700 K, which results in a low turnover for thermodynamic reasons. Note that the oxidation of HCl is only mildly exothermic by −59 kJ/mol(Cl_2), so that the final yield at 700 K is given by equilibrium conversion of only 70−80%. Over the past 140 years, numerous strategies have been pursued to overcome the problems with the original Deacon process, albeit only with limited success.[549−556]

Therefore, the Deacon process had largely been displaced by electrolysis, a highly energy-consuming process.[557] In the electrolysis of aqueous HCl, Cl_2 and H_2 are produced by the chlorine (CER) and hydrogen evolution reaction (HER) (cf. section 8.3). Modern electrolyzers use the produced H_2 in a kind of fuel cell (gas diffusion electrodes) to produce water, thereby reducing the electric power consumption by 30%.[557] Still about 1600−1700 kWh/t(Cl_2)[558] are required which makes up a substantial part of the total cost for HCl recovering by electrolysis.

Around the year 2000 Sumitomo Chemical[518] has developed an efficient and stable Deacon-type process on the basis of RuO_2 coated on rutile-TiO_2 (Sumitomo process). The Sumitomo process is a breakthrough in recent catalysis research since chlorine is now recycled from HCl with low energy cost and high conversion yields of 95%. In retrospect RuO_2-based catalysts seem to be the obvious choice for the Deacon process since such catalysts have already been in industrial use as DSAs in chlor-alkali electrolysis for more than 40 years.[559]

Recently, the extraordinary stability of the model catalyst RuO_2 (110) in the Sumitomo process under UHV conditions has been shown to be due to the selective replacement of bridging oxygen (O_{br}, cf. Figure 42) by chlorine, a process which is confined to the topmost layer of $RuO_2(110)$.[405] Sumitomo Chemical improved further the stability of RuO_2 supported on TiO_2 by codepositing SiO_2 in order to suppress sintering of the RuO_2 nanodomains under reaction conditions.[26]

A deeper reduction/chlorination of the oxide has not been observed under UHV-typical conditions[405] nor at higher pressures.[266,560] Surface chlorination by HCl is promoted by saturating the bridging O sites first with hydrogen.[395] The maximum surface chlorination of RuO_2 has been estimated to be 70−80%, both on single crystals[395] and on RuO_2 powder and RuO_2/TiO_2 supported catalysts.[560] From DFT calculations, the (2×1) structure with every second O_{br} replaced by chlorine is 35 kJ/mol more stable than a surface where all O_{br} are replaced by Cl_{br}.[491] The degree of chlorination of $RuO_2(110)$ is not static but dynamic in that it depends critically on the actual reaction mixture. In excess O_2 the bridging Cl atoms are partly replaced by oxygen.[491]

In-situ surface X-ray diffraction (SXRD)[268] reveals that the chlorinated $RuO_2(110)$ and $RuO_2(100)$ model catalysts for the Sumitomo process are long-term stable under reaction conditions where the gas feed $p(HCl)/p(O_2)$ varies from 1:4 to 4:1 for pressures in the mbar range and temperatures as high as 685 K. Even pure HCl exposure in the mbar range is not able to reduce the RuO_2 below 600 K since adsorbed chlorine blocks the under-coordinated Ru sites, and without the presence of under-coordinated surface oxygen further HCl uptake is suppressed for thermodynamic reasons. Above 620 K in pure HCl atmosphere of 1 mbar chemical reduction of the oxide sets in by moving the bridging Cl to the 1f-cus Ru sites. Subsequently, the created bridging O vacancies are filled by the diffusion of lattice oxygen from bulk RuO_2 into these vacancies which can be reduced by HCl. Similar stability results were reported for polycrystalline RuO_2 powder in a recent TAP experiment.[561]

In contrast to bridging O, bridging chlorine is not an active site on $RuO_2(110)$; that is, Cl_{br} cannot accept H. Substituting a bridging oxygen atom by a bridging chlorine (Cl_{br}) atom results in a change of the formal oxidation state of the underlying 2f-cus Ru atoms from +IV 2/3 to +III 2/3. Although it is not very meaningful to apply the concept of formal oxidation states to metallic conducting oxides such as RuO_2, the change in the oxidation state of 2f-cus Ru upon chlorination (being closer to +IV) suggests at least that Cl may exert a stabilizing influence on the $RuO_2(110)$ surface.

In a next step, the reaction mechanism of the HCl oxidation over chlorinated $RuO_2(110)$ was explored using DFT calculations[200,385] and HRCLS experiments[385] (cf. Figure 43). The kinetics of the HCl oxidation reaction over chlorinated $RuO_2(110)$ has been shown to be purely governed by the adsorption energies of the reaction intermediates (water: 109 kJ/mol and on-top Cl: 114 kJ/mol against $^1/_2$ Cl_2). The reaction mechanism of the HCl oxidation over $RuO_2(110)$ is summarized in Figure 43a, while the energy diagram along the reaction coordinate is shown in Figure 43b. Dissociative adsorption forms readily atomic O in atop position of the 1f-cus Ru sites (O_{ot}). HCl adsorbs molecularly on 1f-cus Ru sites only with 30−50 kJ/mol which is too weak to stabilize HCl under reaction conditions above 600 K. Therefore, HCl has to adsorb dissociatively with Cl sitting above a 1f-cus Ru site and the H transforming on-top O (or bridging O) into a hydroxyl group; this process occurs without any noticeable activation barrier and is exothermic by 126 kJ/mol for the case of on-top O. The next HCl molecule can form a second Cl_{ot} species and water; this process is exothermic by 178 kJ/mol. The final production of surface water (H_2O_{ot}) via a H transfer[274,277] is kinetically activated by 29 kJ/mol, an energy barrier that is easily surmounted at typical reaction temperatures of 500−600 K.

Water desorption is endothermic by 109 kJ/mol and desorbs at 420 K. The remaining Cl_{ot} species on the surface have to diffuse along the 1f-cus Ru rows to meet a second Cl_{ot} and to

dx.doi.org/10.1021/cr200247n | Chem. Rev. 2012, 112, 3356−3426

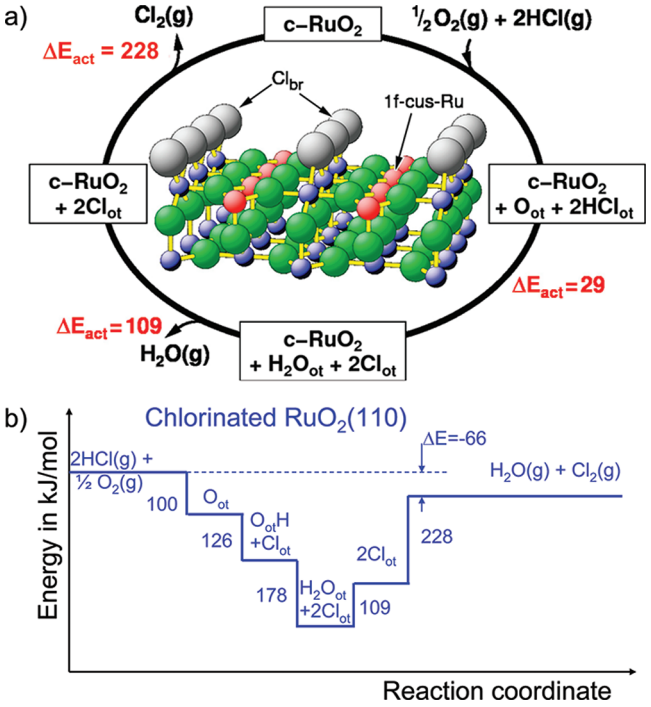

Figure 43. (a) The catalytic cycle of the HCl oxidation over surface chlorinated $RuO_2(110)$. The reactant molecules O_2 and HCl both adsorb first on the 1f-cus Ru sites. O_2 dissociates to form adsorbed O and HCl dehydrogenates via a hydrogen transfer to form Cl_{ot} and $O_{ot}H$ species in terminal positions. H-transfer among the $O_{ot}H$ species leads to water formation which is released from the surface around 400 K. Neighboring on-top Cl atoms recombine to form Cl_2 which is immediately liberated into the gas phase. The activation energies ΔE_{act} are determined by DFT calculations and given in kJ/mol. The elementary step with the highest activation energy constitutes the association of two neighboring Cl_{ot} atoms to form Cl_2.[385] (b) Energy diagram along the reaction coordinate for the HCl oxidation over chlorinated $RuO_2(110)$, providing the adsorption energies of the reaction intermediates. ΔE = calculated reaction energy of −66 kJ/mol. Reprinted with permission from ref 385. Copyright 2008 American Chemical Society.

react with. This diffusion process is activated by 35 kJ/mol and therefore can easily be overcome at typical reaction temperatures of 500−600 K.

The recombination of two on-top Cl to form the desired product Cl_2 constitutes the elementary step with the highest activation barrier of 228 kJ/mol. This value is higher than that reported by Lopez et al.[200] (150 kJ/mol) but is in almost quantitative agreement with that of Studt et al.[448] (220 kJ/mol). The DFT-calculated reaction energy ΔE of −66 kJ/mol agrees quite well with the experimental value of −59 kJ/mol.

Kinetic studies in a flow reactor[200] revealed a pronounced effect of the reaction rate on the oxygen partial pressure. The higher the O_2/HCl ratio (while keeping the partial pressure of HCl), the higher is the Cl_2 production. This finding indicates that the amount of on-top O on the surface is actually too low under reaction conditions. Since the adsorption energy of on-top O is only 100 kJ/mol (against $^1/_2$ O_2), oxygen desorption takes place at a temperature of 400−450 K which is much lower than the reaction temperature of 620 K. Maximum activity is achieved for 620 K, while the reaction starts around 500 K.[200]

Pump−probe experiments of O_2 and HCl in a temporal analysis of products (TAP) reactor verified a Langmuir−Hinshelwood type reaction rather than a Mars van Krevelen mechanism[562] and a strong dependence of the net Cl_2 production on the Cl and O coverage on the RuO_2 surface.[560]

Studt et al.[448] studied the HCl oxidation reaction for various transition metal oxides in order to establish an activity relation over rutile transitions metal oxide catalysts (so-called volcano relation). It turned out that the activity of $RuO_2(110)$ is already very close to the optimum value. This study indicated also that the adsorption energy of on-top O is a good descriptor for the BEP relation, meaning that the adsorption energy is linearly correlated with the adsorption energy of the other reaction intermediates such as on-top Cl.

Only recently[266] the first turn over frequencies have been reported for the HCl oxidation reaction over $RuO_2(110)$ and $RuO_2(100)$. Reactivity measurements in a batch reactor indicate that 0.6 Cl_2 molecules are produced per second and active site at 650 K and partial pressures of $P(HCl)$ = 2 mbar and $P(O_2)$ = 0.5 mbar, independent of the studied surface orientation. Similar TOF values (0.002 1/s at 573 K) can be estimated from space time yields and the BET surface reported for polycrystalline RuO_2[560] or from DFT calculations (10−100 1/s at 573 K and 1 bar).[448]

Actually the Sumitomo process uses RuO_2 supported on rutile-TiO_2 and not bare $RuO_2(110)$. RuO_2 supported on rutile-TiO_2 is significantly more active in the HCl oxidation reaction than RuO_2 supported on anatase-TiO_2.[26,560] DFT calculations were performed to study the oxidation of HCl with oxygen producing Cl_2 and water on the $TiO_2(110)$-supported $RuO_2(110)$.[449] Very important for industrial application is that substantial Ru resources can be saved in the synthesis of the Sumitomo catalyst. According to these DFT calculations already 1 ML of $RuO_2(110)$ coated on $TiO_2(110)$ suffices to maintain practically the full activity of bulk-RuO_2 in the HCl oxidation reaction. The stoichiometric $TiO_2(110)$ is not active in the HCl oxidation reaction.[448,449] However, if the under-coordinated Ti surface atoms are substituted by Ru then the resulting 1/2 ML-RuO_2−$TiO_2(110)$ catalyst is catalytically active with an activation barrier that is only 29 kJ/mol higher than for bulk-$RuO_2(110)$.[449]

Current Deacon-related research concentrates on searching for efficient and stable catalyst materials replacing expensive ruthenium dioxide.[561,563−565] Keeping with the RuO_2-type of catalysts, it would be beneficial to find promoters which can selectively destabilize the on-top chlorine without destabilizing the on-top O species.

8. APPLICATION OF RUO_2 IN ELECTROCATALYSIS

In industrial chemistry RuO_2 is mainly applied in electrocatalysis, in particular as DSA in the chlor-alkali electrolysis to produce Cl_2 (chlorine evolution reaction: CER: section 8.3) and NaOH.[10,566] Roughly 10−15% of the annual production of ruthenium goes into the production of such DSA.[13] Other electrochemical reactions which are efficiently catalyzed by RuO_2 include the oxygen evolution reaction (OER: section 8.4) and the hydrogen evolution reaction (HER: section 8.2). Again I shall be focusing on an atomic scale understanding of these electrocatalyzed reactions (HER, OER, CER). Other applications of DSA-type electrodes include wastewater treatment to remove trace amounts of organic contaminants by electro-oxidation.[567,568] Heterogeneous redox catalysis has been demonstrated for the electro-oxidation of organic molecules (such as formaldehyde) over hydrated RuO_2 layers.[569]

Before starting with the discussion of RuO_2-based applications in electrocatalysis, this section will summarize some important electrochemical and electrocatalytic properties of RuO_2 (section 8.1). An in-depth discussion can be found in

dx.doi.org/10.1021/cr200247n | Chem. Rev. 2012, 112, 3356−3426

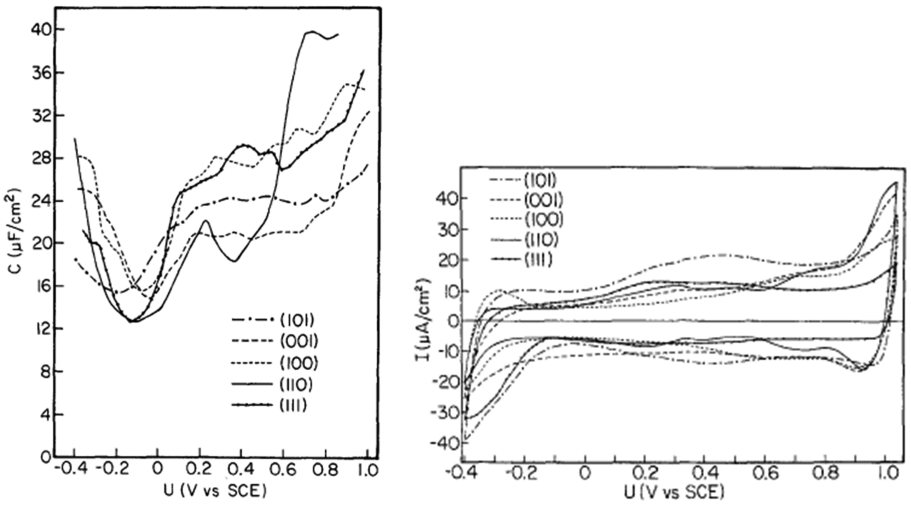

Figure 44. (Left) Potential dependent capacitance C(U) curves for five RuO_2 crystalline orientations in 10^{-3} M Na_2SO_4. (Right) Cyclic voltammetry curves for the five RuO_2 crystalline faces in 10^{-3} M Na_2SO_4; scan speed: 50 mV/s. Potential U is given versus SCE. Reprinted with permission from ref 575. Copyright 1983 The Electrochemical Society.

the literature.[570] In general, the intrinsic electrocatalytic properties of an electrode material can be simplified to the exchange current density and the Tafel slope. High exchange current density, low Tafel slope, and a high density of active sites are beneficial for electrocatalysis.

8.1. General Electrochemical Properties of RuO_2

The electrochemical and interfacial properties of RuO_2 are of utmost importance for a deeper understanding of how RuO_2 catalyzes electrochemical reactions. A number of investigations have pushed forward the idea that most of the features of oxide electrodes may be governed by the acid−base properties of the oxide/solution interface. For instance, the state of oxide surfaces depends critically on solution pH,[571] which may point to the formation of surface hydroxyl complexes.[572] Or the reaction order of the OER and CER in H^+ or in OH^- has often been found to be fractional.[573] Equally important for the state of the electrode surface in solution is the specific adsorption of anions. The acid/base properties of RuO_2(110) are related to the 1f-cus Ru and bridging O sites which serves as Lewis acid/base and Brønsted base, respectively.[267]

The potential of zero charge (PZC) is the potential value at which the surface is uncharged, that is, the surface dipole is compensated. From this one the "potential of zero total charge (PZTC)" is distinguished, which also includes possible adlayer species. Here the overall dipole of the surface + adlayer is compensated. The PZC is governed by the strength of the interaction between the surface Ru atoms and the oxygen of the surface OH groups attached to it. Trasatti concluded that the intermediates of the oxygen evolution are bonded to the 1f-cus Ru sites so that the activation energy is expected to depend on the strength of the Ru−OH bond as well.[574] Therefore electrocatalytic properties and the PZC of oxide surfaces may be intimately interconnected.

The PZC of single crystalline RuO_2 with (100), (101), (001), (110), and (111) orientations was measured by Tomkiewicz et al.[575] These authors found that the PZC of single crystalline RuO_2 in 10^{-3} M Na_2SO_4 is −0.09 V versus saturated calomel electrode (SCE) are independent of the chosen surface orientation (cf. Figure 44, main minimum in C(U)); the assignment of the minimum in C(U) to the PZC is, however, only justified if specific adsorption by anions is ignored. Assuming a linear relation between PZC and the work function, the work function of RuO_2 was estimated to be 4.9 eV,[575] which is substantially lower than found by work function measurements of RuO_2(110) (5.8 eV)[229] and theoretical estimation based on DFT (5.7 eV)[50] of the work function of RuO_2(110). Therefore either the relation between PZC and the work function is not linear or specific adsorption may play an important role.

Using the Gouy−Chapman−Stern model for the double layer, the experimental capacitance is composed of two capacitors in series

$$1/C = 1/C_d + 1/C_i$$

with C_d denoting the diffuse layer capacitance and C_i denoting the inner layer capacitance. The inner capacitance is independent of the electrolyte concentration and can be extracted from concentration-dependent measurements of 1/C. Assuming a planar geometry of the double layer, values of C_i = 60−80 μF/cm^2 are derived,[576] while C_i is 300−500 μF/cm^2 for a spherical double layer.[577] On RuO_2 single crystals of various orientations, the potential dependent capacitance was derived from impedance spectroscopic data (cf. Figure 44) and reveals various minima and maxima which are related to redox transitions observed in CV measurements.[575]

In an aqueous environment the oxide surface is normally covered by OH groups (due to water dissociation) which are stabilized by "coadsorbed" and coordinated water and which mediate the interaction of the underlying metal ions with chemical species in the solution.[578,579] Surface hydration of the oxides has been identified by a nuclear analytical technique.[580] RuO_2 in aqueous solution adsorbs water rapidly with a constant H/Ru ratio throughout the thickness of the oxide layer.[581] Active sites on hydroxylated oxide surfaces act preferentially as Brønsted acids and bases. Hydrous RuO_2 is permeable to protons while dry RuO_2 is not. If protons are constituents of both the solid and the aqueous phase, a Nernstian response results as a consequence of the interfacial equilibrium of H^+ ions. Because of the high electronic conductivity, space charge effects can be neglected for RuO_2.[582]

If the potential of the RuO_2 electrode is varied periodically within the limits inside the stability range of the solvent

dx.doi.org/10.1021/cr200247n | Chem. Rev. 2012, 112, 3356−3426

(cyclic voltammetry: CV), the surface responds (here by the current density) in a characteristic way, rendering CV an electrochemical spectrum.[583] The two distinct peaks in the cathodic scan of Figure 45 are ascribed to a hydrogen adsorption reaction (H_{1C}, H_{2C}), since both peaks are connected with a charge transfer originating from the adsorption of protons coupled with an electron transfer. The next two pairs of anodic/cathodic peaks (R_{1A}, R_{2A}, R_{1C}, R_{2C}) appear in the oxide rearrangement region, while the third region is mainly determined by oxygen reduction (O_{1A}, O_{1C}).

The surface response in CV (cf. Figure 45) is related to redox reactions at the surface active sites which is assisted by proton exchange δH^+ with the solution and electron transfer δe^- according to

$$RuO_x(OH)_y + \delta H^+ + \delta e^- \rightleftharpoons RuO_{x-\delta}(OH)_{y+\delta}$$

This behavior plays an important role for hydrous-RuO_2 when applied as super capacitors (cf. section 9.1).

The ionic adsorption strength on RuO_2 electrodes is constant as the electrode potential is varied.[584] This can be understood by oxidation/reduction of the surface sites which are compensated by release or addition of protons into or from the electrolyte solution.[585] There are two ways to charge an oxide surface: One is driven by the electrode potential, the other by the pH. Both change the electrochemical potential of the electrons. While the electrode potential acts on the metal sites whose charge variation is compensated by proton exchange, the pH variation acts on the surface hydroxyl complexes whose dissociation with the formation of a surface charge is compensated by adsorption of ions from the solution. Therefore, ion adsorption varies as a function of pH at constant potential, while it does not change at constant pH as a function of the potential.[584]

The surface charge involved in the potential change is a direct measure of the number of exchanged protons, so that the surface charge q^*, derived from the integration of the CV (cf. Figure 45), is considered to be proportional to the number

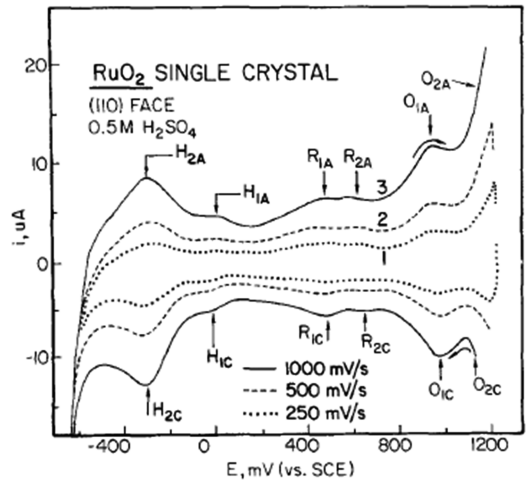

Figure 45. Cyclic voltammetry characteristics for single crystalline RuO_2(110) electrode in 0.5 M H_2SO_4 solution. Scan rates (1) 250, (2) 500, (3) 1000 mV/s. Reprinted with permission from ref 583. Copyright 1984 The Electrochemical Society.

of active sites and therefore proportional the active surface area of the oxide.[586]

The thermodynamic stability of ruthenium in an electrochemical environment is provided by Pourbaix diagrams (cf. Figure 46). Ruthenium exists in the metallic state in the

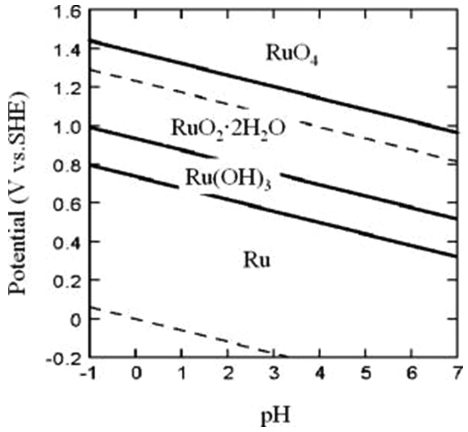

Figure 46. Poubaix diagram of ruthenium indicating the thermodynamically stable phases dependent on the pH value and the applied potential versus SHE.[270,587] The broken lines correspond to HER (bottom) and OER (top). Reprinted with permission from ref 587. Copyright 2008 The Electrochemical Society.

0.0−0.6 V range with respect to the standard hydrogen electrode (SHE), while in the potential range from 0.8 to 1.4 V Ru transforms to Ru-hydrate and hydrous RuO_2 for low pH values. RuO_4 is shown to be thermodynamically stable at potentials higher than 1.4 V.

The scope of electrocatalysis research is to study heterogeneous catalysis at electrodes and to clarify how the reaction rate of an electrode process is altered by specific properties of the electrode material. A thorough electrocatalytic investigation relies on the detailed knowledge of the mechanism of the electrode reaction and the structure of the double layer.

Within the framework of transition state theory (TST), the kinetics of an electrocatalytic reaction at an electrode is described by the Butler−Volmer equation:[41]

$$I = I_o[\exp(\alpha z F\eta/RT) - \exp(-(1-\alpha)zF\eta/RT)]$$

The Butler−Volmer equation correlates the current density I with the overpotential η (F = Faraday constant, R = gas constant, T = temperature in Kelvin, z = number of exchanged electrons in the reaction). The magnitude of the deviation of the electrode potential at the electrode from the equilibrium value, which is corrected for by the ohmic drop is termed overpotential η. There are two parameters in the Butler−Volmer equation which depend on the electrode material (electrocatalysis). These are the exchange current density I_o and the asymmetry parameter α.

The electrocatalytic effect of an electrode material depends on the structure and chemical composition of the material (real electrocatalytic effect) or is simply related to the accessible area of the electrode surface (apparent electrocatalytic effect).[588] In order to discriminate the real from apparent effect, either the actual surface area of the electrode materials has to be determined as accurately as possible (for instance, by estimating the surface charge q^*), or if this is not possible to achieve, the electrocatalytic behavior can best be described by intensive instead of extensive quantities, such as the Tafel slope or the PZC for oxide electrodes.[559]

dx.doi.org/10.1021/cr200247n | Chem. Rev. 2012, 112, 3356−3426

For $|\eta| \geq 100$ mV the Butler–Volmer equation can be approximated by a single exponential function with the so-called Tafel-slope b

$$\text{given by } 1/b = d \log I/d\eta = \alpha zF/RT \text{ or } (1-\alpha)zF/RT$$

To interpret CV data one has to correct for the ohmic drop in the electrolyte solution. This can be accomplished by impedance spectroscopy as shown for instance for the prototypical hydrogen evolution reaction (HER).[589]

The PZC is closely related to the acid–base chemistry of the oxide surface. Since PZC is an intensive property and since electrocatalysis is governed by surface chemical properties, Trasatti[590] suggested using the PZC to disentangle real from apparent factors in the case of oxide electrocatalysis.

In general, a change in the Tafel slopes is considered to be due to a difference in the rate determining step.[42,591] However this view is too simple as documented in a KMC simulation of the electro-oxidation of CO over Pt(111).[592] Although $COOH_{ad} \rightarrow CO_2 + H^+ + e^- + *$ is identified with the rate determining step throughout the potential range, the apparent Tafel slope changes from 40 mV/decade at low potentials, where the OH-coverage is low, to 119 mV/decade at high potentials (with high OH coverage). The take-home message of this model study is that kinetic data in electrochemistry do not allow for an unambiguous conclusion about the rate determining reaction step. This statement is *true* for reaction kinetics in general: kinetic data are not sufficient to determine the reaction mechanism.[593]

The reaction order and the Tafel slope for electrocatalytic reactions involving chemisorbed intermediates have been thoroughly discussed by Tilak and Conway.[594] The reaction order with respect to one species i is given by

$$n = (\partial \ln I/\partial \ln c_i)_{E,T}$$

Although Tafel slope and reaction order are characteristic macro kinetic parameters of a electrocatalyzed reaction, the actual reaction mechanism cannot be retrieved unambiguously from them. The interpretation of the Tafel slope and reaction order in terms of elementary reaction steps depend critically on whether the kinetics is treated within the quasi-equilibrium or the steady state approach and which type of adsorption isotherm is employed relating the surface coverage of the adsorbed intermediates to the bulk concentration of the reactant in the phase from where they originate.

8.2. Hydrogen Evolution Reaction (HER)

HER takes place at the cathode in a variety of important electrocatalytic reactions including chlor-alkali electrolysis and water splitting. HER has been considered as a prototype reaction in surface electrochemistry,[498,595,596] since the reaction comprises a two-electron transfer and is therefore quite simple if compared to the four-electron process of the oxygen reduction reaction (ORR) or the oxygen evolution reaction (OER). Various metals have been identified to be good HER electrocatalysts, first of all platinum but also various Pt alloys.[33,597,598] While various metal electrodes show excellent activity for the HER, oxide surfaces are in general known to be inferior in HER.

For reducible oxides such as RuO_2, one should even expect that the oxide is chemically reduced under HER conditions so that only metallic ruthenium will constitute the active phase for HER. This simple view is however incorrect for the case of RuO_2 and IrO_2.[599−605] RuO_2 is actually a remarkably good electrocatalyst for HER and it resists poisoning by heavy metals.[600] The activity of RuO_2 for HER in acid electrolytes is however lower than that of platinum; the overpotential of RuO_2 is 50 mV higher at a current density of 0.1A/cm^2 than that of Pt.[600]

Upon the first few forward and backward potential cycles ranging from the HER to the OER, RuO_2 electrodes exhibit a considerable hysteresis.[602,605] This hysteresis reflects the activation of the electrode with an increase in the current density for HER.[605] This activation of the oxide layer is a key element of the electrocatalytic behavior of RuO_2 in HER which can reach a 10-fold increase of the cathodic current.[605] Part of the activation process can be traced to a roughening of the RuO_2 surface; that is, the active surface area increases. However, this behavior is also observed on a RuO_2 single crystal electrode so that the activation process of RuO_2 is considered as an intrinsic property of the oxide material.[606]

Both XRD[607] and XPS experiments[608] have shown that during the HER on RuO_2 electrodes neither the bulk oxide nor the surface region is chemically fully reduced to metallic ruthenium. XRD experiments indicate a significant shift of the characteristic diffraction peaks of RuO_2 when it is polarized cathodically in the potential range of HER.[607] The observed expansion of the unit cell of RuO_2 occurs mostly along the a-axis, suggesting that hydrogen is preferentially inserted in the $a-a$ plane (cf. Figure 47). These structural changes are fully

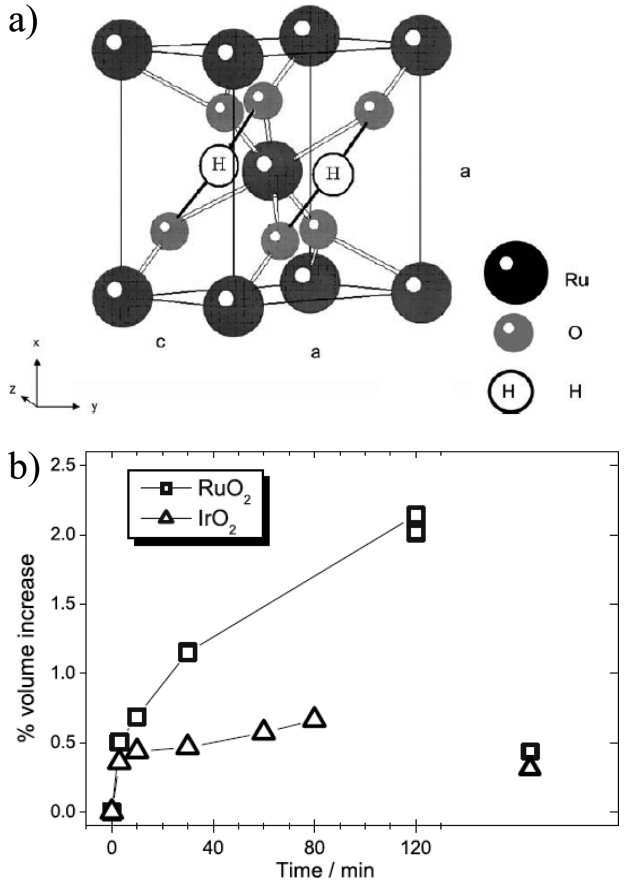

Figure 47. (a) Schematic representation of the unit cell of RuO_2 and how the H is inserted. (b) Volume increase of RuO_2 as a function of polarization time (polarized at −5 V vs SCE). Reprinted with permission from ref 611. Copyright 2004 Elsevier.

dx.doi.org/10.1021/cr200247n | *Chem. Rev.* 2012, 112, 3356–3426

reversible as the characteristic diffraction peaks of RuO_2 move back to their original positions when the polarization was turned off.

The shape of the Ru-3d core level peaks of RuO_2 in XPS does not change during HER. Therefore Rochefort et al.[608] suggested that the atomic arrangement around each Ru center, and the conformation of the RuO_6 octahedrons are not disturbed by H adsorption into the oxide structure. Kötz and Stucki[600] concluded on the basis of their XPS experiments that during the HER the RuO_2 electrode surface is only partly reduced to some oxy-hydroxide, but reduction to metallic Ru can safely be excluded.

At RuO_2 cathodes in alkaline solution the Tafel slopes for HER were reported to be 40 mV to 50 mV/decade at low current densities and 230−240 mV/decade at high current densities.[604] The change in slope on increasing the current density was attributed either to a bend toward a limiting current density at high overpotentials or to a change in reaction mechanism or to bubble formation.[609] A Tafel slope of 60 mV/decade[610] and 40 mV/decade[600] were reported for the HER on pure RuO_2 in acid solution.

In order to discriminate between the three most popular reaction mechanisms for the HER described in the literature, Chen et al.[589] performed current−potential and AC-impedance measurements for HER on RuO_2 in 1 M H_2SO_4 at room temperature together with a detailed kinetic analysis. The tested reaction mechanisms encompass:

(A) The first reaction mechanism goes back to Boodts and Trasatti:[602]

The first step is the electrochemical reduction of the surface active sites:

(i)

$$Ru - OH + H^+ + e^- \rightarrow Ru - OH_2^*$$

which is followed by the formation of a Ru−H bond

(ii)

$$Ru - OH_2^* + e^- \rightarrow Ru - H + OH^-$$

and finally the release of molecular hydrogen

$$Ru - H + H_2O \rightarrow Ru - OH + H_2$$

(B) The second reaction mechanism is a simplified version of the mechanism A, assuming that the first step is always at equilibrium at any overpotential.

(C) The third mechanism is a Volmer-Heyrovsky type scheme:

(i)

$$Ru - OH + H^+ + e^- \rightarrow Ru - OH_2$$

(ii)

$$Ru - OH_2 + H^+ + e^- \rightarrow Ru - OH + H_2$$

Chen et al.[589] showed that only the Volmer-Heyrosky type mechanism can reasonably fit the kinetic data. The mechanism of Boodts and Trasatti can clearly be ruled out on the basis of this study. Another reaction mechanism has been proposed by Burke and Naser.[612] Assuming that RuO_2 or $Ru(OH)_x$ are redox active, the authors[612] postulated a reduced, metastable surface oxide species which acts as a mediator in the HER.

To clarify the actual reaction mechanism of the HER on $RuO_2(110)$, first principle based studies are called for. Solely based on electrochemical kinetic data, it is impossible to give a conclusive answer concerning the reaction mechanism. For theoreticians, the modeling of the HER should not be too demanding since detailed knowledge about the interaction of H with $RuO_2(110)$ (cf. section 4), but also some in situ experiments on the single crystalline $RuO_2(110)$ electrode surface, are already available in the literature. These data will be discussed in the following.

Linear potential scan and CV were applied to various single crystalline RuO_2 surfaces: (110), (001), (111), (101), and (100) in 0.5 M H_2SO_4 solution.[583] Significant differences in the electro adsorption and desorption on these surfaces were observed, which have been correlated with the differences in composition and structure of these surfaces. A cathodic/anodic pair of peaks observed at −0.3 V (SCE) for RuO_2 faces (110), (001), (111), and (101) has been assigned to reversible hydrogen adsorption/desorption on 1f-cus Ru sites. Another cathodic/anodic pair of peaks at 0 V (SCE) which appear only on surfaces with under-coordinated O present ((110) and (001)) has been attributed to H adsorption on under-coordinated O sites (O_{br}).

Water adsorption in 0.1 M NaOH has been studied with in situ SXRD by Chu et al.[434] At a potential close to HER, the network of water-related species is destabilized by a reorientation of the water molecules under the electric field, preceding the eventual evolution of hydrogen (cf. Figure 30). The ordered water layer structure may be important for a theoretical description of OER and HER on $RuO_2(110)$.

In a follow-up paper, Lister et al.[613a] studied with CV and in situ SXRD two orientations of RuO_2, that is, (110) and (100) in sulphuric acid solutions. The CV of $RuO_2(100)$ and $RuO_2(110)$ exhibits a reduction signature near the HER potential concomitant with an expansion of the top Ru layer. This finding led to the conclusion that the oxygen bonds on the surface are elongated by a chemical reaction with hydronium molecules of the solution. In a next paper by the same authors,[613b] the cathodic activation of $RuO_2(110)$ and $RuO_2(100)$ was studied by CV and in situ SXRD. The CV experiments on $RuO_2(110)$ indicate a Ru-metal like behavior, while SXRD show no roughening of the surface during activation until extreme negative potentials are applied. A similar effect has been observed for the initial reduction of $RuO_2(110)$ with molecular hydrogen exposure and annealing to 500 K.[274,428] Maybe the metal-like domains occupy a fraction of the top surface, requiring additional EC-STM work. Activation of the $RuO_2(100)$ surface for HER sets in already under very mild conditions with an irreversible increase of the electrode capacitance and the appearance of new CV peaks.[613b] A structural characterization of the activated $RuO_2(100)$ surface is missing.

8.3. Chlor-Alkali Electrolysis: Dimensionally Stable Anode (DSA)

Chlorine is omnipresent in technical chemistry (50 Mio. t/a)[614] and is mainly produced by chlor-alkali electrolysis. This process is the most important application in electrochemistry and produces Cl_2 and NaOH starting from brine (highly concentrated aqueous NaCl solution). The reaction in the electrolysis cell is summarized as follows:

$$\text{Cathode}: \quad H_2O + 2e^- \rightarrow H_2 + 2OH^-$$

dx.doi.org/10.1021/cr200247n | Chem. Rev. 2012, 112, 3356−3426

$$\text{Anode}: \quad Cl^- \rightarrow Cl_2 + 2e^-$$

Net reaction :

$$Na^+ + 2Cl^- + 2H_2O \rightarrow H_2 + Cl_2 + 2Na^+ + 2OH^-$$

The cathodic reaction corresponds to the HER and has been discussed in the previous section so that in the present section I shall be focusing on the anodic chlorine evolution reaction (CER or ClER). The equilibrium potential of CER under standard conditions is 1.36 eV against SHE at room temperature. Since the equilibrium potential of O_2 evolution is slightly lower, namely, 1.23 eV against SHE, electrochemical Cl_2-evolution at the anode is facing a selectivity problem. Fortunately, anode materials exist, such as RuO_2-based electrocatalysts, for which oxygen evolution is efficiently suppressed against CER if the reaction takes place at low pH values; the overpotential for OER under this condition is higher than that for CER.

Today so-called dimensionally stable anodes (DSA), which consist of a TiO_2/RuO_2 coating supported by a Ti plate substrate (Ti/RuO_2-TiO_2 electrode), are mostly in use in technical chlor-alkali electrolysis.[10] The presence of up to 70% TiO_2 in the RuO_2-based coating does not change the catalytic activity but increases the selectivity toward chlorine evolution, and most importantly TiO_2 imparts the stability of the electrode against dissolution by decreasing the partial current for OER.[615,616] The variation of the PZC as a function of the TiO_2 content indicates that for RuO_2 concentration greater than 20% the surface properties are dominated by RuO_2;[570,617] below 20% of RuO_2 the activity of the coating drops considerably.[10] Still 30% of RuO_2 is required in the TiO_2/RuO_2 coating to keep the electric conductivity high.[205] With DFT calculations it was found that 25% of Ru in the rutile TiO_2 lattice changes the electronic properties dramatically in that $Ti_{0.75}Ru_{0.25}O_2$ becomes metallic conducting[77,618] with an experimentally found electrical conductivity of 0.78 Ω^{-1} cm^{-1}.[619]

A systematic study of DSA type electrodes in terms of coating performance can be found in ref 620. RuO_2-based electrodes show lower overpotentials and smaller Tafel slopes for CER than graphite and other transition metal oxides.[621] Because of their low overpotential for chlorine evolution, RuO_2-coated electrodes are also applied in the degradation of pharmaceuticals, pesticides, and other organic compounds via indirect electrolysis.[622−624]

The activity of RuO_2-based anodes is, however, not better than that of the precious metals themselves.[625,626] In fact, the main contribution to enhancing the activity of DSA is traced to the enhanced surface area. Other authors discuss the activity of DSA in CER to be related to the specific surface redox reactions taking place at the under-coordinated Ru sites.[585,627] Substantial increases in the rates of CER at various potentials have been observed to result from cyclic potential changes which lead to modifications of the states of the oxides on Ru anodes.[628]

In the electrochemical production of chlorine, it is undoubtedly the stability that plays the most important role. RuO_2 is, however, barely stable at high potentials. It is believed that the oxidation of RuO_2 to soluble perruthenates, ruthenates, and RuO_4 is the main source of instability of RuO_2.[95,629−631] Therefore, anodes in the chlor-alkali industry usually comprise RuO_2 and IrO_2 combined intimately with TiO_2 to form an anode which is mechanically robust, readily releases chlorine, and does not undergo passivation or severe dissolution with extensive use.[632−634] The electrocatalytic stability of TiO_2/RuO_2 with variable concentration profiles of RuO_2 has found to be higher than that of pure RuO_2/IrO_2 coatings.[635] The excellent stability and performance of mixed RuO_2-TiO_2 coatings is attributed to the existence of a metastable solid solution of rutile TiO_2 and rutile RuO_2. Because of their excellent chemical and electrochemical resistance under anodic polarization for chlorine evolution, the Ti/RuO_2-TiO_2 electrode can reach very long operating times of up to 35000 Ah cm^{-2} for the brine electrolysis.[620] For this reason the electrodes are termed dimensionally stable anodes (DSA).[10]

The improved stabilization of RuO_2 by titanium has been observed on single crystal surfaces of RuO_2 as well, namely, on $RuO_2(110)$ and $RuO_2(100)$.[636] It turned out that Ti deposition substantially improved the thermal stability of both orientations of RuO_2 in UHV: While the surface region of pure RuO_2 decomposes after 8 h of annealing at 720 K, the Ti-coated RuO_2 surface was stable even at 870 K for 4 h. This stabilization effect is reconciled with the atomic scale reduction process on $RuO_2(110)$ (discussed in section 5.1.7), assuming that Ti stabilizes the under-coordinated surface oxygen O_{br} of $RuO_2(110)$ for instance by replacing the 2f-cus Ru atoms with Ti. From a combination of electrochemical, photoelectrochemical, and UHV surface analysis studies,[636] it was concluded that the electrochemically significant interaction between the oxides of Ru and Ti is confined to the interfacial region.

RuO_2-based DSAs show a typical cracked-mud morphology (cf. Figure 12). Cracks are beneficial since they increase the active surface accessible to the electrolyte. However, the cracks in the RuO_2/TiO_2 coating must not reach the Ti substrate since otherwise the Ti substrate becomes covered by poorly conducting TiO_x which in turn increases the ohmic potential drop across the anode. Fortunately, RuO_2 is able to form mixed RuO_2-TiO_2 solid solutions with sufficiently high electrical conductivity[637] so that this detrimental effect of TiO_x is reduced.

In comparison with the OER the CER is considered a "facile" reaction which proceeds at high rates on many electrode materials.[638] For the chlorine evolution reaction over RuO_2 and other oxides various reaction mechanisms have been proposed based on observed Tafel slopes and reaction orders.[639,640] The three most frequently discussed reaction mechanisms are

(i) Volmer−Tafel:[641]

$$2^* + 2Cl^- \rightarrow 2Cl^* + 2e^- \rightarrow 2^* + Cl_2 + 2e^-$$

(ii) Volmer−Heyrovsky:[45,642]

$$^* + 2Cl^- \rightarrow Cl^* + e^- + Cl^- \rightarrow ^* + Cl_2 + 2e^-$$

(iii) Krishtalik:[643]

$$^* + 2Cl^- \rightarrow Cl^* + e^- + Cl^- \rightarrow (Cl^*)^+ + 2e^- + Cl^- \rightarrow ^* + Cl_2 + 2e^-$$

Here, * stands for an active surface site, which may be under-coordinated O (O_{br}, O_{ot}) or 1f-cus Ru.

CER proceeds on RuO_2 and other active oxide electrodes with a Tafel slope of 40 mV/decade, indicating that the second electron transfer is rate determining.[45] Therefore a reaction order of 2 in Cl^- is expected for the Volmer−Tafel and Volmer−Heyrovsky mechanisms, which actually is not observed in the experiments.[638] Rather the experimentally

dx.doi.org/10.1021/cr200247n | Chem. Rev. 2012, 112, 3356−3426

found reaction order in Cl^- is +1 which is fulfilled with the Krishtalik mechanism put forward by Erenburg et al.[644−646] and by Krishtalik.[643] This mechanism is characterized by the formation of adsorbed chlorine in a first step, with further oxidation of Cl* to $(Cl^*)^+$ in a second step without involvement of another Cl^- from the solution. Hepel et al. suggested from single crystal experiments that the $(Cl^*)^+$ intermediate in the Krishtalik mechanism is ascribed to a surface OCl^+ group.[647]

An early ex-situ XPS measurement identified substantial amounts of chlorine on the RuO_2 electrode surface after extensive Cl_2 evolution.[648] Unfortunately, the O1s, Ru3p, and Cl2p core levels are shifted by about 10 eV to higher binding energies if compared to more recent XPS data, and the assignment of $Cl2p_{3/2}$ doublets is rather related to the spin−orbit splitting of Cl2p. The interested reader can find in the literature a brief history including a thorough discussion and comparison of proposed reaction mechanisms for the CER up to 1987.[638]

A distinct feature of CER kinetics on oxides is the pH-dependence of the reaction rate in the pH range from 1 to 3. For polycrystalline RuO_2 a reaction order of −1 with H^+ was found.[649] None of the above three reaction mechanisms predicts such a pH-dependence. Therefore, Erenburg[646] proposed a surface oxidation of the active sites, which results in an activation of the surface for chlorine evolution: $-Ru-OH \rightarrow -Ru-O + H^+ + e^-$ and which accounts for the observed pH-dependence. Detailed kinetic investigations of the CER on electrochemically oxidized ruthenium are consistent with the Erenburg−Krishtalik mechanism.[650]

With RuO_2-based electrodes, a complex Tafel pattern is often observed in a wider potential range with a region of discontinuity on the current axis. This behavior has been traced to the high activity of RuO_2 which results in a Cl_2 diffusion-limited reaction rate.[651]

Voltammetric curves of polycrystalline RuO_2 can provide only qualitative information on morphology and only indirect insight can be gained into the atomic structure. The latter requires investigations on well-defined surfaces of single crystals. As expected, the voltammetric curves of the single crystal faces show better resolved features, yet qualitatively they do not differ substantially from those for polycrystalline electrodes.[647,649,652] The various surfaces of RuO_2 can be classified into two groups. The first group consisting of the surfaces (110) and (001) has an ideal surface termination exposing both under-coordinated oxygen and ruthenium atoms, while the bulk-truncated surfaces of the second group (such (111) or (101)) have only under-coordinated ruthenium atoms or only O atoms in the topmost layer. Hepel et al.[653] studied therefore $RuO_2(110)$ and $RuO_2(101)$ in order to have one representative from each group. It turned out that $RuO_2(110)$ and $RuO_2(101)$ reveal the same anodic Tafel slope of 40 mV/decade.[647]

It has been suggested that the Krishtalik mechanism[643] is operative with $Cl^* + e^- + Cl^- \rightarrow (Cl^*)^+ + 2e^- + Cl^-$ being the rate determining step and chlorine Cl and chloronium ion Cl^+ adsorbing on different sites.[647,652] Considering the atomic structure of $RuO_2(110)$ one could think of

(i)

$$O_{ot} + Cl^- \rightarrow O_{ot} - Cl^+ + 2e^-$$

or

(ii)

$$O_{br} + Cl^- \rightarrow O_{br} - Cl^+ + 2e^-$$

In CV significant differences between both RuO_2 orientations occur for the chlorine evolution reaction. It is suggested that only $RuO_2(110)$ provides active oxygen centers for the formation of surface $O-Cl^+$ intermediates in the Krishtalik mechanism. However, at higher anodic overvoltages (>300 mV), the limiting currents in the experiments are not reconciled with the Krishtalik mechanism. The probable change in the reaction mechanism at higher overvoltages is not well understood.

The dependence of the activity in CER on the pH value of the electrolyte solution was studied in detail on $RuO_2(110)$ and $RuO_2(230)$. The (230) surface is more open than the (110) orientation and has been shown to be more active in the Cl_2 evolution. For $RuO_2(110)$, it turns out that the reaction rate is independent of pH, while for the (230) face a reaction order of −1 with H^+ is observed, compatible with data for polycrystalline samples.[649] Trasatti related the pH-independence of CER activity on the (110) face to the higher overpotential for OER compared to that for CER.[45]

In a recent paper the CER and OER were studied on well-defined RuO_2 nanocrystals with a typical size of 10−50 nm.[199] It was found that depending on the preparation temperature the shape of the nanocrystals varies in a characteristic way. The CER turned out to be insensitive to the nanocrystal shape with a Tafel slope of 118 mV/decade. This value is, however, much higher than that found on single crystalline RuO_2 electrode.[652] CER experiments on RuO_2 deposited on conductive diamond were proposed to reveal a radical spillover mechanism at the electrode with the lowest RuO_2 loadings.[654] The Tafel slope is 150 mV for high RuO_2 loadings and 65 mV for low RuO_2 loadings.

Recent developments in ab initio theory of electrochemical reactions based on DFT[655−657] have paved the way to study the CER (also termed ClER) over $RuO_2(110)$ on the atomic level, relying, however, on some crude approximations for the applied potential and the electrode−electrolyte layer.[658] The changes in the interaction between the liquid electrolyte and the surface upon adsorption of molecules are assumed to be small as long as all hydrogen bonds are saturated. By applying an electrothermodynamical approach,[655] it is possible to construct surface Pourbaix diagrams and identify the most stable structure of the catalyst surface as a function of potential and pH values. Such a surface phase diagram is depicted in Figure 48.[658]

CER takes place only for low pH values from 0 to 1 and potential higher than 1.55 V, while for higher pH values the OER is preferred. At pH < 1.3 and low potentials, Cl^- and water adsorbs onto 1f-cus Ru, forming on-top Cl and on-top $O_{ot}H$ groups, while the bridging O sites are covered by H, forming $O_{br}H$ groups. On increasing the potential, the on-top OH species oxidizes to on-top O and recombines to O_2 bridging two 1f-cus Ru sites. This recombination process is exothermic by 70 kJ/mol and activated by only 18 kJ/mol. However, the resulting bridging O_2 species is stabilized by 115 kJ/mol against desorption and will therefore be present on the surface under CER conditions. Above a potential of 1.55 V the adsorbed molecular oxygen reacts with chloride ions to form the intermediate $Cl(O_{ot})_2$ from which finally molecular chlorine is produced by a further attack of Cl^-:

$$O_{ot} - O_{ot} + 2Cl^-(aq) \rightarrow (O_2)_{ot} - Cl + Cl^-(aq) + e^- \rightarrow O_{ot} - O_{ot} + Cl_2(g) + 2e^-$$

dx.doi.org/10.1021/cr200247n | Chem. Rev. 2012, 112, 3356−3426

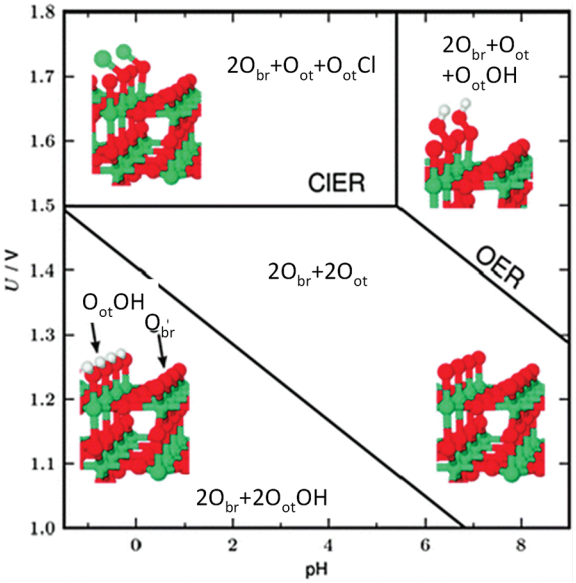

Figure 48. Surface phase diagram for RuO_2 (110) in equilibrium with Cl^-, H^+, and H_2O at 298.15 K and $a_{Cl^-} = 1$. The regions where we expect chlorine evolution (ClER) or oxygen evolution (OER) to become significant have been marked. Reprinted with permission from ref 658. Copyright 2010 Royal Society of Chemistry.

The detailed analysis of Hansen et al.[658] indicates that $Cl(O_{ot})_2$ will form spontaneously on the RuO_2(110) surface at the potential required for CER, suggesting that the CER occurs through this intermediate. This reaction mechanism corresponds to that of Krishtalik when the ominous Cl^+-species is identified with $(O_2)_{ot} - Cl$.

For pH values in the range of 0 to 1 it was found that the potential necessary for CER is always smaller than that for OER. Hansen et al.[658] explained this finding by the fact that in the OER three intermediates have to optimally bind on the electrode surface, while CER involves only a single intermediate for which an optimal bonding situation is easier to find.

8.4. Oxygen Evolution Reaction (OER): Electrolysis of Water

Trasatti qualifies the OER as a "demanding" reaction that is highly sensitive to the chemical nature and actual structure of the electrocatalyst.[659] OER is important in industrial applications such as water electrolysis and metal electro winning processes.[632] The major problem with the OER is to find a stable electrocatalyst since no metal is thermodynamically stable in the potential region of the OER. The metal electrode polarized in the potential region of the OER either dissolves or it passivates. The electronic conductivity of the passivating film is obviously an important parameter for the proper choice of the anode material in OER.

In Figure 49,[660] the stability of platinum group metals and oxides is shown as a function of the applied potential (Pourbaix diagram[270]). Only the light blue regions in the diagram indicate metallic conductivity. The filled red bars indicate the potential where the OER starts with a current denisity of 1 mA/cm^2 on the corresponding metal electrode. From this diagram it becomes clear that only IrO_2 and RuO_2 are electronically conducting and stable under OER, thus qualifying them as promising OER electrocatalysts. The stability of IrO_2 is somewhat better than that of RuO_2. Ruthenium dioxide is,

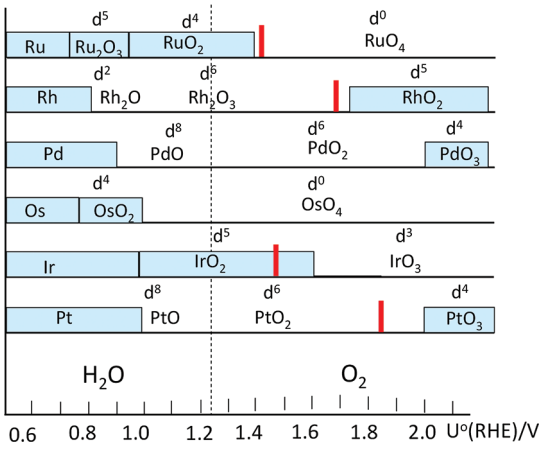

Figure 49. Stability diagram of typical platinum group metal and metal oxides (Ru, Rh, Pd, Os, Ir, Pt) according to Pourbaix. Light blue areas: Regions with metallic conductivity. Filled red bars: potential at which O_2 evolution of 1 mA cm^{-2} in 1 M H_2SO_4 on the corresponding metal electrode takes place. The thin dashed line at 1.23 eV indicates the reversible potential for OER under standard conditions.[660]

however, one of the most active electrocatalysts for OER as indicated by the lower overpotential in Figure 49.[661,662]

There are two clear Tafel lines observed for the OER on RuO_2 anodes. One is in the lower potential region of <1.52 V, exhibiting a slope of 30−60 mV on RuO_2 particles[661,663] and 59 mV on RuO_2(110),[664] while at potentials higher than 1.52 V, the Tafel slope increased to 120 mV/decade. Solely based on the Tafel slopes, a reaction mechanism has been proposed (M = metal):[627,643,659]

(i) The first step consists of an discharge of water molecules (in acid solution) or of OH^- (in alkaline solution) and the oxidation of the surface-active sites

$$-M - OH + H_2O \rightarrow -M < \begin{matrix} OH^* \\ OH \end{matrix} + H^+ + e^-$$

(ii) The (unspecified) intermediate OH* species is converted to OH:

$$-M < \begin{matrix} OH^* \\ OH \end{matrix} \rightarrow -M < \begin{matrix} OH \\ OH \end{matrix}$$

(iii) The surface complex $M(OH)_2$ is then oxidized:

$$-M < \begin{matrix} OH \\ OH \end{matrix} \rightarrow -M < \begin{matrix} O \\ OH \end{matrix} + H^+ + e^-$$

(iv) And finally, molecular oxygen is released by decomposition of the two M(OH)O complexes:

$$2 - M < \begin{matrix} O \\ OH \end{matrix} \rightarrow 2 - M - OH + O_2$$

Applying this mechanism to RuO_2, the rate determining step switches at 1.52 V from step (ii) to the water splitting step (i).[664] The OER over RuO_2 is structure sensitive in that the Tafel slope depends on the orientation of the single crystal RuO_2.[45,665] For RuO_2 the reaction order in H^+ is −1.5 in acid solution[666] and +1.5 with respect to OH^- in alkaline solution,[643] consistent with the proposed reaction mechanism.

According to the proposed reaction mechanism, the released molecular oxygen can contain oxygen from the oxide lattice (so-called Mars−van Krevelen mechanism[562]). This has been

dx.doi.org/10.1021/cr200247n | Chem. Rev. 2012, 112, 3356−3426

corroborated by isotopic labeling experiments.[271] Mass spectrometry indicated that $^{16}O^{18}O$ evolves from OER of a $H_2{}^{16}O$ solution in contact with a Ru oxide layer previously electro-oxidized by $H_2{}^{18}O$. In the case of a Ru anode, formation of RuO_4 was observed when oxygen evolution takes place,[271,289] while on RuO_2 no RuO_4 formation is observed.

Water adsorption in 0.1 M NaOH has been studied with in situ SXRD by Chu et al.[434] At anodic potentials close to OER, a layer of water molecules is vertically compressed to the surface oxygen layer by the strong electric field. Because of the proximity of water to surface O, the authors infer that these layers may be considered as an oxygen−hydrogen-oxygen stratum with an O−H−O bond distance similar to ice. The formation of this stratum is argued to be the precursor for OER. As the potential decreases, the bilayer is abruptly converted to a simple OH layer bonded to Ru atoms; this should give sharp peaks in the CV. At an even lower potential, the bridging OH layer is converted to a layer of commensurate water via an O···H−O hydrogen network anchored to on-top OH.

Several DFT investigations for the OER over $RuO_2(110)$ are available in the literature.[667,668] Rossmeisl et al.[667] have studied the stability of the reaction intermediates for the OER over $RuO_2(110)$, applying the previously developed method for modeling the thermochemistry of electrochemical reactions.[655,669,670] The effect of water surroundings was included by performing simulations with five water molecules in the unit cell. Depending on the applied voltage U, either the hydroxylated $RuO_2(110)$ surface with all bridging O and on-top O saturated by hydrogen ($U < 1.4$ V) or the oxygen terminated $RuO_2(110)$ is stable for $U > 1.4$ V, with bare bridging O and the 1f cus Ru sites being occupied by on-top O.

On the O-terminated $RuO_2(110)$ surface, the water splitting reaction starts off from on-top O vacancies, in which one water molecule adsorbs forming $O_{ot}H$ and $(H^+ + e^-)$. Next a proton is transferred to the electrolyte leaving O_{ot} on the surface. Another water molecule dissociates above on-top O forming an O_{ot}−OH intermediate and $(H^+ + e^-)$. Finally, the proton from O_{ot}−OH is released which causes O_2 desorption leaving a vacancy at the surface and thereby closing the catalytic cycle. In Figure 50 the free energies along the described reaction

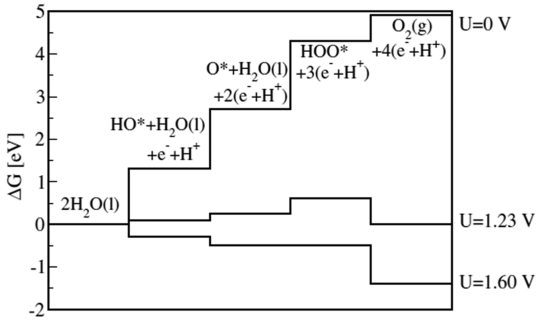

Figure 50. The free energies of the intermediates on O-*-covered RuO_2 (O-* corresponds to O_{ot}) at three different potentials ($U = 0$ V, 1.23 V, 1.60 V) are depicted. At the equilibrium potential ($U = 1.23$ V), the reaction steps are uphill in free energy. At 1.60 V all reaction steps are downhill in free energy. Reprinted with permission from ref 667. Copyright 2007 Elsevier.

coordinate are shown for various potentials. Only when the potential is above 1.6 V, all reaction steps are downhill in free energy, thus making OER feasible.

Performing the same calculation also for the hydroxylated $RuO_2(110)$ surface reveals that all reaction steps become downhill only above 1.73 V. However, at these high voltages, only the oxygen terminated surface of $RuO_2(110)$ is stable.

A more recent theoretical study based on DFT investigated the OER on $RuO_2(110)$ starting from the surface phase diagram and determined also the reaction barriers involved in the elementary reaction steps.[668] One-and-a-half water layers on $RuO_2(110)$ were added as explicit solvent to take the specific interaction between adsorbed surface species and the first water shell into account. The ionic distribution of the electrolyte was modeled by a continuum dielectric medium. Within this approach Fang and Liu[668] were able to explain the switch in mechanism at 1.58 V. Above 1.58 V, the reaction occurs on the fully O-terminated phase (similar to that of Rossmeisl[667]). The rate determining step is identified with the water dissociation above two surface O's, O_{br} and O_{ot} (Eley−Rideal like mechanism). This leads to the formation of a surface O_{ot}−OH intermediate which is stabilized by surrounding water (panel 2 in Figure 51). Next the O_{ot}−OH species releases a

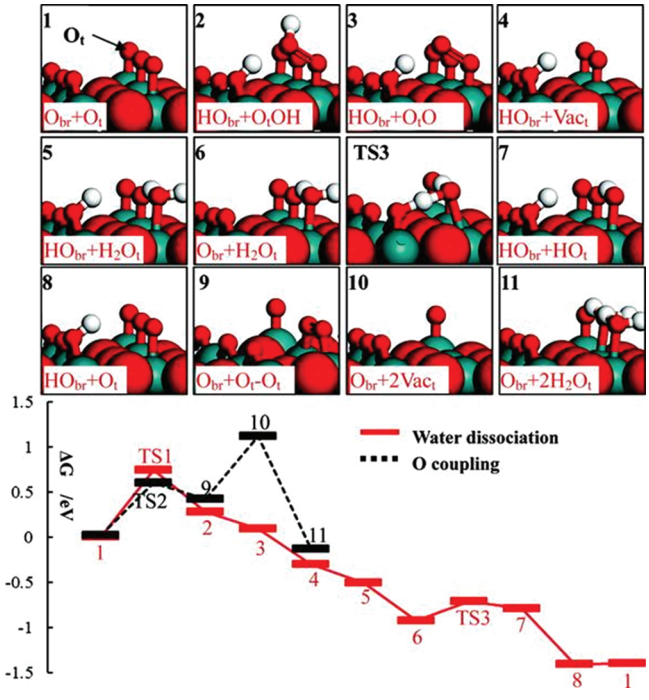

Figure 51. The optimized structures of intermediate states and the free energy profile for OER on the O-terminated phase of $RuO_2(110)$ at 1.58 V. O_{br}, O_t, and Vac_t are the bridging O, the terminal O on 1f.cus Ru and the vacant 1f.cus Ru site, respectively. For the optimized structures, the first H_2O layer is omitted for clarity. O: Red ball; H: white ball; Ru: green ball. Reprinted with permission from ref 668. Copyright 2010 American Chemical Society.

proton to the solution and the resulting O_{ot}-O species desorbs (panel 3 and 4 in Figure 51). Below 1.58 V the reaction takes place on a mixed OH/O phase, where 0.33 ML of the O_{br} form hydroxyl groups and all 1f-cus Ru sites are occupied by on-top O. The lowest energy pathway below 1.58 V involves the local conversion of the mixed OH/O phase into the O-terminated one. The following OER steps are identical to those on the O-terminated phase above 1.58 V.

dx.doi.org/10.1021/cr200247n | Chem. Rev. 2012, 112, 3356−3426

The Tafel slopes were calculated on the basis of the Butler–Volmer equation using a transfer coefficient $\alpha = 0.56$, consistent with an experimentally found value of 0.5.[664] The resulting values for the Tafel slopes of 55 mV/decade below 1.58 V and 105 mV/decade above 1.58 V agree well with the experimental values of 59 mV/decade and 118 mV/decade for single crystalline $RuO_2(110)$.[664]

Among the various oxides, one can observe a volcano behavior for the electrocatalytic activity for the OER as a function of the adsorption energy of oxygen on such oxide surfaces (cf. Figure 52). RuO_2 lies at the apex of the volcano curve,

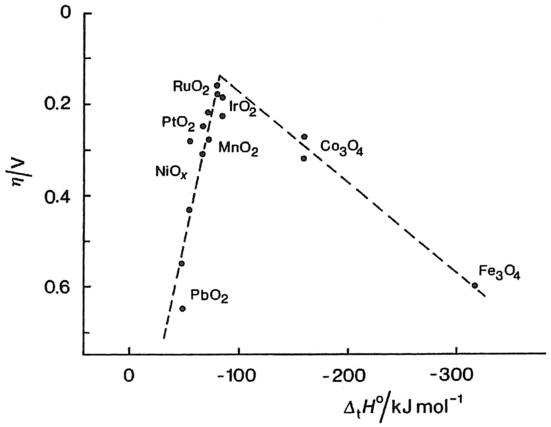

Figure 52. Activity (expressed as overpotential η at 0.1 mA/cm^2) for O_2 evolution (OER) on various electrodes as a function of adsorption enthalpy of oxygen on transition metals from lower to higher oxides.[672,673]

thus being the most active OER catalyst. The ascending branch comprises oxides for which the activity increases with increasing oxygen adsorption energy. On the descending branch oxygen adsorption is too strong to allow for OER.

Trends in electrocatalytic activity of the OER among various oxide surfaces disclose universality in that a universal scaling relation between the adsorption energies of HOO* and HO* exists.[671] The theoretical study of Man et al.[671] identified a fundamental limitation of the maximum achievable OER activity of planar oxide catalysts.

In general, it was observed that materials active for CER are equally active in OER.[673] Doping/mixing of RuO_2 with various elements, such as Ir,[674,675] Co,[676,677] Ce,[678,679] Ni,[680,681] and Pb,[682,683] has been shown to improve the OER activity. The selectivity for electrocatalytic OER on RuO_2 was tailored by Zn substitution[684,685] even in the presence of chlorides. These results are quite encouraging for the development of electrocatalysts for electrolytic seawater splitting. Recall that conventional rutile-type oxide catalysts lose their activity for the OER in the presence of chlorides. Petrykin et al.[684,685] suggested that the presence of Zn ions in the rutile lattice prevents the formation of peroxo bridges between the two O_{ot} sites that imposes the rate determining intermediates for both OER and CER.

8.5. Oxygen Reduction Reaction (ORR)

The oxygen reduction reaction (ORR) on metal electrodes is of high relevance not only for the fundamental research in electrochemistry but also for various applications such as metal oxidation, corrosion, sensor technology, and fuel cells. Recall that electrochemical oxidation processes at one electrode has to be compensated by a corresponding reduction process at the other electrode, which in many cases is the ORR. In fuel cell applications, the ORR imposes the main contribution to the observed overpotential.[686] Although much research has been dedicated to reveal its exact reaction mechanism over Pt(111), there is still no conclusive picture of the ORR on the molecular scale.[687,688] Overall, the ORR involves a demanding four electron reaction:

$$O_2 + 4H^+ + 4e^- \rightarrow 2H_2O$$

Under oxidative reaction conditions at potentials where the ORR is effectively catalyzed, the cathode material is prone to electro-oxidize, thereby poisoning the catalytic ORR.

The standard cathode material for ORR in industrial electrochemical application is based on platinum. However, Pt is expensive so that there is ongoing search for a cost-effective alternative to Pt. Over the past 20 years ruthenium cathodes have been studied quite thoroughly as a promising alternative to platinum-based cathodes. However, the electrocatalytic performance of Ru in the ORR is significantly lower than that of Pt-based cathodes, and Ru cathodes oxidize readily above an operation voltage of 0.8 V forming RuO_2. Part of these problems of Ru can be mitigated by a treatment with chalcogens, such as S, Se, or Te.[689−697]

In particular, selenization of Ru stabilizes the cathode surface against electro-oxidation and the ORR becomes substantially more efficient and selective toward water formation than pure ruthenium. This promotion effect of Se for the ORR over Ru is quite surprising as S and Se are known to be strong poisons in heterogeneous catalysis. In fact for platinum, sulfur was shown to be indeed a strong poison for the ORR.[698] Currently the most active Ru-based ORR catalyst consists of Ru particles of 1−2 nm size supported on carbonaceous soot particles where the optimum Se coverage on the Ru particles is adjusted by annealing the catalyst to 800 °C in a reductive gas atmosphere of H_2 and N_2 (cf. Figure 53).[699] Only firmly bound Se on the

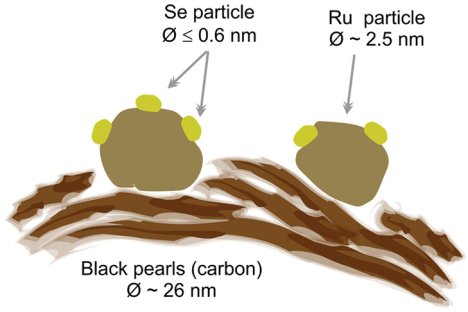

Figure 53. Suggested structural model derived from anomalous small angle X-ray scattering (ASAXS) and small-angle neutron scattering (SANS) measurements of a $RuSe_x/C$ catalyst. Reprinted with permission from ref 697. Copyright 2007 John Wiley and Sons.

Ru particles exert a promoting effect on the catalytic ORR. Nevertheless, platinum is by 30% more efficient than optimized Se−Ru catalysts, therefore hampering a commercial application of Ru-based cathode electrocatalysts.

Recently, fundamental investigations of the ORR over crystalline ruthenium dioxide in acidic solutions have been reported.[700,701] RuO_2-based oxides were coated on a Ti plate substrate (as with DSA) by employing the dip-coating method at 400 °C. The onset potential for the ORR of the RuO_2/Ti

dx.doi.org/10.1021/cr200247n | Chem. Rev. 2012, 112, 3356−3426

electrode was shown to be 0.84 V against RHE.[701] To improve the intrinsically low activity of RuO_2, the surface area of the RuO_2/Ti oxide electrode was enlarged with the help of lanthanum leaching, creating a porous RuO_2 coating.[701] It turned out that the activity of La-treated RuO_2/Ti coating is still significantly lower than that of the Pt-electrode. However, DFT calculations suggest that the adsorption of platinum on RuO_2(110) may become one of the best alternatives to pure Pt as a catalyst in ORR because it combines a high stability together with a moderate activity similar to Pt.[702]

9. ENERGY-RELATED APPLICATIONS OF RUO_2

Electrochemical energy production and electrochemical energy/power storage are at the heart of future sustainable energy/power sources.[703,704] Typical devices for electrochemical energy storage and conversion consist of batteries, fuel cells, and electrochemical capacitors. In all of these systems two electrodes are in contact with an electrolyte solution. The energy-providing processes proceed at the electrode/electrolyte interface, while the electron and ion transport are separated. In batteries and fuel cells, electrical energy is generated by conversion of chemical energy via redox reactions at the anode and cathode either as a thermodynamical closed system (battery) or as an open system (fuel cell). An electrochemical capacitor stores charge in the electrochemical double layer capacitance formed along the electrode/electrolyte interface and/or in a pseudo capacitance resulting from a fast reversible Faradaic process of redox active materials.

Figure 54, a simplified Ragone plot, illustrates the achievable values of specific power and energy (i.e., respective electric

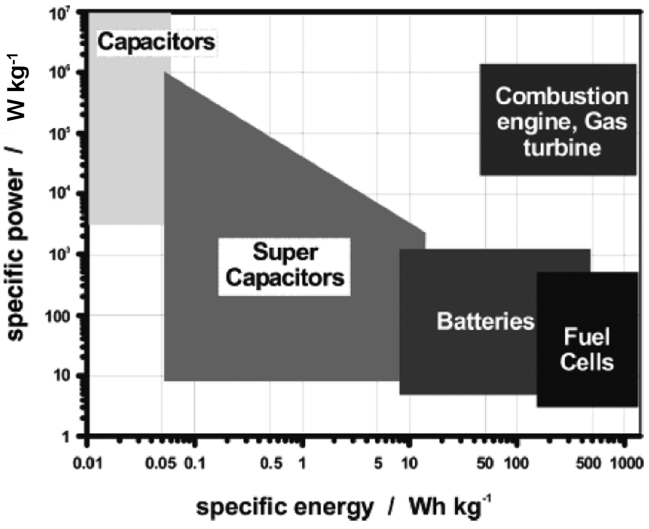

Figure 54. Comparison of the operational characteristics of energy storage and conversion devices in comparison with combustion engines. Adapted with permission from ref 703. Copyright 2004 American Chemical Society.

quantities per kg) for various systems.[703] Batteries and fuel cells offer high specific energy, while their specific power is low. Quite complementary, super capacitors reveal high specific power and low specific energy. For application in automotive propulsion both specific energy and power are required to be high. Figure 54 discloses that no single electrochemical system can compete with the characteristics of the internal combustion engine. Therefore super capacitors have to be combined with batteries or fuel cells in so-called hybrid electrochemical power schemes to approach the performance of internal combustion engines.

In this section super capacitors, fuel cells, and batteries are discussed with the focus on the use of RuO_2. Another topic is related to future hydrogen economy where hydrogen is produced by solar irradiation using semiconductors (e.g., TiO_2) in combination with an efficient cocatalyst such as RuO_2.[705] Fundamental advances in energy conversion and storage devices are closely connected to the development of new, high-performing materials, in particular, to nanomaterials.[706] Consequently, "we must advance the science to advance the technology".[707]

9.1. Super Capacitors

Super capacitors, also called electrochemical capacitors or ultra capacitors, have attracted much attention because of their high pulse power supply, long cycle life (>100000 cycles), and high dynamics of charge propagation. Super capacitors are already widely used in consumer electronics, memory back-up systems, and industrial power and energy management.[708,709]

The electrochemical capacitor boosts the battery in the hybrid electric vehicles to provide the necessary power for acceleration, and additionally allow for recuperation of brake energy. Super capacitors store electric energy by the electrochemical double layer (normal capacitor) and in addition by fast surface redox (Faradic) reactions of an electro-active species (pseudo capacitors).[196,585,710,711] Since electrical capacitors are based on the properties of charge distribution at the interface of an electrode/electrolyte solution, a large surface area is mandatory for these devices such as realized in carbon-based materials.[712] Materials that exhibit high pseudocapacitive storage range from conducting polymers to a variety of transition metal oxides.[713]

One of the most extensively studied metal oxide for use in electrochemical capacitors is hydrous ruthenium oxide. The pseudocapacitance of hydrous RuO_2 is the highest with about 1000 F/g,[714−717] but is prohibitive in price. In order to make most of scare ruthenium in pseudocapacitance, conductive ruthenia nanoskins have been prepared on insulating silica paper.[718,719]

Hydrous ruthenium oxide combines several attractive properties for use as an electrode material in energy-storage applications, most notably reasonable electronic conductivity (1 S cm^{-1}),[720] proton conductivity comparable to Nafion (at 1 mS cm^{-1}),[721] and chemical stability.[722] Small degradation may take place due to Ru-loss via RuO_4 or RuO_4^{2-} formation[271,289,587] at the high potential ends of the anodic voltage excursions. RuO_2 is highly electron conducting so that the screening length is below 1 nm resulting in a high capacitance via the electric double layer. The effects of particle size, hydrous state, and structure on the pseudocapacitive properties of hydrous RuO_2 have been evaluated by using various electrochemical techniques including cyclic voltammetry, hydrodynamic voltammetry, chronoamperometry, and electrochemical impedance spectroscopy.[723] The pseudocapacitance of hydrous RuO_2 has shown to arise from at least two different Faradaic processes together with a high double layer capacitance.[724]

The standard preparation methods for RuO_2-based pseudo capacitors are either similar to the preparation of DSAs by painting $RuCl_3$ on Ti and firing at 350 to 550 °C.[196] It has been shown that the anodic and cathodic charge values derived form integrating the I/U voltammogram plots progressively increased with cycling (charge enhancement factor).[725]

dx.doi.org/10.1021/cr200247n | Chem. Rev. 2012, 112, 3356−3426

It is interesting to note that enhancement of electrocatalysis for anodic Cl_2 evolution at these oxide films follows the charge enhancement factor linearly, suggesting that the latter reflected a progressive increase of accessible oxide surface area.[196] Hydrous ruthenium dioxide thus activated gives a cyclic voltammogram with a shape closely resembling that of an ideal capacitor[35,726−728] (cf. Figure 55). The fraction of the

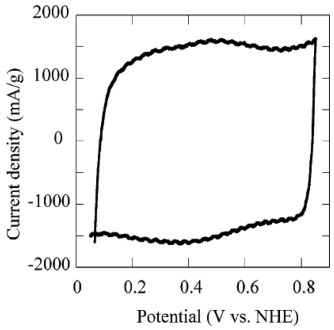

Figure 55. A cyclic voltammogram of $RuO_2 \cdot 0.58H_2O$ taken in 0.5 M H_2SO_4 at a sweep rate of 2 mV/s. Adapted with permission from ref 729. Copyright 2002 American Chemical Society.

RuO_2 film that is accessible to Faradic processes of oxidation and reduction (pseudo capacitance) is substantially larger when the oxide film has been formed by electrochemical cycling in solution, however, with the trade-off that the time response of the pseudo capacitance is slower.

The mechanism of charging hydrous ruthenium oxide electrodes from their discharged state is believed to be a coupled electron−proton transfer process.[730,731] Hydrous RuO_2 acts as a proton condenser.[665,732] When hydrous RuO_2 is placed in solution and its potential is altered, the valency state of the surface metal atoms changes reversibly while being compensated by an exchange of protons with the solution:

$$RuO_x(OH)_y + \delta H^+ + \delta e^- \rightleftharpoons RuO_{x-\delta}(OH)_{y+\delta}$$

This reaction is reversible, taking place over a potential range of about 1.4 V in aqueous solution and is limited only by the decomposition of water. The Ru^{4+} cation is reduced whereas the oxygen ion O^{2-} is protonated. To emphasize the balance of charge and site,[733,734] the full electron/proton reaction is written as

$$Ru^{IV} - O^{2-} + H^+ + e^- \rightleftharpoons Ru^{III} - OH^-$$

In this simplified picture, charge is stored and discharged with the concomitant exchange of protons and electrons from the mixed-conducting hydrous RuO_2. The proton insertion into RuO_2 has been studied by Zheng et al. and a proton diffusion length of greater than 6 nm was obtained in amorphous RuO_2.[735]

When starting directly from hydrous RuO_2 ($RuO_2 \cdot xH_2O$), highest specific capacitance is achieved with $RuO_2 \cdot 0.5H_2O$ by simply annealing the hydrous RuO_2 precursor to 150 °C.[736] With thermogravimetry (TGA), X-ray diffraction (XRD), and X-ray absorption spectroscopy (XANES, EXAFS), the structure of hydrous ruthenium oxides has been determined and directly connected with charge storage properties.[737] Hydrous RuO_2 consists of RuO_6 cores which are connected to chains depending on the water content (cf. Figure 56). Pristine

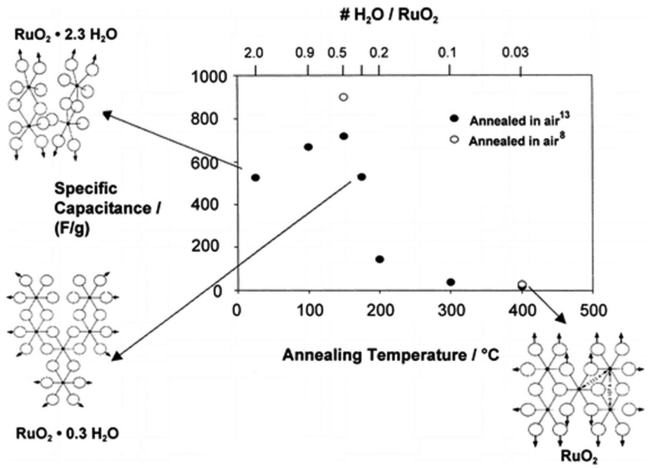

Figure 56. Specific capacitance of various $RuO_2 \cdot xH_2O$ solids as a function of annealing temperature and number of water molecules per RuO_2 unit; the EXAFS-derived local structures[737] that exist at various points on the specific capacitance curve are shown as insets. The specific capacitance was determined in 1 M H_2SO_4 electrolyte. Adapted with permission from ref 737. Copyright 1999 American Chemical Society.

hydrous ruthenium oxide contains 2.3 water molecules per RuO_2 unit and reveals a specific capacitance of 527 F/g.

After annealing to 150 °C hydrous Ru oxide has the approximate formula of $RuO_2 \cdot 0.5H_2O$ with a maximum specific charge capacitance of 720−900 F/g. Beyond an anneal to 150 °C the specific capacitance decreases sharply coincident with the appearance of rutile-RuO_2 related peaks in XRD, that is, a phase transition from amorphous to crystalline RuO_2.[729,738] For an annealing temperature of 400 °C the specific capacitance is only about a few F/g and most of the water has left the hydrous Ru oxide ($RuO_2 \cdot 0.03H_2O$). Rutile-RuO_2 with no structural water exhibits a specific capacitance of 0.75 F/g.

These findings suggest that water is involved in the proton transport. For being a good super capacitor, both electronic and proton conductivity should be reasonably high. The electronic conductivity is highest but the proton mobility is the lowest for rutile-RuO_2. With increasing structural water content in $RuO_2 \cdot xH_2O$ the proton conductivity increases, while the electronic conductivity decreases. An optimum water content is identified with about $x = 0.5$.[736,739,740] A nuclear magnetic resonance (NMR) study verified that the mobility of water molecules within the structure influences the electrochemical capacitance.[741] Transmission electron microscopy (TEM) in combination with electron diffraction[742] confirmed that protons are readily inserted into $RuO_2 \cdot xH_2O$, while the crystalline rutile RuO_2 with a 3D network of octahedral RuO_6 chains inhibits proton insertion. EXAFS suggests that hydrous RuO_2 is truly amorphous for highly hydrated samples.[737] A later publication by Dmowski et al.[729] from the same group demonstrated with X-ray scattering that, even in highly hydrated samples, bulk RuO_2 structure is maintained.

The structure of hydrous RuO_2 is therefore considered to be a bifunctional nanocomposite in which the types of carriers that transport charge are determined by the composition of the nanocomposite.[740] Electron transport takes place through the nanocrystalline RuO_2 wire which becomes the majority volume fraction as hydrous RuO_2 is dehydrated by annealing, while protons are transported only in the disordered hydrous phase which is formed by physi- and chemisorbed water in the

dx.doi.org/10.1021/cr200247n | Chem. Rev. 2012, 112, 3356−3426

grain boundary regions.[729] This model is consistent with electrochemical impedance spectroscopy data reported by Sugimoto et al.,[743] showing that the capacitor frequency response is dominated by protonic conduction.

The transition from amorphous hydrous Ru oxide to crystalline Ru oxide upon annealing at various temperatures was also studied by X-ray photoelectron spectroscopy.[88,194] The appearance of a second $Ru3d_{5/2}$ doublet at 282.6 eV, which is assigned to a surface plasmon,[86] was interpreted as the incipient crystallization of unhydrous RuO_2, while the O1s XP-spectra provide valuable information about the water content in hydrous Ru oxide. Together with capacitance measurements, Foelske et al.[88] identified the material with the highest capacitance of 800 F/g with a chemical formula of $RuO_2{\cdot}0.3H_2O$. The XPS results were discussed within the Sugimoto model.[743] Hydrous $RuO_2{\cdot}0.5H_2O$ consists of 2 nm large primary particles which agglomerate loosely into larger secondary particles with appreciable hydrated micropores. Quite in contrast, anhydrous RuO_2 forms large primary particles whose secondary particles reveal no micropores.

Nanostructuring the redox-active materials increases the capacitance substantially.[711] Sugimoto et al. have prepared hydrated RuO_2 nanosheets with pseudo capacitance exceeding 1300 F/g.[744] Hydrous RuO_2 with nanostructures in a high aspect ratio, that is, in the form of nanotubes, has shown to exhibit high specific capacitance of 1300 F/g together with excellent charge/discharge behavior at 100 mV/s and frequencies as high as 4−8 kHz.[197,745] The specific capacitance can even be improved to 1500 F/g, provided that good electronic conductivity among the RuO_2 nanoparticles and to the back-contact is accomplished.[724] The 3D mesoporous RuO_2 films produced by the evaporation-induced self-assembled method[746] demonstrated extraordinarily high power performance, for example, excellent capacitive behavior at 10 V/s, ultrahigh-frequency capacitive responses, and 2.6 MW/kg with an acceptable density of 4.6 Wh/kg.

9.2. Fuel Cells

Development of anode catalysts with higher tolerance to catalyst poisons such as CO and better stability are major issues that must be resolved for a widespread commercialization of direct fuel cells operating on reformed fuel but also for the direct conversion of methanol fuel to electric power in a direct methanol fuel cell (DMFC).[747] In DMFC the methanol oxidation kinetics on the anode electrocatalyst is slow,[748] while in low-temperature polymer membrane electrolyte fuel cells (PMEFC) the kinetics of the oxygen reduction reaction (ORR) is slow.

CO is formed during the stepwise dehydrogenation of methanol[749] or is present in ppm concentration in the hydrogen gas produced by steam reforming and partial oxidation of fossil fuels.[750] The carbon-supported platinum−ruthenium system is considered as one of the most promising anode catalysts for such fuel cells.[751] Platinum is rather active but suffers from a high sensitivity toward CO poisoning because CO adsorbs strongly on the active Pt sites, thereby inhibiting the successive reaction of the fuel. To overcome the problem with CO surface blocking, ruthenium and other metals are alloyed into platinum.[33,752] The promotional effect of Ru has mainly been discussed in terms of the so-called "bi-functional" mechanism,[495] where CO is oxidized by OH species generated on Ru sites, and/or the ligand effect.[499] The ligand effect assumes that the energy levels of the metal catalyst are modified in a way that the binding energy of CO is reduced.

The Pt−Ru catalysts are not single-phase materials, but rather they consist of mixtures of alloyed and nonalloyed platinum and ruthenium together with the hydrous or anhydrous oxides of Ru.[40] Several papers have appeared discussing controversially the catalytic function of ruthenium oxides in the process of methanol oxidation: Some of these publications report an increase in the activity upon formation of RuO_2,[753−755] while others report a detrimental effect on the activity.[756−758]

Rolison et al.[40,753] noted the importance of hydrous ruthenium oxides in the activity for methanol oxidation in DMFC. Cao and co-workers reported a new nanocomposite $Pt/RuO_2{\cdot}xH_2O$ supported on carbon nanotubes with higher activity in the methanol oxidation compared to commercial PtRu catalysts.[759] Recently, new XPS evidence has been provided for hydrous ruthenium oxide in PtRu nanoparticles supported on functionalized carbon for DMFC application.[760] Wrapping monoparticulate layers of 2−3 nm RuO_2 around the fibers comprising porous SiO_2 filter paper has shown to be promising as a carbon- and ionomere-free gas diffusion electrode for methanol oxidation in direct methanol fuel cells.[719] Hydrous RuO_2 (without anhydrous RuO_2 and metallic Ru) serves as a promoter for the platinum catalyzed methanol electro-oxidation.[761]

If Pt-nanoparticles are supported on RuO_2-nanorods, then the electroactive surface area is much larger than that of the as-prepared Pt nanoparticles on glassy carbon. The presence of RuO_2 nanorods greatly increases the electrochemical activity of RuO_2/Pt electrodes toward methanol oxidation by increasing the current density and by lowering the onset potential of methanol electro-oxidation by 200 mV.[762]

But not only activity of the used electrocatalysts counts for the efficiency of fuel cells. To ensure optimum conditions for effective catalyst utilization, an environment must be assured which allows for an adequate supply of reactants as well as providing a good connection of the active sites to the electron and ion conducting phases.[763] These three requirements have to be fulfilled simultaneously, a problem which is known as the three-phase boundary problem. The commonly used high specific surface carbon black (e.g., Vulcan SC-72C) for supporting the catalytically active material faces problems in optimizing the contact in the three phase boundaries, since Nafion, the proton conducting polymer, is not able to reach the Pt particles anchored in the micropores. Therefore, it is beneficial to integrate intrinsic proton conductivity directly into the support. Hydrous ruthenium dioxide ($RuO_2{\cdot}xH_2O$ or RuO_xH_y) is a mixed electronic−protonic conductor which is stable over a large potential range. The combination of these properties makes hydrous ruthenium dioxide an attractive support material for DMFC.[764] Hydrous RuO_2 offers the additional advantage that this support material reveals high corrosion stability.[765]

9.3. Rechargeable Li-Ion Batteries

Rechargeable Li-ion batteries consist of two electrodes in which Li^+ ions can be reversibly intercalated and the Li^+ conducting electrolyte, for example, $LiPF_6$ (cf. Figure 57).[766] If the battery is fully charged, Li^+ is intercalated in the carbonaceous material (host 2 in Figure 57) with a low-potential for intercalation−deintercalation,[767] while the second electrode (host 1 in Figure 57) is empty of Li^+ and consists in general of a transition metal oxide with strong affinity to Li^+ insertion. The two electrodes have therefore different chemical potentials for Li^+ insertion, determining the electromotive force. When these electrodes are connected to an external device, electrons spontaneously flow from the negative electrode to the positive electrode, while Li^+

dx.doi.org/10.1021/cr200247n | Chem. Rev. 2012, 112, 3356−3426

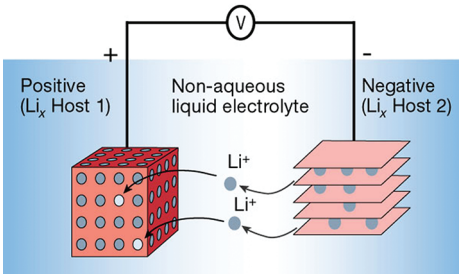

Figure 57. Schematic representation and operation of a rechargeable Li^+ battery. Adapted with permission from ref 766. Copyright 2001 Nature.

ions are transported though the electrolyte to maintain charge balance.

On discharging the battery, Li^+ ions are extracted from the negative electrode and inserted in the positive electrode, leading to a lithiation of the oxide. In order to achieve a cell with a high voltage, high-potential insertion compounds are needed for the positive electrode. In the first Li^+ cell commercialized by Sony Corporation,[768] the positive electrode consisted of $LiCoO_2$. This type of Li-ion cell, which is currently used in portable electronic devices, delivers a voltage of 3.6 V and reaches a gravimetric energy density of about 120−150 Wh/kg.

The lithiation of the transition oxide MO_x leads to formation of a M/LiO_2 nanocomposite in which nanometer-scale metal clusters are embedded in a LiO_2 matrix.[769]

The optimum Li^+ ion battery should possess both high Li storage capacity together with high Coulombic efficiency (ratio of extracted Li^+ to inserted Li^+).[770] Many of the cathode materials currently in use have shown high capacity values, but suffer from moderate Coulombic efficiencies of less than 75% at the first cycle. This reduces the energy densities of the Li ion batteries significantly. It has been shown that RuO_2 can homogeneously and heterogeneously store lithium ions with both a high capacity of 1130 mAh/g and Coulombic efficiency of as high as 98%.[189] Li^+ insertion involves three electrochemical steps: (i) formation of a Ru/LiO_2 nanocomposite (heterogeneous), (ii) formation of a Li-containing surface film, and (iii) interfacial deposition of Li^+ within the Ru/LiO_2 matrix (homogeneous). The reversibility of the Li^+ storage is traced to Ru/LiO_2 nanocomposite during discharging and nano-RuO_2 formation during Li^+ extraction. RuO_2 is considered as a well-suited model material for understanding the reversibility of Li^+ storage through complex heterogeneous solid-state electrochemical reactions. Electrochemical lithiation and subsequent delithiation can also be used to synthesize nanoporous RuO_2.[188]

For achieving high rate capability of Li^+ batteries, rapid ionic and electronic diffusion is necessary. These can be accomplished by introducing a hierarchical, self-similar mixed conducting 3D network of mesoporous TiO_2/RuO_2 nanocomposite as the anode material of Li^+ batteries.[771]

Lithium iron phosphate ($LiFePO_4$) with an olivine structure has attracted extensive interest as a potential candidate for replacing the commercial layered $LiCoO_2$ material.[772] The main shortcoming of $LiFePO_4$ is its sluggish mass and charge transport[773] which can be mitigated by coating $LiFePO_4$ with the widely applied carbon-coating technique.[774] Yet, at high current rates the electronically conducting network of carbon turned out to be insufficiently interconnected. The use of nanometer-size RuO_2 can overcome this connectivity problem, leading to improved kinetics and rate capability of the C-$LiFePO_4$−RuO_2 composite.[775]

9.4. Photocatalysis

A dream reaction would be to directly convert sunlight into hydrogen and oxygen by sustaining photodecomposition of water.[776−778] In 1972 Fujishima and Honda discovered the photocatalytic splitting of water by TiO_2 electrodes, having ignited tremendous research efforts.[438] In general, the photon with appropriate energy promotes the electron from the valence band into the conduction band of the semiconducting TiO_2 material, thereby creating an electron and a hole. Both charged species are able to induce chemical reactions at the surface.[776] In the subsequent deexcitation processes, electrons are able to reduce water to form molecular hydrogen, while holes oxidize water to produce molecular oxygen (cf. Figure 58).[22]

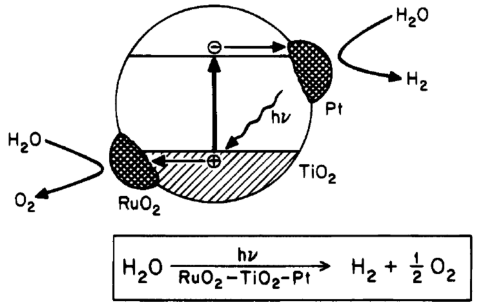

Figure 58. Photo splitting of water on a composite catalyst consisting of the actual photocatalyst TiO_2 and the cocatalysts Pt and RuO_2 for HER and OER, respectively. Adapted with permission from ref 22. Copyright 1995 American Chemical Society.

The presence of Pt and RuO_2 in Figure 58 are required as cocatalyst to significantly reduce the overpotentials for H_2 and O_2 evolution reactions, respectively. While the anode material Pt can be replaced by efficient and abundant (and therefore cost-effective) materials such as intermetallic phases $MoCo_3$, WNi_3, NNi_3, or WFe_3,[779] the catalytic photo oxidation of water remains a major research challenge.[705]

It should be emphasized that solar hydrogen production is only sustainable when the electron for proton reaction is ultimately produced from water during oxygen evolution and not by the oxidation of sacrificial molecules. The key problem with oxygen liberation from water is that the most efficient thermodynamic potential of 1.23 V requires a four-electron extraction process (cf. OER in section 8.4) which needs an efficient catalyst, such as RuO_2.

Besides searching for alternative OER catalysts replacing RuO_2, there are a couple of other issues to be solved prior to producing hydrogen from sunlight in an economic way. First of all, one has to find stable (under irradiation) and abundant photocatalysts (semiconductors) with a band gap narrower than that of TiO_2 where the redox state of H_2/H_2O is below the conduction band and that of O_2/H_2O is above the valence band. The photon-generated electron−hole pair has to migrate with high mobility to the surface without recombining and then electron and holes have to initiate the chemical reduction and oxidation reaction at two different places on the surface, respectively. Because of small diffusion lengths (of the order of some nanometers) for the charge carrier, nanostructuring of

dx.doi.org/10.1021/cr200247n | Chem. Rev. 2012, 112, 3356−3426

TiO_2 is required for photoinduced charge carriers to reach the surface by migration. Partly substitution of the cationic or the anionic lattice is able to reduce the band gap of TiO_2 and to improve the performance of the photocatalyst.[440,780−783] Unfortunately, this band narrowing of TiO_2 goes hand in hand with the formation of more bulk defects, serving as recombination centers for the light induced electron hole pairs, and a reduction of the mobility of e^- and h^+. So far the band gap narrowing has not been able to enhance the photocatalytic activity.

An alternative to solid state photocatalysts represents Ru-complexes used for harvesting the sunlight in the so-called Grätzel cells.[784] We will not elaborate on this topic but rather refer the interested reader to a recent review article.[785]

10. APPLICATIONS OF RUO_2 IN ELECTRONIC INDUSTRY

10.1. EUV Lithography: Catalysis Meets Lithography

Extreme ultraviolet lithography (EUVL, λ = 13.5 nm) is the leading candidate for future high volume semiconductor manufacturing[786] for the 22 nm node: The short wavelength of the incident illumination allows one to print small structures below 22 nm in size. But light with such a short wavelength is strongly adsorbed by any material including the gas atmosphere.

Therefore, the exposure tools and the associated tools in EUV lithography have to be kept in high vacuum conditions of better than 10^{-6} mbar and reflective optics rather than transmission optics must be used to image the mask onto the wafer. UHV conditions cannot be achieved in EUVL exposure tool for technical reasons.

Figure 59 depicts a schematic of an EUV lithography system,[787] which was built by EUVLLC and operated at Sandia National Laboratories. A plasma source for EUV radiation illuminates

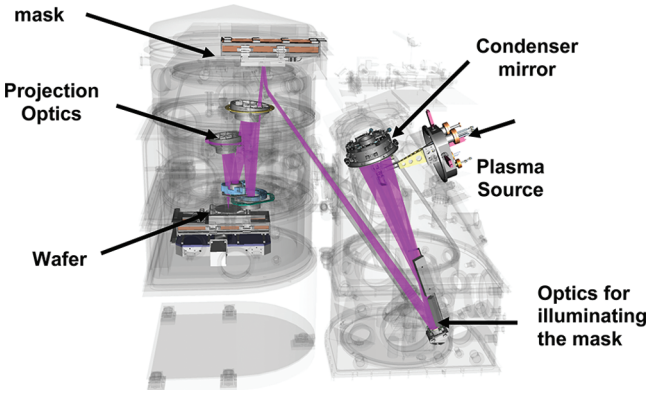

Figure 59. Schematic of an extreme ultraviolet lithography (EUVL) system (engineering test stand: ETS).[787]

the mask by using the condenser mirrors. The projection optics image patterns of the photomask onto photoresists coated wafers.[787]

One of the challenges for EUVL is the lifetime of the imaging and the collector optics, usually consisting of 40−50 alternating layers of Si and Mo that form reflective multilayer coatings with a combined thickness of 6.8 nm per bilayer[117] (cf. Figure 60). Here nanotechnology is needed in the optics design of the exposure tool to be able to manufacture nanoscaled mass products.

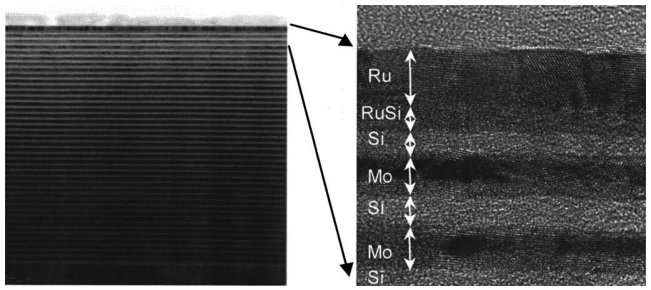

Figure 60. TEM image of a multilayer mirror that is composed of a Si/Mo multilayer stack with a period of 6.8 nm, that is, half the EUV wavelength (13.5 nm) protected by a layer of Ru (capping layer). Reprinted with permission from ref 788. Copyright 2009 American Vacuum Society.

The maximum reflectivity reached with the multilayer mirrors is about 70%.[117] The combination of exposure to high-intensity EUV radiation ($h\nu$ = 92 eV) and the presence of hydrocarbons and water in the residual gas causes fast degradation of the optical reflectivity due to growth of carbon layers and the oxidation of the multilayer[789−793] (cf. Figure 61).

One solution toward improving the optics lifetime is the use of protective capping layers. The ideal capping layer should exert negligible absorption of EUV light and be inert against water and hydrocarbon species, thermally and chemically stable, easy to synthesize on and to be integrated with the Mo−Si multilayer (wetting properties) and permeation of oxygen and hydrogen through the capping layer should be efficiently suppressed. It has been shown that ruthenium-based capping layers of 2−3 nm thickness are promising for the protection of the Si/Mo multilayer systems. Ruthenium has shown to successfully prevent the oxidation of the topmost Si layer.[117] However, ruthenium also undergoes oxidation and carbon contamination in a typical EUV tool environment, although the degradation of the optical reflectivity is significantly slowed down.[786,794]

In order to achieve long-term stability of the EUVL mirror and to warrant reflectivity degradation of less than 1% over 5 years (according to the roadmap for EUVL),[793] the molecular level processes at the Ru-based capping layer surface under EUVL environment (base pressure 10^{-7} mbar and typical EUV irradiation) must be fully understood, and reliable ways of mitigations and technically feasible operation conditions have to be identified. Besides carbon uptake, the oxidation of Ru to RuO_2 is one of the primary reasons for the optical degradation of Ru-protected EUVL mirrors,[786] and oxidation proceeds already at room temperature.

While thermal oxidation requires at least 500 K even for a 6 nm thick Ru layer,[118] oxidation under EUVL conditions occurs already at room temperature, thus being closer to electro-oxidation than to gas phase oxidation. We should bear in mind that photon-induced secondary electrons may even lead to charging of the EUVL mirror and thus may initiate electro-chemical oxidation. Oxygen plasma treatment leads to oxidation and corrosion of Ru capping layers at room temperature.[288] Detailed modeling studies of carbon uptake and oxidation of Ru surfaces under EUV radiation have been reported.[791,792] Consistent with recent surface science studies,[795] the oxidation under EUVL conditions is driven by EUV photon-assisted (direct photon or secondary electron induced fragmentation) water fragmentation (cf. Figure 61). The weakly adsorbed water molecule on the Ru capping layer surface is

dx.doi.org/10.1021/cr200247n | Chem. Rev. 2012, 112, 3356−3426

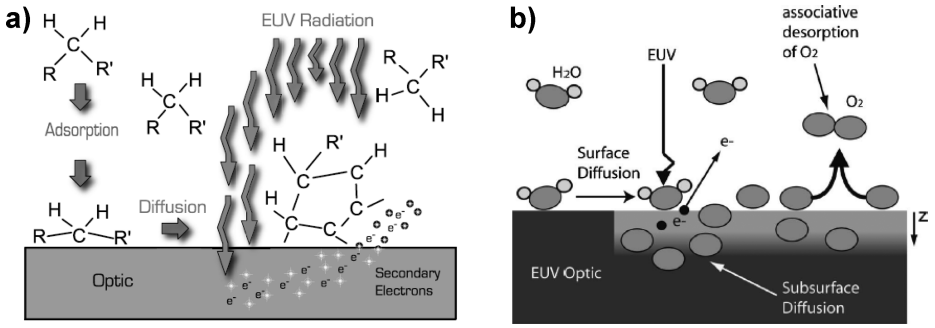

Figure 61. (a) EUV light induced carbon uptake: adsorption, diffusion, and dissociation of large parent hydrocarbons into a graphitic-like, but partially hydrogenated, layer.[790] (b) EUV-induced oxidation of the EUVL mirror by water splitting.[791] Reprinted with permission from ref 791. Copyright 2006 American Vacuum Society.

fragmented due mainly to secondary electrons released by EUV illumination. In this way atomic oxygen is accumulated on the Ru capping layers surface which further may drive the in-depth oxidation of the 2 nm thick Ru film. Experimentally, a few nanometers thick Ru capping layers have been shown to oxidize in depth upon EUV irradiation in a 10^{-7} mbar environment of water and hydrocarbons molecules after a short time interval.[794] The carbon uptake is also due to secondary electrons which fragment weakly adsorbed hydrocarbon coming from the residual gas atmosphere which then can strongly stick to the EUVL mirror surface (cf. Figure 60). For further details, consult recent review articles.[143,795]

Both Ru and RuO_2 are prone to take up hydrocarbons from the gas phase via dehydrogenation. Therefore it is important to identify efficient cleaning procedures to remove the carbon containing species from the capping layers at room temperature. On ruthenium the mildest method for removal of carbon contamination is chemical reduction by hydrogen. Hydrogenation of alkenes, alkynes will lead to alkanes which immediately desorb into the gas phase, as alkanes are only physisorbed on the Ru capping layer surface. But also carbon and other fragments of hydrocarbons can efficiently be removed by hydrogenation as ruthenium is known to be an excellent hydrogenation catalyst.[155,504] Actually, Nishiyama et al. have demonstrated that carbon contaminated Ru capping layers can efficiently be cleaned by exposing atomic hydrogen to the mirror surface at room temperature.[100,290] Alternative ways to remove carbon from EUV multilayer coated optics were proposed and tested with minimal or no reflectivity loss.[796−798] Recently, an effective wet cleaning procedure was designed to remove C contamination from Ru capping layers.[799]

On the other hand, RuO_2 is a poor hydrogenation catalyst. Hydrogen exposure will rather form OH groups which in turn are the precursor for a reduction of the RuO_2 surface. Therefore the only way to remove carbon deposits from the RuO_2 surface is the total oxidation to CO_2 and water. This approach is very general but it is also quite harsh in that it needs temperatures as high as 500 K or higher,[383] at least when molecular oxygen is applied as the oxidizing agent. This temperature is far too high to preserve the integrity of the multilayer mirror system. However, at lower temperatures partial oxidation may take place rather than total oxidation. For instance, for the methanol oxidation formaldehyde is formed below 400 K which in turn can polymerize on the surface. This is even worse than methanol adsorption. Recently, it has been shown that carbon contamination can be inhibited by a mixture of O_2/O_3 even at room temperature.[800]

The worst situation for a EULV mirror system is presumably encountered when the capping layer contains both metallic Ru and RuO_2 patches on the surface. Then the capping layer is optically rough, and it can take up hydrocarbons very efficiently, while for the removal of carbon deposits both reduction and oxidation would be necessary which is hard to achieve at the same time. Therefore much care has to be taken to prevent the formation of such heterogeneous capping layer surfaces. Unfortunately such a heterogeneous surface will inevitably develop with time on the Ru capping layer under typical EUVL conditions so that an efficient reduction recipe has to be devised to reduce the partly oxidized Ru capping layer. Nishiyama et al.[100] showed that with atomic hydrogen exposure (produced by plasma discharge) the chemical reduction of RuO_2 into Ru is complete below 323 K.

Another serious problem with Ru-based capping layers in EUVL is related to surface contamination by small particles which are introduced by chemical etching of the photoresist in various phases of the lithography process. These particles cannot be removed by conventional cleaning technology. Using UV/ozone or oxygen plasma for the removal of these particles leads to significant oxidation and corrosion of Ru.[788] The mildest way to remove particles from the Ru capping layer was found to be wet chemical treatments by a sulfuric acid and hydrogen peroxide mixture.[788]

In conclusion, the proceeding discussion of protecting capping layers based on Ru may be best summarized as "lithography meets catalysis".[143]

10.2. RuO_2 Films for Electronic Industry Applications

Ultrathin films of metallic conductive ruthenium oxide (RuO_2) have found many applications in large scale integrated circuits due to their quite low resistivity, excellent diffusion barrier properties, good thermal stability, and high chemical corrosion resistance. This is also reflected by the increasing demand of ruthenium in the electronic industry, where about 20 t/year are deployed.[13] Ruthenium and ruthenium dioxide remain chemically stable in contact with high-k dielectric materials such as hafnium oxide and aluminum oxide, even at high temperatures.[801] Both Ru and RuO_2 are being considered as a seed layer for the deposition of copper layers, which is important for interconnections in microelectronics, capacitor electrodes for memory devices, and gate contacts for metal-oxide semiconductor field-effect transistors.[802−805] RuO_2 is a promising candidate material for the bottom electrode in capacitors with a high dielectric constant and/or ferroelectric thin films. In addition, the etching capability of RuO_2 is superior to Pt, one of its competitors, since RuO_2 can be easily patterned by reactive

dx.doi.org/10.1021/cr200247n | Chem. Rev. 2012, 112, 3356−3426

ion etching (RIE) in O_2/CF_4 discharges.[806] As a consequence of favorable process compatibility, good thermal stability, and relative ease of etching, ruthenium and ruthenium dioxide are among the many candidates proposed to replace poly-Si gate electrodes for advanced processes.[807]

High dielectric constant materials (high-k) such as tantalum pentoxide and barium strontium titanate have been considered as dielectrics for capacitors in future high-density dynamic random access memory (DRAM) devices.[808,809] Deposition of these high-k materials directly on silicon and the following thermal treatments lead to the formation of an interfacial layer[810] which severely degrades the properties of the capacitor. By inserting a metal electrode between the high-k dielectrics and Si, the formation of the interfacial layer can be avoided. Among the various possible metal electrodes, ruthenium is identified as a suitable electrode for future DRAMs, mainly due to its conducting stable oxide phase (RuO_2).[811] Recently, capacitors with RuO_2 electrodes and TiO_2 dielectrics having sub-nanometer equivalent oxide thickness were successfully prepared.[812,813] To achieve high density capacitance in DRAM technology, 3D cylinders or trench geometries should be used.[150,814] The conformal growth of such RuO_2 films can be accomplished by using atomic layer deposition.[150,153]

Ferroelectric materials have been introduced as capacitor dielectrics for the application in random access memory (FeRAM) devices.[815] FeRAM shows advantageous memory properties such as nonvolatility, low power consumption, high write endurance, and high-speed operation. Lead zirconate titanate (PZT), a promising FeRAM material, has the principal advantages of relatively low crystallization temperature, compatible with metal-oxide−semicoductor fabrication, and high permanent polarization.[816] However, PZT shows poor endurance with Pt electrodes. The use RuO_2 instead of Pt electrodes increases the durability significantly together with introducing good diffusion barrier characteristics and the capability to compensate oxygen vacancies for eliminating the polarization fatigue.[817,818]

The use of RuO_2 as thick or thin film resistors is another attractive application in the microelectronic industry.[819,820] Reactively sputtered RuO_2 thin−film resistors exhibit near zero temperature coefficient of resistance.[142] Ruthenium oxide-based thick film resistors can be used as temperature sensors in cryogenic applications. The main disadvantage of thick-film based resistors is their inherent lack of sensitivity for temperatures ranging from 0 to 4 K.[821] Improved sensitivity of RuO_2-based temperature sensors can be achieved by using a nanopowder approach.[822]

The potential application of RuO_2 thin films as buffer layers or contact electrodes to high temperature superconducting $YBa_2Cu_3O_{7-x}$ thin films have been investigated because of the good thermal stability and high thermal conductivity of the RuO_2 thin films, as well as their structural and chemical compatibility with $YBa_2Cu_3O_{7-x}$.[823]

11. CONCLUDING REMARKS AND SYNOPSIS

Ruthenium reveals a rich chemistry in homogeneous coordination chemistry, inorganic chemistry, electrochemistry, and surface chemistry.[1,2,107,824] The main reason for this chemical variability of ruthenium is traced to the range of possible oxidation states of ruthenium from −II to +VIII.[2] Accordingly ruthenium is quite intensively employed in various fields of catalysis, including homogeneous catalysis (Ru-complexes: e.g., Grubbs catalysts), heterogeneous catalysis (RuO_2: Deacon process, Ru: Ammonia synthesis), and electrocatalysis (RuO_2: chlor-alkali electrolysis, water electrolysis). A cross-fertilization of these catalysis disciplines may be expected by interchanging scientific ideas for the case of ruthenium but also for other platinum group metals (PGM). This "unifying concepts in catalysis"[825] will be discussed in this concluding section for the case of ruthenium (sections 11.2 to 11.4). However, the first part of these concluding remarks addresses specific surface properties, rendering RuO_2 a versatile oxidation catalyst.

11.1. What Makes RuO_2 an Active (Oxidation) Catalyst?

A well-performing catalyst has to fulfill three major properties: selectivity, activity, and stability. Selectivity is a more formidable task than activity as for the former the difference of activation energies and entropies are responsible and activity depends mainly on the activation barrier of the rate determining step.[826] The most demanding property is the stability of catalysts since long-term stability is not easily accessible by typical surface science approaches.

Let us start with the discussion of the atomic scale description of the catalytic activity of RuO_2. The presence of under-coordinated surface atoms is mandatory to achieve high catalytic activity.[21] In particular, the under-coordinated Ru sites (1f-cus Ru) are able to bind the reactants to the catalyst's surface. The 1f-cus-Ru sites serves both as basic and acidic Lewis sites. This gives the $RuO_2(110)$ surface a flexible adsorption behavior. Various molecules are strongly but not too strongly bound to these active sites (Sabatier principle). In addition to become an active oxidation catalyst, easily available (atomic) oxygen must be present on the surface. For $RuO_2(110)$, these are the bridging O and the on-top O species. With an initial sticking coefficient of 0.7 on $RuO_2(110)$, dissociative adsorption of molecular oxygen is facile and does therefore not impose a bottleneck in the oxidation reaction. For comparison, on stoichiometric TiO_2 the dissociative adsorption of oxygen is endothermic and therefore oxidation activity is strongly inhibited.

For dehydrogenation reactions, the presence of Brønsted basic sites at the surface is mandatory in order to accept the eliminated hydrogen from the reactant molecule or the fragments of it.[827] For the case of RuO_2, these (Brønsted) basic sites are identified with the under-coordinated bridging O and the on-top O atoms. For the oxidation of HCl and NH_3 both the 1f-cus Ru and the under-coordinated O sites are required. The NH_3 molecules adsorb first on the 1f-cus Ru sites. Subsequently, the sequential H abstraction proceeds via under-coordinated O atoms through hydroxyl and water formation. The HCl adsorption takes place dissociatively, thus requiring neighboring 1f-cus Ru and under-coordinated O atoms to accept the Cl and H fragments.

Whenever weakly bound atomic oxygen is available on the surface, total oxidation of molecules is preferred over partial oxidation. This has been observed for the methanol oxidation of RuO_2.[282,383] However, under typical methanol oxidation conditions RuO_2 quickly reduces in a way to self-optimize the activity and selectivity. The resulting transient surface oxide (TSO) phase is considered to be neither the Ru metal nor the RuO_2, but is rather considered to be a subsurface oxygen phase. The TSO phase improves the selectivity toward formaldehyde.[282] The catalyzed partial oxidation of methanol is a nice example of the chemical flexibility of RuO_2 in that it adjusts its structure to optimize reaction conditions. Even under strongly oxidizing

dx.doi.org/10.1021/cr200247n | Chem. Rev. 2012, 112, 3356−3426

reaction conditions for which the RuO_2 catalyst has been shown to deactivate in the CO oxidation reaction,[249] the catalyst can adjust to the actual reaction mixture, revealing again high catalytic activity after a long induction period of many hours.[458] RuO_2 is easy to chemically reduce. This property is important for the activity since additional oxygen from the lattice RuO_2 is available to the reaction similar to the case of CeO_2 serving as an oxygen buffer.

Selectivity of RuO_2 is less well pronounced as shown for the partial oxidation of methanol to form various products[28] or the oxidation of ammonia.[412] NH_3 oxidation over RuO_2 powder leads to N_2, NO, and N_2O.[412] A systematic DFT study has identified some rules for selectivity in oxidation processes on $RuO_2(110)$.[398] According to this study (missing) selectivity of RuO_2 is attributed to the basicity of the surface O atoms in combination with binding energies of the reactants and products to the surface. However, chlorine can act as a promoter to enhance selectivity to useful products. This was demonstrated with the electrocatalytic ethene epoxidation.[828] Chlorine acts as epoxidation promoter that switches off the combustion pathway toward CO_2 and enables the epoxidation reaction.

Stability is another key issue for qualifying a material as a good catalyst. Stability is indispensable for instance in the HCl oxidation reaction (Deacon process) and the chlor-alkali electrolysis, even more important than the actual activity. Under reducing reaction conditions, the decomposition of RuO_2 starts by removing the bridging O species, thereby destabilizing the surface. In order to stabilize the RuO_2 surface against chemical reduction, one has to stabilize the bridging O (O_{br}) positions. Stabilization can be achieved by replacement of O_{br} with chlorine in the HCl oxidation reaction[405] or with CO in the CO oxidation reaction. In the methanol dehydrogenation, there is no stabilizing intermediate. Accordingly, RuO_2 is easily reduced to the TSO.[282]

The stability of RuO_2 under strongly oxidizing reaction conditions is more challenging than under reducing conditions, such as encountered in the oxygen evolution reaction (OER) in electrocatalysis. Here Ru in the form of RuO_4 can leach into the electrolyte solution,[95] and the question arises how to stabilize the electrode by proper choice of the electrolyte solution. In an oxygen gas atmosphere, supported RuO_2 catalyst transforms into a deactivated state when keeping the oxide at high temperatures around 800−1000 K.[249] There is some theoretical evidence that this transformation is connected with a surface reconstruction in which sp^3-hybridized surface Ru atoms are formed.[437]

In comparison with other platinum group metals oxide RuO_2 seems to be at the optimum of stability and activity. Either the oxide is very stable but then it is also not very active in oxidative reactions or vice versa. Systematic DFT calculations of the CO oxidation on various PGM surfaces (Ru(0001), Rh(111), Pd(111), Os(0001), Ir(111), Pt(111)) in comparison with corresponding $MO_2(110)$ surfaces in rutile structure[470] revealed that in all cases the oxide surface is more active than the corresponding metal surface. The reason for this general behavior was traced to a geometric effect of the metal oxide, on which the transition state (O--CO) is allowed to be achieved without a significant O movement, while on the metal surfaces the O atoms have to move from the 3-fold hollow site to bridge position in the transition state. This study indicates also that RuO_2 is not the most active oxide catalyst in the CO oxidation. However, the more active oxide surfaces such as PtO_2 and RhO_2 are significantly less stable than RuO_2 at least in the rutile phase.

11.2. Surface Chemistry versus Homogeneous Coordination Chemistry

Surface science and homogeneous coordination chemistry have a long and fruitful common tradition. Unfortunately, this common background of surface and coordination chemistry has somehow faded during the past decades. In the early days of surface chemistry the bond formation of CO, NO, H_2O, and other small molecules to metal surfaces was compared to and rationalized by corresponding bonds in transition metal (TM) complexes such as carbonyls, nitrosyls, and hydrates. The most prominent example is the bond formation of CO on transition metal surfaces, which is described within the Blyholder model,[426] a model directly adopted from homogeneous coordination chemistry. CO binds to TM through a charge transfer from the 5σ to metal d states with σ symmetry concomitant with back-donation from metal-d states with π symmetry to the $2\pi^*$ orbital of CO. The main rationale behind this close correlation between coordination and surface chemistry is that bonds of molecules at surfaces by and large are localized.[829]

Homogeneous coordination chemistry is closely related to homogeneous catalysis. In particular, catalyst design by adapting proper ligands is at the heart of homogeneous catalyst design in terms of superior activity and selectivity. Chlorine is frequently used in Ru-based complexes to adjust the electronic and chemical properties of the Ru-complex for a particular reaction. Cl serves electronically as an "anti-CO" ligand. The ligand CO is a σ-donor and a π acceptor in the bonding to Ru, while Cl serves as σ acceptor and π donor. Cl−Ru complexes have successfully been employed for instance in the olefin metathesis as a homogeneous Grubbs' catalyst.[830]

Successful strategies of homogeneous catalysis may be beneficial to the field of heterogeneous catalysis. For the case of RuO_2 one may speculate that a direct comparison with Ru-oxo-complexes[824] may help to improve heterogeneous Ru-based oxidation catalysis. Bridging the gap between "homo-" and "hetero-" catalysis is a formidable but rewarding task.[831,832] One apparent strategy to merge homogeneous with heterogeneous catalysis constitutes the immobilization of metal atoms in nanoporous oxidic solids.[833] However, there are also striking gaps between these fields: For instance, the active site of the catalyst[834] is unambiguously defined in homogeneous coordination chemistry/homogeneous catalysis, while in heterogeneous catalysis this concept is still a controversially discussed issue. But even if homogeneous and heterogeneous catalysis show similar performance as with the selective activation of alkynes over single gold atoms (homogeneous catalysis) and gold particles (heterogeneous catalysis), the origin for the observed selectivity can be different.[835]

The correlation of coordination chemistry and surface chemistry is particularly close for oxide surfaces (cf. Figure 62). For instance, the under-coordinated 1f-cus-Ru sites of $RuO_2(110)$ can be envisioned as the metal core of a pentacoordinated Ru-complex with one unsaturated bond. The five ligands of 1f-cus-Ru atoms represent the attached O and Ru atoms in the first or second coordination shell. To fine-tune the chemistry of the 1f-cus-Ru sites, one can vary the coordination shell for instance by substituting the attached O atoms at the surface by other species (e.g., Cl or S) or substituting the attached Ru atoms by another TM metal atom (alloying: ligand effect). This leads to the active field of mixed oxide catalysis.[836] One may speculate that in this way the chemistry of the active site on RuO_2 can be tuned to optimize the catalytic performance in terms of activity and selectivity. Also the orientation of the RuO_2 surface changes the

dx.doi.org/10.1021/cr200247n | Chem. Rev. 2012, 112, 3356−3426

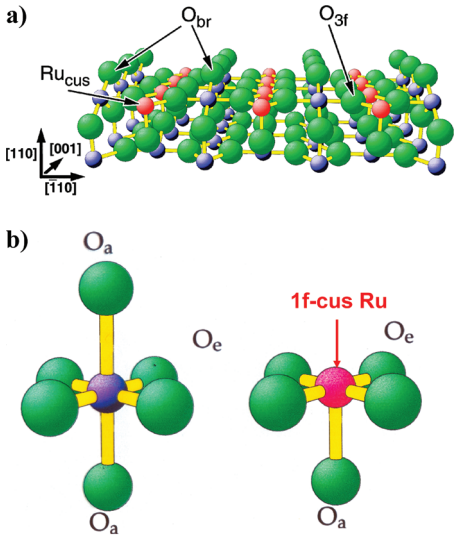

Figure 62. (a) Ball and stick model of the RuO_2 (110) surface. (b) RuO_6 octahedron of bulk coordinated Ru in rutile RuO_2 in comparison with the RuO_5 complex of 1f-cus Ru on the RuO_2 (110) surface. The equatorial O are denoted O_e, the apical O_a.

coordination shell of the 1f-cus Ru "surface complexes" and may therefore affect the catalytic behavior. The 1f-cus Ru on RuO_2(110) is coordinated only to saturated O atoms, while the 1f-cus Ru on RuO_2(100) is coordinated to both saturated O and one unsaturated bridging O atom.

There are of course also distinct differences between homogeneous coordination chemistry and surface chemistry. Metal or metallic oxide particles may offer for instance delocalized electron density, or the prospect of storing chemical species in the subsurface region, such as carbon[837] and hydrogen.[838] These properties cannot be devised with simple metal complexes. On the other hand, metal complexes are much more flexible than massive metal or oxide RuO_2 nanoparticles, a property which is decisive for the obtained selectivity in homogeneous catalysis by designing the ligands.

11.3. Surface Chemistry versus Heterogeneous Catalysis

About 80% of all technical chemicals are manufactured by utilizing heterogeneous catalysis, where reactions take place at the gas/solid or the liquid/solid interface. Therefore one of the major topics in surface chemistry is intimately associated with heterogeneous catalysis, with the ultimate goal to develop novel catalysts and to improve the catalyst's performance based on an atomic scale based knowledge.[839] Rational catalyst design requires the coherent interplay of applied catalysis (e.g., technical chemistry), surface chemistry, and ab initio theory on a particular catalyzed reaction system. So far only very few successful examples have been reported in the literature, and most of these examples originate from Denmark, where physics and chemistry groups from Danish universities and the R&D department of Haldor Topsoe, a leading catalyst company, ran a successful network of catalysis.[840−842] One has to admit that so far no novel catalyst has been invented for direct industrial application by pure surface chemistry. However, the rationale of surface chemistry has a strong bearing on catalysis research by providing the catalysis researchers in academia and industry with basic concepts which enter the synthesis strategy of current and future catalysts.[843,844]

DFT calculations have become a powerful tool in catalysis research when looking at general trends along the periodic table in order to tailor surfaces with improved catalytic properties. This approach has been put forward by the groups of Nørskov and of Van Santen & Neurock utilizing so-called Brønsted, Polanyi, Evans (BEP) relations[479,481] and identifying proper descriptors.[34,845] The activation energy of a surface reaction parallels the binding energy of the critical surface intermediate species. For instance, the activation barrier in the CO oxidation reaction over TM metal surface is frequently correlated with the adsorption energy of the oxygen on the metal surface. If the metal-O bond is too strong, then the recombination of CO with O is strongly activated.[482] If the metal-O bond is too weak, then oxygen dissociation becomes rate limiting.

Multiscale modeling methods are considered to be the key to deciphering some of the most intricate problems in surface chemistry.[846−849] Processes in catalysis, both heterogeneous and electrocatalysis, take place on several different length- and time-scales so that a combination of theoretical methods is required for a comprehensive description. This combination includes

(1) Ab initio quantum-mechanics (e.g., DFT) to study elementary reaction steps
(2) Molecular mechanics/dynamics to bridge the regime of rather small length- and short time-scales accessible by DFT studies with that of macroscopic scales
(3) "Ab-initio atomistic thermodynamics" approach, which combines quantum-mechanical calculations with thermodynamic concepts to evaluate the structure and stability of gas/catalyst surface under realistic temperatures and pressures
(4) Kinetic Monte Carlo (KMC) to understand the structure and the behavior of catalytic reactions at the gas/catalyst surface at longer time-scales (>1 s)

The ultimate goal of theoretical surface chemistry is to be predictive. But even for simple reaction systems such as the oxidation of CO, NH_3, and HCl over RuO_2(110) the adsorption energies as well as the activation energies for reaction and diffusion do scatter by more than 40 kJ/mol (and henceforth the derived predictions) among various theoretical groups. For more complex surface reactions, where selectivity comes into play, the predictive power of ab initio calculations is even more discouraging. Selectivity is determined by small energy differences of a few meV which are beyond the precision limits of present ab initio calculations. Here experiments are required to guide the first principles calculations. On the other hand, experimental data need frequently appropriate support based on theory. Altogether, I think that (at least) for the near future a close collaboration between experiment and theory is mandatory in order to accomplish new and deep insights into catalytic systems.[267]

11.4. Surface Chemistry versus Electrochemistry, Heterogeneous Catalysis versus Electrocatalysis

The revival of electrochemistry research is driven by current applications in energy storing and energy producing devices including fuel cells, supercapacitors, and batteries. The application of RuO_2 in chemistry is mainly related to electrochemistry as well, in particular electrocatalysis including chlorine and oxygen evolution (CER, OER) with its direct applications in chlor-alkali electrolysis and the water electrolysis, respectively. For RuO_2 being a good electrocatalyst, high electronic conductivity is a major presumption to be fulfilled. RuO_2 bears an electronic conductivity which is as high as that of metallic ruthenium.

dx.doi.org/10.1021/cr200247n | Chem. Rev. 2012, 112, 3356−3426

Similar to heterogeneous catalysis, fundamental insight into electrochemical processes is expected to be gained only if proper model systems with low structural complexity and under well-defined ultra pure reaction conditions are studied in the so-called surface science approach.[686,850,851] A deeper understanding on the atomic scale of the processes at the electrode surface requires the application of in situ techniques. Only when surface chemistry had entered the field of heterogeneous catalysis, the atomic-scale understanding of catalytic processes has been advanced by applying the tool box of surface science techniques.[852] Currently basic understanding of electrocatalysis is boosted by ab initio calculations,[655,670,853−857] although a validation of the theoretical results by modern experiments is required.

In surface chemistry catalytic reactions take place at the interface between a solid and a gas phase (i.e., surface) whose activity and selectivity is controlled by tuning the applied partial pressures and temperature. Electrochemistry, on the other hand, deals with reactions at the electrified solid/liquid interface and, besides temperature, and pressure, the applied electrostatic potential controls the reaction. Regardless of apparent differences of electrochemistry and surface chemistry, many concepts known from heterogeneous catalysis in surface chemistry can either be directly transferred to or at least have apparent analogues in electrocatalysis and vice versa.[655,857] These similarities of electrocatalysis and heterogeneous gas phase catalysis have so far mostly been neglected or underestimated.

A tight connection between surface chemistry and electrochemistry represents a formidable challenge since it demands the ability of the researcher to understand both scientific languages.[41] Recently Keith and Jacob have nicely demonstrated how ab initio theory may be able to bridge the scientific gap between surface science and electrochemistry[687,688] and to deepen our understanding of electrochemical reactions. These authors demonstrated that starting from the surface science approach of water formation on Pt(111) by exposing gaseous oxygen and hydrogen, they were able to gain deep insights into the kinetics of the electrochemical oxygen reduction reaction on Pt(111) model electrodes.

A critical issue of an electrocatalyst is its stability under electrochemical reaction conditions and how to gain information of the underlying processes. For the case of RuO_2-based electrodes the large number of stable oxidation states of Ru atoms makes it quite demanding to study the stability of RuO_2 electrode surface. In particular the analysis of ruthenium leaching into the electrolyte is correlated with the formation of a whole bunch of Ru complexes (→ connection to homogeneous coordination chemistry) depending on the chemical nature of the electrolyte. Quite in contrast, under gas atmosphere ruthenium cannot vaporize easily and the gas phase chemistry of ruthenium is much simpler.

The flexibility of RuO_2 is also indicated in electrocatalysis where RuO_2 is known to be an excellent oxidation catalyst in OER and CER. However, under strongly reducing conditions under electrochemical control hydrous RuO_2 is formed which is able to catalyze such a reducing reaction as HER.[600] Hydrous-RuO_2 may be even more versatile in heterogeneous catalysis than RuO_2, since hydrous RuO_2 is an efficient oxidation catalyst for the CO oxidation (heterogeneous catalysis) even at room temperature without facing poisoning by water.[36] There is a close correlation between the supercapacitance of RuO_2-based electrodes and reactivity, as advocated by Rolison et al. for methanol oxidation in fuel cell applications[40] and by Yu et al.[39] This observation may be of general relevance for the application of hydrous transition metal oxides in heterogeneous catalysis and may be utilized to find new high-performing catalysts in heterogeneous catalysis.

There are particular reactions in electrocatalysis which have direct counterparts in heterogeneous catalysis. For instance, the chlorine evolution reaction (CER) is similar to the HCl oxidation (Deacon process) and the oxygen reduction reaction (ORR) is akin to water formation by O_2 and H_2 exposure from the gas phase, while the oxygen evolution reaction (OER) is the back reaction of the ORR. Most surprisingly RuO_2 is an extraordinarily active catalyst for these pairs of reactions and one could have anticipated that also the involved reaction mechanisms are similar. This is actually not the case, neither for the CER nor for the OER. However, systematic DFT calculations have indicated[658,667] that the O-metal bond strength is a good "descriptor"[34] for searching for a good electrocatalyst and heterogeneous catalyst for both types of oxidation reactions. For the OER[667] and CER,[658] it turned out that RuO_2 reveals the optimum O-metal binding energy, not too strong to poison the catalyst and not too weak to make O adsorption rate limiting (Sabatier principle). The main reason why metal-O is an appropriate descriptor for these catalyzed reactions is that the important reaction intermediates in CER and OER bind in a similar way as oxygen.

AUTHOR INFORMATION

Corresponding Author

*E-mail: herbert.over@phys.chemie.uni-giessen.de.

Notes

The authors declare no competing financial interest.

Biography

Professor Herbert Over studied electrical engineering at the University of Applied Sciences (FH) in Bingen, Germany, and physics as well as mathematics at the Technical University in Berlin, Germany. In 1991 he graduated from the Fritz Haber Institute and received his Ph.D. from the chemistry department at the Free University in Berlin. Following a postdoctoral appointment at the physics department in Milwaukee (UWM) he jointed the FHI in Berlin (Prof. Dr. G. Ertl), in 1993, where he completed his habilitation in physical chemistry (Free University Berlin) in 1996. In 2001 he became permanent research associate at the Max Planck Institute for solid state research in Stuttgart, Germany, building up a new scientific service group "Surface Analysis". In 2002 he was appointed C3 Professor at the Justus Liebig University in Gießen (Chemistry Department, Physical Chemistry). His current research interests focus on an atomistic understanding of

elementary reaction steps on transition metal (oxide) surfaces and how this knowledge can be applied in model systems of heterogeneous- and electrocatalysis.

ACKNOWLEDGMENTS

The author is grateful to all group members and collaborators, past and present, who contributed to the research described and referenced in this review article. In particular, I thank Dr. Attila Farkas for critical comments on and proofreading of the manuscript, Prof. Dr. Timo Jacob and Prof. Dr. Sebastian Fiechter for valuable comments on the electrocatalysis part, Prof. Dr. Edvin Lundgren for providing me recent results on the oxidation of Pd(110), and Dr. Johan Gustafson for providing me Figure 22. I thank Philipp Krause and Stefan Rohrlack for their great help in figure design and Franziska Hess for providing me providing me unpublished DFT calculations. My group has run a fruitful long-term collaboration with Dr. Ari Seitsonen over the past 15 years, best described as "Intimate Interplay of Theory and Experiments in Model Catalysis";[267] thanks a lot for this inspiring time. Financial support from the DFG, BMBF, and EU and computing time from LRZ Munich and HRZ Darmstadt is gratefully acknowledged.

ACRONYMS

ASAXS	anomalous small angle X-ray scattering
BEP relation	Brønsted, Polanyi, Evans relation
CER, ClER	chlorine evolution reaction
CLS	core level shift
cus	coordinatively unsaturated sites; 1f-cus, 2f-cus: one-fold or 2-fold coordinatively unsaturated sites
CV	cyclic voltammetry
CVD	chemical vapor deposition
c(2×2)	centered 2×2 structure
DSA	dimensional stable anode(s)
DFT	density functional theory
DOS	density of states
DMFC	direct methanol fuel cell
DRAM	dynamic random access memory
DRIFTS	diffuse reflection infrared Fourier transform spectroscopy
EC	electrochemistry
EC-STM	electrochemical STM
EUVL	extreme ultraviolet lithography
EXAFS	extended X-ray absorption fine structure
FeRAM	Ferro electric random access memory
FTIR	Fourier transform infrared
GGA	generalized gradient approximation
HER	hydrogen evolution reaction
HP-XPS	high-pressure XPS
HRCLS	high resolution core level shift spectroscopy
HREELS	high resolution electron energy loss spectroscopy
HRTEM	high resolution transmission electron microscopy
KMC	kinetic Monte Carlo
L	Langmuir, 1 L is the gas phase exposure, when 1.33×10^{-6} mbar of gas is introduced into the chamber for one second
LDA	local density approximation
LEED	low energy electron diffraction
LEEM	low energy electron microscopy
MC	Monte Carlo
ML	monolayer = number of adsorbed atoms relative to the number of substrate atoms in the topmost layer
MBE	molecular beam epitaxy
MO	molecular orbital
MOCVD	metal−organic chemical vapor deposition
NHE	standard hydrogen electrode: E_0 = 0.000 V for a proton activity of a (H^+) = 1
NMR	nuclear magnetic resonance
OER	oxygen evolution reaction
ORR	oxygen reduction reaction
PMEFC	polymer membrane electrolyte fuel cells
PEEM	photoelectron emission microscopy
PGM	platinum group metals
PLD	pulse laser deposition
PZC	point of zero charge
RAIRS	reflection adsorption infrared spectroscopy
rds	rate determining step
RHE	reversible hydrogen electrode: E_0 = 0.000−0.059*pH
SANS	small angle neutron scattering
SCE	saturated calomel electrode
SEM	scanning electron microscopy
SPEM	scanning photoelectron emission microscopy
STM	scanning tunneling microscopy
SXRD	surface X-ray diffraction
TAP	temporal analysis of products
TEM	transmission electron microscopy
TGA	thermogravimetric analysis
TOF	turnover frequency = number of produced molecules per second and active site
TPD	temperature programmed desorption
TPR	temperature programmed reaction/reduction
TSO	transient surface oxide
UHV	ultra high vacuum
UPS	ultraviolet photoelectron spectroscopy
XANES	X-ray absorption near edge spectroscopy
XPS	X-ray photoemission spectroscopy
XRD	X-ray diffraction

REFERENCES

(1) Rard, J. A. *Chem. Rev.* **1985**, *85*, 1.
(2) Seddon, E. A.; Seddon, K. R. *The Chemistry of Ruthenium*; Elsevier: Amsterdam, 1984.
(3) Higgins, S. *Nat. Chem.* **2010**, *2*, 1100.
(4) Olivier, C.; Costuas, K.; Choua, S.; Maurel, V.; Turek, P.; Saillard, J.-Y.; Touchard, D.; Rigaut, S. *J. Am. Chem. Soc.* **2010**, *132*, 5632.
(5) Mallat, T.; Baiker, A. *Chem. Rev.* **2004**, *104*, 3037.
(6) Naoto, T.; Takaya, H.; Murahashi, S.-I. *Chem. Rev.* **1998**, *98*, 2599.
(7) Hinrichsen, O.; Rosowski, F.; Muhler, M.; Ertl, G. *Chem. Eng. Sci.* **1996**, *51*, 1683.
(8) Honkala, K.; Hellman, A.; Remediakis, I. N.; Logadottir, A.; Carlsson, A.; Dahl, S.; Norskov, J. K. *Science* **2005**, *307*, 555.
(9) Over, H.; Kim, Y. D.; Seitsonen, A. P.; Wendt, S.; Lundgren, E.; Schmid, M.; Varga, P.; Morgante, A.; Ertl, G. *Science* **2000**, *287*, 1474−1476.
(10) Trasatti, S. *Electrochim. Acta* **2000**, *45*, 2377.
(11) Lutz, A.; Heubach, D.; Lang-Koetz, C. Report, BMBF Research Project ColoSol, Fraunhofer-Institut für Arbeitswirtschaft und Organisation: Stuttgart, Germany, 2007.
(12) http://www.infomine.com/chartsanddata/ Retrieved: 2Dec2011.
(13) Johnson Matthey reports "Platiunum 2010", http://www.platinum.matthey.com/uploaded_files/Int2010/int10_other_platinum_group_metals.pdf

(14) Ertl, G. *Angew. Chem., Int. Ed.* **2008**, *47*, 3524.
(15) Savchenko, V. I.; Boreskov, G. K.; Kalinkin, A. V.; Salanov, A. N. *Kinet. Catal.* **1984**, *24*, 983.
(16) Cant, N. W.; Hicks, P. C.; Lennon, B. S. *J. Catal.* **1978**, *54*, 372−379.
(17) Kiss, J. T.; Gonzalez, R. D. *J. Phys. Chem.* **1984**, *88*, 892.
(18) Peden, C. H. F.; Goodman, D. W. *J. Phys. Chem.* **1986**, *90*, 1360.
(19) Hendriksen, B. L. M.; Frenken, J. W. M. *Phys. Rev. Lett.* **2002**, *89*, 46101.
(20) Gustafson, J.; Westerstrom, R.; Resta, A.; Mikkelsen, A.; Andersen, J. N.; Balmes, O.; Torrelles, X.; Schmid, M.; Varga, P.; Hammer, B.; Kresse, G.; Baddeley, C. J.; Lundgren, E. *Catal. Today* **2009**, *145*, 227.
(21) Over, H. *Appl. Phys. A: Mater. Sci. Process.* **2002**, *75*, 37.
(22) Linsebigler, A. L.; Lu, G. Q.; Yates, J. T. *Chem. Rev.* **1995**, *95*, 735.
(23) Diebold, U. *Surf. Sci. Rep.* **2003**, *48*, 53.
(24) Dohnalek, Z.; Lyubinetsky, I.; Rousseau, R. *Prog. Surf. Sci.* **2010**, *85*, 161.
(25) Pang, C. L.; Lindsay, R.; Thornton, G. *Chem. Soc. Rev.* **2008**, *37*, 2328.
(26) Seki, K. *Catal. Surv. Asia* **2010**, *14*, 168.
(27) Yamaguchi, K.; Mizuno, N. *Angew. Chem.* **2003**, *115*, 1518.
(28) Liu, H.; Iglesia, E. *J. Phys. Chem. B* **2005**, *109*, 2155−2163.
(29) Cui, X.; Zhou, J.; Ye, Z.; Chen, H.; Li, L.; Ruan, M.; Shi, J. *J. Catal.* **2010**, *270*, 310.
(30) Pan, H. Y.; Minet, R. G.; Benson, S. W.; Trotsis, T. T. *Ind. Eng. Chem. Res.* **1994**, *33*, 2996.
(31) Seki, K.; Iwanaga, K.; Hibi, T. Improved hydrogen chloride oxidation process: Characterization of the RuO_2/TiO_2 catalyst, Abstracts of Papers, 229th ACS National Meeting, San Diego, CA, United States, March 13−17, 2005, INOR-233; American Chemical Society: Washington.
(32) Deacon, H. U.S. Patent 1868,85,370.
(33) Stamenkovic, V. R.; Fowler, B.; Mun, R. S.; Wang, G.; Ross, P. N.; Lucas, C. A.; Markovic, N. M. *Science* **2007**, *315*, 493.
(34) Norskov, J. K.; Bligaard, T.; Rossmeisl, J.; Christensen, C. H. *Nat. Chem.* **2009**, *1*, 37.
(35) Conway, B. E. *J. Electrochem. Soc.* **1991**, *138*, 1539.
(36) Zang, L.; Kisch, H. *Angew. Chem.* **2000**, *112*, 4075; *Angew. Chem., Int. Ed.* **2000**, *39*, 3921.
(37) Rolison, D. R. *Science* **2003**, *299*, 1698.
(38) Yamaguchi, K.; Kim, J. W.; He, J.; Mizuno, N. *J. Catal.* **2009**, *268*, 343.
(39) Yu, H.; Fu, X.; Zhou, C.; Peng., F.; Wang, H.; Yang, J. *Chem. Commun.* **2009**, 2408.
(40) Rolison, D. R.; Gagans, P. L.; Swider, K. E.; Long, J. W. *Langmuir* **1999**, *15*, 774.
(41) Bockris, J. O'M; Reddy, A. K. N. *Modern Chemistry 2, A Plenum/Rosetta Edition* **1973**, 883.
(42) Trasatti, S. In *Handbook of Fuel Cells-Fundamentals, Technology and Applications*;Vielstich, W., Gasteiger, H. A., Lamm, A., Eds.; John Wiley & Sons: New York, 2003; Vol 2: Electrocatalysis, p 79.
(43) Cotton, F. A.; Wilkinson, G.; Murillo, C. A.; Bachmann, M. *Advanced Inorganic Chemistry*; John Wiley & Sons, Inc: New York, 1999.
(44) Mar, S. Y.; Chen, C. S.; Huang, Y. S.; Tiong, K. K. *Appl. Surf. Sci.* **1995**, *90*, 497.
(45) Trasatti, S.; Lodi, G. In *Electrodes of Conductive Metallic Oxides Anodes, Part B*; Trasatti, S., Ed.; Elsevier: Amsterdam, 1981; p 521.
(46) Schafer, H. *Chemical Transport Reactions*; Academic Press: New York, 1964.
(47) Horkans, J.; Shafer, M. W. *J. Electrochem. Soc.* **1977**, *124*, 1202.
(48) Burke, L. D.; Murphy, O. J.; O'Neill, J. F. *J. Electroanal. Chem.* **1977**, *81*, 391.
(49) Hollemann, A. F.; Wiberg, E. *Lehrbuch der Anorganischen Chemie*; Walter de Gruyter: Berlin, 1995; p 1538.
(50) Reuter, K.; Scheffler, M. *Phys. Rev. B* **2001**, *65*, 035406.
(51) Wang, H.; Schneider, W. F. *J. Chem. Phys.* **2007**, *127*, 064706.
(52) Grillo, M. E. *Phys. Rev. B* **2004**, *70*, 184115.
(53) Delheusy, M.; Stierle, A.; Zweidinger, S.; Over, H.; Dosch, H. Unpublished SXRD experiments of the low temperature oxidation of Ru(0001), 2011.
(54) Huang, Y. S.; Park, H. L.; Pollak, F. H. *Mater. Res. Bull.* **1982**, *17*, 1305.
(55) Rao, K. V. K.; Iyengar, L. *Acta Crystallogr. A* **1969**, *25*, 302.
(56) Haines, J.; Leger, J. M.; Schulte, O. *Science* **1996**, *271*, 629.
(57) Lundin, U.; Fast, L.; Nordstrom, L.; Johansson, B.; Wills, J. M.; Eriksson, O. *Phys. Rev. B* **1998**, *57*, 4979.
(58) Tse, J. S.; Klug, D. D.; Uehara, K.; Li, Z. Q.; Haines, J.; Leger, J. M. *Phys. Rev. B* **2000**, *61*, 10029.
(59) Ryden, W. D.; Lawson, A. W.; Sartain, C. C. *Phys. Rev. B* **1970**, *4*, 1494.
(60) Vadimsky, R. G.; Frankenthal, R. P.; Thompson, D. E. *J. Electrochem. Soc.* **1979**, *126*, 2017.
(61) Triggs, P. *Helv. Phys. Acta* **1985**, *58*, 657.
(62) Soratin, P. I.; Schwarz, K. *Inorg. Chem.* **1992**, *31*, 567.
(63) Cox, P. A. *Transition Metal Oxides: an Introduction to Their Electronic Structure and Properties*; Oxford University Press: Oxford, 1995.
(64) Graebner, J. E.; Greiner., E. S.; Ryden., W. D. *Phys. Rev. B* **1976**, *13*, 2426.
(65) Mattheis, L. F. *Phys. Rev. B* **1976**, *13*, 2433.
(66) Yavorsky, B. Y.; Krasovska, O. V.; Krasovskii, E. E.; Yaresko, A. N.; Anatonov, V. N. *Physica B* **1996**, *225*, 243.
(67) Marcus, S. M.; Butler, S. R. *Phys. Lett. A* **1968**, *26*, 518.
(68) Marcus, S. M. *Phys. Lett. A* **1968**, *28*, 191.
(69) Slivka, R. T.; Langenberg, D. N. *Phys. Lett. A* **1968**, *28*, 169.
(70) (a) Over, H.; Seitsonen, A. P.; Lundgren, E.; Smedh, M.; Andersen, J. N. Unpublished valence PES experiments of $RuO_2(110)$, 2000. (b) Seitsonen, A. P. Unpublished DFT calculations of DOS of $RuO_2(110)$, 2011.
(71) Riga, J.; Tenret-Noel, C.; Pireaux, J. J.; Caudano, R.; Verbist, J. J.; Gobillon, Y. *Phys. Scr.* **1977**, *16*, 351.
(72) Beatham, N.; Orchard, A. F. *J. Electron Spectrosc. Relat. Phenom.* **1979**, *16*, 77.
(73) Daniela, R. R.; Margaritondo, G.; Georg, C.-A.; Levy, F. *Phys. Rev. B.* **1984**, *29*, 1813.
(74) Cox, P. A.; Goodenough, J. B.; Tavener, P. J.; Telles, D.; Edgell, R. G. *J. Solid State Chem.* **1986**, *62*, 360.
(75) Kötz, R.; Stucki, S. *Electrochim. Acta* **1986**, *31*, 1311.
(76) Xu, J. H.; Jarlborg, T.; Freeman, A. J. *Phys. Rev. B* **1989**, *40*, 7939.
(77) (a) Glassford, K. M.; Chelikowsky, J. R. *Phys. Rev. B* **1993**, *47*, 1732. (b) Glassford, K. M.; Chelikowsky, J. R. *Phys. Rev. B* **1993**, *47*, 12550.
(78) Wu, R.; Weber, W. H. *J. Phys.: Condens. Matter* **2000**, *12*, 6725.
(79) de Almeida, J. S.; Ahuja, R. *Phys. Rev. B* **2006**, *73*, 165102.
(80) Di Valentin, C.; Pacchioni, G.; Selloni, A. *Phys. Rev. Lett.* **2006**, *97*, 166803.
(81) Papageorgiou, A. C.; Geglitis, N. S.; Pang, C. L.; Teobaldi, G.; Cabailh, G.; Chen, Q.; Fisher, A. J.; Hofer, W. A.; Thornton, G. *Proc. Natl. Acad. Sci. U.S.A.* **2010**, *107*, 2391.
(82) Jean, Y.; Volatron, F.; Burdett, J. *An Introduction to Molecular Orbitals*; Oxford University Press: New York, 1993; p 192.
(83) Goel, A. K.; Skorinko, G.; Pollak, F. H. *Phys. Rev. B* **1981**, *24*, 7342.
(84) Mondio, G.; Neri, F.; Allegrini, M. *J. Appl. Phys.* **2000**, *39*, 2083.
(85) Krasovska, O. V.; Karsockii, E. E.; Antonov, V. V. *Phys. Rev. B* **1995**, *52*, 11825.
(86) Over, H.; Seitsonen, A. P.; Lundgren, E.; Smedh, M.; Andersen, J. N. *Surf. Sci.* **2002**, *504*, L196.
(87) Böttcher, A.; Starke, U.; Conrad, H.; Blume, R.; Niehus, H.; Gregoratti, L.; Kaulich, B.; Barinov, A.; Kiskinova, M. *J. Chem. Phys.* **2002**, *117*, 8104.
(88) Foelske, A.; Barbieri, O.; Hahn, M.; Kötz, R. *Electrochem. Sol. Stat. Lett.* **2006**, *9*, A268.

(89) Over, H.; Seisonen, A. P.; Lundgren, E.; Wiklund, M.; Andersen, J. N. *Chem. Phys. Lett.* **2001**, *342*, 467.
(90) Kim, Y. J.; Gao, Y.; Chambers, S. A. *Appl. Surf. Sci.* **1997**, *120*, 250.
(91) Huang, Y. S.; Pollak, F. H. *Solid State Commun.* **1982**, *43*, 921.
(92) Rosenblum, S. S.; Weber, W. H.; Chamberland, B. L. *Phys. Rev. B* **1997**, *56*, 529.
(93) Bohnen, K.-P.; Heid, R.; de la Pena Seaman, O.; Renker, B.; Adelmann, P.; Schober, H. *Phys. Rev. B* **2007**, *75*, 092301.
(94) Lee, D. G.; Van den Engh, M. *Can. J. Chem.* **1972**, *50*, 2000.
(95) Kötz, R.; Stucki, S.; Scherson, D.; Kolb, D. M. *J. Electroanal. Chem.* **1984**, *172*, 211.
(96) Snels, M.; Sassi, M. P.; Quack, M. *Mol. Phys.* **1991**, *72*, 145.
(97) Bewick, A.; Guitierrez, C.; Larramona, G. *J. Electronanal. Chem.* **1992**, *332*, 155.
(98) Bell, W. E.; Tagami, M. *J. Phys. Chem.* **1963**, *67*, 2432.
(99) Lewerenz, H. J.; Stucki, S.; Kotz, R. *Surf. Sci.* **1983**, *126*, 893.
(100) Nishiyama, I.; Oizumi, H.; Motai, K.; Izumi, A.; Ueno, T.; Akiyama, H.; Namiki, A. *J. Vac. Sci. Technol. B* **2005**, *23*, 3129.
(101) Chan, H. Y.; Takoudis, C. G.; Weaver, M. J. *J. Catal.* **1997**, *172*, 336.
(102) Iwasaki, Y.; Izumi, A.; Tsurumaki, H.; Namiki, A.; Oizumi, H.; Nishiyama, I. *Appl. Surf. Sci.* **2007**, *253*, 8699.
(103) Kim, Y. D.; Over, H.; Krabbes, G.; Ertl, G. *Top. Catal.* **2001**, *14*, 95.
(104) Atanasoska, Lj.;; O'Grady, W. E.; Atanasoski, R. T.; Pollak, F. H. *Surf. Sci.* **1988**, *202*, 142.
(105) Krause, P. P. T.; Farkas, A.; Lin, C.; Over, H. Unpublished Raman experiments of RuO_2 single crystals, which were grown in Dr. C. Lin's group at the Max Planck Institute for Solid State Research in Stuttgart, 2011.
(106) Narkhede, V.; Aßmann, J.; Muhler, M. *Z. Phys. Chem.* **2005**, *219*, 979.
(107) Assmann, J.; Narkhede, V.; Breuer, N. A.; Muhler, M.; Seitsonen, A. P.; Knapp, M.; Crihan, D.; Farkas, A.; Mellau, G.; Over, H. *J. Phys.: Condens. Matter* **2008**, *20*, 184017.
(108) Knapp, M.; Korte, C.; Over, H. Unpublished scanning electron microscopy images of micro-crystalline RuO_2 powder. The orientations of the facets were determined by using electron back scattering diffraction, 2008.
(109) He, Y. B.; Knapp, M.; Lundgren, E.; Over, H. *J. Phys. Chem.* **2005**, *109*, 21825.
(110) Kim, Y. D.; Schwegmann, S.; Seitsonen, A. P.; Over, H. *J. Phys. Chem B* **2001**, *105*, 2205.
(111) Zhang, H. J.; Lu, B.; Lu, Y. H.; Xu, Y. F.; Li, H. Y.; Bao, S. N.; He, P. *Surf. Sci.* **2007**, *601*, 2297.
(112) Over, H.; Seitsonen, A. P.; Knapp, M.; Lundgren, E.; Schmid, M.; Varga, P. *Chem. Phys. Chem.* **2004**, *5*, 167.
(113) Rizzi, G. A.; Magrin, A.; Granozzi, G. *Surf. Sci.* **1997**, *443*, 277.
(114) Chambers, S. A. *Adv. Mater.* **2010**, *22*, 219.
(115) Meier, D. C.; Rizzi, G. A.; Granozzi, G.; Lai, X.; Goodman, D. W. *Langmuir* **2002**, *18*, 698.
(116) Zhao, X. Y.; Hrbek, J.; Rodriguez, J. A. *Surf. Sci.* **2005**, *575*, 115.
(117) Bajt, S.; Alameda, J. B.; Barbee, T. W. Jr.; Clift, W. M.; Folta, J. A.; Kaufman, B.; Spiller, E. *A. Opt. Eng.* **2002**, *41*, 1797.
(118) He, Y. B.; Goriachko, A.; Korte, C.; Farkas, A.; Mellau, G.; Dudin, P.; Gregoriatti, L.; Barinov, A.; Kiskinova, M.; Stierle, A.; Kasper, N.; Bajt, S.; Over, H. *J. Phys. Chem. C* **2007**, *111*, 10988.
(119) Kelly, P. J.; Arnell, R. D. *Vacuum* **2000**, *56*, 159.
(120) Hsu, C. C.; Coburn, J. W.; Graves, D. B. *J. Vac. Sci. Technol. A* **2006**, *24*, 1.
(121) Yunogami, I.; Nojiri, K. *J. Vac. Sci. Technol. B* **2000**, *18*, 1911.
(122) Kim, J. H.; Lee, J. H.; Kato, H.; Horimoto, N.; Kawai, M.; Lee, Y. S. *J. Korean Phys. Soc.* **2003**, *42*, 408.
(123) Abe, Y.; Kawamura, M.; Sasaki, K. *Jpn. J. Appl. Phys.* **2002**, *41*, 6857.
(124) Oh, S. H.; Park, C. G.; Park, C. *Thin Sol. Films* **2000**, *359*, 118.
(125) Battaglin, G.; Rigato, V.; Zndolin, S.; Benedetti, A.; Ferro, S.; Nanni, L.; De Battisti, A. *Chem. Mater.* **2004**, *16*, 946.
(126) Kolawa, E.; So, F. C. T.; Flick, W.; Zhao, X.-A.; Pan, E.T.-S.; Nicolet, M.-A. *Thin Sol. Films* **1989**, *173*, 217.
(127) Green, M. L.; Gross, M. E.; Papa, L. E.; Schones, K. J.; Brasen, D. *J. Electrochem. Soc.* **1985**, *132*, 2677.
(128) Si, J.; Desu, S. B. *J. Mat. Res.* **1993**, *8*, 2644.
(129) Takagi, T.; Oizuki, I.; Kobuyashi, I.; Okada, M. *Jpn. J. Appl. Phys.* **1995**, *34*, 4104.
(130) Liao, P. C.; Mar, S. Y.; Ho, W. S.; Huang, Y. S.; Tiong, K. K. *Thin Sol. Films* **1996**, *287*, 74.
(131) Bai, G.-R.; Wang, A.; Foster, C. M.; Vetrone, J. *Thin Sol. Films* **1997**, *310*, 75.
(132) Kim, J. J.; Jung, D. H.; Kim, M. S.; Kim, S. H.; Yoon, D. Y. *Thin Sol. Films* **2002**, *409*, 28.
(133) Yuan, Z.; Puddlephatt, R. J.; Sayer, M. *Chem. Mater.* **1993**, *5*, 908.
(134) Han, J. H.; Lee, S. W.; Choi, G.-J.; Lee, S. Y.; Hwang, C. S.; Dussarat, C.; Gatineau, J. *Chem. Mater.* **2009**, *21*, 207.
(135) Han, J. H.; Lee, S. W.; Kim, S. K.; Han, S.; Hwang, C. S.; Dussarat, C.; Gatineau, J. *Chem. Mater.* **2010**, *22*, 5700.
(136) Kleinmann-Shwarsctein, A.; Laursen, A. B.; Cavalcy, F.; Tang, W.; Dahl, S.; Chorckendorff, I. *Chem. Commun.* **2012**, *48*, 967.
(137) Bhaskar, S.; Majumder, S. B.; Dobal, P. S.; Katiyar, R. S.; Morales Cruz, A. L.; Fachini, E. R. *Mater. Res. Soc. Symp. Proc.* **2000**, *606*, 69.
(138) Bhaskar, S.; Dobal, P. S.; Majumder, S. B.; Katiyar, R. S. *J. Appl. Phys.* **2001**, *89*, 2987.
(139) Yi, J. H.; Thomas, P.; Manier, M.; Mersurio, J. P. *J. Phys. IV France* **1998**, *8*, 45.
(140) Aparicio, M.; Klein, L. C. *J. Sol-Gel Sci. Technol.* **2004**, *29*, 81.
(141) Armelao, L.; Barreca, D.; Moraru, B. *J. Non-Crystal. Sol.* **2003**, *316*, 364.
(142) Jia, Q. X.; Shi, Z. Q.; Jiao, K. L.; Anderson, W. A.; Colins, F. M. *Thin. Sol. Films* **1991**, *196*, 29.
(143) Over, H.; He, Y. B.; Farkas, A.; Mellau, G.; Korte, C.; Knapp, M.; Chandhok, M.; Fang, M. *J. Vac. Sci. Technol. B* **2007**, *25*, 1123.
(144) Fang, X.; Tachiki, M.; Kobayashi, T. *Jpn. J. Appl. Phys.* **1997**, *36*, L511.
(145) Hiratani, M.; Matsui, Y.; Imagawa, K.; Kimura, S. *Thin Sol. Films* **2000**, *366*, 102.
(146) Gsell, S.; Fischer, M.; Schreck, M.; Stritzker, B. *J. Cryst. Growth* **2009**, *311*, 3731.
(147) Zhitomirsky, I.; Gal-Or, L. *Mater. Lett.* **1997**, *31*, 155.
(148) Hu, C.-C.; Chang, K.-H. *Electrochim. Acta* **2000**, *45*, 2685.
(149) Aaltonen, T.; Alen, P.; Ritala, M.; Leselä, M. *Chem. Vap. Dep.* **2003**, *9*, 45.
(150) Kim, S. K.; Lee, S. W.; Han, J. H.; Lee, B.; Han, S.; Hwang, C. S. *Adv. Mater.* **2010**, *20*, 2989.
(151) Kim, J.-H.; Kil, D.-S.; Yeom, A.-J.; Roh, J.-S.; Kwak, N.-J.; Kim, J.-W. *Appl. Phys. Lett.* **2007**, *91*, 052908.
(152) Wang, H.; Alvis, R.; Ulfrig, R. M. *Chem. Vap. Dep.* **2009**, *15*, 312.
(153) Husekova, K.; Dobrocka, E.; Rosova, A.; Soltys, J.; Satka, A.; Fillot, F.; Fröhlich, K. *Thin Solid Films* **2010**, *518*, 4701.
(154) Bielawa, H.; Hinrichsen, O.; Birkner, A.; Muhler, M. *Angew. Chem. Intl. Ed.* **2001**, *40*, 1061.
(155) Rosowski, F.; Hornung, A.; Hinrichsen, O.; Herein, D.; Muhler, M.; Ertl, G. *Appl. Catal., A* **1997**, *151*, 443.
(156) Murata, S.; Aika, K. *J. Catal.* **1992**, *136*, 118.
(157) Rossetti, N.; Forni, L. *Appl. Catal. A: Gen* **2005**, *282*, 315.
(158) Hansen, T. W.; Hansen, P. L.; Dahl, S.; Jacobsen, C. J. H. *Catal. Lett.* **2002**, *84*, 7.
(159) Zheng, Y.; Li, Z. H.; Yu, H. Y.; Wang, R.; Wie, K. M. *J. Mol. Catal. A: Chem.* **2009**, *301*, 79.
(160) Seetharamulu, P.; Reddy, K. H. P.; Padmasri, A. H.; Rao, K. S. R.; Raju, B. D. *Catal. Today* **2009**, *141*, 94.
(161) Aßmann, J.; Löffler, E.; Birkner, A.; Muhler, M. *Catal. Today* **2003**, *85*, 235.
(162) Aßmann, J.; Narkhede, V.; Löffler, E.; Hinrichsen, O.; Over, H.; Muhler, M. *J. Phys. Chem. B* **2004**, *108*, 14634−14642.

(163) Rossi, L. M.; Dupont, J.; Machado, G.; Fichtner, P. F. P.; Radtke, C.; Baumvol, I. J. R.; Teixeira, S. R. *J. Braz. Chem. Soc.* **2004**, *15*, 904.
(164) Vidoni, O.; Philippot, K.; Amiens, C.; Chaudret, B.; Balmes, O.; Malm, J. O.; Bovin, J. Q.; Senocq, F.; Casanove, M. J. *Angew. Chem., Int. Ed.* **1999**, *38*, 3736.
(165) Miyazaki, A.; Balint, L.; Aika, K.; Nakano, Y. *J. Catal.* **2001**, *204*, 364.
(166) Kurihara, L. K.; Chow, G. M.; Schoen, P. E. *Nanostruct. Mater.* **1995**, *5*, 607.
(167) Zhan, B.-Z.; White, M. A.; Sham, T.-K.; Pincock, J. A.; Doucet, R. J.; Rao, K. V. R.; Robertson, K. N.; Cameron, T. S. *J. Am. Chem. Soc.* **2003**, *125*, 2195.
(168) Zhan, B.-Z.; White, M. A.; Pincock, J. A.; Robertson, K. N.; Cameron, T. S.; Sham, T.-K. *Can. J. Chem.* **2003**, *81*, 764.
(169) Altwasser, S.; Glaser, R.; Lo, A. S.; Liu, P. H.; Chao, K. J.; Weitkamp, J. *Microporous Mesoporous Mater.* **2006**, *89*, 109.
(170) Zhan, B.-Z.; Iglesia, E. *Angew. Chem., Int. Ed.* **2007**, *46*, 3697.
(171) Joo, S. H.; Park, J. Y.; Renzas, J. R.; Butcher, D. R.; Huang, W.; Somorjai, G. A. *Nano Lett* **2010**, *10*, 2709.
(172) Macak, J. M.; Tsuchiya, H.; Ghicov, A.; Yasuda, K.; Hahn, R.; Bauer, S.; Schmuki, P. *Curr. Opin. Solid State Mat. Sci.* **2007**, *11*, 3.
(173) Fan, H. J.; Gosele, U.; Zacharias, M. *Small* **2007**, *3*, 1660.
(174) Kim, M. H.; Lee, B.; Lee, S.; Larson, C.; Baik, J. M.; Yavuz, C. T.; Seifert, S.; Vajda, S.; Winans, R. E.; Moskovits, M.; Stucky, G. D.; Wodtke, A. M. *Nano Lett.* **2009**, *9*, 4138.
(175) Hsieh, C.-S.; Tsai, D.-S.; Chen, R.-S.; Huang, Y.-S. *Appl. Phys. Lett.* **2004**, *85*, 3860.
(176) Chen, C. C.; Chen, R. S.; Tsai, T. Y.; Huang, Y. S.; Tsai, D. S.; Tiong, K. K. *J. Phys.: Conden. Matt.* **2004**, *16*, 8475.
(177) Korotcov, A.; Huang, Y.-S.; Tsai, T.-Y.; Tsai, D.-S.; Tiong, K.-K. *Nanotechnology* **2006**, *17*, 3149.
(178) Satishkumar, B. C.; Govindaraj, A.; Nath, M.; Rao, C. N. R. *J. Mater. Chem.* **2000**, *10*, 2115.
(179) Chu, S.-Z.; Wada, K.; Inoue, S.; Hishita, S.-I.; Kurashima, K. *J. Phys. Chem. B* **2003**, *107*, 10180.
(180) Lin, Y.-T.; Chen, C.-Y.; Hsiung, C.-P.; Cheng, K.-W.; Gan, J.-Y. *Appl. Phys. Lett.* **2006**, *89*, 063123.
(181) Chueh, Y.-L.; Hsieh, C.-H.; Chang, M.-T.; Chou, L. J.; Lao, C. S.; Song, J. H.; Gan, J.-Y.; Wang, Z.-L. *Adv. Mater.* **2007**, *19*, 143.
(182) Cheng, K. W.; Lin, Y. T.; Chen, C. Y.; Hsiung, C. P.; Gan, J. Y.; Yeh, J. W.; Hsieh, C. H.; Chou, L. J. *Appl. Phys. Lett.* **2006**, *88*, 043115.
(183) Ducati, C.; Dawson, D. H.; Saffell, J. R.; Midgley, P. A. *Appl. Phys. Lett.* **2004**, *22*, 5385.
(184) Chen, C. A.; Chen, Y. M.; Chen, K. Y.; Chi, J. K.; Huang, Y. S.; Tsai, D. S. *J. Alloys Compd.* **2009**, *485*, 524.
(185) Liu, Y.-L.; Wu, Z.-Y.; Lin, K.-J.; Huang, J.-J.; Lin, Y.-H.; Jian, W.-B.; Lin, J.-J. *Appl. Phys. Lett.* **2007**, *90*, 013105.
(186) Chen, Y. M.; Korotcov, A.; Hsu, H. P.; Huang, Y. S.; Tsai, D. S. *New J. Phys.* **2007**, *9*, 130.
(187) Zhang, B.; Zhang, C.; He, H.; Yu, Y.; Wang, L.; Zhang, J. *Chem. Mater.* **2010**, *22*, 4056.
(188) Hu, Y.-S.; Guo, Y.-G.; Sigle, W.; Hore, S.; Balaya, P.; Maier, J. *Nat. Mat.* **2006**, *5*, 713.
(189) Balaya, P.; Li, H.; Kienle, L.; Maier, J. *Adv. Funct. Mater.* **2003**, *13*, 621.
(190) Shen, W.; Shi, J.; Chen, H.; Gu, J.; Zhu, Y.; Dong, X. *Chem. Lett.* **2005**, *34*, 390.
(191) Ruan, J. V.; Berry, A. D.; Anderson, M. L.; Long, J. W.; Stroud, R. M.; Cepak, V. M.; Browning, V. M.; Rolison, D. R.; Merzbacher, C. I. *Nature* **2000**, *406*, 169.
(192) Viswanathamurthi, P.; Bhattarai, N.; Kim, C. K.; Kim, H. Y.; Lee, D. R. *Inorg. Chem. Commun.* **2004**, *7*, 679.
(193) Ostermann, R. Ph.D. Thesis, *Design and Physica-Chemical Characterization of Nanowires and Multicomponent Metal Oxide Films with Tailored Mesostructure and Crystallinity*; JLU: Gießen, 2011. http://geb.uni-giessen.de/geb/volltext/2011/8086.
(194) Chang, K.-H.; Hu, C.-C. *J. Electrochem. Soc.* **2004**, *151*, A958.
(195) Zheng, P. J.; Cygan, P. J.; Jow, T. R. *J. Electrochem. Soc.* **1995**, *142*, 2699.
(196) Conway, B. E. *Electrochemical Supercapacitors: Scientific Fundamentals and Technological Applications*; Kluwer Academic: New York, 1999.
(197) Hu, C.-C.; Chang, K.-K.; Lin, M.-C.; Wu, Y.-T. *Nano Lett.* **2006**, *6*, 2690.
(198) Chang, K. H.; Hu, C. C. *Appl. Phys. Lett.* **2006**, *88*, 193102.
(199) Jirkovsky, J.; Hoffmannova, H.; Klementoca, M.; Krtil, P. *J. Electrochem. Soc.* **2006**, *153*, E111.
(200) Lopez, N.; Gomez-Segura, J.; Marin, R. P.; Perez-Ramirez, J. *J. Catal.* **2008**, *255*, 29.
(201) Trasatti, S.; Lodi, G. In *Conductive Metal Oxides*; Trasatti, S., Ed.; Elsevier: Amsterdam, 1980; Vol. A; p 338.
(202) Komeyama, K.; Shohji, S.; Onoue, S.; Nishimura, K.; Yahikozawa, K.; Takasu, Y. *J. Electrochem. Soc.* **1993**, *140*, 1034.
(203) Panic, V.; Dekanski, A.; Milonjic, S.; Atanasoski, R.; Nikolic, B. *Colloids Surf. A* **1999**, *157*, 269.
(204) Panic, V.; Dekanski, A.; Milonjic, S.; Atanasoski, R.; Nikolic, B. *Electrochim. Acta* **2000**, *46*, 415.
(205) Aromaa, J.; Forsen, O. *Electrochim. Acta* **2006**, *51*, 6104.
(206) Zhitomirsky, I. *J. Mat. Sci.* **1999**, *34*, 2441.
(207) Zhitomirsky, I. *Adv. Colloid Interface Sci.* **2002**, *97*, 279.
(208) Chen, R. Y.; Trieu, V.; Natter, H.; Stowe, K.; Maier, W. F.; Hempelmann, R.; Bulan, A.; Kintrup, J.; Weber, R. *Chem. Mater.* **2010**, *22*, 6215.
(209) Madey, T. E.; Engelhardt, H. A.; Menzel, D. *Surf. Sci.* **1975**, *48*, 304.
(210) Lindroos, M.; Pfnür, H.; Held, G.; Menzel, D. *Surf. Sci.* **1989**, *222*, 451.
(211) Wintterlin, J.; Trost, J.; Renisch, S.; Schuster, R.; Zambelli, T.; Ertl, G. *Surf. Sci.* **1997**, *394*, 159.
(212) Parrot, L.; Praline, G.; Koel, B. E.; White, J. M.; Taylor, T. N. *J. Chem. Phys.* **1979**, *71*, 3352.
(213) Pfnür, H.; Held, G.; Lindroos, M.; Menzel, D. *Surf. Sci.* **1989**, *43*, 220.
(214) Corriol, C.; Calleja, F.; Arnau, A.; Hinarejos, J. J.; Vazquez de Parga, A. L.; Hofer, W. A.; Miranda, R. *Chem. Phys. Lett.* **2005**, *405*, 131.
(215) Surnev, L.; Rangelov, G.; Bliznakov, G. *Surf. Sci.* **1985**, *159*, 299.
(216) Over, H.; Lundgren, E.; Schmidt, M.; Varga, P. Unpublished STM images, 2001.
(217) Mitchell, W. J.; Xie, J.; Lyons, K. J.; Weinberg, W. H. *J. Vac. Sci. Technol. A* **1994**, *12*, 2250.
(218) Kostov, K. L.; Gsell, M.; Jakob, P.; Moritz, T.; Widdra, W.; Menzel, D. *Surf. Sci.* **1997**, *394*, L138.
(219) Kim, Y. D.; Wendt, S.; Schwegmann, S.; Over, H.; Ertl, G. *Surf. Sci.* **1998**, *418*, 267.
(220) Jakob, P.; Gsell, M.; Menzel, D. *J. Chem. Phys.* **2001**, *114*, 10075.
(221) Stampfl, C.; Schwegmann, S.; Over, H.; Scheffler, M.; Ertl, G. *Phys. Rev. Lett.* **1996**, *77*, 3371.
(222) Over, H. *Prog. Surf. Sci.* **1998**, *58*, 249.
(223) Rahman, T. S.; Anton, A. B.; Avery, N. R.; Weinberg, W. H. *Phys. Rev. Lett.* **1983**, *51*, 1979.
(224) Mitchell, W. J.; Weinberg, W. H. *J. Chem. Phys.* **1996**, *104*, 9127.
(225) He, P.; Jacobi, K. *Phys. Rev. B* **1997**, *55*, 4751.
(226) Stampfl, C.; Scheffler, M. *Phys. Rev. B* **1996**, *54*, 2868.
(227) Stampfl, C.; Kreuzer, H. J.; Payne, S. H.; Scheffler, M. *Appl. Phys. A: Mater. Sci. Process.* **1999**, *69*, 471.
(228) Kim, Y. D.; Seitsonen, A. P.; Wendt, S.; Wang, J.; Fan, C.; Jacobi, K.; Over, H.; Ertl, G. *J. Phys. Chem. B* **2001**, *105*, 3752.
(229) Böttcher, A.; Niehus, H. *Phys. Rev. B* **1999**, *60*, 14396.
(230) Malik, I. J.; Hrbek, J. *J. Vac. Sci. Technol. A* **1992**, *10*, 2565.
(231) Hrbek, J.; van Campen, D. G.; Malik, I. J. *J. Vac. Sci. Technol. A* **1995**, *13*, 1409.

(232) Bottcher, A.; Conrad, H.; Niehus, H. *J. Chem. Phys.* **2000**, *112*, 4779.
(233) Herd, B.; Knapp, M.; Over, H. Unpublished STM experiments, 2011.
(234) Over, H.; Seitsonen, A. P. *Science* **2002**, *297*, 2003.
(235) Ernst, M. A.; Sloof, W. G. *Surf. Interface Anal.* **2008**, *40*, 334.
(236) Kim, Y. D.; Seitsonen, A. P.; Over, H. *Surf. Sci.* **2000**, *465*, 1.
(237) Over, H.; Seitsonen, A. P.; Lundgren, E.; Schmid, M.; Varga, P. *Surf. Sci.* **2002**, *515*, 143.
(238) Lin, W. F.; Zei, M. S.; Kim, Y. D.; Over, H.; Ertl, G. *J. Phys. Chem.* **2000**, *104*, 6040.
(239) Blume, R.; Hävecker, M.; Zafeiratos, S.; Teschner, D.; Kleimenov, E.; Knop-Gericke, A.; Schlögl, R.; Barinov, A.; Dudin, P.; Kiskinova, M. *J. Catal.* **2006**, *239*, 345.
(240) Blume, R.; Niehus, H.; Conrad, H.; Böttcher, A.; Aballe, L.; Gregoratti, L.; Barinov, A.; Kiskinova, M. *J. Phys. Chem. B* **2005**, *109*, 14052.
(241) Blume, R.; Hävecker, M.; Zafeiratos, S.; Teschner, D.; Knop-Gericke, A.; Schlögl, R.; Lizzit, S.; Dudin, P.; Barinov, A.; Kiskinova, M. *Phys. Chem. Chem. Phys.* **2007**, *9*, 3648.
(242) Qian, G. X.; Martin, R. M.; Chadi, D. J. *Phys. Rev. B* **1988**, *38*, 7649.
(243) Scheffler, M.; Dabrowski, J. *Phil. Mag. A* **1988**, *58*, 107.
(244) Stampfl., C. *Catal. Today* **2005**, *105*, 17.
(245) Stuckless, J. T.; Al-Saraf, N.; Wartnaby, C. E.; King, D. A. *J. Chem. Phys.* **1997**, *106*, 2012.
(246) Böttcher, A.; Krenzer, B.; Conrad, H.; Niehus, H. *Surf. Sci.* **2002**, *504*, 42−58.
(247) Flege, J. I.; Hrbek, J.; Sutter, P. *Phys. Rev. B* **2008**, *78*, 165407.
(248) Flege, J. I.; Sutter, P. *J. Phys. Cond. Matter.* **2009**, *21*, 314018.
(249) Aßmann, J.; Crihan, D.; Knapp, M.; Lundgren, E.; Löffler, E.; Muhler, M.; Narkhede, V.; Over, H.; Schmid, M.; Varga, P. *Angew. Chem., Int. Ed.* **2005**, *116*, 939−942.
(250) Todorova, M.; Li, W. X.; Ganduglia-Pirovano, M. V.; Stampfl, C.; Reuter, K.; Scheffler, M. *Phys. Rev. Lett.* **2002**, *89*, 096103.
(251) Quinn, P.; Brown, D.; Woodruff, D. P.; Noakes, T. C. Q.; Bailey, P. *Surf. Sci.* **2001**, *491*, 208.
(252) Reuter, K.; Ganduglia-Pirovano, M. V.; Stampfl, C.; Scheffler, M. *Phys. Rev. B.* **2002**, *65*, 165403.
(253) Vukmirovic, M. B.; Sabatini, R. L.; Adzic, R. R. *Surf. Sci.* **2001**, *572*, 269.
(254) Campbell, C. T. *Phys. Rev. Lett.* **2006**, *96*, 066106.
(255) Dudin, P.; Barinov, A.; Gregoratti, L.; Kiskinova, M.; Goriachko, A.; Over, H. *J. Electron Relat. Phenom.* **2008**, *89*, 166−167.
(256) Gustafson, J.; Mikkelsen, J.; Borg, M.; Lundgren, E.; Kohler, L.; Kresse, G.; Schmid, M.; Varga, P.; Yuhara, J.; Torrelles, X.; Quiros, C.; Andersen, J. N. *Phys. Rev. Lett.* **2004**, *92*, 126102.
(257) Dri, C.; Africh, C.; Esch, F.; Comelli, G.; Dubay, O.; Kohler, L.; Mittendorfer, F.; Kresse, G.; Dudin, P.; Kiskinova, M. *J. Chem. Phys.* **2006**, *125*, 094701.
(258) Gustafson, J.; Mikkelsen, J.; Borg, M.; Andersen, J. N.; Lundgren, E.; Klein, C.; Hofer, W.; Schmid, M.; Varga, P.; Kohler, L.; Kresse, G.; Kasper, N.; Stierle, A.; Dosch, H. *Phys. Rev. B.* **2005**, *71*, 115442.
(259) He, Y. B.; Stierle, A.; Li, W. X.; Farkas, A.; Kasper, N.; Dosch, H.; Over, H. *J. Phys. Chem. C* **2008**, *112*, 11946.
(260) Orent, T. W.; Hansen, R. S. *Surf. Sci.* **1977**, *67*, 325.
(261) Poulston, S.; Tikhov, M.; Lambert, R. M. *Langmuir* **1997**, *13*, 5356.
(262) Schwegmann, S.; Seitsonen, A. P.; De Renzi, V.; Dietrich, H.; Bludau, H.; Gierer, M.; Over, H.; Jacobi, K.; Scheffler, M.; Ertl, G. *Phys. Rev. B* **1998**, *57*, 15487.
(263) Zhang, H. J.; Lu, B.; Li, H. Y.; Bao, S. N.; He, P. *Surf. Sci.* **2004**, *556*, 63.
(264) Blume, R.; Christen, W.; Niehus, H.; Rademann, K. *J. Phys. Chem C* **2007**, *111*, 4774.
(265) Knapp, M.; Seitsonen, A. P.; Kim, Y. D.; Over, H. *J. Phys. Chem. B* **2004**, *108*, 14392.
(266) Zweidinger, S.; Hofmann, J. P.; Balmes, O.; Lundgren, E.; Over, H. *J. Catal.* **2010**, *272*, 169.
(267) Seitsonen, A. P.; Over, H. *Surf. Sci.* **2009**, *603*, 1717.
(268) Over, H.; Gierer, M.; Bludau, H.; Ertl, G.; Tong, S. Y. *Surf. Sci.* **1994**, *314*, 243.
(269) Wang, J. X.; Marinkovic, N. S.; Zajonz, H.; Ocko, B. M.; Adzic, R. R. *J. Phys. Chem. B* **2001**, *105*, 2809.
(270) Pourbaix, M., Ed. *Atlas of Electrochemical Equilibria in Aqueous Solutions*; NACE: Houston, TX, 1974.
(271) Wohlfahrt-Mehrens, M.; Heitbaum, J. *J. Electroanal. Chem.* **1987**, *237*, 251.
(272) Walker, R. C.; Bailes, M.; Peter, L. M. *Electrochim. Acta* **1998**, *44*, 1289.
(273) Malik, I. J.; Hrbek, J. *J. Phys. Chem.* **1991**, *95*, 10188.
(274) Knapp, M.; Crihan, D.; Seitsonen, A. P.; Lundgren, E.; Resta, A.; Andersen, J. N.; Over, H. *J. Phys. Chem. C* **2007**, *111*, 5363−5373.
(275) Chung, W. H.; Tsai, D. S.; Chen, Y. M.; Huang, Y. S.; Chou, C. C.; Liu, C. J. *Solid State Commun.* **2008**, *146*, 462.
(276) Lobo, A.; Conrad, H. *Surf. Sci.* **2003**, *523*, 279.
(277) Knapp, M.; Crihan, D.; Seitsonen, A. P.; Over, H. *J. Am. Chem. Soc.* **2005**, *127*, 3236.
(278) Kim, S. H.; Wintterlin, J. *J. Chem. Phys.* **2009**, *131*, 064705.
(279) Knapp, M. Ph.D. Thesis, *Die Schlüsselrolle des Wasserstoffs im Reaktionsverhalten einer oxidischen Katalysatoroberfläche am Beipiel von $RuO_2(110)$*; JLU Giessen: Mai, 2006.
(280) Knapp, M.; He, Y. B.; Lundgren, E.; Over, H. Unpublished In-situ SXRD measurements during the chemical reduction of $RuO_2(110)$ by molecular hydrogen, 2008.
(281) Over, H.; Balmes, O.; Lundgren, E. Unpublished SXRD experiments (ESRF, ID03, beamtime), August 2008.
(282) Blume, R.; Hävecker, M.; Zafeiratos, S.; Teschner, D.; Knop-Gericke, A.; Schlögl, R.; Dudin, P.; Barinov, A.; Kiskinova, M. *Catal. Today* **2007**, *124*, 71.
(283) Balint, I.; Miyazaki, A.; Aika, K.-I. *React. Kinet. Catal. Lett.* **2003**, *80*, 81.
(284) Prudenziati, M.; Morten, B.; Travan, E. *Mater. Sci. Eng., B* **2003**, *98*, 167.
(285) Bond, G. C.; Coq, B.; Dutartre, R.; Ruiz, J. G.; Hooper, A. D.; Proietti, M. G.; Sierra, M. C. S.; Salla, J. C. *J. Catal.* **1996**, *161*, 480.
(286) Vogel, W.; Le Rhun, V.; Garnier, E.; Alonso-Vante, N. *J. Phys. Chem. B* **2001**, *105*, 5238.
(287) Vogel, W.; Alonso-Vante, N. *J. Catal.* **2005**, *232*, 395.
(288) Belau, L.; Park, J. Y.; Liang, T.; Somorjai, G. A. *J. Vac. Sci. Technol. B* **2008**, *26*, 2225.
(289) Kötz, R.; Lewerenz, H. J.; Stucki, S. *J. Electrochem. Soc.* **1983**, *130*, 825.
(290) Motai, K.; Oizumi, H.; Miyagaki, S.; Nishiyama, I.; Izumi, A.; Ueno, T.; Namiki, A. *Thin Sol. Films* **2008**, *516*, 836.
(291) Schick, M.; Xie, J.; Mitchell, W. J.; Weinberg, W. H. *J. Chem. Phys.* **1996**, *104*, 7713.
(292) Xie, J.; Mitchell, W. J.; Lyon, K. J.; Wang, Y.; Weinberg., W. H. *J. Vac. Sci. Technol. A* **1994**, *12*, 2210.
(293) Peuckert, M. *J. Phys. Chem.* **1985**, *89*, 2481.
(294) Peuckert, M.; Bonzel, H. P. *Surf. Sci.* **1985**, *145*, 239.
(295) Ackermann, M.; Pedersen, T.; Hendriksen, B.; Robach, O.; Bobaru, S. C.; Popa, I.; Quiros, C.; Kim, H.; Hammer, B.; Ferrer, S.; Frenken, J. W. M. *Phys. Rev. Lett.* **2005**, *95*, 255505.
(296) Seriani, N.; Mittendorfer, F. *J. Phys.: Condens. Matter* **2008**, *20*, 184023.
(297) Lundgren, E.; Mikkelsen, A.; Andersen, J. N.; Kresse, G.; Schmid, M.; Varga, P. *J. Phys.: Condens. Matter* **2006**, *18*, R481.
(298) Diebold, U.; Li, S.-C.; Schmid, M. *Annu. Rev. Phys. Chem.* **2010**, *61*, 129.
(299) Altman, E. I.; Schwarz, U. D. *Adv. Mater.* **2010**, *22*, 2854.
(300) Knudsen, J.; Merte, L. R.; Peng, G.; Vang, R. T.; Rest, A.; Lagsgard, E.; Andersen, J. N.; Mavrikakis, M.; Besenbacher, F. *ACS Nano* **2010**, *4*, 4380.
(301) Wang, Y. M.; Li, Y. S.; Mitchell, K. A. R. *Surf. Sci.* **1995**, *343*, L1167.

(302) Wang, Y. M.; Li, Y. S.; Mitchell, K. A. R. *Surf. Sci.* **1997**, *380*, 540.
(303) Comelli, G.; Dhanak, V. R.; Kiskinova, M.; Prince, K.,C.; Rosei, R. *Surf. Sci. Rep.* **1998**, *32*, 165.
(304) Schwegmann, S.; Over, H.; De Renzi, V.; Ertl, G. *Surf. Sci.* **1997**, *375*, 91.
(305) Schwegmann, S.; Over, H. *Surf. Sci.* **1997**, *393*, 179.
(306) Kohler, L.; Kresse, G.; Schmid, M.; Lundgren, E.; Gustafson, J.; Mikkelsen, A.; Borg, M.; Yuhara, J.; Andersen, J. N.; Marsman, M.; Varga, P. *Phys. Rev. Lett.* **2004**, *93*, 266103.
(307) Gibson, K. D.; Viste, M.; Sibener, S. J. *J. Chem. Phys.* **2000**, *112*, 9582.
(308) Wider, J.; Greber, T.; Wetli, E.; Kreutz, T. J.; Schwaller, P.; Osterwalder, J. *Surf. Sci.* **1998**, *417*, 301.
(309) Gustafson, J.; Resta, A.; Mikkelsen, A.; Westerstrom, R.; Andersen, J. N.; Lundgren, E; Weissenrieder, J.; Schmid, M.; Varaga, P.; Kasper, N.; Torelles, X.; Ferrer, S.; Mittendorfer, F.; Kresse, G. *Phys. Rev. B.* **2006**, *74*, 035401.
(310) Lundgren, E.; Gustafson, J.; Resta, A.; Weissenrieder, J.; Mikkelsen, A.; Andersen, J. N.; Kohler, L.; Kresse, G.; Klikovits, J.; Biedermann, A.; Schmid, M.; Varga, P. *J. Electron Spectrosc. Relat. Phenom.* **2005**, *144*, 367.
(311) Klikovits, J.; Schmid, M.; Gustafson, J.; Mikkelsen, A.; Resta, A.; Lundgren, E.; Andersen, J. N.; Varga, P. *J. Phys. Chem. B* **2006**, *110*, 9966.
(312) Mercer, J. R.; Finetti, P.; Scantlebury, M. J.; Beierlein, U.; Dhanak, V. R.; McGrath, R. *Phys. Rev. B* **1997**, *55*, 10014.
(313) Baraldi, A.; Dhanak, V. R.; Comelli, G.; Prince, K. C.; Rosei, R. *Phys. Rev. B* **1997**, *56*, 10511.
(314) Shen, Y. G.; Qayyum, A.; O'Connor, D. J.; King, B. V. *Phys. Rev. B* **1998**, *58*, 10025.
(315) Baraldi, A.; Cerda, J.; Martyn-Gago, J. A.; Comelli, G.; Lizzit, S.; Paolucci, G.; Rosei, R. *Phys. Rev. Lett.* **1999**, *82*, 4874.
(316) Norris, A. G.; Schedin, F.; Thronton, G.; Dhanak, V. R.; Turner, T. S.; McGrath, R. *Phys. Rev. B* **2000**, *62*, 2113.
(317) Zhan, R. R.; Vesselli, E.; Baraldi, A.; Lizzit, S.; Comelli, G. *J. Chem. Phys.* **2010**, *133*, 214701.
(318) Kiskinova, M. *Chem. Rev.* **1996**, *96*, 1431.
(319) Gierer, M.; Over, H.; Ertl, G.; Wohlgemuth, H.; Schwarz, E.; Christmann, K. *Surf. Sci.* **1993**, *297*, L73.
(320) Vesselli, E.; Africh, C.; Baraldi, A.; Comelli, G.; Esch, F.; Rosei, R. *J. Chem. Phys.* **2001**, *114*, 4221.
(321) Africh, C.; Esch, F.; Li, W. X.; Corso, M.; Hammer, B.; Rosei, R.; Comelli, G. *Phys. Rev. Lett.* **2004**, *93*, 126104.
(322) Africh, C.; Kohler, L.; Esch, F.; Corso, M.; Dri, C.; Bucko, T.; Kresse, G.; Comelli, G. *J. Am. Chem. Soc.* **2009**, *131*, 3253.
(323) Klikovits, J.; Schmid, M.; Merte, L. R.; Varga, P.; Westerstrom, R.; Resta, A.; Andersen, J. N.; Gustafson, J.; Mikkelsen, A.; Lundgren, E.; Mittendorfer, F.; Kresse, G. *Phys. Rev. Lett.* **2008**, *101*, 266104.
(324) Dudin, P.; Barinov, A.; Gregoratti, L.; Kiskinova, M.; Esch, F.; Dri, C.; Africh, C.; Comelli, G. *J. Phys. Chem. B* **2005**, *109*, 13649.
(325) Conrad, H.; Kuppers, J.; Notschke, F.; Plagge, A. *Surf. Sci.* **1977**, *69*, 668.
(326) Zheng, G.; Altman, E. I. *Surf. Sci.* **2000**, *462*, 151.
(327) Zemlyanov, D.; Aszalo-Kiss, B.; Kleimenov, E.; Teschner, D.; Zafeiratos, S.; Hävekcer, M.; Knop-Gericke, A.; Schlögl, R.; Gabasch, H.; Unterberger, W.; Hayek, K.; Klötzer, B. *Surf. Sci.* **2006**, *600*, 983.
(328) Lundgren, E.; Kresse, G.; Klein, C.; Borg, M.; Andersen, J. N.; De Santis, M.; Gauthier, Y.; Konvicka, C.; Schmid, M.; Varga, P. *Phys. Rev. Lett.* **2002**, *88*, 246103.
(329) Kresse, G.; Lundgren, E.; Bergermeyer, W.; Podloucky, R.; Schmid, M.; Varga, P. *Appl. Phys. A: Mater. Sci. Process.* **2003**, *76*, 701.
(330) Westerstrom, R.; Gustafson, J.; Resta, A.; Mikkelsen, A.; Andersen, J. N.; Lundgren, E.; Seriani, N.; Mittendorfer, F.; Schmid, M.; Klikovits, J.; Varga, P.; Ackermann, M. D.; Frenken, J. W. M.; Kasper, N.; Stierle, A. *Phys. Rev. B* **2007**, *76*, 155410.
(331) Zheng, G.; Altman, E. I. *Surf. Sci.* **2002**, *504*, 253.
(332) Todorova, M.; Lundgren, E.; Blum, V.; Mikkelsen, A.; Gray, S.; Gustafson, J.; Borg, M.; Rogal, J.; Reuter, K.; Andersen, J. N.; Scheffler, M. *Surf. Sci.* **2003**, *541*, 101.
(333) Kostelnik, P.; Seriani, N.; Kresse, G.; Mikkelsen, A.; Lundgren, E.; Blum, V.; Sikola, T.; Varga, P.; Schmid, M. *Surf. Sci.* **2007**, *601*, 1574.
(334) Lundgren, E.; Gustafson, J.; Mikkelsen, A.; Andersen, J. N.; Stierle, A.; Dosch, H.; Todorova, M.; Rogal, J.; Reuter, K.; Scheffler, M. *Phys. Rev. Lett.* **2004**, *92*, 246103.
(335) Hendriksen, B. L. M.; Ackermann, M. D.; Van Rijn, R.; Stoltz, D.; Popa, I.; Balmes, O.; Resta, A.; Wermeille, D.; Felici, R.; Ferrer, S.; Frenken, J. W. M. *Nat. Chem.* **2010**, *2*, 730.
(336) Ertl, G.; Rau, P. *Surf. Sci.* **1969**, *15*, 443.
(337) Jo, M.; Kuwahara, Y.; Onchi, M.; Nishijima, M. *Chem. Phys. Lett.* **1986**, *131*, 106.
(338) Goschnik, J.; Wolf, M.; Grunze, M.; Unertl, W. N.; Block, J. H.; Loboda-Cackovic. *J. Surf. Sci.* **1986**, *178*, 831.
(339) He, J.-W.; Norton, P. R. *Surf. Sci.* **1990**, *230*, 150.
(340) Niehus, H.; Achete, C. *Surf. Sci.* **1996**, *9*, 369.
(341) Nishijima, M.; Jo, M.; Kuwahara, Y.; Onchi, M. *Solid State Commun.* **1986**, *60*, 257.
(342) Brena, B.; Comelli, G.; Ursella, L.; Paolucci, G. *Surf. Sci.* **1996**, *375*, 150.
(343) Comelli, G.; Sastry, M.; Paolucci, G.; Prince, K. C.; Olivi, L. *Phys. Rev. B.* **1991**, *43*, 14385.
(344) Tanaka, H.; Yoshinobu, J.; Kawai, M. *Surf. Sci.* **1995**, *327*, 505.
(345) Bennett, R. A.; Poulston, S.; Jones, I. Z.; Bowker, M. *Surf. Sci.* **1998**, *401*, 72.
(346) He, J.-W.; Memmert, U.; Griffiths, K.; Norton, P. R. *J. Chem. Phys.* **1989**, *90*, 5082.
(347) Yagi, K.; Fukutani, H. *Surf. Sci.* **1998**, *412/413*, 489.
(348) Kralj, M.; Pertram, T.; Seriani, N.; Becker, C.; Krupski, A.; Mittendorfer, F.; Wandelt, K. *Surf. Sci.* **2008**, *602*, 3706.
(349) Westerström, R.; Weststrate, C. J.; Resta, A.; Mikkelsen, A.; Schnadt, J.; Andersen, J. N.; Lundgren, E.; Schmid, M.; Seriani, N.; Harl, J.; Mittendorfer, F.; Kresse, G. *Surf. Sci.* **2008**, *602*, 2440.
(350) Westerström, R.; Weststrate, C. J.; Gustafson, J.; Mikkelsen, A.; Schnadt, J.; Andersen, J. N.; Lundgren, E.; Seriani, N.; Mittendorfer, F.; Kresse, G.; Stierle, A. *Phys. Rev. B* **2009**, *80*, 125431.
(351) Gland, J. L.; Sexton, B. A.; Fisher, G. B. *Surf. Sci.* **1980**, *95*, 587.
(352) Campbell, C. T.; Ertl, G.; Kuipers, H.; Segener, J. *Surf. Sci.* **1981**, *107*, 220.
(353) Parker, D. H.; Bartram, M. E.; Koel, B. E. *Surf. Sci.* **1989**, *217*, 489.
(354) Parkinson, C. R.; Walker, M.; McConville, C. F. *Surf. Sci.* **2003**, *545*, 19.
(355) Weaver, J. F.; Chen, J.-J.; Gerrard, A. L. *Surf. Sci.* **2005**, *592*, 83.
(356) Ellinger, C.; Stierle, A.; Robinson, I. K.; Nefedov, A.; Dosch, H. *J. Phys.: Condens. Matter* **2008**, *20*, 184013.
(357) Seriani, N.; Pompe, W.; Ciacchi, L. C. *J. Phys. Chem. B* **2006**, *110*, 14860.
(358) Li, W. X.; Hammer, B. *Chem. Phys. Lett.* **2006**, *409*, 1.
(359) Devarajan, S. P.; Hinojosa, J. A.; Weaver, J. F. *Surf. Sci.* **2008**, *602*, 3116.
(360) Hawkins, J. M.; Weaver, J. F.; Astagiri, A. *Phys. Rev. B* **2009**, *79*, 125434.
(361) Krasnokov, S. A.; Murphy, S.; Gerdunov, N.; McCoy, A. P.; Radican, K. *Nanotechnology* **2010**, *21*, 335301.
(362) Weaver, J. F.; Kan, H. H.; Shumbera, R. B. *J. Phys.: Condens. Matter* **2008**, *20*, 184015.
(363) Gao, F.; Wang, Y.; Cai, Y.; Goodman, D. W. *J. Phys. Chem. C* **2009**, *113*, 174.
(364) Ackermann, M. Ph.D. Thesis, *Operando SXRD: A New View on Catalysis*, Physical Chemistry Institute, Justus Liebig University: Leiden, 2007.
(365) Li, W. X.; Osterlund, L.; Vestergaard, E. K.; Vang, R. T.; Matthiesen, J.; Pedersen, T. M.; Laegsgaard, E.; Hammer, B.; Besenbacher, F. *Phys. Rev. Lett.* **2004**, *93*, 146104.

(366) Wang, J. G.; Li, W. X.; Borg, M.; Gustafson, J.; Mikkelsen, A.; Pedersen, T. M.; Lundgren, E.; Weissenrieder, J.; Klikovits, J.; Schmid, M.; Hammer, B.; Andersen, J. N. *Phys. Rev. Lett.* **2005**, *95*, 256102.
(367) Pedersen, T. M.; Li, W. X.; Hammer, B. *Phys. Chem. Chem. Phys.* **2006**, *8*, 1566.
(368) Komanicky, V.; Menzel, A.; Chang, K.-C.; You, H. *J. Phys. Chem. B* **2005**, *109*, 23543.
(369) Chan, C. M.; Weinberg, W. H. *J. Chem. Phys.* **1979**, *71*, 2788.
(370) He, Y. B.; Over, H. Unpublished LEED analysis of the($\sqrt{3}\times\sqrt{3}$)R30° O-overlayer on Ir(111) prepared by exposing 5000L of NO_2 at 580 K, 2008.
(371) Zhang, H.; Soon, A.; Delley, B.; Stampfl, C. *Phys. Rev. B* **2008**, *78*, 045436.
(372) Chung, W.-H.; Wang, C.-C.; Tsai., D.-S.; Jiang, J.-C.; Cheng, Y.-C.; Fan, L.-J.; Yang, Y.-W.; Huang, Y.-S. *Surf. Sci.* **2010**, *604*, 118.
(373) Kaghazchi, P.; Jacob, T.; Ermanoski, I.; Chen, W.; Madey, T. E. *Nano* **2008**, *2*, 1280.
(374) Seitsonen, A. P.; Over, H. Ruthenium Dioxide, a Versatile Oxidation Catalyst: First Principles Analysis. In *High Performance Computing in Science and Engineering in Munich 2002*; Springer-Verlag: London, 2003; pp 171−180.
(375) Hong, S.; Rahman, T. S.; Jacobi, K.; Ertl, G. *J. Phys. Chem. C* **2007**, *111*, 12361.
(376) Bohnen, K. P.; Heid, R.; de la Penia Seamna, O. *Phys. Rev. B* **2010**, *81*, 081405.
(377) Tasker, P. W. *J. Phys. C − Solid State Physics* **1979**, *12*, 4977.
(378) Kim, Y. D.; Seitsonen, A. P.; Over, H. *Phys. Rev. B.* **2001**, *63*, 5419.
(379) Seitsonen, A. P.; Kim, Y. D.; Knapp, M.; Wendt, S.; Over, H. *Phys. Rev. B* **2002**, *65*, 035413.
(380) Henrichs, V. E.; Cox, P. A. *The Surface Science of Metal Oxides*; Cambridge University Press: Cambridge, 1996.
(381) Wang, J.; Fan, C. Y.; Sun, Q.; Reuter, K.; Jacobi, K.; Scheffler, M.; Ertl, G. *Angew. Chem., Int. Ed.* **2003**, *42*, 2151.
(382) Sun, Q.; Reuter, K.; Scheffler, M. *Phys. Rev. B* **2004**, *70*, 235402.
(383) Madhavaram, H.; Idriss, H.; Wendt, S.; Kim, Y. D.; Knapp, M.; Over, H.; Aßmann, J.; Löffler, E.; Muhler, M. *J. Catal.* **2001**, *202*, 296.
(384) Wang, Y.; Jacobi, K.; Schöne, W.-D.; Ertl, G. *J. Phys. Chem. B* **2005**, *109*, 7883.
(385) Zweidinger, S.; Crihan, D.; Knapp, M.; Hofmann, J. P.; Seitsonen, A. P.; Lundgren, E.; Weststrate, C. J.; Andersen, J. N.; Over, H. *J. Phys. Chem. C* **2008**, *112*, 9966.
(386) Hess, F.; Eifert, B.; Hofmann, J. P.; Seitsonen, A. P.; Over, H. Unpublished DFT calculations, July 2011.
(387) Wang, H.; Schneider, W. F.; Schmidt, D. *J. Phys. Chem. C* **2009**, *113*, 15266.
(388) Kim, K. S.; Winograd, N. *J. Catal.* **1974**, *35*, 66.
(389) Lizzit, S.; Baraldi, A.; Groso, A.; Reuter, K.; Ganduglia-Pirovano, M. V.; Stampfl, C.; Scheffler, M.; Stichler, M.; Keller, C.; Wurth, W.; Menzel, D. *Phys. Rev. B* **2001**, *63*, 205419.
(390) Schiffer, A.; Jacob, P.; Menzel, D. *Surf. Sci.* **1997**, *389*, 116.
(391) Rotaris, G.; Baraldi, A.; Comelli, G.; Kiskinova, M.; Rosei, R. *Surf. Sci.* **1996**, *359*, 1.
(392) Wurth, W.; Schneider, C.; Treichler, R.; Umbach, E.; Menzel, D. *Phys. Rev. B* **1987**, *35*, 7741.
(393) Glarys, M. J.; Mikkelsen, A.; Andersen, J. N.; Held, G. *Phys. Chem. Lett.* **2005**, *414*, 311.
(394) Baraldi, A.; Lizzit, S.; Comelli, G.; Paolucci, G. *Phys. Rev. B* **2001**, *63*, 115410.
(395) Hofmann, J. P.; Zweidinger, S.; Knapp, M.; Seitsonen, A. P.; Schulte, K.; Andersen, J. N.; Lundgren, E.; Over, H. *J. Phys. Chem. C* **2010**, *114*, 10901.
(396) Kim, S. H.; Wintterlin, J. *J. Phys. Chem B* **2004**, *108*, 14565.
(397) Diebold, U.; Anderson, J. E.; Ng, K.-O.; Vanderbilt, D. *Phys. Rev. Lett.* **1996**, *77*, 1322.
(398) Lopez, N.; Novell-Leruth, G. *Phys. Chem. Chem. Phys.* **2010**, *12*, 12217.
(399) Wang, Y.; Lafosse, A.; Jacobi, K. *J. Phys. Chem. B* **2002**, *106*, 5476.
(400) Wang, Y.; Jacobi, K.; Ertl, G. *J. Phys. Chem. B* **2003**, *107*, 13918.
(401) Jacobi, K.; Wang., Y. *Surf. Sci.* **2009**, *603*, 1600.
(402) Paulus, U. A.; Wang, Y.; Bonzel, H. P.; Jacobi, K.; Ertl, G. *Surf. Sci.* **2004**, *566*, 989.
(403) Paulus, U. A.; Wang, Y.; Bonzel, H. P.; Jacobi, K.; Ertl, G. *J. Phys. Chem. B* **2005**, *109*, 2139.
(404) Erlekam, U.; Paulus, U. A.; Wang, Y.; Bonzel, H. P.; Jacobi, K.; Ertl., G. *Z. Phys. Chem.* **2005**, *219*, 891.
(405) Crihan, D.; Knapp, M.; Zweidinger, S.; Lundgren, E.; Weststrade, C. J.; Andersen, J. N.; Seitsonen, A. P.; Over, H. *Angew. Chem., Int. Ed.* **2008**, *47*, 2131.
(406) Kim, S. H.; Paulus, U. A.; Wang, Y.; Wintterlin, J.; Jacobi, K.; Ertl, G. *J. Chem. Phys.* **2003**, *119*, 9729.
(407) Reuter, K.; Scheffler, M. *Phys. Rev. B* **2006**, *73*, 045433.
(408) Kiejna, A.; Kresse, G.; Rogal, J.; De Sarkar, A.; Reuter, K.; Scheffler, M. *Phys. Rev. B.* **2006**, *73*, 035404.
(409) Paulus, U. A.; Wang, Y.; Jacobi, K.; Ertl, G. *Surf. Sci.* **2003**, *547*, 349.
(410) Seitsonen, A. P.; Crihan, D.; Knapp., M.; Resta, A.; Lundgren, E.; Andersen, J. N.; Over, H. *Surf. Sci.* **2009**, *603*, L113.
(411) Wang, H.; Schneider, W. F. *Catal. Today* **2010**, *165*, 49.
(412) Perez-Ramirez, J.; Lopez, N.; Kondratenko, E. V. *J. Phys. Chem C* **2010**, *114*, 16660.
(413) Wang, H.; Schneider, W. F. *Phys. Chem. Chem. Phys.* **2010**, *12*, 6367.
(414) Hong, S.; Karim, A.; Rahman, T. S.; Jacobi, K.; Ertl, G. *J. Catal.* **2010**, *276*, 371.
(415) Fan, C. Y.; Wang, J.; Jacobi, K.; Ertl, G. *J. Chem. Phys.* **2001**, *114*, 10058.
(416) Liu, Z.-P.; Hu, P.; Alavi, A. *J. Chem. Phys.* **2001**, *114*, 5957.
(417) Over, H.; Seitsonen, A. P.; Lundgren, E.; Schmid, M.; Varga, P. *J. Am. Chem. Soc.* **2001**, *123*, 11807.
(418) Over, H.; Muhler, M. *Prog. Surf. Sci.* **2003**, *72*, 3.
(419) Barth, J. V. *Surf. Sci. Rep.* **2000**, *40*, 75.
(420) Crihan, D.; Knapp, M.; Seitsonen, A. P.; Over, H. *J. Phys. Chem B* **2006**, *110*, 22947.
(421) Horokawa, S.; Nogawa, S.; Taniguchi, M.; Utani, K.; Kanai, H.; Imamura, S. *Appl. Catal., A* **2005**, *288*, 67.
(422) Tokarz-Sobieraj, R.; Hermann, K.; Witko, M.; Blume, A.; Wild, U.; Mestl, G.; Knop-Gericke, A.; Schlögl, R. *Surf. Sci.* **2001**, *489*, 107.
(423) Hermann, K.; Witko, M.; Druzinic, R. *Faraday Discuss.* **1999**, *114*, 53.
(424) Surnev, S.; Ramsey, M. G.; Netzer, F. P. *Prog. Surf. Sci.* **2003**, *73*, 117.
(425) Reuter, K.; Scheffler, M. *Phys. Rev. B* **2003**, *68*, 045407.
(426) Blyholder, G. *J. Phys. Chem.* **1964**, *68*, 2772.
(427) Jacobi, K.; Wang, Y.; Ertl, G. *J. Phys. Chem. B* **2006**, *110*, 6115.
(428) Knapp, M.; Crihan, D.; Resta, A.; Lundgren, E.; Andersen, J. N.; Seitsonen, A. P.; Schmid, M.; Varga, P.; Over, H. *J. Phys. Chem. B Lett.* **2006**, *110*, 14007.
(429) Jacobi, K.; Wang, Y.; Ertl, G. *J. Phys. Chem. B* **2006**, *110*, 22948.
(430) Thiel, P.; Madey, T. *Surf. Sci. Rep.* **1987**, *7*, 211.
(431) Hendersen, M. A. *Surf. Sci. Rep.* **2002**, *46*, 5.
(432) Hodgson, A.; Haq, S. *Surf. Sci. Rep.* **2009**, *64*, 381.
(433) Crihan, D. Ph.D. Thesis, HCl Oxidation auf RuO_2(110): Neuartiger Deacon Prozess, Giessen, 2007. http://geb.uni-giessen.de/geb/volltexte/ /2008/6068/
(434) Chu, Y. S.; Lister, T. E.; Cullen, W. G.; You, H.; Nagy. *Z., Phys. Rev. Lett.* **2001**, *86*, 3364.
(435) Farkas, A.; Mellau, G.; Over, H. *J. Phys. Chem. C* **2009**, *113*, 14341.
(436) Knapp, M.; Lundgren, E.; Schmid, M.; Varga, P.; Over, H. Unpublished STM results of the interaction of methanol with RuO_2(110), 2003.
(437) Kresse, G. Unpublished DFT calculations: Structure of RuO_2(100)-c(2×2), 2011.
(438) Fujishima, A.; Honda, K. *Nature* **1972**, *37*, 238.

(439) Thompson, T. L.; Yates, J. T. *Chem. Rev.* **2006**, *106*, 4428.
(440) Fujishima, A.; Zhang, X. T.; Tryk, D. A. *Surf. Sci. Rep.* **2008**, *63*, 515.
(441) Ganduglia-Provano, M. V.; Hofmann, A.; Sauer, J. *Surf. Sci. Rep.* **2007**, *62*, 219.
(442) Rasmussen, M. D.; Molina, L. M.; Hammer, B. *J. Chem. Phys.* **2004**, *120*, 988.
(443) Kowalski, P. M.; Carmellone, M. F.; Nair, N. N.; Meyer, B.; Marx, D. *Phys. Rev. Lett.* **2010**, *105*, 146405.
(444) Lindsay, R.; Wander, A.; Ernst, A.; Montanari, B.; Thornton, G.; Harrison, N. M. *Phys. Rev. Lett.* **2005**, *94*, 246102.
(445) Lindan, P. D. J.; Harrison, N. M. *Surf. Sci.* **2001**, *479*, L275.
(446) Henderson, M. A. *Surf. Sci.* **1999**, *419*, 174.
(447) Lira, E.; Hansen, J. O.; Huo, P.; Bechstein, R.; Galliker, P.; Lagsgaard, E.; Hammer, B.; Wendt, S.; Besenbacher, F. *Surf. Sci.* **2010**, *604*, 1945.
(448) Studt, F.; Abild-Pedersen, F.; Hansen, H. A.; Man, I. C.; Rossmeisl, J.; Bligaard, T. *Chem. Cat. Chem.* **2010**, *2*, 98.
(449) Seitsonen, A. P.; Over, H. *J. Phys. Chem. C* **2010**, *114*, 22624.
(450) Wendt, S.; Sprunger, P. T.; Lira, E.; Madsen, G. K. H.; Li, Z. S.; Hansen, J. O.; Matthiesen, J.; Blekinge-Rasmussen, A.; Lagsgaard, E.; Hammer, B.; Besenbacher, F. *Science* **2008**, *320*, 1755.
(451) Bowker, M.; Bennet, R. A. *J. Phys.: Condens. Matter* **2009**, *21*, 474224.
(452) Goodenough, J. B. *Prog. Solid State Chem.* **1972**, *5*, 145.
(453) Samsonov, G. V. *The Oxide Handbook*; IFI/Plenum Press: New York, 1982.
(454) Valden, M.; Lai, X.; Goodman, D. W. *Science* **1998**, *281*, 1647.
(455) Engel, T.; Ertl, G. *Adv. Catal.* **1979**, *28*, 1.
(456) Lee, H.-I.; White, J. M. *J. Catal.* **1980**, *63*, 261.
(457) Over, H.; Balmes, O.; Lundgren, E. *Cat. Today* **2009**, *145*, 236.
(458) Rosenthal, D.; Girgsdies, F.; Timpe, O.; Weinberg, G.; Schlögl, R. *Z. Phys. Chem.* **2011**, *225*, 57.
(459) Over, H.; Balmes, O.; Lundgren, E. *Surf. Sci.* **2009**, *603*, 298.
(460) Goodman, D. W.; Peden, C. H. F.; Chen, M. S. *Surf. Sci.* **2007**, *601*, L124.
(461) Over, H.; Muhler, M.; Seitsonen, A. P. *Surf. Sci.* **2007**, *601*, 5659.
(462) Goodman, D. W.; Peden, C. H. F.; Chen, M. S. *Surf. Sci.* **2007**, *601*, 5663.
(463) Blume, R.; Niehus, H.; Conrad, H.; Böttcher, A. *J. Chem. Phys.* **2004**, *120*, 3871.
(464) Böttcher, A.; Niehus, H.; Schwegmann, S.; Over, H.; Ertl, G. *J. Phys. Chem. B* **1997**, *101*, 11185.
(465) Gustafson, J.; Westerstrom, R.; Mikkelsen, A.; Torrelles, X.; Balmes, O.; Bovet, N.; Andersen, J. N.; Baddeley, C. J.; Lundgren, E. *Phys. Rev. B* **2008**, *78*, 045423.
(466) Gao, F.; McClure, S. M.; Cai, Y; Gath, K. K.; Wang, Y.; Chen, M. S.; Guo, Q. L.; Goodman, D. W. *Surf. Sci.* **2009**, *603*, 65.
(467) van Rijn, R.; Balmes, O.; Felici, R.; Gustafson, J.; Wermeille, D.; Westerstroem, R.; Lundgren, E.; Frenken, J. W. M. *J. Phys. Chem C* **2010**, *114*, 6875.
(468) Peden, C. H. F. In *Surface Science of Catalysis*; Dwyer, D. J. Hoffmann, F. M., Eds. *ACS Symposium Series 483*; American Chemical Society: Washington, DC, 1992; p 143.
(469) Bowker, M. *The Basis and Application of Heterogeneous Catalysis*; Science Publication: Oxford, 1998.
(470) Gong, X.-Q.; Liu, Z.-P.; Raval, R.; Hu, P. *J. Am. Chem. Soc.* **2004**, *126*, 9.
(471) Farkas, A.; Hess, F.; Over, H. *J. Phys. Chem. C* **2012**, *114*, 581.
(472) Lin, W. F.; Jin, J. M.; Christensen, P. A.; Scott, K. *Electrochim. Acta* **2003**, *48*, 3815.
(473) Wendt, S.; Seitsonen, A. P.; Kim, Y. D.; Knapp, M.; Idriss, H.; Over, H. *Surf. Sci.* **2002**, *505*, 137−152.
(474) Wang, J.; Fan, C. Y.; Jacobi, K.; Ertl, G. *J. Phys. Chem. B* **2002**, *106*, 3427.
(475) Wendt, S.; Seitsonen, A. P.; Over, H. *Catal. Today* **2003**, *85*, 167.
(476) Wendt, S.; Knapp, M.; Over, H. *J. Am. Chem. Soc.* **2004**, *126*, 1537.
(477) Chorkendorff, I.; Niemantsverdriet, J. W. *Concepts of Modern Catalysis and Kinetics*; Wiley-VCH: Weinheim, 2003.
(478) Liu, Z.-P.; Hu, P. *J. Chem. Phys.* **2001**, *115*, 4977.
(479) Pallassana, V.; Neurock, M. *J. Catal.* **2000**, *191*, 301.
(480) Bligaard, T.; Norskov, J. K.; Dahl, S.; Matthiesen, J.; Christensen, C. H.; Sehested, J. *J. Catal.* **2004**, *224*, 206.
(481) Van Santen, R. A.; Neurock, M.; Shetty, S. G. *Chem. Rev.* **2010**, *110*, 2005.
(482) Norskov, J. K.; Bligaard, T.; Logadottir, A.; Bahn, S.; Hansen, L. B.; Bollinger, M.; Hammer, B.; Sljivancanin, Z.; Mavrikakis, M.; Xu, Y.; Dahl, S.; Jacobsen, C. J. H. *J. Catal.* **2002**, *209*, 275.
(483) Petersen, M.; Wagner, F.; Hufnagel, L.; Scheffler, M.; Blaha, P.; Schwarz, K. *Comput. Phys. Commun.* **2000**, *126*, 294.
(484) Kresse, G.; Furthmüller, J. *Comput. Mater. Sci.* **1995**, *6*, 15. Kresse, G.; Joubert, D. *Phys. Rev. B* **1998**, *59*, 1758.
(485) Blöchl, P. *Phys. Rev. B* **1994**, *50*, 17953.
(486) Hammer, B. *Surf. Sci.* **2000**, *49*, 323.
(487) Reuter, K.; Frenkel, D.; Scheffler, M. *Phys. Rev. Lett.* **2004**, *93*, 116105.
(488) Hess, F.; Farkas, A.; Seitsonen, A. P.; Over, H. *J. Comp. Chem.* **2011**, *33*, 757−766.
(489) Rosenthal, D.; Girgsdies, F.; Timpe, O.; Blume, R.; Weinberg, G.; Teschner, D.; Schlögl, R. *Z. Phys. Chem.* **2009**, *223*, 183.
(490) Kanzler, C.; Hofmann, J. P.; Over, H. Unpublished experiments, 2009.
(491) Hofmann, J. P.; Zweidinger, S.; Seitsonen, A. P.; Farkas, A.; Knapp, M.; Balmes, O.; Lundgren, E.; Andersen, J. N.; Over, H. *Phys. Chem. Chem. Phys.* **2010**, *12*, 15358.
(492) Rossler, M.; Gunther, S.; Wintterlin, J. *J. Phys. Chem. C* **2007**, *111*, 2242.
(493) Wang, H. Y.; Schneider, W. F. *Surf. Sci.* **2009**, *603*, L91.
(494) Gilman, S. *J. Phys. Chem.* **1964**, *68*, 70.
(495) Watanabe, M.; Motoo, S. *J. Electroanal. Chem.* **1975**, *60*, 267.
(496) Santos, E.; Leiva, E. P. M.; Vielstich, W. *Electrochim. Acta* **1991**, *36*, 555.
(497) Lebedeva, N. P.; Koper, M. T. M.; Feliu, J. M.; Van Santen, R. A. *J. Phys. Chem. B* **2002**, *106*, 12938.
(498) Markovic, N. M.; Ross, P. N. *J. Cat. Tech.* **2000**, *4*, 110.
(499) Frelink, T.; Visscher, W.; Van Veen, J. A. *Surf. Sci.* **1995**, *335*, 353.
(500) Frelink, T.; Visscher, W.; Van Veen, J. A. *Langmuir* **1996**, *12*, 3702.
(501) Wang, W. B.; Zei, M. S.; Ertl, G. *Chem. Phys. Lett.* **2002**, *355*, 301.
(502) (a) Kim, Y. K.; Morgan, G. A.; Yates, J. T. *J. Phys. Chem. C* **2007**, *111*, 3366. (b) Vendelbo, S. B.; Johansson, M.; Mowbray, D. J.; Andersson, M. P.; Abild-Pedersen, F.; Nielsen, J. H.; Norskov, J. K.; Chorkendorff, I. *Top. Catal.* **2010**, *53*, 357.
(503) Sljivancanin, Z.; Hammer, B. *Phys. Rev. B.* **2010**, *81*, 121413(R).
(504) Matsumoto, M.; Ito, S. *J. Chem. Soc., Chem. Commun.* **1981**, 907.
(505) Yamaguchi, K.; Mizuno, N. *Angew. Chem.* **2002**, *41*, 4538.
(506) Musawir, M.; Davey, P. N.; Kelly, G.; Kozhevnikov, I. V. *J. Chem. Soc. Chem. Commun.* **2003**, 1414.
(507) Yamaguchi, K.; Mizuno, N. *Chem.—Eur. J.* **2003**, *9*, 4353.
(508) Mizuno, N.; Yamaguchi, K. *Catal. Today* **2008**, *132*, 16.
(509) Fu, X. B.; Yu, H.; Peng, F.; Wang, H. J.; Qian, Y. *Appl. Catal., A* **2007**, *321*, 190.
(510) Pintar, A.; Batista, J.; Tisler, T. *Appl. Cata. B: Environ.* **2008**, *84*, 30.
(511) Nowakowski, P.; Dallas, J.-P.; Viallain, S.; Kopia, A.; Gavarri, J.-R. *J. Solid State Chem* **2008**, *181*, 1005.
(512) Li, F.; Chen, J.; Zhang, Q.; Wang, Y. *Green Chem.* **2008**, *10*, 553.
(513) Kim, J.-W.; Yamaguchi, K.; Mizuno, N. *Angew. Chem., Int. Ed.* **2008**, *47*, 9249.

(514) Villain, K.; Kirschhock, C. E. A.; Martens, J. A.; Liang, D.; Van Tendeloo, G. *Angew. Chem. Int. Ed.* **2006**, *45*, 3106.
(515) (a) Tschamber, V.; Jeguirim, M.; Villani, K.; Martens, J.; Ehrburger, P. *Appl. Catal. B: Environ.* **2007**, *72*, 299. (b) Jeguirim, M.; Tschmaber, V.; Villani, K.; Brilhac, J. F.; Martens, J. A. *Chem. Eng. Technol.* **2009**, *32*, 830.
(516) Okumoto, H.; Ohtsuka, K.; Banjoya, S. *Synlett.* **2007**, *20*, 3201.
(517) Yan, N.; Chen, W.; Chen, J.; Qu, Z.; Guo, Y.; Yang, S.; Jia, J. *Environ. Sci. Technol.* **2011**, *45*, 5725.
(518) Iwanaga, K.; Seki, K.; Hibi, T.; Issoh, K.; Suzuta, T.; Nakada, M.; Mori, Y.; T. Abe, T. *Sumitomo Kagaku* **2004-I**, 1−11.
(519) Baerns, M.; Imbihl, R.; Kondratenko, V. A.; Kraehnert, R.; Offermans, W. K.; van Santen, R. A.; Scheibe, A. *J. Catal.* **2005**, *232*, 226 and references therein.
(520) Twigg, M. V. *Catal. Today* **2006**, *117*, 407.
(521) Adeyemo, A.; Hunter, G.; Dutta, P. K. *Sensors Actuators B: Chem.* **2011**, *152*, 307.
(522) Macyk, W.; Kisch, H. *Monatsh. Chem.* **2007**, *138*, 935.
(523) Yamaguchi, K.; He, J.; Oishi, T.; Mizuno, N. *Chem.—Eur. J.* **2010**, *16*, 7199.
(524) Nikaidou, F.; Ushiyama, H.; Yamaguchi, K.; Yamashita, K.; Mizuno, N. *J. Phys. Chem. C* **2010**, *114*, 10873.
(525) Park, J.-N.; Shon, J. K.; Jin, M.; Kong, S. S.; Moon, K.; Park, G. O.; Boo, J.-H.; Kim, J. M. *React. Kinet. Mech. Cat.* **2011**, *103*, 87.
(526) Weldon, M. K.; Friend, C. M. *Chem. Rev.* **1996**, *96*, 1391.
(527) Mavrikakis, M.; Barteau, M. A. *J. Mol. Catal. A: Chem.* **1998**, *131*, 135.
(528) Salmeron, M.; Schlogl, R. *Surf. Sci. Rep.* **2008**, *63*, 169.
(529) Li, W.; Liu, H.; Iglesia, E. *J. Phys. Chem. B* **2006**, *110*, 23337.
(530) Wagner, E.; Fetzer, T. In *Handbook of Heterogeneous Catalysis*; Ertl, G.; Knözinger, H.; Weikamp, J., Eds.; Wiley: New York, 1997; Vol. *4*, p 1748.
(531) Mieher, W. D.; Ho, W. *Surf. Sci.* **1995**, *322*, 151.
(532) Bradley, J. M.; Hopkinson, A.; King, D. A. *J. Phys. Chem.* **1995**, *99*, 17032.
(533) Imbihl, R.; Scheibe, A.; Zeng, Y. F.; Günther, S.; Kraehnert, R.; Kondratenko, V. A.; Baerns, M.; Offermans, W. K.; Jansen, A. P. J.; van Santen, R. A. *Phys. Chem. Chem. Phys.* **2007**, *9*, 3522.
(534) Nilsen, O.; Kjekshus, A.; Fjellvag, H. *Appl. Catal., A* **2001**, *207*, 43.
(535) Hannevold, L.; Nilsen, O.; Kjekshus, A.; Fjellvag, H. *Appl. Catal., A* **2005**, *284*, 163.
(536) Sadykov, V. A.; Isupova, L. A.; Zolotarskii, I. A.; Bobrova, L. N.; Noskov, A. S.; Parmon, V. N.; Brushtein, E. A.; Telyatnikova, T. V.; Chernyshev, V. I.; Lunin, V. V. *Appl. Catal., A* **2000**, *204*, 59.
(537) Perez-Ramirez, J.; Vigeland, B. *Angew. Chem., Int. Ed.* **2005**, *44*, 1112.
(538) Wang, C.-C.; Yang, Y.-J.; Jiang, J. *Phys. Chem. C* **2009**, *113*, 2816.
(539) Wang, C.-C.; Yang, Y.-J.; Jiang, J.-C.; Tsai, D.-S.; Hsieh, H.-M. *J. Phys. Chem. C* **2009**, *113*, 17411.
(540) Schriber, T. J.; Parravano, G. *Chem. Eng. Sci.* **1967**, *22*, 1067.
(541) Qin, J. Y.; Aika, K. *Appl. Catal. B-Environ.* **1998**, *16*, 261.
(542) Barbier, J. Jr.; Oliviero, L.; Renard, B.; Duprez, D. *Catal. Today* **2002**, *75*, 29.
(543) Lee, D. K.; Cho, J. S.; Yoom, W. L. *Chemoshpere* **2005**, *61*, 573.
(544) Li, Y.; Armor, J. N. *Appl. Catal., B* **1997**, *13*, 131.
(545) Amblard, M.; Burch, R.; Southward, B. W. L. *Appl. Catal. B: Environ.* **1999**, *22*, L159.
(546) Mah, D. T.; Weidner, J. W.; Motupally, S. *J. Electrochem. Soc.* **1999**, *146*, 3924.
(547) Seki, K. *Shokubai* **2009**, *51*, 540.
(548) Deacon, H. U.S. Patent 1875,165,6802.
(549) Allen, J. A.; Clark, A. J. *Rev. Pure Appl. Chem.* **1971**, *21*, 145.
(550) Quant, J. T.; van Dam, J.; Engel, F.; Wattemena, F. *Chem. Eng. (July/August)* **1963**, 224.
(551) Mitsui Toatsu Chemicals: A Modern Version of the Deacon Process. *Chemical Week* **1987**, June 24, 18.
(552) Mortensen, M.; Minet, R. G.; Tsotsis, T. T.; Benson, S. *Chem. Eng. Sci.* **1996**, *15*, 2031.
(553) Nieken, U.; Watzenberger, O. *Chem. Eng. Sci.* **1999**, *54*, 2619.
(554) Itoh, H.; Kono, Y.; Ajioka, M.; Takezaka, S.; Katzita, M. U.S. Patent 4803,065,1989.
(555) Kiyoura, T.; Kogure, Y.; Nagayama, T.; Kanaya, K. U.S. Patent 4822,589,1989.
(556) Yasuaki, T. *Stud. Surf. Sci. Catal.* **1995**, *92*, 41.
(557) Gestermann, F.; Ottaviani, A. *Mod. Alkali Technol.* **2001**, *8*, 49−56.
(558) Jörissen, J.; Turek, T.; Weber, R. *Chemie in unserer Zeit* **2011**, *45*, 172.
(559) Trasatti, S. In *Interfacial Electrochemistry: Theory, Practice, Applications*; Wieckowski, A., Ed.; Marcel Dekker: New York, 1999; p 769.
(560) Hevia, M. A.; Amrute, A. P.; Schmidt, T.; Perez-Ramirez, J. *J. Catal.* **2010**, *276*, 141.
(561) Amrute, A. P.; Mondelli, C.; Hevia, M. A. G.; Perez-Ramirez, J. *J. Phys. Chem. C* **2011**, *115*, 1056.
(562) Mars, P.; van Krevelen, D. W. *Chem. Eng. Sci. (Spec. Suppl.)* **1954**, *3*, 41.
(563) Tarabanko, V. E.; Tarabanko, N. V.; Koropachinskaya, N. V. *Catal. Ind.* **2010**, *2*, 259.
(564) Mondelli, C.; Amrute, A. P.; Schmidt, T.; Perez-Ramirez, J. *Chem. Commun.* **2011**, *47*, 7173.
(565) Amrute, A. P.; Modelli, C.; Hevia, M. A. G.; Perez-Ramirez, J. *ACS Catal.* **2011**, *1*, 583.
(566) Beer, H. B. *Improvements in or relating to electrodes for electrolysis*, British Patent, 1,147,442, Appl. 20133/65, 12.5.1965, p 10.
(567) Li, M.; Feng, C. P.; Hu, W. W.; Zhang, Z. Y.; Sugiura, N. *J. Hazard. Mat.* **2009**, *162*, 455.
(568) Radjenovic, J.; Bagastyo, A.; Rozendal, R. A.; Mu, Y.; Keller, J.; Rabaey, K. *Water Res.* **2011**, *45*, 1579.
(569) (a) Lyons, M. E. G.; Lyons, C. H.; Michas, A.; Bartlett, P. N. *J. Electroanal. Chem.* **1993**, *351*, 245. (b) O'Sullivan, E. J. M.; White, J. R. *J. Electrochem. Soc.* **1989**, *136*, 2576.
(570) Ardizzone, S.; Trasatti, S. *Adv. Colloid Interface Sci.* **1996**, *64*, 173.
(571) Lodi, G.; Zucchini, G.; De Battisti, A.; Sivieri, E.; Trasatti, S. *Mater. Chem.* **1978**, *3*, 179.
(572) Burke, L. D.; Scannell, R. A. *J. Electroanal. Chem.* **1984**, *175*, 119.
(573) Kokoulina, D. V.; Kraovitskaya, Y. I.; Ivanova, T. V. *Elektrokhimiya* **1978**, *14*, 470.
(574) Trasatti, S. *J. Electroanal. Chem.* **1980**, *111*, 125.
(575) Tomkiewicz, M.; Huang, Y. S.; Pollak, F. H. *J. Electrochem. Soc.* **1983**, *130*, 1514.
(576) Pirovano, C.; Trasatti, S. *Colloids Surf.* **1983**, *7*, 15.
(577) Kleijn, J. M.; Lyklema, J. *J. Colloid Interface Sci.* **1987**, *120*, 511.
(578) Daghetti, A.; Lodi, G.; Trasatti, S. *Mater. Chem. Phys.* **1983**, *8*, 1.
(579) Trasatti, S.; Petrii, O. A. *Pure Appl. Chem.* **1991**, *63*, 711.
(580) Safonova, T. Y.; Petrii, O. A.; Gudkova, E. A. *Elektrokhimiya* **1980**, *16*, 1607.
(581) Battaglin, G.; Canera, A.; Della Mea, G.; Lodi, G.; Trasatti, S. *J. Chem. Soc., Faraday Trans.* **1985**, *81*, 2995.
(582) Siviglia, P.; Daghetti, A.; Trasatti, S. *Colloids Surf.* **1983**, *7*, 15.
(583) Hepel, T.; Pollak, F. H.; O'Grady, W. E. *J. Electrochem. Soc.* **1984**, *131*, 2094.
(584) Kazarinov, V. E.; Andreev, V. N.; Mayorov, A. P. *J. Electronanal. Chem.* **1981**, *130*, 277.
(585) Trasatti, S. In *The Electrochemistry of Novel Materials*; Lipkowski, J.; Ross, P. N., Eds.;VCH Publishers: New York, 1994; p 207.
(586) Savinell, R. F.; Zeller, R. L. III; Adams, J. A. *J. Electrochem. Soc.* **1990**, *137*, 489.
(587) Sugawara, Y.; Yadav, A. P.; Nishikata, A.; Tsuru, T. *J. Electrochem. Soc.* **2008**, *155*, B897.
(588) Trasatti, S. In *Advances in Electrochemistry and Electrochemical Engineering*; Gerischer, H,; Tobias, C. W., Eds.; VHC: Weinheim, 1990; Vol *2*, p 1.

(589) Chen, L.; Guay, D.; Lasia, A. *J. Electrochem. Soc.* **1996**, *143*, 3576.
(590) Trasatti, S. *Croat. Chem. Acta* **1990**, *63*, 313.
(591) Vidal-Iglesias, F. J.; Solla-Gullon, J.; Campina, J. M.; Herrero, E.; Aldaz, A.; Feliu, J. M. *Electrochim. Acta* **2009**, *54*, 4459.
(592) Koper, M. T. M.; Jansen, A. P. L.; v. Santen, R. A.; Lukien, J. J.; Hilbers, P. A. J. *J. Chem. Phys.* **1998**, *109*, 6051.
(593) Laidler, K. J. *Chemical Kinetics*; Harper & Row: New York, 1987.
(594) Tilak, B. V.; Conway, B. E. *Electrochim. Acta* **1992**, *37*, 51.
(595) Kibler, L. A. *Chem. Phys. Chem.* **2006**, *7*, 985.
(596) Breiter, M. W. In *Handbook of Fuel Cells: Fundamentals, Technology and Applications*; Vielstich, W.; Lamm, A.; Gasteiger, H., Eds.; Wiley: Chichester, 2003; Vol. 2, p 361.
(597) Beard, B. C.; Ross, P. N. *J. Electrochem. Soc.* **1990**, *137*, 3368.
(598) Greeley, J.; Jaramillo, T. F.; Bonde, J.; Chorkendorff, I.; Norskov, J. N. *Nat. Mat.* **2006**, *5*, 909.
(599) Nidola, A.; Schira, R. *J. Electrochem. Soc.* **1986**, *133*, 1653.
(600) Kötz, E. R.; Stucki, S. *J. Appl. Electrochem.* **1987**, *17*, 1190.
(601) Ardizzone, S.; Fregonara, G.; Trasatti, S. *J. Electroanal. Chem.* **1989**, *266*, 191.
(602) Boodts, J. C. F.; Trasatti, S. *J. Appl. Electrochem.* **1989**, *19*, 255.
(603) Wen, T. C.; Hu, C. C. *J. Electrochem. Soc.* **1992**, *139*, 2158.
(604) Cornell, A.; Simonsson, D. *J. Electrochem. Soc.* **1993**, *140*, 3123.
(605) Blouin, M.; Guay, D. *J. Electrochem. Soc.* **1997**, *144*, 573.
(606) Chen, L.; Guay, D.; Pollak, F. H.; Levy, F. *J. Electroanal. Chem.* **1997**, *429*, 185.
(607) Chabanier, C.; Irissou, E.; Guay, D.; Pelletier, J. F.; Sutton, F.; Lurio, L. B. *Electrochem. Solid-State Lett.* **2002**, *5*, E40.
(608) Rochefort, D.; Dabo, P.; Guay, D.; Sherwood, P. M. A. *Electrochim. Acta* **2003**, *48*, 4245.
(609) Harrison, J. A.; Caldwell, D. L.; White, R. E. *Electrochim. Acta* **1984**, *29*, 203.
(610) Kodinstev, I. M.; Trasatti, S. *Electrochim. Acta* **1994**, *39*, 1803.
(611) Chabanier, C.; Guay, D. *J. Electroanal. Chem.* **2004**, *570*, 13.
(612) Burke, L. D.; Naser, N. S. *J. Appl. Electrochem.* **2005**, *35*, 931.
(613) (a) Lister, T. E.; Chu, Y.; Cullen, W.; You, H.; Yonco, R. M.; Mitchell, J. F.; Nagy, Z. *J. Electroanal. Chem.* **2002**, *201*, 524−525. (b) Lister, T. E.; Tolmachev, Y. V.; Chu, Y.; Cullen, W. G.; You, H.; Yonco, R.; Nagy, Z. *J. Electroanal. Chem.* **2003**, *71*, 554−555.
(614) EuroChlor, *Chlorine Industry Review*, 2007−2008.
(615) Pecherckii, M. M.; Gorodeskii, V. V.; Bune, N. Ya.; Losev, V. V. *Elektrokimiya* **1982**, *18*, 415.
(616) Makarichev, Yu.B.; Spasskaya, E. K.; Khedkievich, S. D.; Yakimenko, L. M. *Elektrokimiya* **1976**, *12*, 994.
(617) De Faria, L. A.; Trasatti, S. *J. Electronanal. Chem.* **1992**, *340*, 145.
(618) Eben, D.; Hui, R.; Zhang, J.; Liu, Z.-S.; Shi, Z. *J. Phys. Chem. C* **2010**, *114*, 13162.
(619) Colomer, M. T.; Jurado, J. R. *Chem. Mater.* **2000**, *12*, 923.
(620) Comninellis, Ch.; Vercesi, G. P. *J. Appl. Electrochem.* **1991**, *21*, 335.
(621) De Nora, O. *Chem.-Ing.-Tech.* **1970**, *43*, 182.
(622) Malpass, G. R.; Miwa, D. W.; Machado, S. A.; Olivi, P.; Motheo, A. J. *J. Hazard. Mater.* **2007**, *137*, 565.
(623) Carlesi Jara, C.; Fino, D.; Specchia, V.; Saracco, G.; Spinelli, P. *Appl. Catal. B: Environ.* **2007**, *70*, 479.
(624) Gallard, H.; Leclercq, A.; Croue, J. P. *Chemosphere* **2004**, *56*, 465.
(625) Matsumoto, Y.; Sato, E. *Electrochim. Acta* **1980**, *25*, 585.
(626) Tilak, B. V. *J. Electrochem. Soc.* **1979**, *126*, 1343.
(627) Efremov, B. N.; Tarasevich, M. R. *Elektrokhimiya* **1981**, *17*, 1672.
(628) Mozota, J.; Vukovic, M.; Conway, B. E. *J. Electroanal. Chem.* **1980**, *114*, 1533.
(629) Hine, F.; Ysuda, M.; Noda, T.; Yoshida, T.; Okuda, J. *J. Electrochem. Soc.* **1979**, *126*, 1439.
(630) Bondar, R. U.; Kalinovskii, A. E. *Elektrokhimiya* **1978**, *14*, 730.
(631) Mills, A.; Davies, H. *J. Chem. Soc. Faraday Trans.* **1990**, *86*, 955.
(632) Nidola, A. In *Electrodes of Conductive Metallic Oxides, Part B*; Trasatti, S., Ed.; Elsevier, Amsterdam, 1980; p 627.
(633) Horacek, J.; Puschaver, S. *Chem. Eng. Prog.* **1971**, *67*, 71.
(634) Yi, Z.; Kangning, C.; Wei, W.; Wang, J.; Lee, S. *Ceram. Int.* **2007**, *33*, 1087.
(635) Jovanovic, V. M.; Dekanski, A.; Depotov, P.; Nikolic, B. Z.; Atanasosko, R. T. *J. Electroanal. Chem.* **1992**, *339*, 147.
(636) Atanasoska, Lj.; Atanansoski, R. T.; Pollak, F. H.; O'Grady, W. E. *Surf. Sci.* **1990**, *230*, 95.
(637) Gerrard, W. A.; Steele, B. C. H. *J. Appl. Electrochem.* **1978**, *8*, 417.
(638) Trasatti, S. *Electrochim. Acta* **1987**, *32*, 369.
(639) Burke, L. D.; O'Neill, J. F. *J. Electroanal. Chem.* **1979**, *101*, 341.
(640) Petkov, L. *Oxidation Commun.* **2009**, *32*, 654.
(641) Trasatti, S.; O'Grady, W. E. *Adv. Electrochem. Eng.* **1981**, *12*, 117.
(642) Janssen, L. J. J.; Starmans, L. M. C.; Visser, J. G.; Barendrecht, E. *J. Electrochim. Acta* **1977**, *22*, 1093.
(643) Krishtalik, L. I. *Electrochim. Acta* **1981**, *26*, 329.
(644) Erenburg, R. G.; Krishtalik, L. I.; Yaroshevskaya, I. P. *Elektrokhimiya* **1975**, *11*, 1236.
(645) Erenburg, R. G.; Krishtalik, L. I.; Yaroshevskaya, I. P. *Elektrokhimiya* **1975**, *11*, 1068.
(646) Erenburg, R. G. *Elektrokhimiya* **1984**, *20*, 1602.
(647) Hepel, T.; Pollak, F. H.; O'Grady, W. E. *J. Electrochem. Soc.* **1986**, *133*, 69.
(648) Augustynski, J.; Balsenc, L.; Hinden, J. *J. Electrochem. Soc.* **1978**, *125*, 1093.
(649) Consonni, V.; Trasatti, S.; Pollak, F.; O'Grady, W. E. *J. Electroanal. Chem.* **1987**, *228*, 393.
(650) Thomassen, M.; Karlsen, C.; Borresen, B.; Tunold, R. *Electrochim. Acta* **2006**, *51*, 2909.
(651) Losev, V. V.; Bune, N. Y.; Chuvaeva, L. E. *Electrochim. Acta* **1989**, *34*, 929.
(652) Guerrini, E.; Consonni, V.; Trasatti, S. *J. Sol. Stat. Electrochem* **2005**, *9*, 320.
(653) Hepel, T.; Pollak, F. H.; O'Grady, W. E. *J. Electroanal. Chem.* **1985**, *188*, 281.
(654) Ferro, S.; De Battisti, A. *J. Phys. Chem B* **2002**, *106*, 2249.
(655) Nørskov, J. K.; Rossmeisl, J.; Logadottir, A.; Lindqvist, L.; Kitching, J. R.; Bligaard, T.; Jonsson, H. *J. Phys. Chem. B* **2004**, *108*, 17886.
(656) Filhol, J. S.; Neurock, M. *Angew. Chem., Int. Ed.* **2006**, *45*, 402.
(657) Zhang, T.; Anderson, A. B. *Electrochim. Acta* **2007**, *53*, 982.
(658) Hansen, H. A.; Man, I. C.; Studt, F.; Abild-Pedersen, F.; Bligaard, T.; Rossmeisl, J. *Phys. Chem. Chem. Phys.* **2010**, *12*, 283.
(659) Trasatti, S. In *Electrochemical Hydrogen Technologies*; Wendt, H., Ed.; Elsevier: Amsterdam, 1990; p 104.
(660) Stucki, S.; Menth, A. *Ber. Bunsenges. Phys. Chem.* **1980**, *84*, 1008.
(661) Lodi, G.; Sivieri, E.; De Battisti, A.; Trasatti, S. *J. Appl. Electrochem.* **1978**, *8*, 135.
(662) Chang, C. C.; Wen, T. C. *J. Appl. Electrochem.* **1997**, *27*, 355.
(663) Guerrini, E.; Trasatti, S. *Russ. J. Electrochem.* **2006**, *42*, 1017.
(664) Castelli, P.; Trasatti, S.; Pollak, F. H.; O'Grady, W. E. *J. Electroanal. Chem.* **1986**, *210*, 189.
(665) Trasatti, S.; Buzzanca, G. *J. Electroanal. Chem.* **1971**, *29*, A1.
(666) Angeletta, C.; Falciola, M.; Trasatti, S. *J. Electroanal. Chem.* **1986**, *205*, 347.
(667) Rossmeisl, J.; Qu, Z.-W.; Zhu, H.; Kroes, G.-J.; Norskov, J. K. *J. Electroanal. Chem.* **2007**, *607*, 83.
(668) Fang, Y.-H.; Liu, Z.-P. *J. Am. Chem. Soc.* **2010**, *132*, 18214.
(669) Stamenkovic, V.; Moon, B. S.; Mayrhofer, K. J. J.; Ross, P. N.; Markovic, N. M.; Rossmeisl, J.; Greeley, J.; Norskov, J. K. *Angew. Chem., Int. Ed.* **2006**, *45*, 2897.
(670) Rossmeisl, J.; Norskov, J. K.; Taylor, C. D.; Janik, M. J.; Neurock., M. *J. Phys. Chem. B* **2006**, *110*, 21833.

(671) Man, I. C.; Su, H.-Y.; Calle-Vallejo, F.; Hansen, H. A.; Martinez, J. I.; Inoglu, N. G.; Kitchin, J.; Jaramillo, T. F.; Norskov, J. K.; Rossmeisl, J. *ChemCatChem* **2011**, *3*, 1159.
(672) Trasatti, S.; O'Grady, W. E. In *Advances in Electrochemistry and Electrochemical Engineering*; Gericher, H.; Tobias, C. W., Eds.; Wiley: New York, 1980; Vol *13*, p 177.
(673) Trasatti, S. *Electrochim. Acta* **1984**, *29*, 1503.
(674) Ye, Z. G.; Meng, H. M.; Sun, D. B. *Electrochim. Acta* **2008**, *53*, 5639.
(675) Di Blasi, A.; S'Urso, C.; Baglio, V.; Antonucci, V.; Arico, A. S.; Ornelas, R.; Matteucci, F.; Orozco, G.; Beltran, D.; Meas, Y.; Arriaga, L. G. *J. Appl. Electrochem.* **2009**, *39*, 191.
(676) Da Silva, L. M.; Boodts, J. F. C.; De Faira, L. A. *Electrochim. Acta* **2001**, *46*, 1369.
(677) Jirkovsky, J.; Makarova, M.; Krtil, P. *Electrochem. Commun.* **2006**, *8*, 1417.
(678) Santana, M. H. P.; De Faira, L. A. *Electrochim. Acta* **2006**, *51*, 3578.
(679) Fernandes, K. C.; Da Silva, L. M.; Boodts, J. F. C.; De Faira, L. A. *Electrochim. Acta* **2006**, *51*, 2809.
(680) Macounova, K.; Jirkovsky, J.; Makarova, M. V.; Franc, J.; Krtil, P. *J. Sol. Stat. Electrochem.* **2009**, *13*, 959.
(681) Macounova, K.; Makarova, M. V.; Jirkovsky, J.; Franc, J.; Krtil, P. *Electrochim. Acta* **2008**, *53*, 6126.
(682) Musiani, M.; Furlanetto, F.; Bertoncello, R. *J. Electroanal. Chem.* **1999**, *465*, 160.
(683) Bertoncello, R.; Cattarin, S.; Frateur, I.; Musiani, M. *Electroanal. Chem.* **2000**, *492*, 145.
(684) Petrykin, V.; Macounova, K.; Shlyakhtin, O. A.; Krtil, P. *Angew. Chem., Int. Ed.* **2010**, *49*, 4813.
(685) Petrykin, V.; Macounova, K.; Franc, J.; Shlyakhtin, O. A.; Klementova, M.; Mukerjee, S.; Krtil, P. *Chem. Mater.* **2011**, *23*, 200.
(686) Markovic, N. M.; Ross, P. N. Jr. *Surf. Sci. Rep.* **2002**, *45*, 117−229.
(687) Keith, J. A.; Jerkiewicz, G.; Jacob, T. *Chem. Phys. Chem.* **2010**, *11*, 2779.
(688) Keith, J. A.; Jacob, T. *Angew. Chem., Int. Ed.* **2010**, *49*, 9521.
(689) Vante, N.; Tributsch, H. *Nature* **1986**, *323*, 431−432.
(690) Tributsch, H.; Bron, M.; Hilgendorff, M.; Schulenburg, H.; Dorbandt, I.; Eyert, V.; Bogdanoff, P.; Fiechter, S. *J. Appl. Electrochem.* **2001**, *31*, 739−748.
(691) Hara, Y.; Minami, N.; Itagaki, H. *Appl. Catal., A* **2008**, *340*, 59−66.
(692) Babu, P. K.; Lewera, A.; Chung, J. H.; Hunger, R.; Jaegermann, W.; Alonso-Vante, N.; Wieckowski, A.; Oldfield, E. *J. Am. Chem. Soc.* **2007**, *129*, 15140−15141.
(693) Cao, D.; Wieckowki, A.; Inukai, J.; Alonso-Vante, N. *J. Electrochem. Soc.* **2006**, *153*, A869−A874.
(694) Colmenares, L.; Jusys, Z.; Behm, R. J. *J. Phys. Chem. C* **2007**, *111*, 1273−1283.
(695) Fiechter, S.; Dorbandt, I.; Bogdanoff, P.; Zehl, G.; Schulenburg, H.; Tributsch, H.; Bron, M.; Radnik, J.; Fieber-Erdmann, M. *J. Phys. Chem.* **2007**, *111*, 477−487.
(696) Inukai, J.; Cao, D.; Wieckowski, A.; Chang, K.-C.; Menzel, A.; Komanicky, V.; You, H. *J. Phys. Chem C* **2007**, *111*, 16889.
(697) Zehl, G.; Schmithals, G.; Hoell, A.; Haas, S.; Hartnig, Ch.; Dorbandt, I.; Bogdanoff, P.; Fiechter, S. *Angew. Chem., Intl. Ed.* **2007**, *46*, 7311−7314.
(698) Garsany, Y.; Baturina, O.; Swider-Lyons, K. *J. Electrochem. Soc.* **2007**, *154*, B670.
(699) Zehl, G.; Bogdanoff, P.; Dorbandt, I.; Fiechter, S.; Wippermann, K.; Hartnig, C. *J. Appl. Electrochem.* **2007**, *37*, 1475−1484.
(700) Takasu, Y.; Sugimoto, W.; Yoshitake, M. *Electrochemistry* **2007**, *75*, 105.
(701) Takasu, Y.; Oohori, K.; Yoshinaga, N.; Sugimoto, W. *Catal. Today* **2009**, *146*, 248.
(702) Liu, P.; Muckerman, J. T.; Adzic, R. R. *J. Chem. Phys.* **2006**, *124*, 141101.
(703) Winter, M.; Brodd, R. J. *Chem. Rev.* **2004**, *104*, 4245.
(704) Dresselhaus, M. S.; Thomas, I. L. *Nature* **2001**, *414*, 331.
(705) Tributsch, H. *Int. J. Hydrogen Energy* **2008**, *33*, 5911.
(706) Li, Y.; Somorjai, G. A. *Nano Lett.* **2010**, *10*, 2289.
(707) Arico, A. S.; Bruce, P.; Scrosati, B.; Tarascon, J.-M.; Van Schalkwijk, W. *Nat. Mat.* **2005**, *4*, 366.
(708) Miller, J. R.; Simon, P. *Science* **2008**, *321*, 651.
(709) Conte, M. *Fuel Cells* **2010**, *10*, 806.
(710) Kötz, R.; Carlen, M. *Electrochim. Acta* **2000**, *45*, 2483.
(711) Simon, P.; Gogotsi, Y. *Nat. Mat.* **2008**, *7*, 845.
(712) Zhang, L. L.; Zhao, X. S. *Chem. Soc. Rev.* **2009**, *38*, 2520.
(713) Rolison, D. R.; Long, J. W.; Lytle, J. C.; Fischer, A. E.; Rhodes, C. P.; McEvoy, T. M.; Bourg, M. E.; Lubers, A. M. *Chem. Soc. Rev.* **2009**, *38*, 226.
(714) Jow, T. R.; Zheng, J. P. *J. Electrochem. Soc.* **1998**, *145*, 49.
(715) Hu, C.-C.; Chen, W.-C.; Chang, K.-H. *J. Electrochem. Soc.* **2004**, *151*, A281.
(716) Naoi, K.; Simon, P. *Interface* **2008**, *17*, 34.
(717) Fang, W. C.; Huang, J. H.; Chen, L. C.; Su, Y. L. O.; Chen, K. H. *J. Power Source* **2006**, *160*, 1506.
(718) Chervin, C. N.; Lubers, A. M.; Pettigrew, K. A.; Long, J. W.; Westgate, M. A.; Fontanella, J. J.; Rolison, D. R. *Nano Lett.* **2009**, *9*, 2316.
(719) Chervin, C. N.; Lubers, A. M.; Long, J. W.; Rolison, D. R. *J. Electroanal. Chem.* **2010**, *644*, 155.
(720) Zheng, J. P.; Jow, T. R. *J. Electrochem. Soc.* **1995**, *142*, L6.
(721) Swider, K. E.; Merzbacher, C. I.; Hagans, P. L.; Rolsin, D. R. *Chem. Mater.* **1997**, *9*, 1248.
(722) Park, B. O.; Lokhande, C. D.; Park, H. S.; Jung, K. D.; Joo, O. S. *Mater. Chem. Phys.* **2004**, *87*, 59.
(723) Sugimoto, W.; Yokoshima, K.; Murakami, Y.; Takasu, Y. *Electrochim. Acta* **2006**, *52*, 1742.
(724) Sopcic, S.; Mandic, Z.; Inzelt, G.; Kraljic Rokovic, M.; Mstrovic, E. *J. Power Sources* **2011**, *196*, 4849.
(725) Hadzi-Jordanov, S.; Kozlowska, H. A.; Conway, B. E. *J. Electroanal. Chem.* **1975**, *60*, 359.
(726) Galizzioli, D.; Tantardini, F.; Trasatti, S. *J. Appl. Electrochem.* **1974**, *4*, 57.
(727) Hadzi-Jordanov, S.; Kozlowska, H. A.; Vukovic, M.; Conway, B. E. *J. Electrochem. Soc.* **1978**, *125*, 1473.
(728) Pell, W.; Liu, T. C.; Conway, B. E. *Electrochim. Acta* **1997**, *42*, 3541.
(729) Dmowski, W.; Egami, T.; Swider-Lyons, K. E.; Love, C. T.; Rolison, D. R. *J. Phys. Chem. B* **2002**, *106*, 12677.
(730) Trasatti, S. *Electrochim. Acta* **1991**, *36*, 225.
(731) Sarangapani, S.; Tilak, B. V.; Chen, C.-P. *J. Electrochem. Soc.* **1996**, *132*, 3791.
(732) Dobelhofer, K.; Metikos, M.; Ogumi, Z.; Gericher, H. *Ber. Bunsen Ges. Phys. Chem.* **1978**, *82*, 1046.
(733) Yamada, A.; Goodenough, J. B. *J. Electrochem. Soc.* **1998**, *145*, 737.
(734) Mo, Y.; Antonio, M. R.; Scherson, D. A. *J. Phys. Chem B* **2000**, *104*, 9777.
(735) Zheng, J. P.; Jow, T. R.; Jiam, Q. X.; Wu, X. D. *J. Electrochem. Soc.* **1996**, *143*, 1068.
(736) Zheng, J. P.; Cygan, P. J.; Jow, T. R. *J. Electrochem. Soc.* **1995**, *142*, 2699.
(737) McKeown, D. A.; Hagans, P. L.; Carette, L. P. L.; Russell, A. E.; Swider, K. E.; Rolison, D. R. *J. Phys. Chem. B* **1999**, *103*, 4825.
(738) Kim, H.; Popov, B. N. *J. Power Sources* **2002**, *204*, 52.
(739) Mills, A.; Giddings, S.; Patel, I.; Lawrence, C. *J. Chem. Soc. Faraday Trans. 1* **1987**, *83*, 2331.
(740) Adams, D. M.; Brus, L.; Chidsey, C. E .D.; Creager, S.; Creutz, C.; Kagan, C. R.; Kamat, P. V.; Lieberman, M.; Lindsay, S.; Marcus, R. A.; Metzger, R. M.; Michel-Beyerle, M. E.; Millller, J. R.; Newton, M. D.; Rolison, D. R.; Sankey, O.; Schanze, K. S.; Yardley, J.; Zhu, X. *J. Phys. Chem. B* **2003**, *107*, 6668.
(741) Ma, Z. R.; Zheng, J. P.; Fu, R. Q. *Chem. Phys. Lett.* **2000**, *331*, 64.

(742) Zheng, J. P.; Xin, Y. *J. Power Source* **2002**, *110*, 86.
(743) Sugimoto, W.; Iwata, H.; Yokoshima, K.; Murakami, Y.; Takasu. *J. Phys. Chem. B* **2005**, *109*, 7330.
(744) Sugimoto, W.; Iwata, H.; Yasunaga, Y.; Murakami, Y.; Takasu, Y. *Angew. Chem., Int. Ed.* **2003**, *42*, 4092.
(745) Fukunaka, Y.; Motoyama, M.; Konishi, Y.; Ishii, R. *Electrochem. Solid-State Lett.* **2006**, *9*, C62.
(746) Lin, K.-M.; Chang, K.-H.; Hu, C.-C.; Li, Y.-Y. *Electrochim. Acta* **2009**, *54*, 4574.
(747) Gewirth, A. A.; Throum, M. S. *Inorg. Chem.* **2010**, *49*, 3557.
(748) Ferrin, P.; Nilekar, A. U.; Greeley, J.; Mavrikakis, M.; Rossmeisl. *J., Surf. Sci.* **2008**, 3364.
(749) Jarvi, T. D.; Stuwe, E. M. In *Electrocatalysis* Lipkowski, J.; Ross, P.N., Eds.; Wiley: New York, 1998; p 75.
(750) Kawatsu, S. *J. Power Sources* **1998**, *71*, 150.
(751) Antolini, E. *Mater. Chem. Phys.* **2003**, *78*, 563.
(752) Gasteiger, H. A.; Markovic, N. M. *Science* **2009**, *324*, 48.
(753) Long, J. W.; Stroud, R. M.; Swider-Lyons, K. E.; Rolison, D. R. *J. Phys. Chem. B* **2000**, *104*, 9772.
(754) Villullas, H. M.; Mattos-Costa, F. I.; Bulhoes, L. O. S. *J. Phys. Chem. B* **2004**, *108*, 12898.
(755) Lasch, K.; Jorissen, L.; Friedrich, K. A.; Garche, J. *J. Sol. Stat. Electrochem.* **2003**, *7*, 619.
(756) Sirk, A. H. C.; Hill, J. M.; Kung, S. K. Y.; Birss, V. I. *J. Phys. Chem. B* **2004**, *108*, 689.
(757) Arico, A. S.; Monforte, G.; Modica, E.; Antonucci, P. L.; Antonucci, V. *Electrochem. Commun.* **2000**, *2*, 466.
(758) Bock, C.; Blakely, M. A.; MacDougall, B. *Electrochim. Acta* **2005**, *50*, 2401.
(759) Cao, L.; Scheiba, F.; Roth, C.; Schweiger, F.; Cremers, C.; Stimming, U.; Fuess, H.; Chen, L. Q.; Zhu, W. T.; Qiu, X. P. *Angew. Chem., Int. Ed.* **2006**, *45*, 5315.
(760) Gomez de la Fuente, J. L.; Martinez-Heurta, M. V.; Rojas, S.; Hernandez-Fernandez, P.; Terreros, P.; Fierro, J. L. G.; Pena, M. A. *Appl. Catal. B: Environ.* **2009**, *88*, 505.
(761) Ma, J.-H.; Feng, Y.-Y.; Yu, J.; Zhao, D.; Wang, A.-J.; Xu, B.-Q. *J. Catal.* **2010**, *275*, 34.
(762) Antolini, E.; Giorgi, L.; Pozio, A.; Passalaqua, E. *J. Power Sources* **1999**, *77*, 136.
(763) Gu, Y.-J.; Wong, W.-T. *J. Electrochem. Soc.* **2006**, *153*, A1714.
(764) (a) Thomas, S. C.; Ren, X.; Gottesfeld, S. *J. Electrochem. Soc.* **1999**, *146*, 4354. (b) Scheiba, F.; Scholz, M.; Cao, L.; Schafranek, R.; Roth, C.; Cremers, C.; Qiu, X.; Stimming, U.; Fuess, H. *Fuel Cells* **2006**, *6*, 439.
(765) Pylypenko, S.; Blizanac, B. B.; Olson, T. S.; Konopka, D.; Atanassov, P. *Appl. Mater. Interfaces* **2009**, *1*, 604.
(766) Tarascon, J.-M.; Armand, M. *Nature* **2001**, *414*, 359.
(767) Mohri, M.; Yangisawa, N.; Tajimay, Y.; Tanaka, H.; Mitate, T.; Nakajima, S.; Yoshida, M.; Yoshimoto, Y.; Suzuki, T.; Wada, H. *J. Power Sources* **1989**, *26*, 545.
(768) Nagaura, T.; Tozawa, K. *Prog. Battery Solar Cells* **1990**, *9*, 209.
(769) Poizot, P.; Laruelle, S.; Grugeon, S.; Dupont., L.; Tarascon, J.-M. *Nature* **2000**, *407*, 496.
(770) Armand, M.; Tarascon, J.-M. *Nature* **2008**, *451*, 652.
(771) Guo, Y.-G.; Hu, Y.-S.; Sigle, W.; Maier, J. *Adv. Mater.* **2007**, *19*, 2087.
(772) Padhi, A. K.; Nanjundaswamy, K. S.; Goodenough, J. B. *J. Electrochem. Soc.* **1997**, *144*, 1188.
(773) Herle, P. S.; Ellis, B.; Coombs, N.; Nazar, L. F. *Nat. Mater.* **2004**, *3*, 147.
(774) Dominko, R.; Bele, M.; Gaberscek, M.; Remskar, M.; Hanzel, D.; Pejovnik, S.; Jamnik, J. *J. Electrochem. Soc.* **2005**, *152*, A607.
(775) Hu, Y.-S.; Guo, Y.-G.; Dominko, R.; Gaberscek, M.; Jamnik, J.; Maier, J. *Adv. Mater.* **2007**, *19*, 1963.
(776) Bard., A. J. *Science* **1980**, *207*, 139.
(777) Bockris, J. O'M.; Kainthla, R. C. *Int. J. Hydrogen Energy* **1988**, *13*, 375.
(778) Bard, A. J.; Fox, M. *A., Acc. Chem. Res.* **1995**, *28*, 141.
(779) Jaksic, M. M. *Mater. Chem. Phys.* **1989**, *22*, 19.
(780) Ni, M.; Leung, M. K. H.; Leung, D. Y. C.; Sumathy, K. *Renewable Sustainable Energy Rev.* **2007**, *11*, 401.
(781) Kitano, M.; Tsujimaru, K.; Anpo, M. *Top. Catal.* **2008**, *49*, 4.
(782) Kudo, A.; Miseki, Y. *Chem. Soc. Rev.* **2009**, *38*, 253.
(783) Chen, X.; Mao, S. S. *Chem. Rev.* **2007**, *107*, 2891.
(784) Grätzel, M. *Nature* **2001**, *414*, 338.
(785) Youngblood, W. J.; Lee, S.-H. A.; Maeda, K.; Mallouk, T. E. *Acc. Chem. Res.* **2009**, *42*, 1966.
(786) Borodovsky, Y. *Proc. SPIE* **2006**, *6153*, 615302.
(787) Tichenor, D. A.; Kubiak, G. D.; Replogle, W. C.; Klebanoff, L. E.; Wronosky, J. B.; Hale, L. C.; Chapman, H. N.; Taylor, J. S.; Folta, J. A.; Montcalm, C.; Hudyma, R. M.; Goldberg, K. A.; Naulleau, P. P. *Proc. SPIE* **2000**, *3997*, 48.
(788) Belau, L.; Park, J. Y.; Liang, T.; Seo, H.; Somorjai, G. A. *J. Vac. Sci. Technol. B* **2009**, *27*, 1919.
(789) Mertens, B.; Weiss, M.; Meiling, H.; Klein, R.; Louis, E.; Kurt, R.; Wedowski, M.; Trenkler, H.; Wolschrijn, B.; Jansen, R.; van de Runstraat, A.; Moors, R.; Spee, K.; Plöger, S.; Van de Kruijs, R. *Microelectron. Eng.* **2004**, *16*, 73−74.
(790) Hollenshead, J.; Klebanoff, L. In *Emerging Lithography Technologies VIII*; Mackay, R. S., Ed.; *Proc. SPIE* **2004**, *5374*, 675.
(791) Hollenshead, J.; Klebanoff, L. *J. Vac. Sci. Technol. B* **2006**, *24*, 64.
(792) Hollenshead, J.; Klebanoff, L. *J. Vac. Sci. Technol. B* **2006**, *24*, 118.
(793) Benoit, N.; Schröder, S.; Yulin, S.; Feigl, T.; Duparre, A.; Kaiser, N.; Tünnermann, A. *Appl. Opt.* **2008**, *47*, 3455.
(794) Bajt, S.; Dai, Z. R.; Nelson, E. J.; Wall, M. A.; Alameda, J. B.; Nguyen, V.; Baker, S. L.; Robinson, J. C.; Taylor, J. S.; Aquila, A.; Edwards, N. V. *J. Microlith. Microfab. Microsyst.* **2006**, *5*, 023004.
(795) Madey, T. E.; Faradzhev, S.; Yakshinskiy, B. Y.; Edwards, N. V. *Appl. Surf. Sci.* **2006**, *253*, 1681.
(796) Koster, N.; Mertens, B.; Jansen, R.; Van de Runstraat, A.; Stietz, F.; Wedowski, M.; Meiling, H.; Klein, R.; Gottwald, A.; Scholze, F.; Visser, M.; Kurt, R.; Zalm, P.; Louis, E.; Yakshin, A. *Microelectron. Eng.* **2002**, *65*, 61−62.
(797) Hamamoto, K.; Tanaka, T.; Watanabe, T.; Sakaya, N.; Hosoya, M.; Shoki, T.; Hada, H.; Hishinuma, N.; Sugahara, H.; Kinoshita, H. *J. Vac. Sci. Technol. B* **2005**, *23*, 247.
(798) Graham, S.; Steinhaus, C.; Clift, M.; Klebanoff, L. *J. Vac. Sci. Technol. B* **2002**, *20*, 2393.
(799) Seo, H.; Park, J. Y.; Liang, T.; Somorjai, G. A. *J. Electrochem. Soc.* **2010**, *157*, H414.
(800) Niibe, M.; Koida, K.; Kakutani, Y. *J. Vac. Sci. Technol. A* **2011**, *29*, 011030.
(801) Papadatos, F.; Spyridon, S.; Zubin, P.; Steven, C.; Eric, E. *Mater. Res. Soc. Symp. Proc.* **2002**, *716*, B2.4.1−B2.4.5.
(802) (a) Kwon, O.-K.; Kim, J.-H.; Park, H.-S.; Kang, S. W. *J. Electrochem. Soc.* **2004**, *151*, C753. (b) Kwon, O.-K.; Kim, J.-H.; Park, H.-S.; Kang, S. W. *J. Electrochem. Soc.* **2004**, *151*, G109.
(803) Kang, S. Y.; Choi, K. H.; Lee, S. K.; Hwang, C. S.; Kim, H. J. *J. Electrochem. Soc.* **2000**, *147*, 1161.
(804) Yim, S.-S.; Lee, D.-J.; Kim, K.-S.; Lee, M.-S.; Kim, S.-H.; Kim, K.-B. *Electrochem. Solid-State Lett.* **2008**, *11*, K89.
(805) Kang, S. Y.; Hwang, C. S.; Kim, H. J. *J. Electrochem. Soc.* **2005**, *152*, C15.
(806) Saito, S.; Kuramasu, K. *Jpn. J. Appl. Phys.* **1992**, *31*, 135.
(807) Zhong, H.; Heuss, G.; Suh, Y. S.; Misra, V.; Hong, S. N. *J. Electron. Mater.* **2001**, *30*, 1493.
(808) Tsuzumitani, A.; Okuno, Y.; Shibata, J.; Shimiziu, T.; Yamamoto, K.; Mori, Y. *Jpn. J. Appl. Phys. Part 1* **2000**, *39*, 2073.
(809) Aoyama, T.; Yamazaki, S.; Imai, K. *Jpn. J. Appl. Phys. Part 1* **2000**, *39*, 6348.
(810) Grahn, V.; Hellberg, P. E.; Olsson, E. *J. Appl. Phys.* **1998**, *84*, 1632.
(811) Vijay, D. P.; Desu, S. B. *J. Electrochem. Soc.* **1993**, *140*, 2640.
(812) Kim, S. K.; Lee, S. Y.; Seo, M.; Choi, G.-J.; Hwang, C. S. *Appl. Phys.* **2007**, *102*, 024109.

(813) Fröhlich, K.; Tapajna, M.; Rosova, A.; Dobrocka, E.; Husekova, K.; Aarik, J.; Aidla, A. *Electrochem. Sol. Stat. Lett.* **2008**, *11*, G19.
(814) Kuesters, K. H.; Beug, M. F.; Schroeder, U.; Nagel, N.; Bewersdorff, U.; Dallman, G.; Jakschik, S.; Knoefler, R.; Kudelka, S.; Ludwig, C.; Manger, D.; Mueller, W.; Tilke, A. *Adv. Eng. Mater.* **2009**, *11*, 241.
(815) Kohlstedt, H.; Mustafa, Y.; Gerber, A.; Petraru, A.; Fitsilis, M.; Meyer, R.; Bottger, U.; Waser, R. *Microelectron. Eng.* **2005**, *80*, 296.
(816) Norga, G. J.; Fe, L.; Wouters, D. J.; Maes, H. E. *Appl. Phys. Lett.* **2000**, *76*, 1318.
(817) Choi, Y. C.; Lee, B. S. *Japn. J. Appl. Phys. Part 1* **1999**, *38*, 4876.
(818) Jia, Z.; Ren, T.-I.; Liu, T.-Z.; Hu, H.; Zhang, Z.-G.; Xie, D.; Liu, L.-T. *Mater. Sci. Eng., B* **2007**, *138*, 219.
(819) Kolawa, E.; So, F. C. T.; Pan, E.T.-S.; Nicolet, M.-A. *Appl. Phys. Lett.* **1987**, *50*, 854.
(820) Krusin-Elbaum, L.; Wittmer, M.; Yee, D. S. *Appl. Phys. Lett.* **1987**, *50*, 1879.
(821) Bat'ko, I.; Flachbart, K.; Somora, M.; Vanicky, D. *Cryogenics* **1995**, *35*, 105.
(822) Sahul, R.; Tasovski, V.; Sudarrsham, T. S. *Sensors & Actuators A* **2006**, *125*, 358.
(823) Jia, X.Q.; Anderson, W. A. *Appl. Phys. Lett.* **1990**, *57*, 304.
(824) Meyer, T. J.; Huynh, H. V. *Inorg. Chem.* **2003**, *42*, 8140.
(825) (a) Thomas, J. M.; Thomas, W. J. *Principles and Practice of Heterogeneous Catalysis*; VCH: Weinheim, 1997. (b) www.unicat.tu-berlin.de/ Retrieved 1June2011.
(826) Zaera, F. *Acc. Chem. Res.* **2009**, *42*, 1152.
(827) Seitsonen, A. P.; Over, H. In *High Performance Computing in Science and Engineering Garching/Munich 2007*; Wagner, S., Steinmetz, M., Bode, A., Brehm, M., Eds; Springer: Berlin Heidelberg, 2009; p 187.
(828) Jirkovsky, J.; Busch, M.; Ahlberg, E.; Panas, I.; Krtil, P. *J. Amer. Chem. Soc* **2011**, *133*, 5882.
(829) Shustorovich, E.; Sellers, H. *Surf. Sci. Rep.* **1998**, *31*, 5.
(830) Grubbs, R. H.; Chang, S. *Tetrahedron* **1998**, *54*, 4413.
(831) Somorjai, G. A.; Contreas, A. M.; Montano, M.; Rioux, R. M. *Proc. Natl. Acad. Sci. U.S.A.* **2006**, *103*, 10577.
(832) Koper, M. T. M.; Bouwman, E. *Angew. Chem., Int. Ed.* **2010**, *49*, 3723.
(833) Thomas, J. M.; Hernandez-Carrido, J. C.; Raja, R.; Bell, R. G. *Phys. Chem. Chem. Phys.* **2009**, *11*, 2799.
(834) Thomas, J. M. *Top. Catal.* **2006**, *38*, 3.
(835) Garcia-Mota, M.; Cabello, N.; Maseras, F.; Echavarren, A. M.; Perez-Ramirez, J.; Lopez, N. *Chem. Phys. Chem.* **2008**, *9*, 1624.
(836) Wachs, I. E. *Catal. Today* **2005**, *100*, 79.
(837) Teschner, D.; Borsodi, J.; Wootsch, A.; Revay, Z.; Havecker, M.; Knop-Gericke, A.; Jackson, S. D.; Schlögl, R. *Science* **2008**, *320*, 86.
(838) Doyle, A. M.; Shaikhutdinov, S; Freund, H. J. *Angew. Chem., Int. Ed.* **2005**, *44*, 629.
(839) Ertl, G.; Knözinger, H.; Schüth, F.; Weitkamp, J., Eds. *Handbook of Heterogeneous Catalysis*, VCH: Weinheim, 2008.
(840) Besenbacher, F.; Chorkendorff, I.; Clausen, B. S.; Hammer, B.; Molenbroek, A. M.; Norskov, J. K.; Steensgaard, I. *Science* **1998**, *279*, 1913.
(841) Jacobsen, C. J. H.; Dahl, S.; Clausen, B. S.; Bahn, S.; Logadottir, A.; Norskov, J. N. *J. Am. Chem. Soc.* **2001**, *123*, 8404.
(842) Hansen, T. W.; Wagner, J. B.; Hansen, P. L.; Dahl, S.; Topsøe, H.; Jacobsen, C. J. H. *Science* **2001**, *294*, 1508.
(843) Sinfelt, J. H. *Surf. Sci.* **2002**, *500*, 923.
(844) Somorjai, G. A.; Li, Y. *Proc. Natl. Acad. Sci. U.S.A.* **2011**, *108*, 918.
(845) Norskov, J. K.; Abild-Pedersen, F.; Studt, F.; Bligaard, T. *Proc. Natl. Acad. Sci. U.S.A.* **2011**, *108*, 939.
(846) Stampfl, C.; Ganduglia-Pirovano, M. V.; Reuter, K.; Scheffler, M. *Surf. Sci.* **2002**, *500*, 368.
(847) Koop, J.; Deutschmann, O. *Appl. Catal. B: Environ.* **2009**, *91*, 47.
(848) Jacob, T. Ab-initio Atomistic Thermodynamics for Electrocatalysis. In *Fuel Cell Catalysis: A Surface Science Approach*; Koper, M. T. M., Wieckowski, A., Eds.; John Wiley & Sons Inc.: New Jersey, USA, 2009.
(849) Neurock, M. *Ind. Eng. Chem. Res.* **2010**, *49*, 10183.
(850) Conway, B. E. *Prog. Surf. Sci.* **1995**, *49*, 331.
(851) *Handbook of Fuel Cells – Fundamentals, Technology, and Applications*; Vielstich, W.; Gasteiger, H. A.; Lamm, A., Eds.; Wiley: New York, 2003; Vol. 2. Electrocatalysis.
(852) Ertl, G.; Freund, H. J. *Phys. Today* **1999**, *52*, 32.
(853) Taylor, C. D.; Wasileski, S. A.; Filhol, J. S.; Neurock, M. *Phys. Rev. B* **2006**, *73*, 165402.
(854) Otani, M.; Hamada, I.; Sugino, O.; Morikawa, Y.; Okamoto, Y.; Ikeshoji, T. *J. Phys. Soc. Jpn.* **2008**, *77*, 024802.
(855) Jinnouchi, R.; Anderson, A. B. *Phys. Rev. B* **2008**, *77*, 245417.
(856) Wang, H. F.; Liu, Z. P. *J. Phys. Chem. C* **2009**, *113*, 17502.
(857) Jacob, T. *J. Electroanal. Chem.* **2007**, *607* (1–2), 158–166.